Bottom Quark Production in 1.8-TeV Proton-Antiproton Collisions

September 1991

Fumihiko Ukegawa

Submitted in partial fulfillment of the requirements
for the Degree of Doctor of Science
in the Doctoral Program in
University of Tsukuba

Abstract

We have studied the production of the inclusive electrons and the bottom quark in proton-antiproton collisions at a center-of-mass energy of 1.8 TeV.

In the QCD-improved parton model, the production of heavy quarks in hadron collisions is described in terms of the parton-parton hard scattering cross sections, proton structure functions and the coupling constant of the strong interactions. Recent calculations of the heavy quark production cross sections in the next-to-leading order show that the correction to the lowest order is large. The analysis presented here is the first measurement of the bottom quark production at the Tevatron energy, and thus provides a good testing ground for the above picture.

The data were collected in 1988-89 using the Collider Detector at Fermilab (CDF), located at the B0 interaction region of the Tevatron collider.

We first study the inclusive production of high transverse momentum electrons in the central rapidity region. It is expected that the heavy quark decays, bottom quark decays in particular, are the dominant source of these electrons. We detect them using the CDF central electromagnetic calorimeter (CEM). We describe the identification of the electrons and the separation from non-physics backgrounds. It is shown that the identification capability of the CEM is very good, and the background levels are manageable. The statistical isolation of heavy quark decay electrons, especially semileptonic bottom decays, is shown to be possible.

We demonstrate that our electrons originate mostly from bottom quark decays by partially reconstructing the semileptonic B hadron decays. In the electron events we observe the charm and strange particles, produced in the decays $b \to e\nu c$, and $c \to s$, at predicted rates.

The production rate of the electrons is converted to the bottom quark rate using the kinematical relationship between the electron and the parent bottom quark, the estimated electron detection efficiencies, and the semileptonic decay branching fractions from other experiments. We measure the bottom quark production cross section as a function of its transverse momentum. We obtain from the inclusive electron rates $\sigma(\bar{p}p \to bX) = 1220 \pm 390$, 220 ± 70, and 56 ± 18 nb for the rapidity range of $|y| < 1$ and the transverse momentum ranges of $p_T > 15$, 23 and 32 GeV/c, respectively, where the uncertainty is dominated by the systematic effects. From the rate of the associated charm production we obtain $\sigma(\bar{p}p \to bX) = 440 \pm 100 \pm 130$ nb for the kinematic range of $|y| < 1$ and $p_T > 19$ GeV/c, where the first uncertainty is statistical and the second is systematic. Two methods give consistent results each other. An extrapolation to a lower transverse momentum is consistent with another independent measurement using the full reconstruction of B meson decays into J/ψ and kaon, performed by other collaborators in CDF. The theoretical predictions are somewhat lower than our results.

Acknowledgements

I would like to thank my advisor, Professor Koji Takikawa, for his guidance and encouragement throughout my graduate years. He has provided me with advice in many phases of my study. I would like to thank Professor Kunitaka Kondo, who gave me the opportunity to join the CDF experiment and the support in working on CDF.

My deep appreciation is due to Dr. Barry Wicklund, who has been my advisor and co-worker since the beginning of my association with Argonne back in 1986. His keen insight into physics brought the bottom quark physics at CDF into reality, and his advice and patience made my days at Argonne fruitful ones. I would also like to thank all other members of the Argonne CDF group, led by Dr. Lawrence Nodulman, who gave me a good place to work at. In particular Dr. James Proudfoot is appreciated for his encouragement and advice in and out of the electron and heavy flavor analyses.

My many thanks go to Dr. Paul Tipton, who taught me a lot about B physics.

I would like to thank the members of the Tsukuba high energy physics group for their help and discussion. They include Shigeyuki Miyashita, Shinhong Kim, Itsuo Nakano, and Kiyoshi Yasuoka.

It has been my pleasure to know and be with many colleagues of CDF, who provided me with help in their own ways. I thank Taiji Yamanouchi, Masanori Mishina, Teruki Kamon, Milciades Contreras, Luc Demortier, Richard Hughes, Tim Rohaly, Steve Hahn and John Cooper, to name a few.

Finally I would like to thank the late Dr. Yoshimi Funayama, with whom I cannot share a good time any more.

This work was supported by the Ministry of Education, Science and Culture of Japan, and the U. S. Department of Energy, Division of High Energy Physics, Argonne National Laboratory, Contract W-31-109-ENG-38.

Contents

The CDF Collaboration

F. Abe,[8] D. Amidei,[4] G. Apollinari,[11] M. Atac,[4] P. Auchincloss,[14] A. R. Baden,[6] A. Bamberger,[a] A. Barbaro-Galtieri,[9] V. E. Barnes,[12] F. Bedeschi,[11] S. Behrends,[2] S. Belforte,[11] G. Bellettini,[11] J. Bellinger,[18] J. Bensinger,[2] A. Beretvas,[4] J. P. Berge,[4] S. Bertolucci,[5] S. Bhadra,[7] M. Binkley,[4] R. Blair,[1] C. Blocker,[2] A. W. Booth,[4] G. Brandenburg,[6] D. Brown,[6] E. Buckley,[14] A. Byon,[12] K. L. Byrum,[18] C. Campagnari,[3] M. Campbell,[3] R. Carey,[6] W. Carithers,[9] D. Carlsmith,[18] J. T. Carroll,[4] R. Cashmore,[a] F. Cervelli,[11] K. Chadwick,[4] G. Chiarelli,[5] W. Chinowsky,[9] S. Cihangir,[4] A. G. Clark,[4] D. Connor,[10] M. Contreras,[2] J. Cooper,[4] M. Cordelli,[5] D. Crane,[4] M. Curatolo,[5] C. Day,[4] S. Dell'Agnello,[11] M. Dell'Orso,[11] L. Demortier,[2] P. F. Derwent,[3] T. Devlin,[14] D. DiBitonto,[15] R. B. Drucker,[9] J. E. Elias,[4] R. Ely,[9] S. Errede,[7] B. Esposito,[5] B. Flaugher,[14] G. W. Foster,[4] M. Franklin,[6] J. Freeman,[4] H. Frisch,[3] Y. Fukui,[8] Y. Funayama,[16] A. F. Garfinkel,[12] A. Gauthier,[7] S. Geer,[6] P. Giannetti,[11] N. Giokaris,[13] P. Giromini,[5] L. Gladney,[10] M. Gold,[9] K. Goulianos,[13] H. Grassmann,[11] C. Grosso-Pilcher,[3] C. Haber,[9] S. R. Hahn,[4] R. Handler,[18] K. Hara,[16] R. M. Harris,[9] J. Hauser,[3] T. Hessing,[15] R. Hollebeek,[10] L. Holloway,[7] P. Hu,[14] B. Hubbard,[9] B. T. Huffman,[12] R. Hughes,[10] P. Hurst,[7] J. Huth,[4] M. Incagli,[11] T. Ino,[16] H. Iso,[16] H. Jensen,[4] C. P. Jessop,[6] R. P. Johnson,[4] U. Joshi,[4] R. W. Kadel,[4] T. Kamon,[15] S. Kanda,[16] D. A. Kardelis,[7] I. Karliner,[7] E. Kearns,[6] R. Kephart,[4] P. Kesten,[2] R. M. Keup,[7] H. Keutelian,[7] S. Kim,[16] L. Kirsch,[2] K. Kondo,[16] S. E. Kuhlmann,[1] E. Kuns,[14] A. T. Laasanen,[12] J. I. Lamoureux,[18] W. Li,[1] T. M. Liss,[7] N. Lockyer,[10] C. B. Luchini,[7] P. Maas,[4] M. Mangano[11] J. P. Marriner,[4] R. Markeloff,[18] L. A. Markosky,[18] R. Mattingly,[2] P. McIntyre,[15] A. Menzione,[11] T. Meyer,[15] S. Mikamo,[8] M. Miller,[3] T. Mimashi,[16] S. Miscetti,[5] M. Mishina,[8] S. Miyashita,[16] Y. Morita,[16] S. Moulding,[2] A. Mukherjee,[4] L. F. Nakae,[2] I. Nakano,[16] C. Nelson,[4] C. Newman-Holmes,[4] J. S. T. Ng,[6] M. Ninomiya,[16] L. Nodulman,[1] S. Ogawa,[16] R. Paoletti,[11] A. Para,[4] E. Pare,[6] J. Patrick,[4] T. J. Phillips,[6] R. Plunkett,[4] L. Pondrom,[18] J. Proudfoot,[1] G. Punzi,[11] D. Quarrie,[4] K. Ragan,[10] G. Redlinger,[3] J. Rhoades,[18] M. Roach,[17] F. Rimondi,[a] L. Ristori,[11] T. Rohaly,[10] A. Roodman,[3] A. Sansoni,[5] R. D. Sard,[7] A. Savoy-Navarro,[a] V. Scarpine,[7] P. Schlabach,[7] E. E. Schmidt,[4] M. H. Schub,[12] R. Schwitters,[6] A. Scribano,[11] S. Segler,[4] Y. Seiya,[16] M. Sekiguchi,[16] P. Sestini,[11] M. Shapiro,[6] M. Sheaff,[18] M. Shochet,[3] J. Siegrist,[9] P. Sinervo,[10] J. Skarha,[18] K. Sliwa,[17] D. A. Smith,[11] F. D. Snider,[3] R. St. Denis,[6] A. Stefanini,[11] R. L. Swartz, Jr.,[7] M. Takano,[16] K. Takikawa,[16] S. Tarem,[2] D. Theriot,[4] M. Timko,[15] P. Tipton,[9] S. Tkaczyk,[4] A. Tollestrup,[4] G. Tonelli,[11] J. Tonnison,[12] W. Trischuk,[6] Y. Tsay,[3] F. Ukegawa,[16] D. Underwood,[1] R. Vidal,[4] R. G. Wagner,[1] R. L. Wagner,[4] J. Walsh,[10] T. Watts,[14] R. Webb,[15] C. Wendt,[18] W. C. Wester, III,[9] T. Westhusing,[11] S. N. White,[13] A. B. Wicklund,[1] H. H. Williams,[10] B. L. Winer,[9] A. Yagil,[4] A. Yamashita,[16] K. Yasuoka,[16] G. P. Yeh,[4] J. Yoh,[4] M. Yokoyama,[16] J. C. Yun,[4] F. Zetti[11]

[1] *Argonne National Laboratory, Argonne, Illinois 60439*

[2] *Brandeis University, Waltham, Massachusetts 02254*

[3] *University of Chicago, Chicago, Illinois 60637*

[4] *Fermi National Accelerator Laboratory, Batavia, Illinois 60510*

[5] *Laboratori Nazionali di Frascati, Istituto Nazionale di Fisica Nucleare, Frascati, Italy*

[6] *Harvard University, Cambridge, Massachusetts 02138*

[7] *University of Illinois, Urbana, Illinois 61801*
[8] *National Laboratory for High Energy Physics (KEK), Tsukuba, Ibaraki 305, Japan*
[9] *Lawrence Berkeley Laboratory, Berkeley, California 94720*
[10] *University of Pennsylvania, Philadelphia, Pennsylvania 19104*
[11] *Istituto Nazionale di Fisica Nucleare, University and Scuola Normale Superiore of Pisa, I-56100 Pisa, Italy*
[12] *Purdue University, West Lafayette, Indiana 47907*
[13] *Rockefeller University, New York, New York 10021*
[14] *Rutgers University, Piscataway, New Jersey 08854*
[15] *Texas A&M University, College Station, Texas 77843*
[16] *University of Tsukuba, Tsukuba, Ibaraki 305, Japan*
[17] *Tufts University, Medford, Massachusetts 02155*
[18] *University of Wisconsin, Madison, Wisconsin 53706*
[a] *Visitor*

Chapter 1

Introduction

In this chapter we discuss the production of heavy quarks in hadron collisions. Here a heavy quark refers to either charm quark or bottom quark, but an emphasis is on bottom quark. The history of the heavy quarks has begun in 1974 with the discovery of the J/ψ resonance [1], a charmonium state, at a mass of 3.1 GeV/c^2. Charmonium is the name for a bound state composed of a charm quark (c) and its antiquark ($\bar{c}$). In general, the word quarkonium is used to refer to any quark-antiquark bound state with zero net flavor; they are said to have "hidden" flavor. Two years later, the first D mesons were observed [2], which are composed of a charm quark and a light antiquark. They have a net charm quantum number; they are called "open" flavors. These hadrons decays into non-charm states via weak interactions.

In 1977, the discovery of the Υ states followed [3], at a mass near 9 GeV/c^2. This was soon interpreted as the quarkonium state with a new flavor, the bottom (b) quark. These resonances were confirmed with e^+e^- annihilation experiments [4]. The B mesons, equivalents to the D mesons for the charm quark, are observed at the $\Upsilon(4S)$ resonance [5]. This state has a much large intrinsic width, about 20 MeV, compared with those of $\Upsilon(1S, 2S, 3S)$ states which are smaller than the resolution of the experimental apparatus. Therefore this state is considered to decay into B mesons by strong interactions. The high yield of large momentum leptons, expected from semileptonic B decays, also support

this interpretation.

Heavy hadrons give us opportunities to study weak decays of the heavy quarks. Much progress has been made for the understanding of the heavy quark decays mainly by e^+e^- annihilation experiments. Hadronization of the heavy quarks into hadrons are also studied. However, hadronic production properties of heavy quarks are yet to be investigated, especially for the bottom quark production, including the production cross section and the dynamics.

1.1 Hadroproduction of heavy quarks

Hard scattering processes in proton-antiproton collisions (or hadron-hadron collisions in general) are described in terms of the perturbative quantum chromodynamics (QCD) [6] and the parton model [7]. The basic picture of hard processes is that structureless, quasi-free partons (quarks and gluons) in hadrons undergo elastic scattering and emerge with high transverse momenta. As long as the momentum transfer in the process is large compared to the confinement scale, of order of GeV, the process can be treated with the perturbation theory. The various experimental results, the total hadronic cross section in e^+e^- annihilation, deep inelastic electron, muon or neutrino scattering off hadrons, high transverse momentum ($p_{\rm T}$) hadronic jet production, high-mass lepton pair production by the Drell-Yan process [8] including intermediate vector boson ($W^{\pm}, Z^0$) production, support the perturbative QCD quantitatively [9].

Hadroproduction of the heavy quarks is described by this picture as well. The lowest order processes [10] are the gluon fusion and the quark-antiquark annihilation ("flavor creation") processes, of which Feynman diagrams are shown in Figure 1.1. As seen in the figure, all the propagators in these processes are off mass shell by at least $4M_Q^2$, where M_Q is the mass of the heavy quark Q. Therefore these are always a short distance process, regardless of the momenta of the final state heavy quarks. Hence it is expected that the production of a sufficiently heavy quark is reliably predicted with the perturbative

approach for all the phase space. This is quite contrary to the case with light quarks and gluons, particles with nearly zero masses, where a lower cutoff of order of hadronic mass scale is necessary.

According to the factorization theorem [11], the inclusive cross section for the associated production of a heavy quark Q and its antiquark $\bar{Q}$ is expressed as a convolution of the subprocess cross sections with parton number densities $f_i(x_i, Q^2)$, with momentum fraction x_i at the scale Q^2:

$$d\sigma(hN \to Q\bar{Q}X) \simeq \sum_{a,b} \int dx_1 dx_2 \, f_a^h(x_1, Q^2) \, f_b^N(x_2, Q^2) \, d\hat{\sigma}(ab \to Q\bar{Q}). \qquad (1.1)$$

The features of the dynamics [12] of these lowest order processes are summarized as follows:

- Heavy quark pair is produced back-to-back in the parton center of mass system. Then the pair is back-to-back in the transverse plane in the laboratory frame.
- The net transverse momentum of the $Q\bar{Q}$ pair is small.
- The cross section for these subprocesses is proportional to $\alpha_s^2/\hat{s}$, where α_s is the strong interaction coupling constant, and $\sqrt{\hat{s}}$ is the parton center of mass energy.
- The transverse momentum $p_{\rm T}$ of the heavy quark is of order of its mass on the average, and falls rapidly with increasing $p_{\rm T}$.
- The rapidity difference between two heavy quarks is of order of 1.

Recently full next-to-leading order calculations for the single particle inclusive production of a heavy quark are complete for both the total cross section [13] and the differential cross section with respect to the transverse momentum and rapidity [14]. Examples of the higher order diagrams are given in Figure 1.2. The results show that the correction to the leading order calculation is fairly large.

In addition to the quantitative change in the cross section, which is normally referred to as the "K factor", the qualitatively new process is introduced by the higher order

correction. For example, there is a process called "gluon splitting", in which a virtually massive gluon is produced in the final state and splits into a quark antiquark pair, which can be a heavy quark pair when the gluon is massive enough. Since the pair is produced from a gluon with high $p_{\rm T}$, two heavy quarks emerge close together in the phase space, in contrast to the back-to-back feature in the lowest order processes. This is a process of order α_s^3, and a gluon splits into a heavy quark pair only a fraction $\alpha_s(m^2)/2\pi$ of the time [15]. However, the process $gg \rightarrow gg$ is about hundred times more frequent than the flavor creation process at the collider energy, and then it occurs at a comparable rate in the end.

There is another process called "flavor excitation" [16] as shown in Figure 1.3(a). This process had been considered to be one of the lowest order processes, with intrinsic, on-shell heavy quark component in the initial hadrons. The discrepancy between the charm hadroproduction data and the theoretical calculations were partly[1] ascribed to the importance of this process in addition to the flavor creation process. However, this process is infrared divergent when the momentum transfer t of the exchanged gluon goes to zero. Hence the cross section is highly sensitive to an arbitrary cutoff value of t. It is realized [11] that this process should be considered as a part of the higher order process shown in Figure 1.3(b). In this figure, the internal quark line is highly off-shell; its virtual mass is greater than that of the exchanged gluon. Therefor, this process is a higher order hard process, which is calculable with perturbative approach. In this process, one of the heavy quarks is produced with very low transverse momentum and usually escapes detection.

In spite of the large amount of radiative correction and the qualitatively new processes, the differential spectra with respect to the transverse momentum and the rapidity stay almost the same [14]. This is shown in Figure 1.4. The $p_{\rm T}$ spectrum with the radiative correction and that with the lowest order calculation multiplied by a factor 2.5

[1]There is a question of whether the charm quark is heavy enough to be dealt with the perturbative approach.

are shown for three different rapidity values.

Although QCD gives quantitative prediction for the production cross section of the heavy quarks, it is uncertain to some extent. The following three are the major sources of the uncertainty.

- Choice of the mass of the quark. We do not know the mass of the quark. We only know that it is of order of heavy meson masses. A change in the bottom quark mass from 5.0 GeV to 4.6 GeV results in the increase in the cross section by about a factor of two. A change from 5.0 GeV to 5.4 GeV gives the decrease by about a factor of two also.

- Structure functions. We know only poorly the gluon density at the relevant value of x and Q^2. Most of the structure function measurements come from electron, muon or neutrino deep inelastic scattering experiments. They are for large x and small Q^2, while in collider energy region those for small x and large Q^2 are important.

- Choice of the evolution (renormalization) scale (Q^2) for the strong coupling constant $\alpha_s(Q^2)$. This is an intrinsic theoretical uncertainty. It is only known that it should be chosen of order of the energy scale of the hard collision process. Commonly used choices include $Q^2 = m_Q^2$, $4m_Q^2$, and $\hat{s}$.

These sources result in overall uncertainty in the cross section at a factor of two level. For example, Figure 1.5 shows the evolution scale (it is called μ in the plot) dependence of the total bottom quark cross section in second and third order at the Tevatron energy, as discussed in [13]. The cross section is approximately doubled by the inclusion of the higher order corrections, and it does not help stabilizing the cross section under changes of the scale Q or μ. It shows that the prediction of the bottom quark production at collider energies is quite uncertain. This is contrary in the case of the top quark, which is much heavier.

Now let us look at the experimental results. The UA1 experiment [17] at the CERN SPS collider has used muons to tag bottom quark production, including inclusive single

muons, dimuons, and high p_T J/ψ's. The muon cross sections are directly measured, and are related to the parent bottom quark momentum. Inclusive muons are expected to come from the semileptonic decays of the heavy quarks. Dimuons can come from sequential decay $b \to \mu^- + c$, $c \to \mu^+ + s$, or the double semileptonic decays of a heavy quark pair. The former process gives small dimuon mass because two muons come from the same bottom quark, while the latter gives larger mass as two quarks are almost back-to-back in the transverse plane in the lowest order processes.

They obtained the cross section at $\sqrt{s} = 630$ GeV for the restricted range of the transverse momentum and rapidity of the b quark. The cross section is presented as a function of the lower cutoff of the b quark p_T, as shown in Figure 1.6. Curves are the theoretical calculations by Nason, Dawson and Ellis [14], with their estimation of the theoretical uncertainty. A good agreement is claimed between the data and the calculation.

Figure 1.7 shows the corresponding theoretical calculations at the Tevatron energy.

1.2 Heavy flavor tagging in hadron collisions

Because the vast majority of the hard hadron collisions comes from those of light quarks and gluons, it is not an easy task to selectively pick up events with heavy flavors. Prompt leptons are a popular way to tag heavy flavors in hadron collision experiments. This is because they are produced at a sizable rate, about 10% for each electron and muon channel, and the light quark and gluon processes do not usually produce such leptons. Multilepton final states are especially distinctive.

Leptons from heavy flavor decays are not in general isolated; they are produced in jets or accompanied by additional hadrons. Hence it is not trivial to identify such leptons. It is commonly believed that muons are more effective and efficient to be identified in such cases compared with electrons. However, the calorimeter system with finely segmented cells relative to the jet size enables us to identify such electrons.

In this analysis we use the proton-antiproton collisions at 1.8 TeV center-of-mass energy collected using the Collider Detector at Fermilab (CDF). In the CDF central detector, the calorimeter consists of projective towers with a cell size of 0.11 in pseudorapidity η and 0.26 radians (15°) in azimuth ϕ. This is fairly small compared to the typical size of the hadronic jets expanding over the cone of $0.5 \sim 0.7$ in the η-ϕ space, which corresponds to 27 to 53 towers.

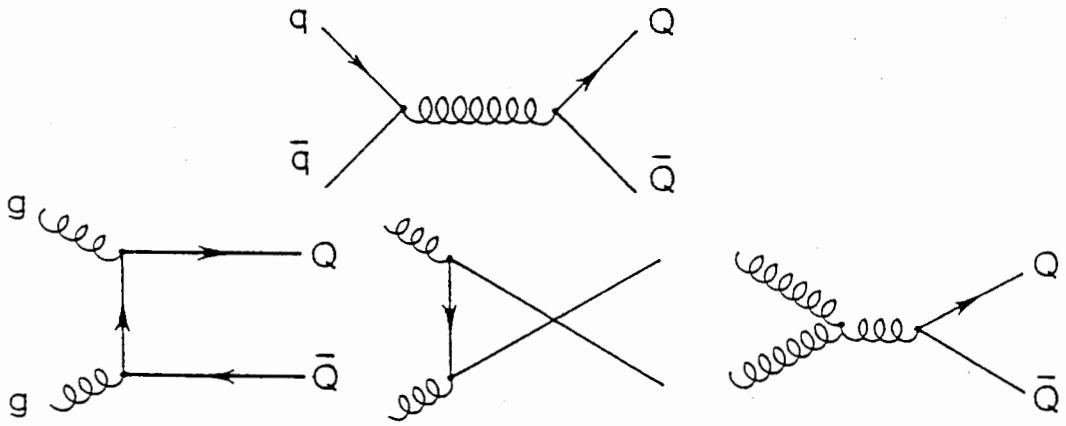

Figure 1.1: Feynman diagrams of the lowest order processes of heavy quark production.

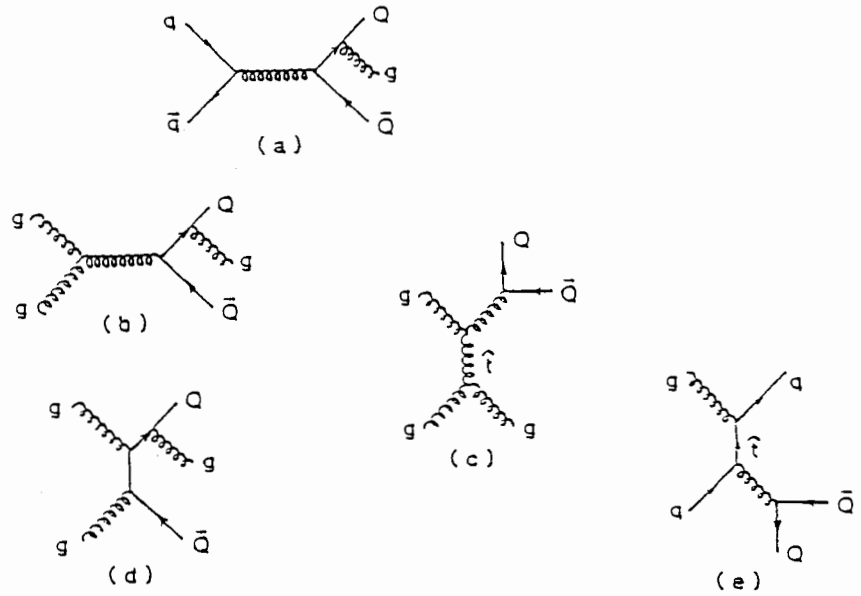

Figure 1.2: Example Feynman diagrams of the next-to-leading order processes of heavy quark production.

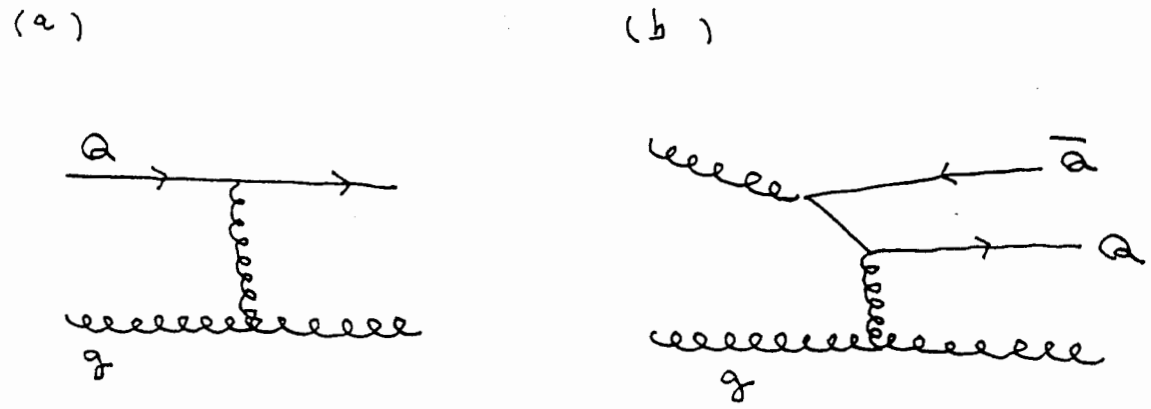

Figure 1.3: Feynman diagram of the "flavor excitation" heavy quark production process.

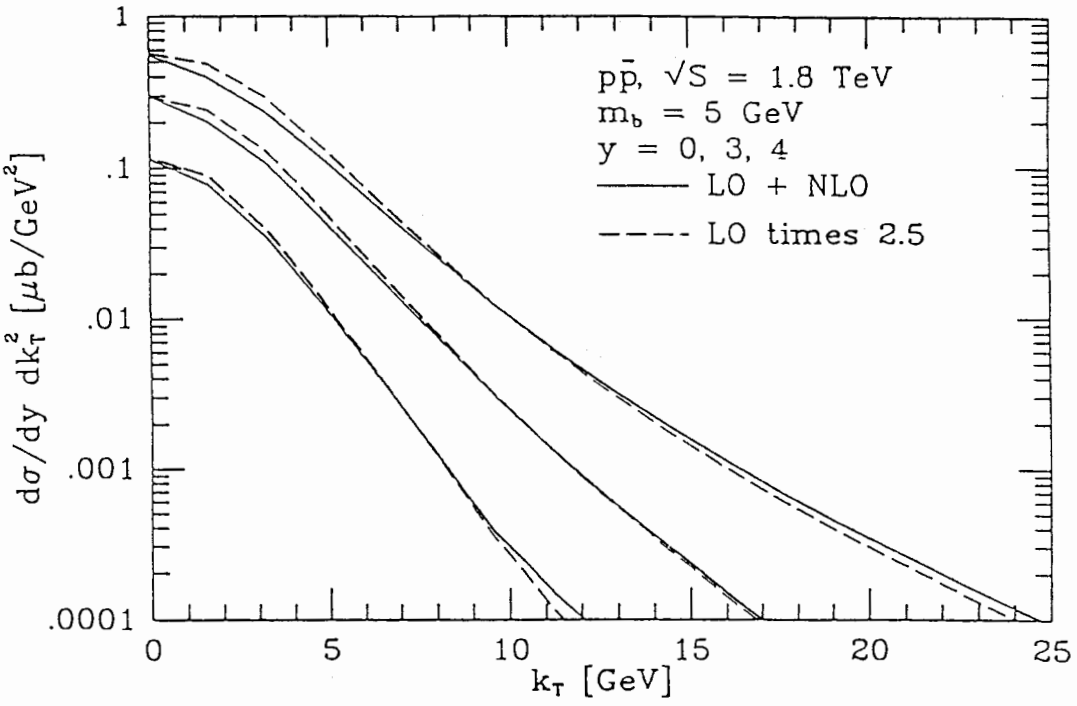

Figure 1.4: Bottom quark transverse momentum spectra calculated in the lowest order only and with the next-to-leading order processes. Taken from Ref. [14].

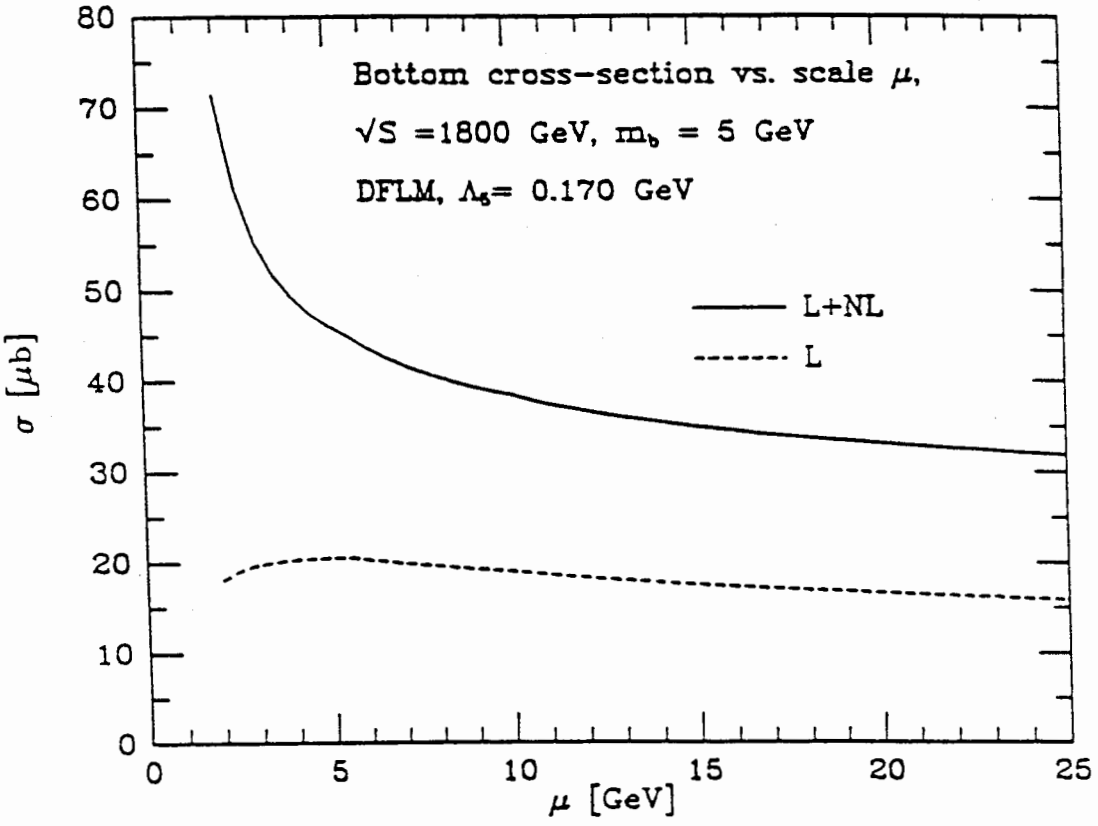

Figure 1.5: Scale dependence of the bottom quark production cross section at the Tevatron energy in second and third order. Taken from Ref. [9] (Figure 49).

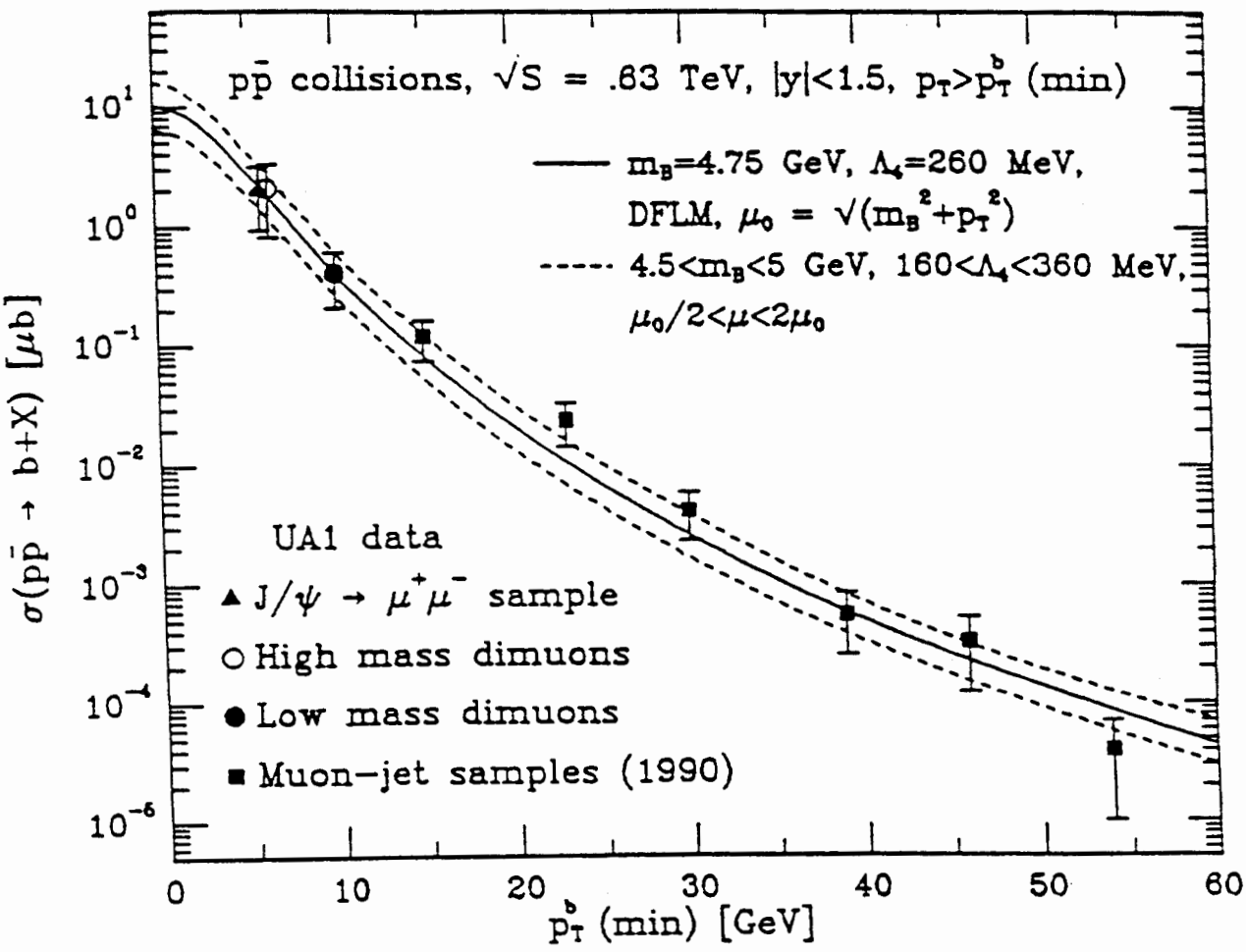

Figure 1.6: The cross section for bottom quark production at CERN energy as a function of the lower cutoff p_T of the b quark. Theoretical calculation by Nason, Dawson and Ellis [14], and data points from UA1 [17].

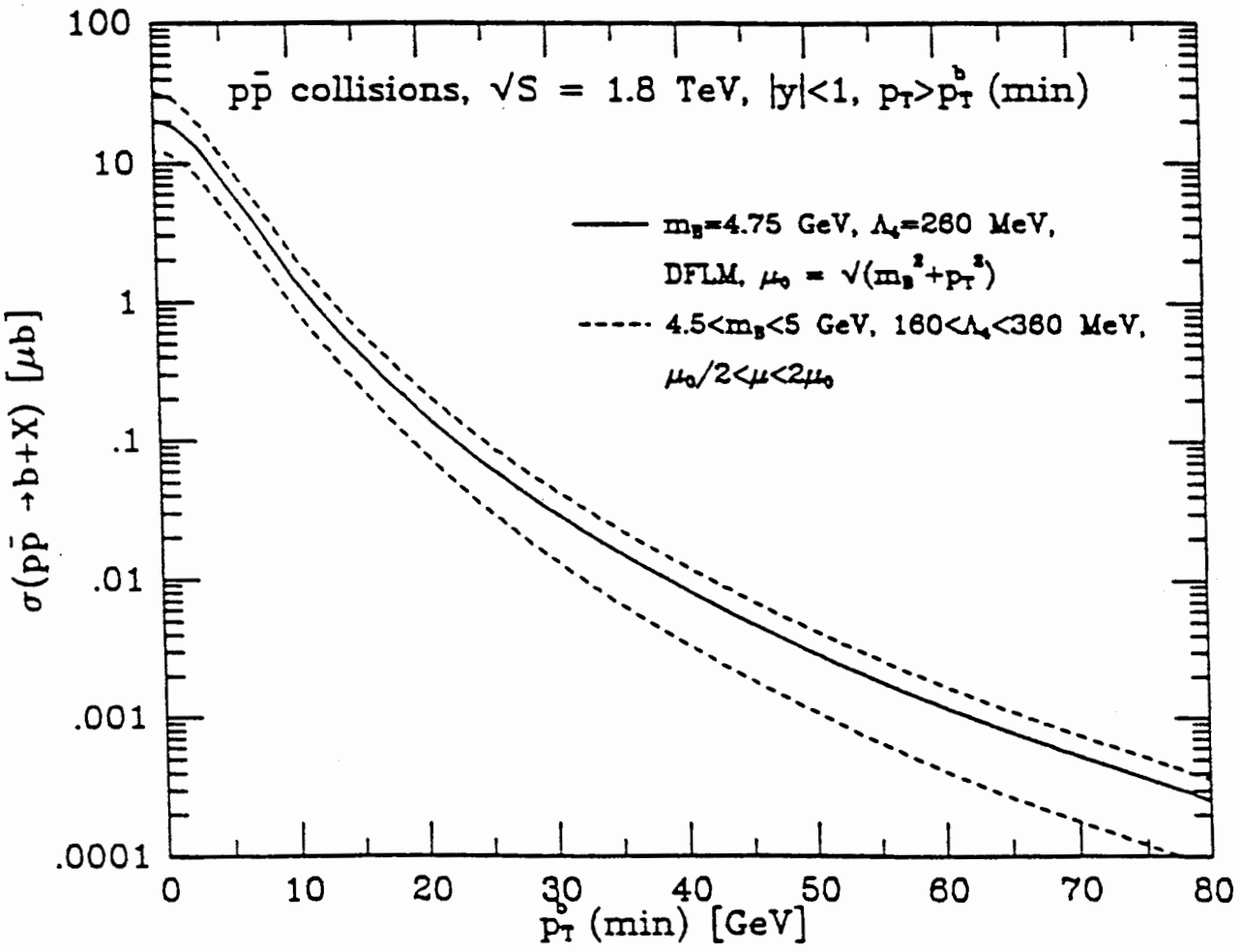

Figure 1.7: The cross section for bottom quark production at FNAL energy [14].

Chapter 2

The CDF Detector

In this chapter we describe the experimental apparatus, the Collider Detector at Fermilab (CDF). The emphasis will be on the central part of the CDF detector, where our sample of the electron candidates is selected and used for the study of the bottom quark production.

The CDF detector [18] is a general purpose magnetic detector which was designed to study the proton-antiproton collisions at 1.8 TeV center-of-mass energy. The detector covers almost all of the solid angle, down to 2° with respect to the beam direction and 2π in azimuth. It consists of three parts, central, forward and backward, as shown in Figure 2.1.

The calorimetric devices are used in order to measure the energy flow of particles from the collision, and the tracking devices measure the tracks of individual charged particles. Calorimeters are segmented into towers with projective geometry; each tower points back to the nominal interaction point. The size of the tower is typically 15 degrees in azimuth and 0.1 in pseudorapidity η, defined by $\eta = -\ln \tan \theta/2$, where θ is the polar angle with respect to the proton beam direction (z). The pseudorapidity rather than θ is used as the tower segmentation variable because the distributions of any particles or hadronic jets in hadron colliders are roughly flat in this variable.

2.1 Tracking chambers

In the central region of the detector (Figure 2.2), tracking chambers reside within a 1.4 T solenoid coil [19]. They allow precise momentum analysis of charged particles. We describe two tracking chamber systems below.

The vertex time projection chamber (VTPC) [20] is located just outside the beam pipe. It consists of eight time projection chamber modules along the beam direction z, and has a good track reconstruction capability in r-z plane. The main role of the VTPC is to determine the primary event vertex along the beam axis. The Tevatron beam has an r.m.s. width of about 35 cm along this axis. The VTPC determines the event vertex with an accuracy of about 2 mm.

The central tracking chamber (CTC) [21] is a large cylindrical drift chamber, 1.3 m in diameter and 3.2 m long. It is located outside the VTPC and covers the angular region $40° < \theta < 140°$ ($-1 < \eta < 1$). The chamber consists of 84 layers of sense wires grouped into 9 "superlayers". Five of them consist of 12 axial wires, and four of them consist of 6 stereo wires which have angles of $\pm 3°$ relative to the beam direction. The resolution of a single hit point is about 200 μm, and gives a momentum resolution of

$$\Delta p_{\mathrm{T}}/p_{\mathrm{T}} \simeq 0.002\, p_{\mathrm{T}}, \tag{2.1}$$

where p_{T} is the transverse momentum of a charged particle in GeV/c.

2.2 Calorimetry

A calorimetric device plays an important role in high energy experiments, especially in hadron collider experiments. This is because it can measure the energy of neutral particles as well as charged particles. Identification of a particular class of particles, an electron for example, is also possible.

The CDF calorimeters consist of three parts (central, plug and forward) depending

on the angular region. Each calorimeter has two longitudinal components, the electromagnetic in front and the hadronic behind. In this way an electromagnetic shower can be separated from a hadronic shower, because an electromagnetic (hadronic) shower has a faster (slower) development as a function of the amount of materials a particle passes through. All CDF calorimeters are of the sampling type, which consists of a passive absorber to create particle showers and an active medium to detect secondary particles in the showers.

The CDF central electromagnetic calorimeter (CEM) [22] consists of alternative layers of a plastic scintillator as a sampling medium and a lead sheet as a showering material. It is segmented into 24 modules in azimuth, and two along the beam direction, total of 48 wedge shaped modules (Figure 2.3). A "wedge" module has 10 towers, each of which covers 15 degrees in azimuth and about 0.11 in η.

The CEM has 31 scintillator and 30 lead layers, corresponding to a total amount of materials of 16 radiation lengths (X_0). The layers are placed parallel to the beam line; each layer keeps the same distance from the beam irrespective of the angle θ. This means that a particle which is away from the 90 degrees passes more material per layer. In order for a particle to pass through a constant amount of materials as a function of the polar angle θ, some of the lead layers in some towers are replaced with acrylic plates. Also some of the scintillator layers are painted black, in order to keep the output signal for a given energy of particle independent of the angle θ.

A typical size of a tower cell is 46 cm in r-ϕ (x) direction and 24 cm along the beam direction z. This is larger than the size of the electromagnetic showers, which is only a few cm's wide laterally.

Scintillation lights are converted in two wavelength shifter plates located at ϕ-boundaries of a tower, and are guided through light pipes to photomultiplier tubes (PMTs). Optical properties of the scintillator (SCSN-38) and the wavelength shifter (Y7) are given in [23].

Overall, a high photoelectron yield of

$$N_{\text{p.e.}} \sim 100\,/\text{GeV}\,/\text{PMT}, \tag{2.2}$$

is achieved.

Each of the CEM towers is calibrated using the electron beam of 50 GeV momentum. The calibration is maintained using the ^{137}Cs radioactive sources for the overall calorimeter response and the LED and Xenon flasher system for the phototubes and light pipes [24].

The energy resolution of the CEM is measured using the test beam electrons to be

$$\frac{\sigma(E)}{E} = \frac{0.135}{\sqrt{E \sin\theta}}, \tag{2.3}$$

where E is the energy measured in GeV and θ is the polar angle. The dependence on the polar angle is due to the increase in the absorber thickness in lower angle towers.

The response of CEM varies as a function of the position within a tower because of the light attenuation in the scintillator plates. Detailed response maps are obtained using test beam electrons [25] and cosmic ray muons [26].

A layer of wire proportional chamber (CES) is imbedded near shower maximum of the CEM (nominal depth at 5.9 X_0 including the coil). A chamber has two orthogonal views, anode wires measuring the r-ϕ view of the showers and cathode strips measuring the z view. A channel has a typical width of 1.5 cm. The fine segmentation enables us to measure more precise profiles of showers than with CEM towers. The position resolution of a few mm's is achieved for electromagnetic showers.

Behind the CEM there exist the central (CHA) and the wall (WHA) hadron calorimeters [27]. They both consist of layers of plastic scintillator and iron absorber. Towers have the same segmentation as the CEM.

Calorimeters covering the plug ($1.1 < |\eta| < 2.4$) and forward ($2.2 < |\eta| < 4.2$) regions of the detector employ gas proportional chambers with cathode pad readout as

detection device, and lead and iron plates as showering material for electromagnetic and hadron components, respectively. A tower size of $\Delta\eta \times \Delta\phi = 0.1 \times 5^\circ$ is used.

2.3 Trigger and data acquisition system

2.3.1 Data acquisition system

The CDF detector has a total of about 100,000 electronics channels, consisting of calorimeter phototubes, gas chambers (wires, strips and pads), drift chambers and so on. Calorimeter signals are sent to an analog front-end system called the RABBIT system [28]. It consists of amplifier cards including the sample-and-hold circuits and a digitizer card. After the signals are digitized, they are read out by scanners called MXs [28], which are interfaced to the Fastbus data acquisition system [29]. Drift chamber signals are shaped at the detector and then sent to commercial Fastbus TDC modules. They are then read out by scanners called SSPs [29]. The data acquisition system reads out events with an approximate event size of 100 kbytes at 10-20 Hz, and sends them to the level 3 trigger system described below.

2.3.2 Trigger system

The Tevatron was operated in the 1988-89 run with six bunches of protons and antiprotons, respectively. They cross each other at the B0 interaction region every 3.5 μsec. The $\bar{p}p$ inelastic cross section at 1.8 TeV is about 50 mb, and results in a total event rate of 50 kHz at a luminosity of 1×10^{30} cm^{-2}. Therefore we need to reduce it to a manageable level, a few Hz, by selecting events of physics interest.

The CDF trigger consists of four levels, level 0, 1, 2 and 3. The level 0 trigger requires the occurrence of an inelastic collision. The beam-beam counter (BBC) system, scintillator hodoscopes located in front of the forward and the backward detectors, is used to provide a coincidence signal and to tag the inelastic events.

The level 1 and 2 triggers [30] use signals from the calorimeters and the tracking

chambers to make decisions on the events accepted by the level 0 trigger. Calorimeter signals are summed into trigger towers with a size of $\Delta\eta \times \Delta\phi = 0.2 \times 15°$. In this way the whole CDF calorimeter is represented by a 42×24 array for both electromagnetic and hadronic energies. They are sent to the trigger electronics modules. The level 1 trigger makes a decision based on calorimeter signals in excess of a programmable threshold, a stiff CTC track from a fast hardware track processor [31], and the muon triggers [32]. The level 2 trigger can form clusters of energies using the 42×24 array. Other information can be combined to form the level-2 trigger. For example, a calorimeter cluster is required for an associated CTC track to form an electron trigger.

The level 3 trigger system performs a more sophisticated event selection by executing FORTRAN-77 programs. It uses an Advanced Computer Program (ACP) [33] processor located in VME creates, and its processing capacity is equivalent to about 67% of a VAX 11/780. In the 1988-89 run 50 such processors were used.

We had two triggers for the inclusive electrons on the central detector in the last run, employing different transverse energy ($E_{\rm T}$) thresholds. One uses a threshold at 12 GeV and the other at 7 GeV. The 12 (7) GeV trigger requires a trigger tower with electromagnetic transverse energy deposition in excess of 6 (3) GeV at level 1. At Level 2, the trigger required an electromagnetic cluster of $E_{\rm T}$ above 12 (7) GeV, and a small hadronic energy (HAD/EM < 0.125), and a matched CTC track with a $p_{\rm T}$ of at least 6 (4.8) GeV/c. The 12 GeV trigger had existed for the full period of the run. The 7 GeV trigger was implemented later in the run when the level 3 trigger became fully functional. It also used a pre-scaling of a factor of four at level 2.

2.4 Luminosity measurement

The luminosity can be obtained by counting the rate of a certain process of which cross section is known. We use inelastic $\bar{p}p$ events, and the BBC's to detect them. That is,

we have

$$\mathcal{L} = \frac{R_{\rm BBC}}{\sigma_{\rm BBC}}, \tag{2.4}$$

where $\mathcal{L}$ is the luminosity, $R_{\rm BBC}$ is the BBC event rate, and $\sigma_{\rm BBC}$ is the effective cross section visible to the BBC's. We estimate $\sigma_{\rm BBC}$ at 1800 GeV as follows.

We first calculate the corresponding quantity for the UA4 experiment at 546 GeV, using their absolute measurements of the total and elastic $\bar{p}p$ cross sections, to be 38.9 ± 1.8 mb. A small correction due to the difference in the geometry of the trigger counters at CDF and UA4 is made in order to convert the above quantity into the corresponding CDF quantity at 546 GeV, $\sigma_{\rm BBC}^{546}$. We then relate it to the value at 1800 GeV, $\sigma_{\rm BBC}^{1800}$, by using the measurements of the Tevatron luminosities ($\mathcal{L}_{\rm acc}$) based on accelerator parameters, and the observed BBC rates $R_{\rm BBC}$ at the two energies. They have a relation

$$\frac{\sigma_{\rm BBC}^{1800}}{\sigma_{\rm BBC}^{546}} = \frac{R_{\rm BBC}(1800)}{R_{\rm BBC}(546)} \cdot \frac{\mathcal{L}_{\rm acc}(546)}{\mathcal{L}_{\rm acc}(1800)}. \tag{2.5}$$

We obtain

$$\sigma_{\rm BBC}^{1800} = 46.8 \pm 3.2 \text{ mb}, \tag{2.6}$$

or a 7% uncertainty in the luminosity measurement. More details on this subject may be found in [34] and references therein.

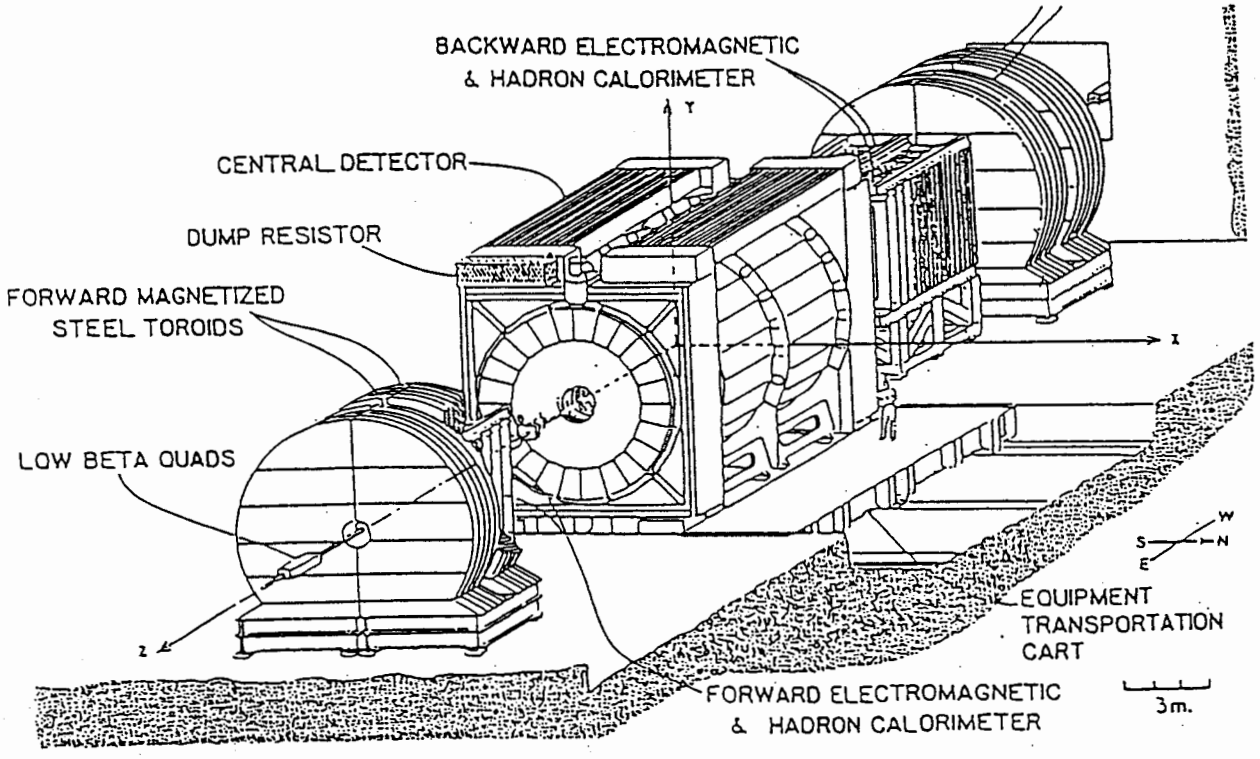

Figure 2.1: A perspective view of the CDF detector.

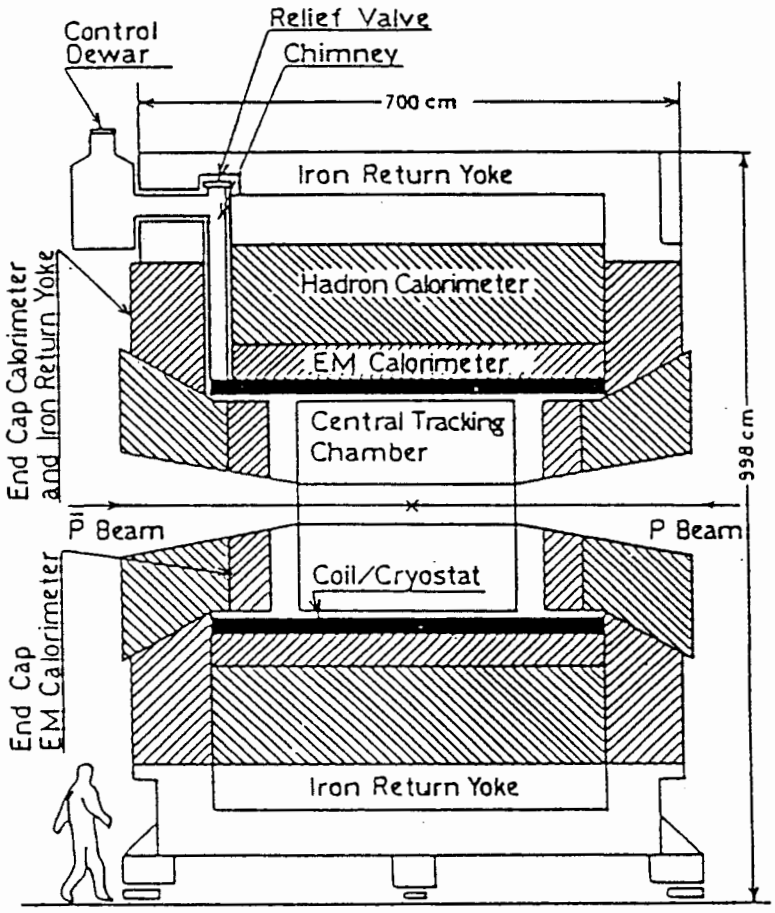

Figure 2.2: An elevation view of the CDF central detector.

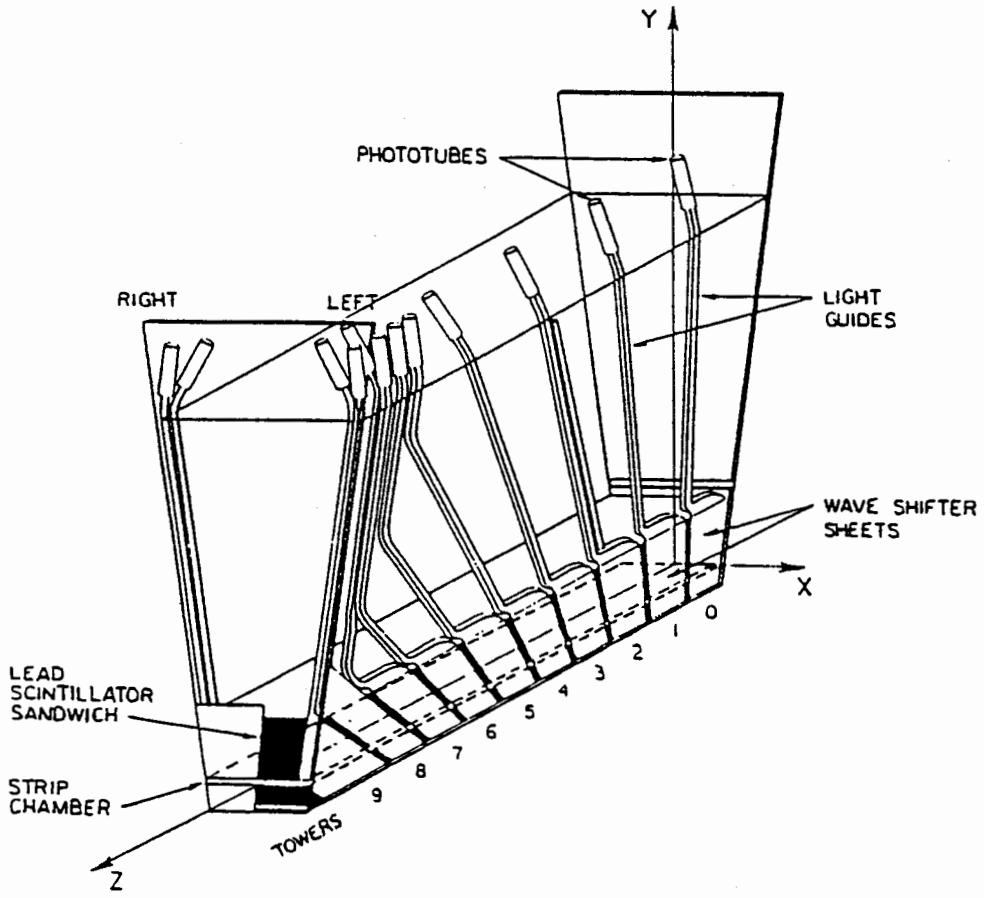

Figure 2.3: A central electromagnetic calorimeter (CEM) module.

Chapter 3

Electron Identification

In this and the following chapter we describe the electron identification and the extraction of the bottom quark events. In high energy hadron collisions hadronic jets from the gluon and the light quarks are copiously produced with high transverse momenta. The rate of these events are a few orders of magnitude higher than that of heavy quarks. Thus it is very difficult to identify heavy quarks through their hadronic decays.

An alternative is to select events containing one or more leptons. As described in Appendix A, the heavy quarks have substantial branching fractions for semileptonic decay modes (of order 10% each in electron and muon channels), which will be a source of single leptons. Multilepton signature can come from double semileptonic decays of a heavy quark pair, sequential decays of the b quark, and the B hadron decays involving J/ψ, followed by its dilepton decays.

Since there exists no mechanism of producing prompt leptons in gluon and light quark jets, these leptons are a good signature of the heavy quark production. The semileptonic bottom and charm quark decays are expected to be the dominant source of single leptons. The present analysis uses the inclusive electrons in the central detector.

In this chapter the identification of the electrons is described, along with the backgrounds to the electrons.

3.1 Identification methods

The CDF electron triggers on the central calorimeter select events having a large energy deposit on the electromagnetic calorimeter with a small hadronic leakage and an associated high transverse momentum track. At this level of event selection most of the events are backgrounds, rather than real electrons. The "electron" signature can occur by an overlap of multiple photons (which create electromagnetic energy deposit) and a charged particle (which leaves a signal in the tracking chamber). These overlap events occur at a high rate because their source is the jets of light quarks and gluons, which produce mainly pions.

In order to suppress these overlap events, we require that the observed "electron" cluster behave in a consistent way as expected for a real electron. We examine signals on the calorimeter and the tracking chambers and require that they are consistent with the patterns expected for a single electromagnetic particle. We use

- Longitudinal shower shape.
- Lateral shower shape.
- Geometrical matching of the calorimeter shower and the track positions.
- Comparison of the calorimeter energy and the track momentum.

We will discuss each item in more detail later in this Section.

Heavy flavor decay electrons are not isolated; they accompany additional hadrons or the lighter flavor jet. For example, a bottom quark decay is expressed at the parton level as

$$b \rightarrow e^{-} \bar{\nu} c, \tag{3.1}$$

where the c quark forms hadrons. Since the transverse momentum of the parent bottom quark is larger than its mass in the kinematic region now under consideration, the electron and the c quark are emitted in nearly the same direction. If electrons are completely buried in the jet, such electrons cannot be identified.

The identification capability depends on how finely calorimeter cells are segmented. The central calorimeter tower size is 0.11 in pseudorapidity η and 0.26 (15 degrees) in azimuth ϕ. A typical hadronic jet extends over a cone of $0.5 \sim 0.7$ in the η-ϕ space. The calorimeter tower size is smaller than the size of the jets, and thus we expect that we can identify those heavy flavor decay electrons. As described below, the isolation of electrons in three central calorimeter towers is required to identify electrons. This would be the minimal degree of isolation we have to require, implicitly or explicitly.

3.1.1 Identification variables

In this subsection we describe various tools to identify electrons. Before going into each item, the clustering algorithm is briefly described.

We first note that the physical size of the central electromagnetic calorimeter (CEM) tower is typically 24 cm by 46 cm and is much larger than the size of the electromagnetic showers, which is only a few cm's wide. A single electron deposits its energy on a single tower almost entirely, unless it hits near the tower boundary. Therefore we do not really need to form a cluster, unlike the case of hadronic jets.

The electron clustering algorithm first looks for a seed tower with an electromagnetic energy deposit above a certain threshold value (typically 3 GeV in transverse energy), and adds an adjacent tower on each side of the seed tower in the same azimuthal wedge when its energy deposit is above a lower threshold (typically 0.1 GeV in transverse energy). In the case of CEM clusters, the maximum number of towers in a cluster is limited to three, a seed tower and towers on each side in η. Towers adjacent in ϕ are not added because an electromagnetic shower does not extend over the ϕ boundary of wedges by construction. For the same reason a cluster across the 90° wedge boundary is prohibited.

Longitudinal shower shape: HAD/EM

An electron and a hadron show different longitudinal shower profiles. The former shows a faster development as a function of the amount of material it passes through. The CDF central calorimeter has the electromagnetic (CEM) and the hadronic (CHA) components, and we can differentiate electromagnetic showers from hadronic showers by comparing energy deposits on CEM and CHA and requiring a small hadronic energy. Figure 3.1 shows a typical distribution of the hadronic energy for high energy electrons.

After a cluster is formed, electromagnetic and hadronic energies of the cluster are compared. The cluster is accepted as "electromagnetic" when the ratio of the hadronic to electromagnetic energy (HAD/EM) is below a certain value. We usually use 0.1 for this ratio as a starting point. Later we tighten the cut in order to purify the sample.

Lateral shower shape: LSHR

First let us consider to reject background from QCD jets, namely overlapping charged hadrons and photons. We require an electron to be isolated in three CEM towers in η direction. As noted earlier in this subsection, a CEM tower is large enough to contain a full electromagnetic shower. Suppose an electron hits a region in a CEM tower well away from its boundary. Its energy deposit will be observed on that tower and nearly none on adjacent towers. This will be the shape of a single electron (strictly speaking, a single electromagnetic particle) on three CEM towers. On the other hand, overlap events would show a different distribution. Naively the shape of these overlaps is expected to be flat in the three towers because they consist of multiple particles reflecting the larger size of the parent jets. These are illustrated in Figure 3.2. To be quantitative and to treat properly the case in which the electron impact point is close to the tower boundary, a variable called LSHR [35] is defined as follows:

$$\mathrm{LSHR} = 0.14 \sum_k \frac{M_k - P_k}{\sqrt{0.14^2\, E_{\mathrm{cl}} + (\Delta P_k)^2}}, \tag{3.2}$$

where the sum is over towers adjacent to the seed tower in the cluster, M_k is a measured energy on the adjacent tower k, P_k is the same quantity predicted using the impact point in z on the strip chamber, the event vertex and the shower profile obtained from the test beam measurement. ΔP_k is an error in P_k associated with a 1 cm variation in the impact point, and $E_{\rm cl}$ is the cluster electromagnetic energy. The factor 0.14 represents a statistical fluctuation. The value of ΔP_k is very small most of the time, since a CEM tower with 24 cm width in z has full containment of showers (>99%) when a shower is more than 2 cm away from the z boundary.

This variable LSHR gives zero when an observed shape matches the expectation for a single electromagnetic particle. For overlapping multiple particles extending over towers, extra energies are observed on adjacent towers and the LSHR value becomes larger than zero. We shall demonstrate that 0.2 is an appropriate cut value.

For an overlap of charged and neutral hadrons, the momentum p of a charged particle measured by the tracking chamber is smaller than the calorimeter cluster energy E. This characteristics is well shown in Figure 3.3, the distribution of E/p for the sample of all "electron" clusters. Here an electron cluster is defined as any cluster with HAD/EM ratio below 0.1 with at least one track pointing to the cluster. The distribution is flat over the range, and no peak is seen. After applying an LSHR cut of 0.2, the sample is cleaned up and a peak is observable at $E/p \sim 1$. Also shown is the same distribution for the sample with LSHR larger than 0.2, where no peak is observable.

Lateral shower shape: CES χ^2

LSHR is useful in rejecting multiple particle showers extending over more than one CEM towers. However, a single CEM tower is still large enough to contain a few particles in it. Some QCD jets (or a part of them) with a few well collimated particles can produce such a shape. The strip chamber (CES) provides useful information in rejecting such kind of background by virtue of its finer segmentation than CEM towers.

The minimum distance d between two photons from a π^0 decay at the depth of the

CES (184.15 cm from the beam line) is expressed as

$$d \approx \frac{50}{p_{\mathrm{T}}} \text{ cm}, \tag{3.3}$$

where p_{T} is the transverse momentum of the π^0 in GeV/c. The distance d is about 7 cm (2 cm) for 7 (25) GeV/c π^0's.

A typical electron shower spreads over several CES channels and enables us to measure its shape and position. By applying a single shower hypothesis and checking the consistency between a measured shower shape and a predicted one, showers from multiple photons, namely π^0's, can be rejected. A least squares fit is performed for a measured CES cluster with the shower center as a free parameter. The χ^2 is defined as

$$\chi^2 = \frac{1}{4}\sum_{i=1}^{n} \frac{(q_i^{\mathrm{obs}} - q_i^{\mathrm{pred}})^2}{\sigma_{q_i}^2}, \tag{3.4}$$

where q_i is a normalized pulse height on channel i, n is the number of channels in a cluster. σ_{q_i} is an error in q_i and is defined as

$$\sigma_{q_i}^2 = (0.026)^2 + q_i^{\mathrm{pred}}(0.096)^2, \tag{3.5}$$

for 10 GeV electrons. The shape of the electron shower is measured using test beam electrons [36]. Let us denote the shower density by ρ, with the normalization

$$\int_{-\infty}^{\infty} \rho(x)\, dx = 1, \tag{3.6}$$

where x is the distance from the shower centroid. We define an integral shape I by

$$I(x) = \int_{x}^{\infty} \rho(x')\, dx'. \tag{3.7}$$

The $I(x)$ represents a fraction of shower which resides outside a certain distance x from its centroid. Figure 3.4 shows the shape I on the CES for 50 GeV/c test beam electrons.

A two component exponential function is fitted to data and is shown by curves in the plot.

The standard CES clustering algorithm uses a fixed number of channels, 11 by default, corresponding to a half width of about 8 cm. It ensures that both high p_T photons from a π^0 decay are contained in a single cluster, when the π^0 has a transverse momentum of 7 GeV/c or above. This in turn results in a larger χ^2 value when the profile is examined with a single shower hypothesis. This way we can achieve rejection of π^0's or QCD jets. Also expected is the rejection of charged pions. We show the CES χ^2 distributions for electrons and charged pions in Figure 3.5.

Here we mention the energy dependence of the χ^2 value. Since the shower fluctuation scales with the number of secondary electrons, it is plausible to assume χ^2 scales with $1/\sqrt{E}$. The error used for the χ^2 evaluation above does not include this energy dependence. Since the CES gives a relatively poor pulse height measurement[1], we use the CEM energy to correct the CES χ^2 value. The CES is located at a fixed depth ($\sim 5.9\,X_0$) in the CEM. Therefore it sees a different age of the longitudinal shower development depending on the electron energy, and shows a nonlinear response. We use a parameterization based on test beam measurements:

$$E_{\rm CES} = 2.11^{\ln(E_{\rm CEM})} \times 1.792, \tag{3.8}$$

where $E_{\rm CES}$ and $E_{\rm CEM}$ are pulse heights in GeV. We cut on the average of the χ^2's in two views at 10, after correcting for the energy dependence.

Position matching

Requiring a geometrical matching in the CES shower and the extrapolated track positions is useful in rejecting the overlaps, where the main part of energy deposit comes from photons, instead of a charged hadron, which usually leaves only a minimum ionizing

[1]The resolution of CES pulse height is about 20% and 30% in r.m.s. for 50 GeV/c and 10 GeV/c electrons, respectively.

signal on the CES.

The intrinsic position resolution of the CES is measured using test beam electrons to be a few mm's. In the real data the resolution of the tracking chamber contributes also. We apply the correction for the wedge alignment [37]. Figure 3.6 shows the distributions of the differences in the CES shower and the extrapolated track positions in both $r\phi$ and z views for the W electrons and inclusive 12 GeV electrons. We usually require

$$\begin{aligned} |\Delta r\phi| &< 1.4 \text{ cm}, \\ |\Delta z \sin\theta| &< 2.5 \text{ cm}. \end{aligned} \tag{3.9}$$

The $\sin\theta$ dependence is used in order to make the CES resolution constant.

The number of associated charged tracks

We usually require that one and only one track is pointing to the calorimeter electron cluster towers. The reason is twofold. First, we want to measure the electron energy accurately. Existence of an additional track, which is most likely a charged hadron, always increases the calorimeter energy. The subtraction on an event-by-event basis is almost impossible, since hadron showers fluctuate in a complicated way. The other is because the requirement makes the estimate of the electron selection efficiency easier and more reliable. Hadrons in the electron cell deposit their energies on the hadronic compartment, as well as on the electromagnetic compartment. The estimate of the cut efficiency of the hadronic energy fraction thus requires a detailed knowledge of hadron showers and their simulation, although not impossible.

Energy and momentum comparison

After applying the cuts on the variables described above, we are left with a sample of electron candidates. We should see a matching in the calorimeter energy and the track momentum, because we have selected electrons which are isolated in three CEM towers. Figure 3.7 shows the E/p distribution for the sample. We see a peak around E/p of

unity.

Fiducial region

In order to measure electron showers properly, we limit ourselves to the electrons found in a fiducial region

$$\begin{aligned} |r\phi| &< 21.5 \text{ cm}, \\ 9 \text{ cm} < |z| &< 200 \text{ cm}. \end{aligned} \tag{3.10}$$

In addition to these we require the electron is located on CEM towers 0 through 6 ($|\eta| \leq 0.8$). This is to achieve high acceptance of CTC tracks used for particle reconstruction (Section 4.2).

3.1.2 Other backgrounds

A combination of calorimeter and tracking information described above removes the overlap events and cleans up the initial sample to an electron-rich sample. However, there still remain backgrounds. They include an isolated charged hadron showering early in the calorimeter, and a photon conversion electron. They both can satisfy the identification cuts and reside on the peak of the E/p distribution.

Photon conversion electrons

Photons are copiously produced in jets, mainly through decays of neutral pions. They can convert to a pair of an electron and a positron while traversing detector material preceding the tracking chamber. Electron-positron pairs are also produced in the Dalitz decays of π^0's.

Some of them are removable on an event-by-event basis. We use the fact that the pair mass is of order of the electron mass, or practically zero. We should see a pair of tracks coming from a common point on the detector. In the axial magnetic field they separate in $r\phi$ view and are approximately collinear in rz view. Thus we look for a

partner CTC track satisfying

$$\begin{aligned} |S| &< 0.2 \text{ cm}, \\ |\Delta \cot\theta| &< 0.06, \end{aligned} \tag{3.11}$$

where S is the separation of two tracks in $r\phi$ plane at the point where they are tangent (conversion point). If a partner track satisfying the above requirement is found for an electron, we remove it as a photon conversion electron. Figure 3.8 shows the distributions of the above cut variables. The bottom plot shows the $r\phi$ separation S for pairs with $|\Delta \cot\theta| < 0.06$. In the $\Delta \cot\theta$ plot the solid (dotted) histogram corresponds to all pairs (pairs with $|S| > 0.2$ cm). We see a correlated peak at zero in S and $\Delta \cot\theta$. We call this method of identifying photon conversion pairs a pair algorithm.

Another handle on the photon conversions is hits on the VTPC [38]. When the conversion occurs at the outer wall of the VTPC or at the inner wall of the CTC, no signal will be observed on the VTPC.

The radial distribution of the conversion points is shown in Figure 3.9, which reveals the detector structure. The shaded area corresponds to pairs with low VTPC hit occupancy, which come from the walls as expected.

In our method of identifying photon conversion pairs (pair algorithm), the partner track has to be found and reconstructed in the CTC. As we shall see later the p_{T} spectrum of the conversion partner peaks strongly at zero where the track finding efficiency is expected to be low. In this region we can fail to find some of the pairs. We will present the estimate of the residual photon conversion electrons in Section 3.4.

The purity of the identified photon conversions is high; roughly 90% of them are the real electron pairs (Section 3.4). The origin of these pairs is "known" to be QCD jets of gluons and light quarks. Thus they serve as a good control sample to be compared with the prompt electron sample.

Interacting charged pions

Behavior of charged pions in the calorimeter is studied using test beam data. Sometimes a charged pion begins showering early in the detector and deposits almost all of its energy in the electromagnetic component. Although the probability is very small, of the order of 10^{-3}, the initial number of pions produced in collisions is huge enough to compensate the small probability and to make the rate of such hadrons comparable to that of the prompt electrons.

When such a pion is produced isolated within three CEM towers, it contributes as background to electrons. The shape on calorimeter towers (LSHR) will be consistent with the expectation. Since the shower is developed by the pion itself, the position from the track matches automatically the one on the calorimeter. Also since the energy deposit is produced only by the pion, it matches the measured momentum. This way these pions form a background which is hard to reject.

In order to minimize these hadron contamination, we cut on the hadronic leakage energy fraction at 0.04. We estimate the residual hadron background in Section 3.5.

3.2 Inclusive electron sample

In the 1988-89 CDF run we have two inclusive central electron triggers having different transverse energy thresholds. One uses a threshold at 12 GeV, and the other at 7 GeV. The 12 GeV trigger had existed since the beginning of the run, and the sample corresponds to the full luminosity of the run, 4.1 pb^{-1}. On the other hand, the 7 GeV trigger was implemented later in the run, when the level-3 trigger system became fully functional. It also employed the pre-scaling of a factor of four at the level-2 trigger. The 7 GeV sample corresponds to an integrated luminosity of about 250 nb^{-1}.

A full event reconstruction was performed for these data sets. We have extracted events from the output streams called TOS03 for 12 GeV electrons and TOP04 for 7 GeV electrons. The electron candidates are selected with the following cuts:

- LSHR < 0.2.
- CES-track position matching, $|\Delta x| < 1.4$ cm and $|\Delta z \sin\theta| < 2.0$ cm.
- CES $\chi^2 < 10$ on the average of wire and strip views.
- HAD/EM < 0.04.
- Number of charged particles pointing to the cluster is 1.
- $0.75 < E/p < 1.40$

Photon conversion electrons are removed using the method described in the previous Section. After applying the identification cuts, we have about 13,000 and 10,000 events in 12 and 7 GeV samples, respectively. Figure 3.10 shows the transverse momentum ($p_{\rm T}$) spectrum of the electron candidates.

The spectrum consists of two parts; one is a steeply falling part starting at lower $p_{\rm T}$, and the other is a shoulder above about 25 GeV/c. The latter originates from W and Z decay electrons, which exhibit a Jacobian peak at about a half of their masses, 40 GeV. The removal of these W and Z events is the subject of the next Section.

3.3 W and Z decay electrons

W and Z events are rather distinctive in their global event topology. Decays of W's into the electron channel involve an emission of a neutrino, which roughly balances the electron momentum. On the detector, the neutrino is inferred from the imbalance in the observed calorimeter energy, or the missing transverse energy, $\vec{E}_{\rm T}^{\rm miss}$. In the case of Z decay, we should see an additional high $p_{\rm T}$ electron which forms the Z invariant mass (about 91 GeV/c^2) together with the first electron.

The missing transverse energy is defined as

$$\vec{E}_{\rm T}^{\rm miss} = -\sum_i E_{{\rm T}i}\,\hat{n}_i, \tag{3.12}$$

where the sum is over calorimeter cells, E_{Ti} is the transverse energy on tower cell i, and $\hat{n}_i$ is a unit vector in transverse plane pointing to the cell i. In an ideal detector this vector coincides with a neutrino transverse momentum vector. In practice various detector effects introduce a finite and relatively poor resolution in this quantity. Calorimeter resolutions, nonlinear responses of the calorimeter to hadrons, and inactive regions of the detector are the main sources of the missing E_T resolution. To optimize it we scale the hadronic energies of the event (the electron is not included, because the resolution is much better) by a factor of 1.4 [39] and recalculate the $\vec{E}_T^{miss}$ (corrected missing E_T).

We remove W and Z electrons requiring

- Corrected missing E_T $< 8\sqrt{E_T}$, where E_T is the electron transverse energy in GeV/c.
- Mass (e,jet) < 80 GeV/c^2 if the jet has EM fraction above 0.85.

Distributions of the cut variables are shown in Figures 3.11 and 3.12. We see that the separation is good and expect little residual W and Z events.

We show in Figure 3.13 the p_T spectrum of the electron candidates after the W and Z decay electrons are removed. We also show the corresponding distributions for the identified photon conversion electrons (Figure 3.14), and the "charged hadrons", electron candidates with large hadronic energy fraction (HAD/EM > 0.07) (Figure 3.15). We note that the spectra are similar in shape each other. This fact suggests that the background fraction in the prompt electron sample is approximately constant as a function of p_T.

3.4 Residual photon conversion electrons

Photon conversion electrons are one of the background sources to the prompt electrons. We can remove some of them on an event-by-event basis as stated in Section 3.1.2. There it was required that the track of the conversion partner was found and reconstructed

("pair algorithm"). When the p_{T} of the partner is small enough, it will be curled within the axial magnetic field and will not be reconstructed as a track with high efficiency. As we will see later, the spectrum of the conversion partner is soft, and the loss at low p_{T} region is not negligible. This is the main cause of the inefficiency of the pair finding algorithm.

Since we measure the absolute p_{T} spectrum of the photon conversion electrons identified by the pair algorithm, we can calculate the number of residual conversion electrons in the prompt electron sample, once the efficiency for finding the pair is known. We attempt to do this as a function of the p_{T} of the electron.

In an event of a photon conversion in a π^0 decay, we have three particles: an electron, a positron and an unconverted photon. We refer to the primary conversion electron which makes the electron cluster as electron, and to the conversion partner, with normally lower p_{T}, as positron. The electron and the positron point to the same direction in space at the conversion point. As they pass through the magnetic field, they are bent in opposite directions and separate in the r-ϕ plane. They separate also in r-z view, although small, because the momentum difference is in general not zero. As a good approximation, however, two particles have the same z coordinates at any radius.

There are several possible configurations of these particles as seen on the detector, and we divide them into two classes. The first class (we refer to as $N_{\mathrm{track}} = 1$) consists of those events where the electron cluster has only one track pointing to it, and the second ($N_{\mathrm{track}} > 1$) with more than one track. In other words, the first class of events have the partner positron outside the electron cluster towers. The second class of events have both the electron and the positron in the same cluster. The unconverted photon can be anywhere in either case. We ignore the rest of the jet particles so here we have two tracks at most.

The energy E and the momentum p of the electron cluster are expressed using the electron (positron) energy E_- (E_+) and the momentum p_- (p_+) and the energy of the

unconverted photon E_γ as

$$\left.\begin{array}{c} E = E_- \ (+E_\gamma), \\ p = p_-, \end{array}\right\} \ N_{\rm track} = 1 \tag{3.13}$$

for the first class of events. For the second class of events, we have

$$\left.\begin{array}{c} E = E_- + E_+ \ (+E_\gamma), \\ p = \max(p_-, p_+). \end{array}\right\} \ N_{\rm track} > 1 \tag{3.14}$$

In an ideal detector, the energy and the momentum are identical for each particle. We note that the kinematics is different for the two classes, since the positron has to have a large $p_{\rm T}$ to reach the same cell as the electron after going through the magnetic field. The minimum transverse momentum of 1.2 GeV/c is necessary for the positron to reach the same tower as the electron with the infinite momentum, if they are produced on the beam axis, $r = 0$.

We are interested mainly in the first class of events, since for the second class the track finding efficiency is unity by definition. We have shown the observed $E_{\rm T}$ spectra of the "prompt" electrons[2] (Figure 3.13) and the identified photon conversion electrons (Figure 3.14). Contribution of the W and Z decays is removed in the prompt electron sample. Two spectra are similar in shape, steeply falling with $p_{\rm T}$, and the relative rate is about 5 to 1.

3.4.1 Efficiency of the photon conversion removal algorithm

Photon conversion Monte Carlo generator

We use a Monte Carlo calculation to predict the kinematics of the photon conversion events, the spectrum of the partner positron in particular. We provide here a description

[2]The "prompt" electron sample here of course includes fake and non-prompt electron backgrounds. The word "prompt" is used to refer to the electron candidates which are not identified as photon conversion pairs.

of the photon conversion Monte Carlo generator.

An event is generated as follows. We assume that the π^0 is the only source of the photons. We parameterize the π^0 $p_{\rm T}$ spectrum as $p_{\rm T}^{-\alpha}$, where α of 5.5 is used in order to reproduce the observed electron spectrum. The flat distribution in η is used. The π^0 is then decayed to two photons. One of them is picked up at random and then forced to covert to a pair of an electron and a positron. The energy sharing function between the electron and the positron is taken from Ref. [40]. The case for the ultra-relativistic limit is used (Figure 3.16). The radius of the conversion point is generated according to the distribution observed in the real data (Figure 3.9), therefore the Dalitz decays are automatically included. Then each particle is propagated to the CES plane.

The event is passed through the detector simulation (Section 5.3.1) of the CEM and the CES, the reconstruction of the electron cluster and the CES showers, and the electron identification selections (LSHR, CES χ^2, track-shower position matching, E/p). This process is necessary in order to reproduce the situation in real data, because the application of the identification cuts changes the kinematics of the events. For example, the E/p cut explicitly restricts the range of the energy/momentum of the particles other than the electron.

We first demonstrate that our Monte Carlo generator reproduces the $p_{\rm T}$ spectra of the electrons and the positrons in the real data shown in Figure 3.17. Figure 3.18 shows the corresponding Monte Carlo predictions. In comparing the $p_{\rm T}$ spectra, we require the minimum positron $p_{\rm T}$ of 1 GeV and the minimum electron $E_{\rm T}$ of 15 GeV. With these cuts we can avoid possible biases to kinematics due to the inefficiencies in the positron track reconstruction and in the hardware trigger for the electron cluster. We see that the Monte Carlo events reproduce the kinematics of the photon conversion pairs reasonably well.

Track finding efficiency

Figures 3.19 and 3.20 show the electron and the positron spectra without the cut on the positron $p_{\rm T}$. We note that the Monte Carlo positron spectrum is strongly peaked at zero, where the track finding efficiency is expected to be low.

By comparing these positron spectra between the data and the Monte Carlo, we get the track finding efficiency as a function of the positron $p_{\rm T}$. We have normalized the Monte Carlo distribution to data in the region above 2 GeV. The efficiency is shown in Figure 3.21. We refer to this efficiency as $\epsilon_{\rm track}$. We see that the efficiency becomes flat at 1.5 GeV and above. Actually we do not really know the absolute value of the efficiency in the plateau region, although it would be close to unity. We estimate the efficiency in this region later in this subsection.

Efficiency of the cuts

Now we estimate the efficiency of the cuts (Eq. (3.11)) used to identify photon conversion pairs. A pure sample of photon conversion pairs identified by methods other than the pair algorithm enables us to extract the cut efficiency of the pair algorithm. We use two different methods to evaluate the cut efficiency.

The first method relies on VTPC hit information [38] to identify photon conversions occurred at the outer VTPC and the inner CTC walls. These "outer" conversions should appear with low VTPC hit occupancy. We assume that the VTPC is 100% efficient. We define a photon conversion if the VTPC hit fraction[3] is less than 0.2 and an electron track is away from a radial board of VTPC modules. Then we look for a candidate partner track having the minimum value in the squared sum of the $r\phi$ separation S and the $\cot\theta$ difference. We note that the candidate track found here is not necessarily the true partner. If the $p_{\rm T}$ of the real partner positron was very low its track may have been lost.

[3]The VTPC hit fraction is defined as the ratio of the number of active wires to the number of expected hit wires along a road defined by the CTC track parameters for an electron. There are 24 wires along the radial direction for a particle with normal incidence.

Hence the candidate track defined above can be a random particle in the event, which is most likely a charged hadron. In order to reduce this hadron background, we require that the $p_{\rm T}$ of the track be above 1.5 GeV/c, and that the radius of the conversion point for the candidate track pair be between 20 cm and 30 cm, being consistent with the outer conversions. We also require a large pulse height (more than minimum ionizing) on the CES[4]. For those tracks, the distributions of the $\Delta \cot\theta$ and the separation S are plotted in Figure 3.22. It is seen that the distributions are fairly clean. We find the efficiency of the cuts, $|\Delta \cot\theta| < 0.06$ and $|S| < 0.2$ cm, as

$$\epsilon_{\rm cuts} = 525/543 = 0.967 \pm 0.008, \tag{3.15}$$

for the outer conversions.

The second method uses strip information of the CES to identify photon conversions. As described before, a distinct feature of the photon conversion pairs is that the electron and the positron have approximately the same z position at any radius, on the CES plane for example. When the separation in r-ϕ is large enough and the electron and the positron reach different wedges, we can measure the two z positions independently on the CES.

In an event with an electron we look for a charged track pointing to the wedge next to the electron. The charge of the track has to be the opposite of the electron, and has to point to the right wedge as expected from the given charge combination. The track is then extrapolated up to the CES plane. In order to remove charged hadrons, we require a large pulse height both on the strip chamber ($E_{\rm ces}/p > 0.5$) and the CEM ($E/p > 0.7$).

For events passing and failing the cuts we look at the distribution of dz, the difference of the electron and the positron z coordinates, and count the number of events on peaks. We do this for inner ($R < 15$ cm) and outer ($R > 15$ cm) conversions separately. Distributions of dz are shown in Figure 3.23. We obtain the efficiency as

[4]We use the sum of five CES wires around the extrapolated track position.

	Method	
	CES	VTPC
$R < 15\,\mathrm{cm}$	0.961 ± 0.014	
$R > 15\,\mathrm{cm}$	0.953 ± 0.010	0.967 ± 0.008
$R =$ all	0.956 ± 0.010	

Table 3.1: Efficiency of the cuts of photon conversion finding algorithm.

$$\begin{aligned} \epsilon_{\mathrm{cuts}} &= 0.953 \pm 0.010 \quad (R > 15\,\mathrm{cm}), \\ &= 0.961 \pm 0.014 \quad (R < 15\,\mathrm{cm}), \\ &= 0.956 \pm 0.010 \quad (R = \mathrm{all}). \end{aligned} \tag{3.16}$$

We find efficiencies consistent with that obtained by using the VTPC information.

The cut efficiencies are summarized in Table 3.1.

Track finding efficiency above 1.5 GeV/c

We have obtained the (p_{T} dependent) track finding efficiency (ϵ_{tot}) by comparing the observed and the predicted p_{T} spectra of the partner positron. We have normalized them in the region above 2.0 GeV/c, and have found that the efficiency is constant above 1.5 GeV/c (Figure 3.21). We now estimate the track finding efficiency in this region, although we expect that it is fairly close to unity.

We use the CES information again and look for a peak at zero in the difference between the electron and the positron z coordinates (dz). We do this for the events where a track is found and where it is not found.

We first reconstruct CES showers on the "right" next wedge adjacent to the electron tower. We pick up the largest pulse height shower within three towers in η direction. We also require a large pulse height on the CEM ($E/p > 0.7$ assuming $p_{\mathrm{T}} = 1.5$ GeV/c).

In order to ensure that the positron track p_{T} associated with this CES shower is above 1.5 GeV/c, we require that the shower be "close" to the primary electron shower in r-ϕ view. As noted earlier, the separation in r-ϕ space is smaller for the higher p_{T}

positron. Once we fix the conversion point, there exists a unique relationship between the p_T of the positron and the r-ϕ position difference between the electron and the positron. We assume the radius of 30 cm or the maximum possible value. If the conversion had occurred really at a smaller radius, the positron with the same value of r-ϕ separation would have had a larger p_T. Hence this is a safe assumption.

Figure 3.24 shows the distributions of the dz. We find the number of events on the peaks as 707 ± 39 and 40 ± 10 from the fit, and accordingly the track finding efficiency above 1.5 GeV/c as

$$\epsilon_{\rm track}^{>1.5} = 0.947 \pm 0.013. \tag{3.17}$$

Overall efficiency

By using the efficiencies obtained above, we now can calculate the fraction of unseen photon conversions for a given electron E_T. We first fix E_T of the electron. Let $N_{\rm id}$ be the number of identified photon conversions. This is related to the number of total conversions, $N_{\rm prod}$, the sum of the identified and the lost, as

$$N_{\rm id} = N_{\rm prod}\, \epsilon_{\rm tot}. \tag{3.18}$$

We have factorized the total efficiency as

$$\epsilon_{\rm tot} = \epsilon_{\rm track}\, \epsilon_{\rm track}^{>1.5}\, \epsilon_{\rm cuts}. \tag{3.19}$$

Since the track finding efficiency $\epsilon_{\rm track}$ is dependent on the p_T of the partner positron, we need to integrate over the p_T spectrum of the partner positron:

$$N_{\rm id} = \int \frac{dN}{dp_T^+}\, \epsilon_{\rm tot}(p_T^+)\, dp_T^+, \tag{3.20}$$

where the positron spectrum $dN/dp_{\rm T}^{+}$ is normalized so that

$$\int \frac{dN}{dp_{\rm T}^{+}}\, dp_{\rm T}^{+} = N_{\rm prod}. \tag{3.21}$$

The fraction $f_{\rm id}$ of identified photon conversions for a given electron $E_{\rm T}$ is

$$f_{\rm id}^{\rm conv} = N_{\rm id}/N_{\rm prod}. \tag{3.22}$$

We note that $f_{\rm id}^{\rm conv}$ varies as a function of $E_{\rm T}$ of the electron, since positron $p_{\rm T}$ spectrum is dependent on $E_{\rm T}$. Monte Carlo positron spectra are shown in Figure 3.25 for four different electron cluster $E_{\rm T}$ values. We use these positron $p_{\rm T}$ spectra, and the track finding and the cut efficiencies obtained from the real data. The overall efficiency for finding photon conversion pairs We calculate $f_{\rm id}^{\rm conv}$ in this way and plot in Figure 3.26 as a function of electron cluster $E_{\rm T}$. We see that $f_{\rm id}^{\rm conv}$ increases as $E_{\rm T}$ increases. This behavior is expected because the partner positron $p_{\rm T}$ spectrum becomes harder with an increasing cluster $E_{\rm T}$ and then the loss at the low $p_{\rm T}$ region becomes smaller.

We can measure the same quantity directly in the real data by using the VTPC information for the "outer" conversions. We regard the electron candidate as a photon conversion electron when the track has the VTPC hit fraction less than 0.2. By checking whether this event is also identified as a photon conversion electron by the pair algorithm, we obtain the overall efficiency of the pair algorithm as

$$f_{\rm id}^{\rm conv}(12\ {\rm GeV}) = 1219/2379 = 0.512 \pm 0.010, \tag{3.23}$$

$$f_{\rm id}^{\rm conv}(7\ {\rm GeV}) = 803/1799 = 0.446 \pm 0.012, \tag{3.24}$$

integrated over the electron $E_{\rm T}$ spectra in the 12 GeV and 7 GeV electron samples with the mean $E_{\rm T}$ values of 14.6 GeV and 8.8 GeV, respectively. They are plotted also in Figure 3.26.

The Monte Carlo calculation predicts the efficiencies of 0.582 at 14.5 GeV and 0.510

at 8.5 GeV electron $E_{\rm T}$. There exists a relative 13% difference. In order to estimate the residual background in the "prompt" electron sample, we use the $p_{\rm T}$ dependent shape of the efficiency as predicted by the Monte Carlo calculation, and scale the absolute value so as to match the efficiency obtained from the VTPC-identified conversions. The difference of 13% is taken as the systematic uncertainty of the efficiency.

3.4.2 Over-efficiency

The pair finding algorithm can be over-efficient to some extent, due to a contribution of a random track in the event. When a random track in the prompt electron event happens to satisfy the requirement of Eq. (3.11), we misinterpret the electron as a photon conversion electron. Since the magnitude of the effect depends on the event topology, or the source of the electron, we estimate the loss of the electrons due to the over-efficiency using the Monte Carlo b quark events and absorb in the electron selection efficiency. We estimate the loss of b quark decay electrons to be 0.033 ± 0.002 (Section 5.3.5).

Here we study the same effect with a different approach, as a check of the above number. Since the random track picked up by the pair algorithm is most likely a charged hadron, estimating the over-efficiency is equivalent to measuring the fraction of the hadrons in the "conversion" pairs defined by the pair algorithm. We use the strip chamber pulse height information for the purpose.

First we check the CES pulse heights for the real electrons. We start with photon conversion pairs identified by the VTPC hit fraction. We require that the event be also identified by the pair algorithm with a radius of the conversion point consistent with the outer conversions. In order to ensure a high efficiency of the CES pulse height measurement, the momentum of the partner positron is required to be above 1.5 GeV/c. We then extrapolate the positron track to the CES plane and require that the extrapolated position is within the fiducial volume of the CES. We define the pulse height as a sum of 5 wires around the extrapolated track position. Figure 3.27(a) shows the distribution of the pulse height normalized to the track momentum. We observe large pulse heights

as expected for electrons.

We next check the pulse height for a random charged track. We pick up tracks with the same kinematic requirements but those pointing to the "wrong" wedge as expected from a charge of the primary electron. The pulse height distribution is shown in Figure 3.27(b). We see a peak in the first bin (less than 5%) due to the minimum ionizing particles and a tail to larger pulse heights.

Finally we show the pulse heights for the partner "positron" tracks in the photon conversion events identified by the pair algorithm. The pulse height distribution is shown in Figure 3.27(c). It is similar to that for true electrons, Figure 3.27(a), except for an additional small peak in the first bin.

We interpret the last distribution as a sum of the other two distributions, and we find the fraction of the charged hadrons in the photon conversion sample identified by the pair algorithm as

$$f_{\text{charged}} = 0.116 \pm 0.025. \tag{3.25}$$

Since the rate of "prompt electrons" is about five times higher than that of the identified "conversions", the fraction of the lost "electrons" is

$$f_{\text{lost}} \simeq 0.116/5 = 0.023 \pm 0.005. \tag{3.26}$$

3.4.3 Residual conversion fraction in the prompt electron sample

The number of the residual photon conversion electrons N_{res} in the prompt electron sample is expressed as

$$N_{\text{res}} = N_{\text{id}} \frac{1 - \epsilon_{\text{tot}}}{\epsilon_{\text{tot}}}, \tag{3.27}$$

where N_{id} is the number of identified real photon conversions and ϵ_{tot} is the overall efficiency for finding photon conversion pairs. N_{id} is related to the observed, raw number

of photon conversions $N_{\rm obs}$ by

$$N_{\rm id} = N_{\rm obs}\,(1 - f_{\rm charged}). \tag{3.28}$$

The fraction of residual conversion electrons in the "prompt" electron sample is then expressed as

$$f_{\rm conv} \equiv \frac{N_{\rm res}}{N_{\rm prompt}} = \frac{N_{\rm id}}{N_{\rm prompt}}\,\frac{1-\epsilon_{\rm tot}}{\epsilon_{\rm tot}} = \frac{N_{\rm obs}\,(1-f_{\rm charged})}{N_{\rm prompt}}\,\frac{1-\epsilon_{\rm tot}}{\epsilon_{\rm tot}}. \tag{3.29}$$

We show in Figure 3.28 the fraction $f_{\rm conv}$ as a function of the electron $E_{\rm T}$. We observe that the fraction is about 20% and has very little $p_{\rm T}$ dependence. We obtain the uncertainty in $f_{\rm conv}$ by propagating the error in $\epsilon_{\rm tot}$ ($\pm$13% relative). We use

$$f_{\rm conv} = 0.20 \pm 0.05 \tag{3.30}$$

as the final number for the residual photon conversion background.

3.5 Misidentified charged hadrons

This section describes the estimate of the residual hadrons in the prompt electron sample. As we have discussed earlier (Section 3.1.2), a charged hadron can mimic an electron by depositing most of its energy in the electromagnetic compartment of the calorimeter. Although its probability is small, a much higher rate of pions makes such kind of pions a significant source of background to electrons.

3.5.1 Hadronic energy distributions

We consider hadronic energy distributions of electrons and charged hadrons with high momentum, say 10 GeV/c and above. As shown in Figure 3.1 the HAD/EM distribution of electrons (about 50 GeV) peaks near zero hadronic energy and gives few events above,

say, 0.04. On the other hand, hadrons leave only a small (minimum ionizing) signal most of the time. On the CEM the minimum ionizing peak corresponds to a 300 MeV electromagnetic particle. These minimum ionizing hadrons appear as a peak near unity in the hadronic energy fraction distribution. This behavior can be seen in Figure B.4, for example.

Now we want to know the behavior of hadrons in the region of a smaller hadronic energy fraction. Figure B.6 shows the blowups of the hadronic energy fraction distributions for real data charged particles and Figure 3.29 shows the corresponding distributions for test beam 50 GeV pions (curve (a)). Both show a flat distribution in the relevant range of hadronic energy fraction, and no peak near zero is observed, for the relevant range of $p_{\rm T}$ (above 10 GeV/c). In Figure 3.29 (curve (a)) 50 GeV pions show a slight positive slope, and in Figure B.6 10-20 GeV hadrons seem to show an almost zero slope, although the statistics are limited. In any case they exhibit smooth distributions and no peaks.

Now let us look at the real data electron samples. Figure 3.30 shows the HAD/EM distribution for identified photon conversion electrons. As shown in the previous Section they are a very pure (about 90%) sample of real electrons. We thus expect the distribution to be similar to that of test beam and W electrons (Figure 3.1), and it is. A small difference is that the photon conversion electrons have a little larger tail. This can be understood as follows. W and test beam electrons are isolated. The inclusive electrons, prompt or conversion, are produced by particles in jets. They accompany other particles around them. These hadrons can change the hadronic energy in the electron cluster towers. As shown in Appendix B, hadronic showers have a large lateral width of about 10 cm. Thus the showers of hadrons near the electron can leak into the electron cluster towers across boundaries, and create a tail in the distribution.

Figure 3.31 shows the corresponding distribution for the "prompt" electrons. Compared with photon conversion electrons, the tail is much larger. This is most naturally explained with the presence of charged hadrons faking electrons, which show the roughly flat distribution. In other words, the difference between the two distributions is a con-

tribution of charged hadron background.

3.5.2 Estimate of the hadron fraction

The amount of residual hadrons can be estimated by interpreting the observed HAD/EM distribution as a sum of two contributions, one from electrons and the other from pions.

First we look at a region with HAD/EM between 0.04 and 0.08. We do not use the region above 0.08 because the distribution there is biased on account of the level-2 trigger requirement on HAD/EM. In this region the contribution from real electrons is expected to be small. Strictly speaking, the electron contribution in that region cannot be neglected, and we subtract it using the distribution for photon conversion electrons. This can be done with an enough accuracy by normalizing the conversion and "prompt" distributions in the first bin, where electron contribution is much higher than in the tail. In this way we have a HAD/EM distribution for the "pions" in the region between 0.04 and 0.08. We observe a small negative slope as shown in Figure 3.32.

Next we extrapolate the distribution to the low side, below 0.04 of the hadronic energy fraction. Assuming a continuous linear shape, we obtain the fraction of charged hadrons in our "prompt" electron sample in the region of HAD/EM below 0.04 to be 15%.

3.5.3 Systematic uncertainty

We have obtained a pion distribution at a higher value of HAD/EM, and then used it to extrapolate into the electron signal region. Now two questions arise. First, whether or not the distribution we obtained in the "pion" region is correct. Second, if our extrapolation is correct or not.

We do not have many handles on the hadronic energy distribution for these low energy (10-20 GeV) charged hadrons. Test beam data lack high statistics for lower energy pions. Also the contamination of electrons in the beam is not negligible.

We have shown in Figure 3.29 the distributions for 50 GeV test beam pions, where

the statistics are relatively high. The curve (a) in the Figure is for all pions, and has a positive slope. When we select electron events in the real data, we apply the CES χ^2 cut. Also an implicit cut on the CES pulse height is placed through the shower-track position matching requirement, which forces the hadron to deposit a large pulse height on the CES. These cuts select pions which are more like electrons, and the HAD/EM value of such pions may change in correlation with the cut quantities. Curves (b) and (c) in Figure 3.29 correspond to pions after these cuts. The cuts seem to change the distributions slightly. The slope after the cuts is flatter, and a small bump is observable at very small hadronic energy. The latter is most likely due to the electron contamination in the pion beam and probably we do not have to worry about it. The former draws our attention, because the slope determines the number of pions in the electron signal region.

Another question is that how the slope changes as a function of the pion energy. In the real data of high $p_{\rm T}$ tracks we have observed similar, smooth distributions for lower energy hadrons (10 GeV to 20 GeV) (Figure B.6), where we have not applied any CES cuts. The slope for these lower energy hadrons is roughly zero. This could be compared with the positive slope for 50 GeV test beam pions (curve (a) in Figure 3.29). We cannot apply cuts on CES showers for real data charged tracks, since the statistics are already limited, and more importantly the cuts would just pick up real electron events.

We have used real data HAD/EM distributions from photon conversion electrons and "prompt" electrons, and obtained a distribution for the "pions" which has a slight negative slope (Figure 3.32). Presumably the application of the shower cuts has introduced the negative slope into the flat distributions for the unbiased, all pions. And the distribution we obtained for the "pions" is reasonably flat and probably correct.

As for the extrapolation, all the above results show that charged hadrons give smooth distributions. Thus our linear extrapolation is probably right. We consider two cases, one with the flat distribution with zero slope, and the other with a negative slope which gives twice events in the electron signal region as in the "pion" region. We use them as

the systematic uncertainty in the final number. In summary we use

$$f_{\text{hadron}} = 0.15 \pm 0.15 \tag{3.31}$$

as the fraction of residual charged hadrons in our electron sample.

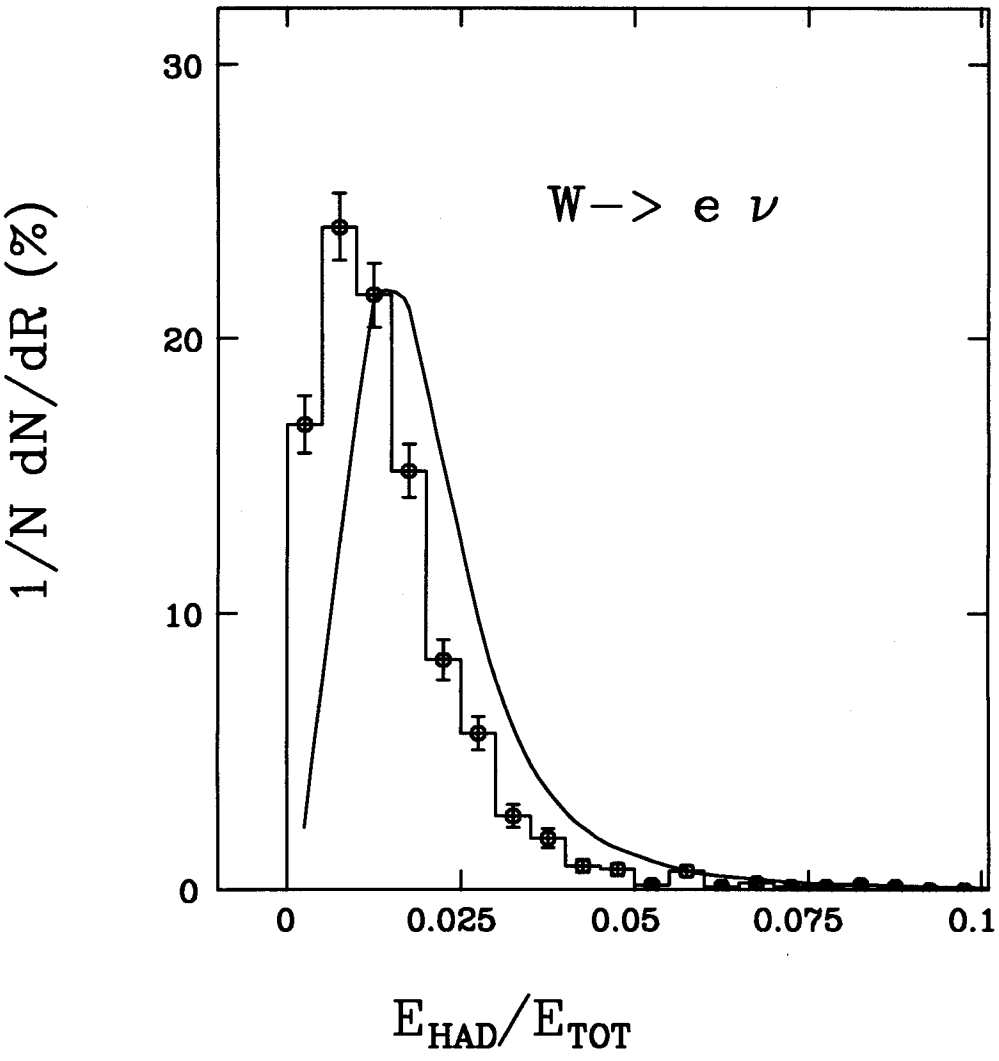

Figure 3.1: Hadronic energy distribution for W electrons (points) and 50-GeV test beam electrons (curve).

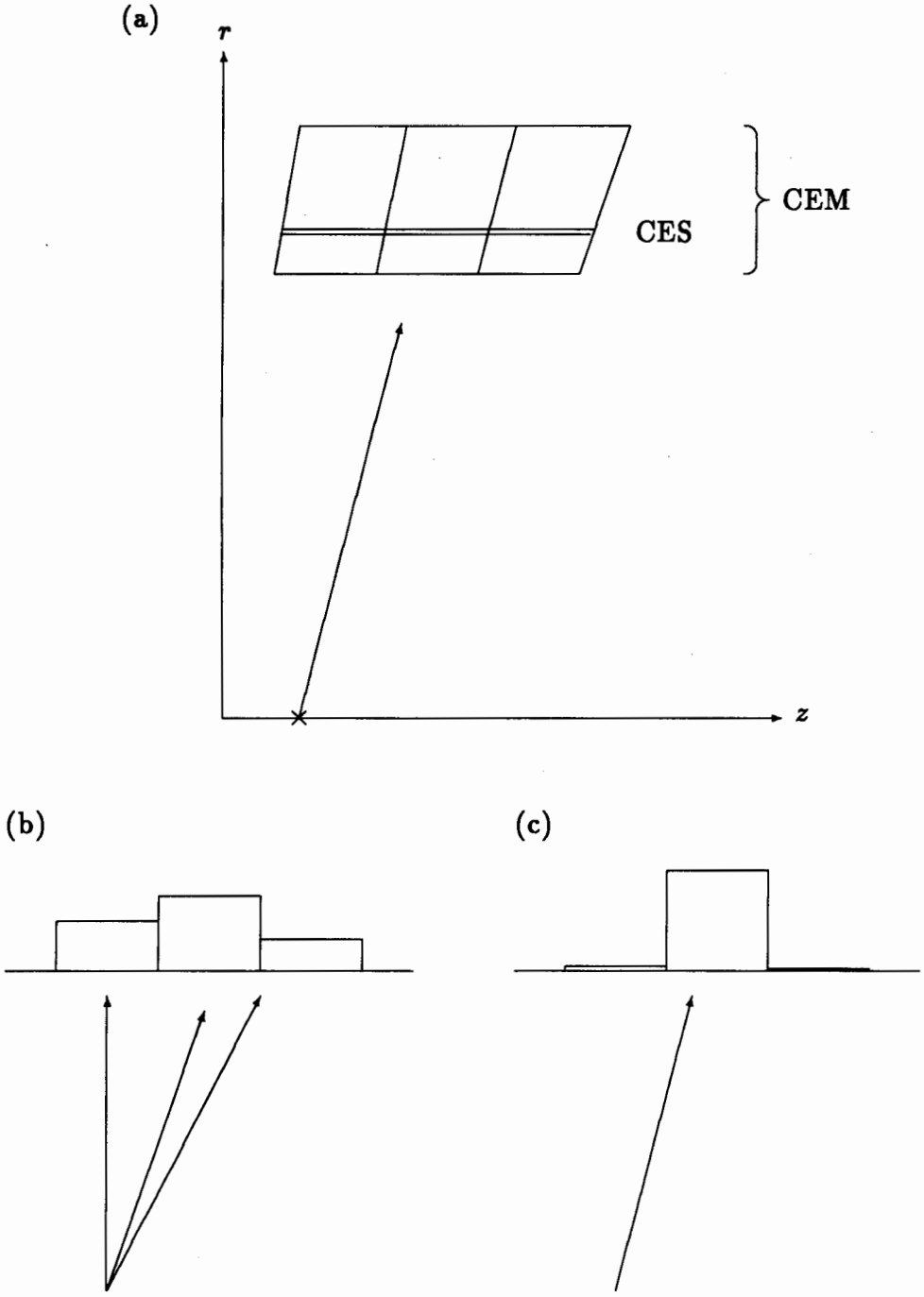

Figure 3.2: (a) Schematic view of CEM towers. Expected energy deposit pattern in three CEM towers for (b) a QCD background (multiple particles) and (c) a single electromagnetic particle.

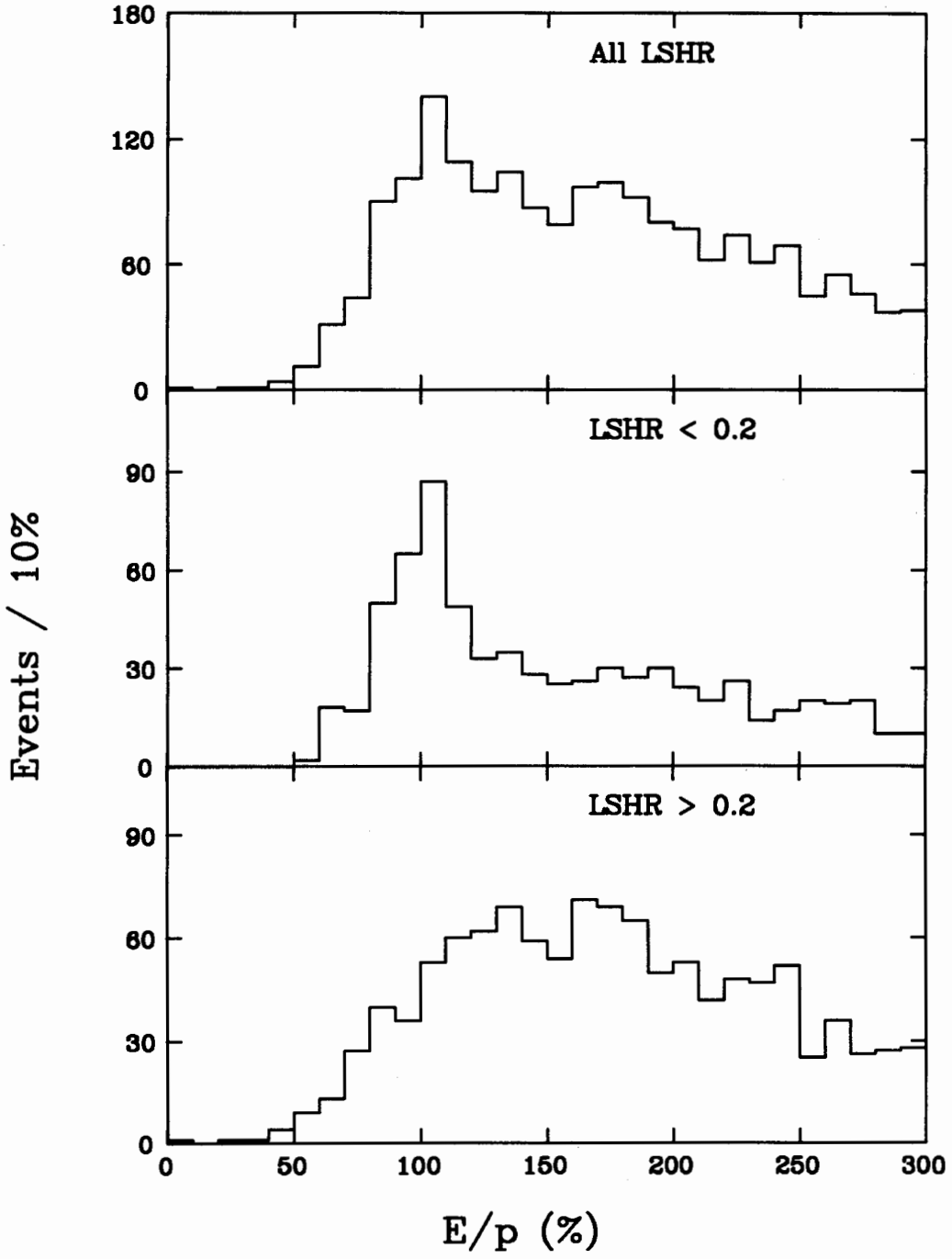

Figure 3.3: E/p distributions before and after the LSHR cut.

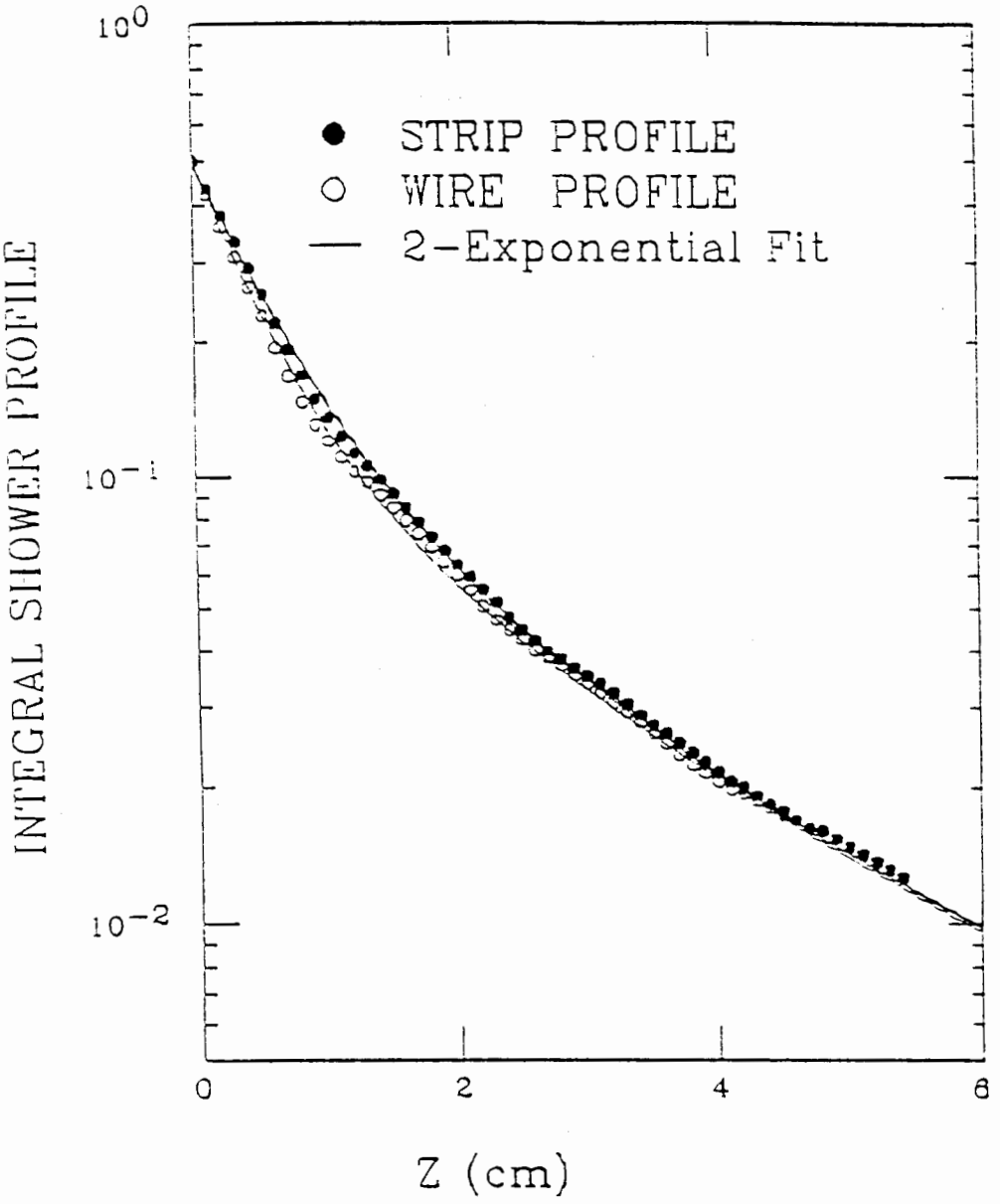

Figure 3.4: Integral shower shape I on CES for test beam electrons.

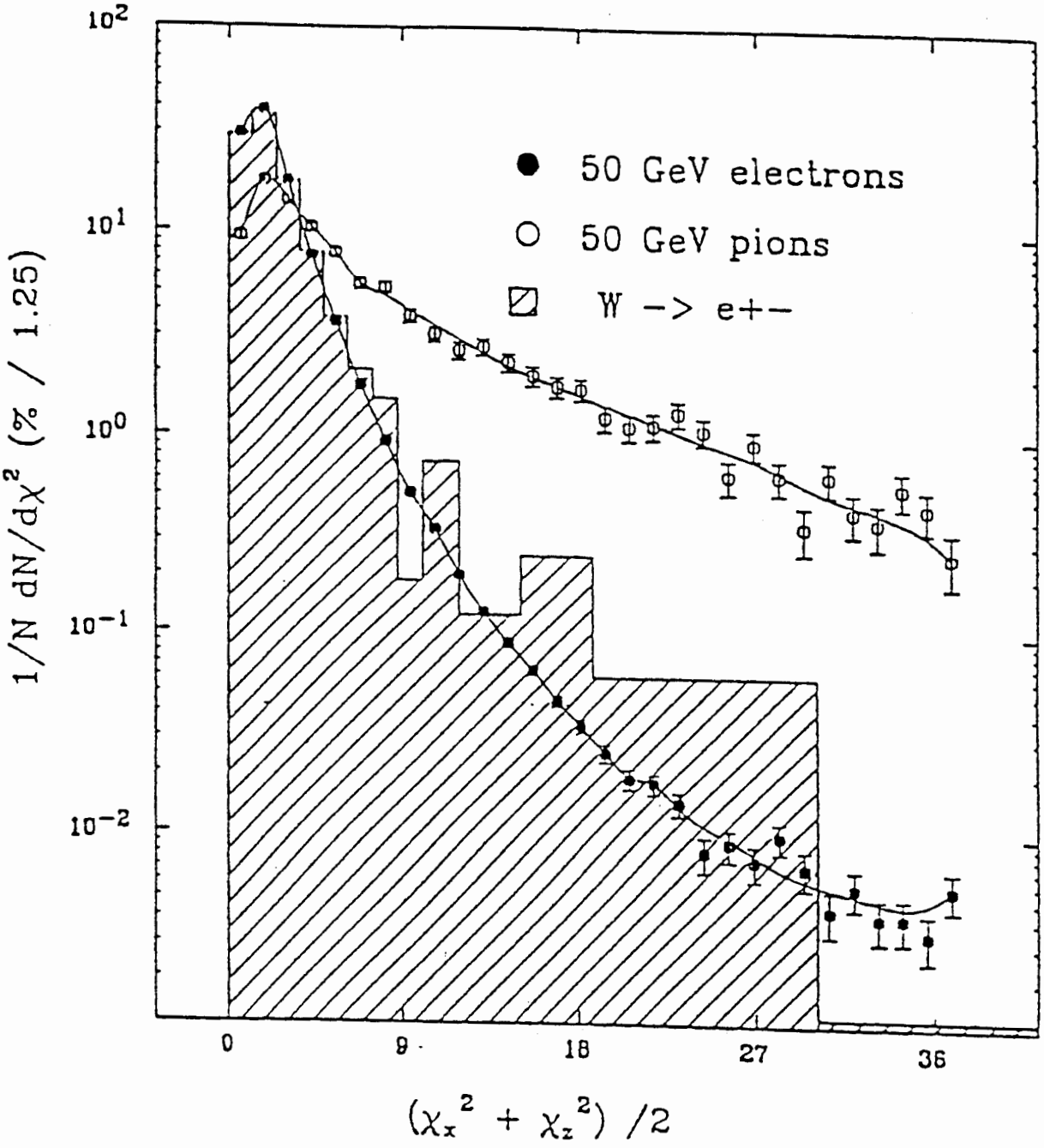

Figure 3.5: CES χ^2 distributions for test beam electrons and pions, and W electrons in real data.

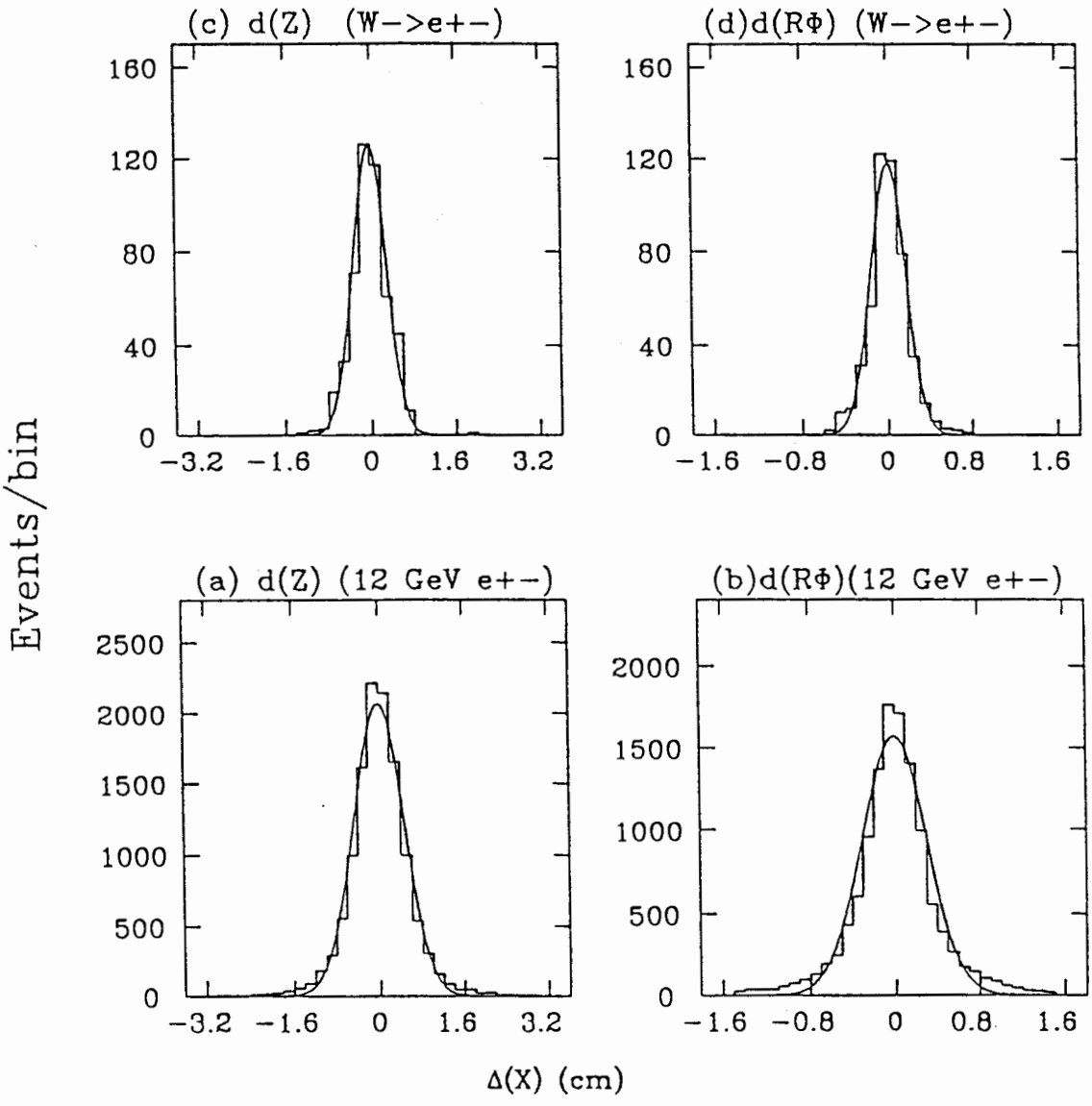

Figure 3.6: Shower-track position matching distributions for inclusive electrons (a,b) and for W electrons (c,d).

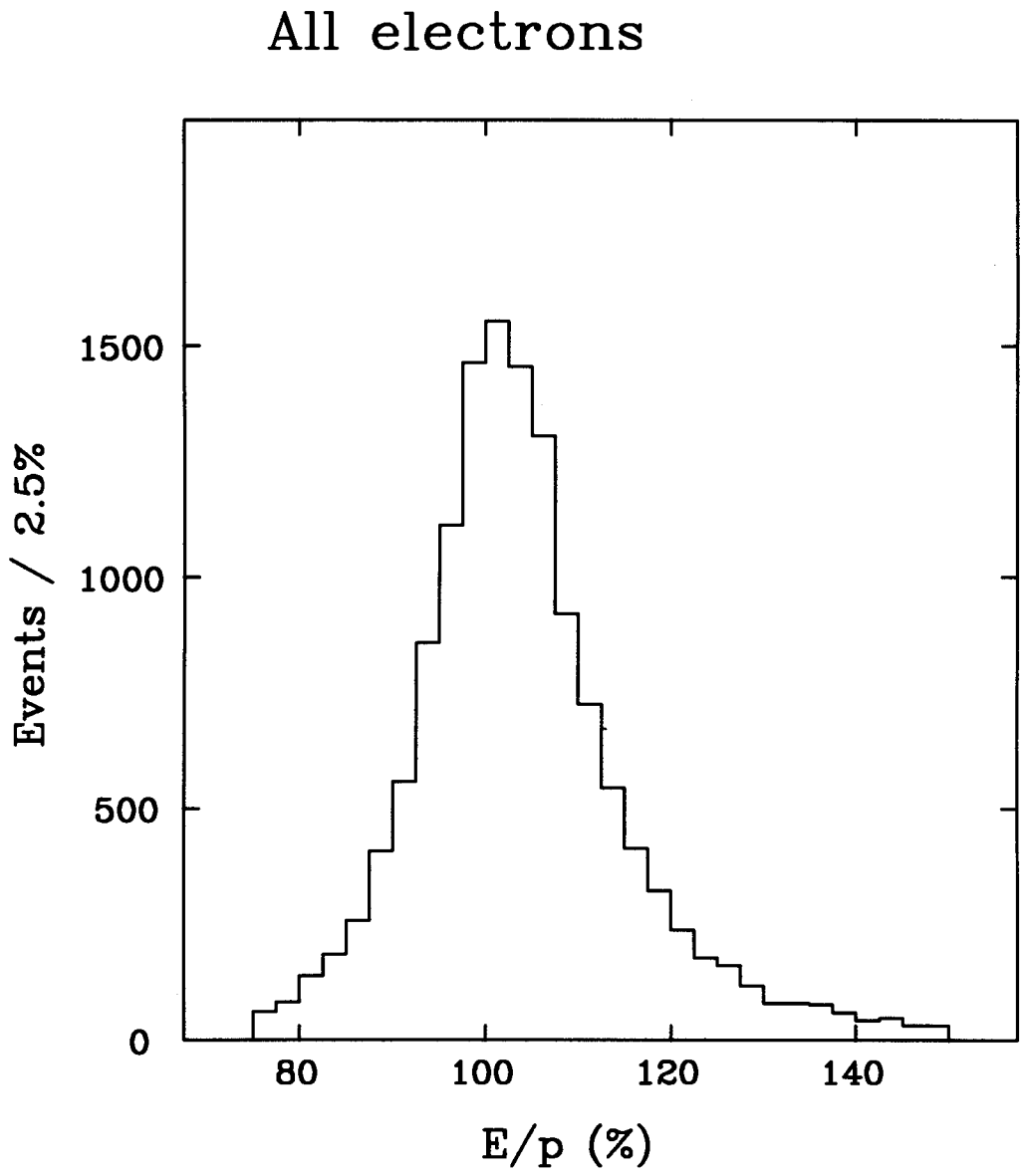

Figure 3.7: E/p distribution for electron candidates after all cuts.

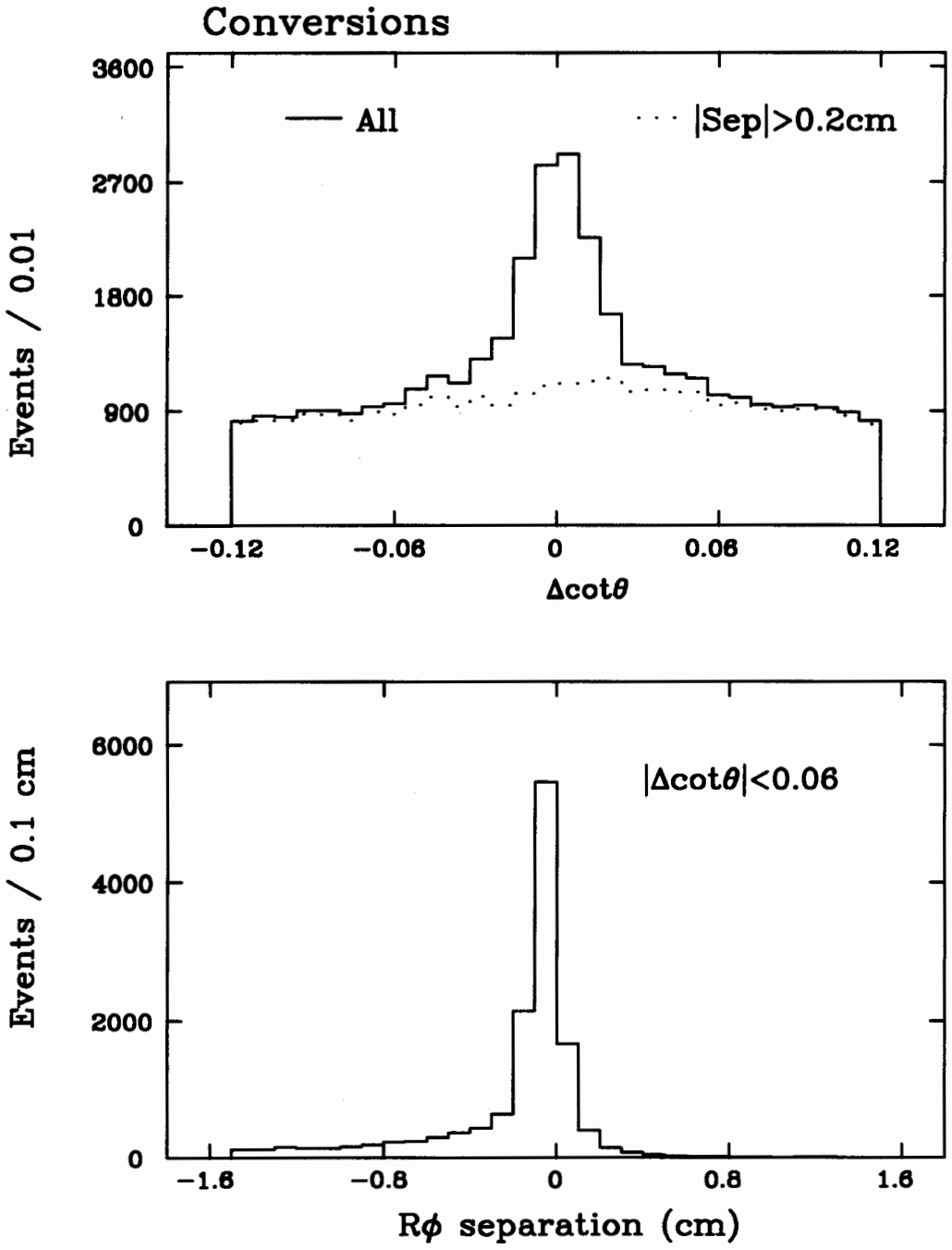

Figure 3.8: Cut variables for photon conversion pair removal.

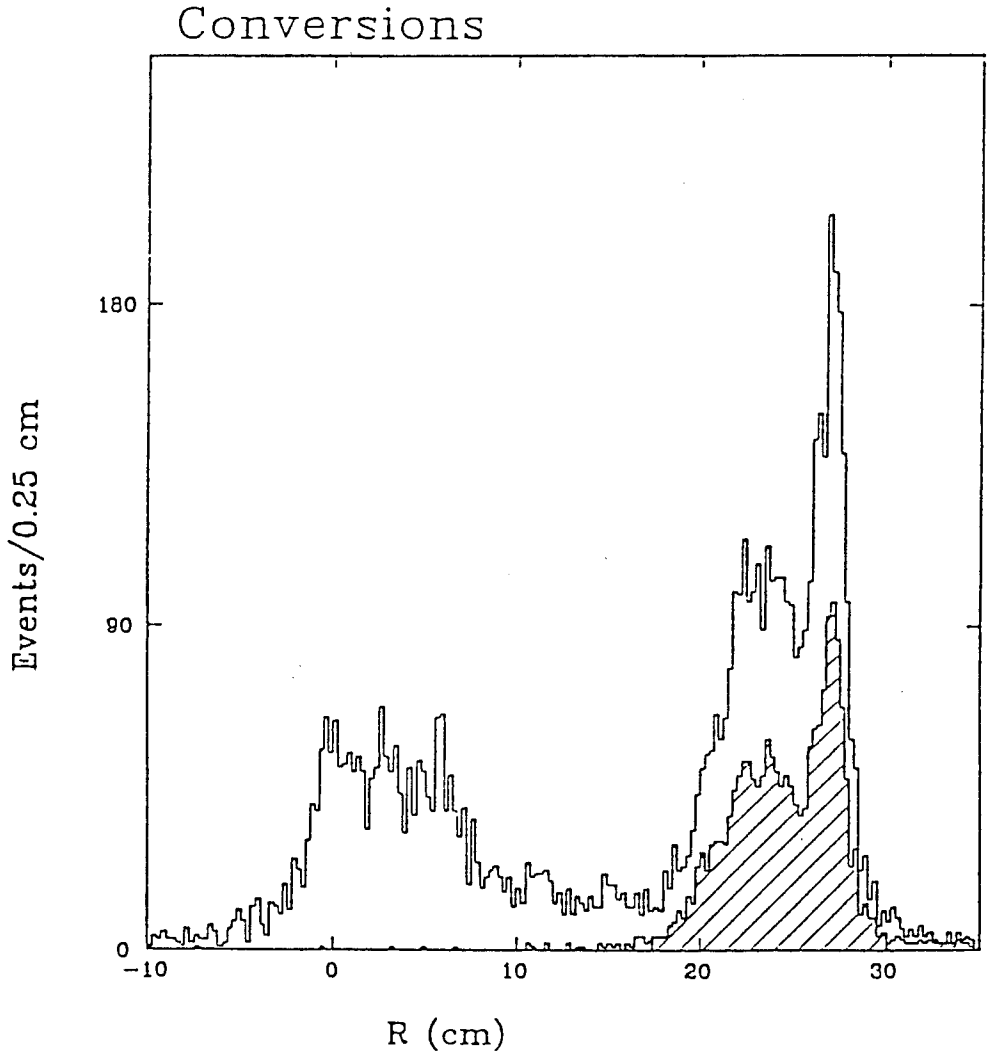

Figure 3.9: The radial distribution of the conversion points. The shaded region indicates a subsample with small VTPC hit fraction.

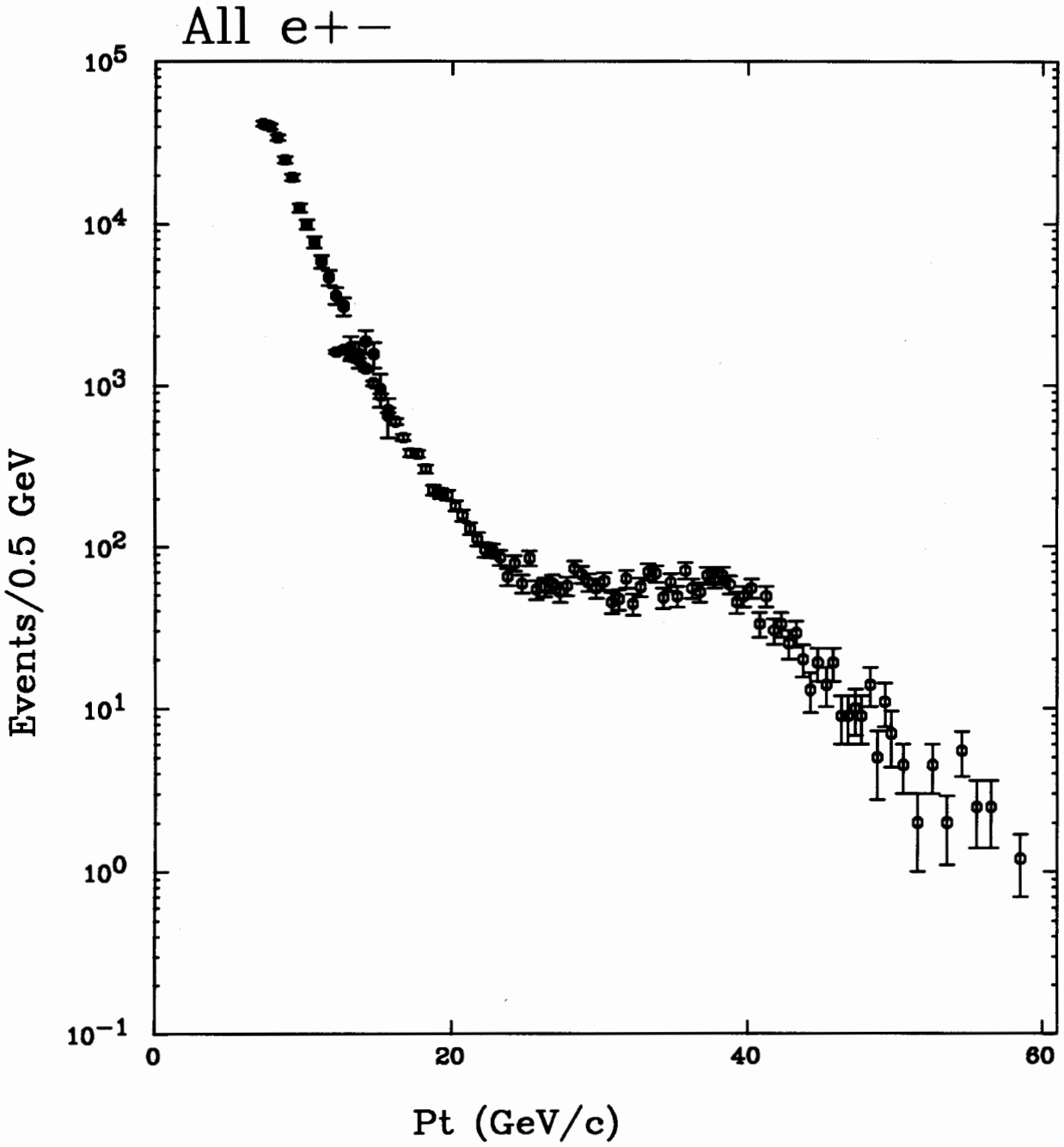

Figure 3.10: The observed "prompt" electron p_T spectrum.

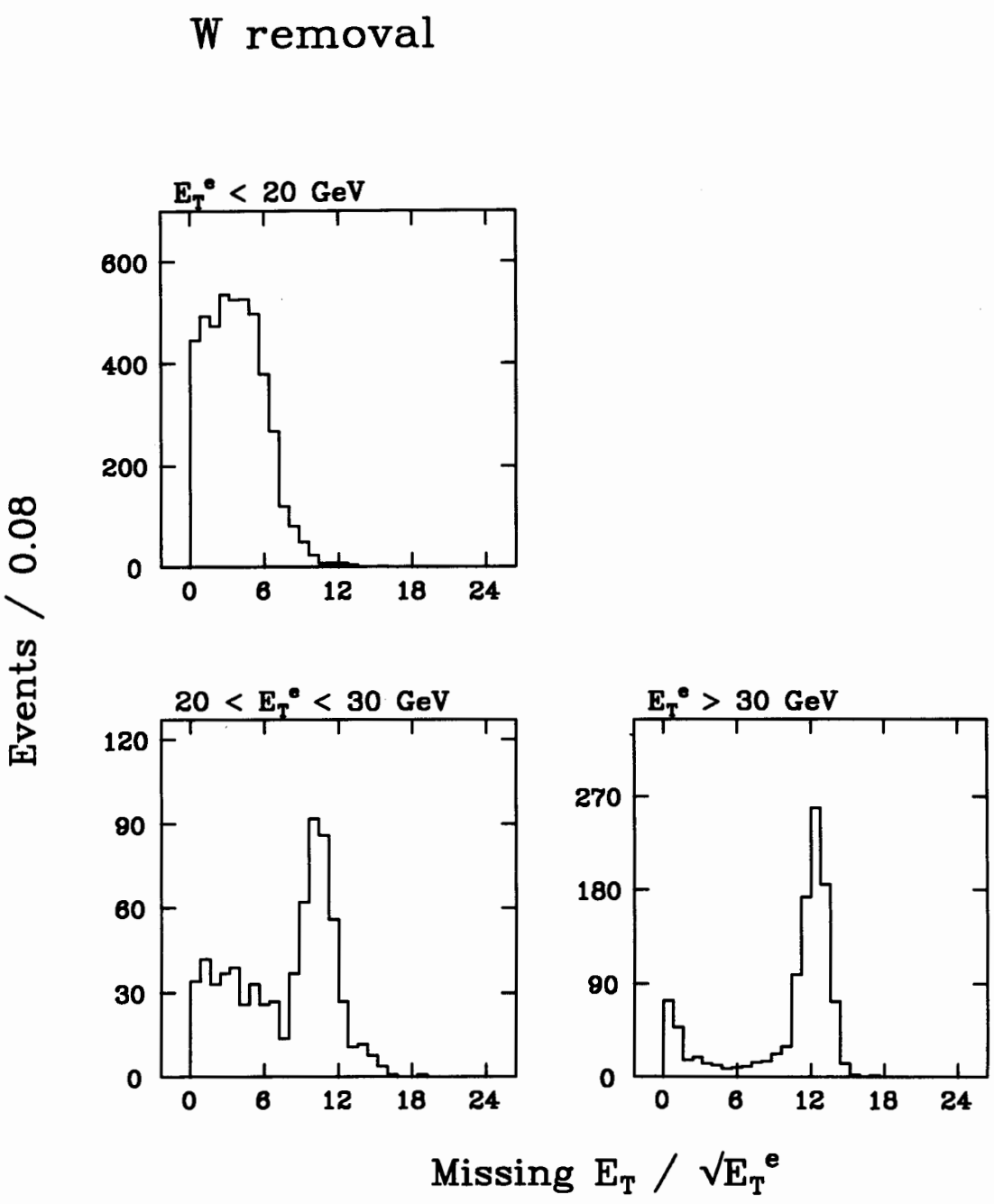

Figure 3.11: W electron removal.

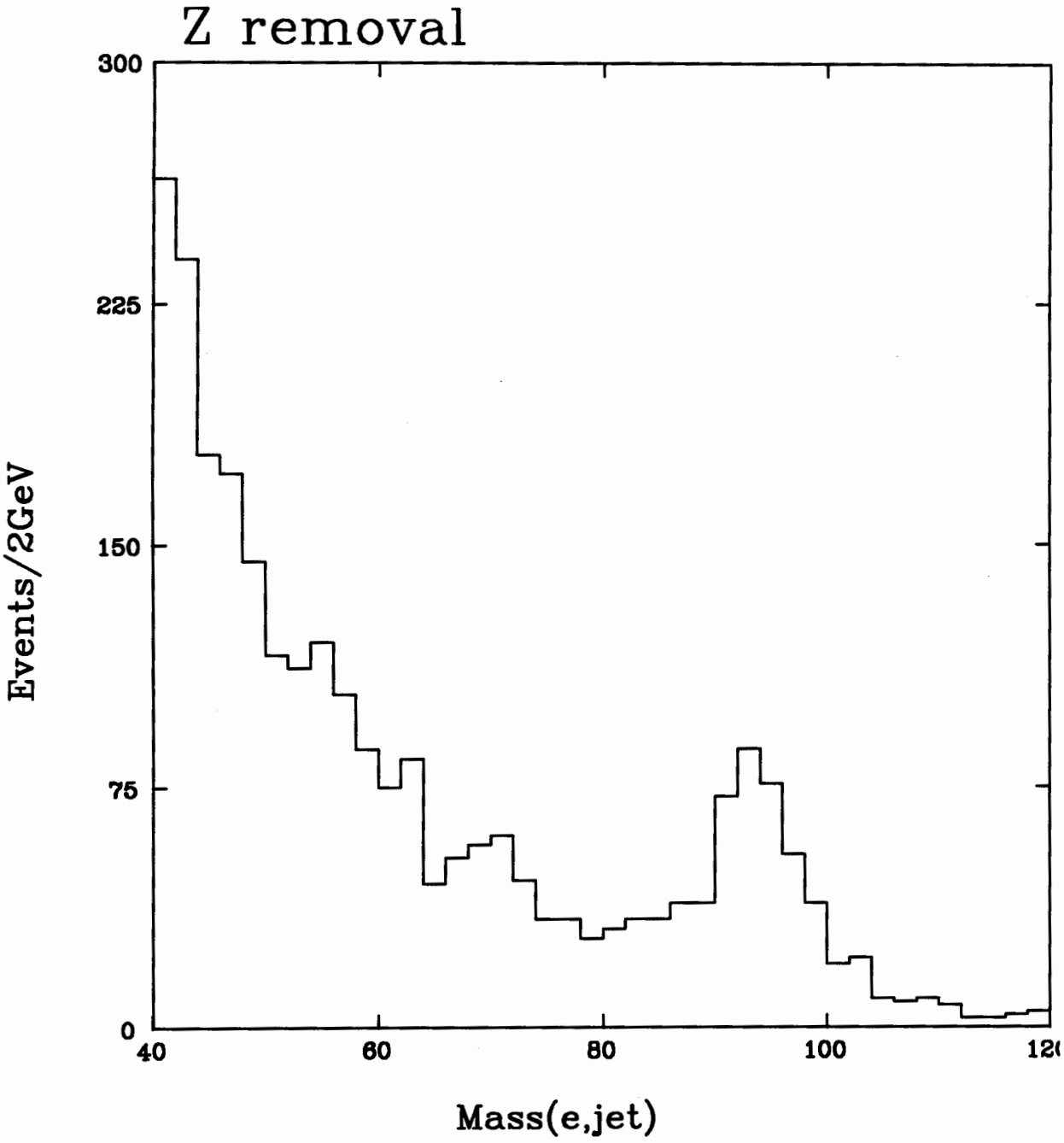

Figure 3.12: Invariant mass distribution of an electron and a jet with large electromagnetic fraction.

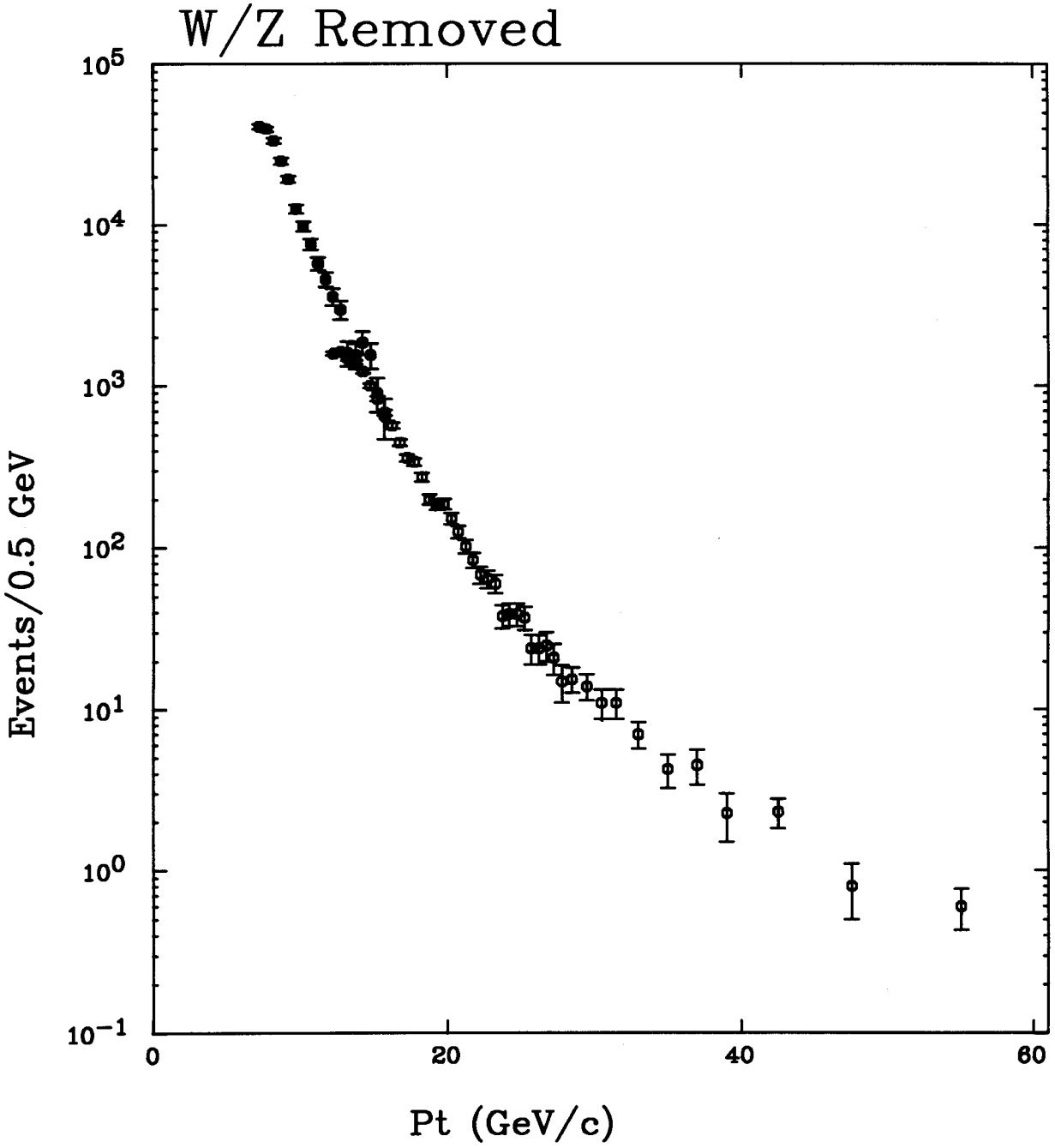

Figure 3.13: Observed electron p_T spectrum with W and Z decays removed.

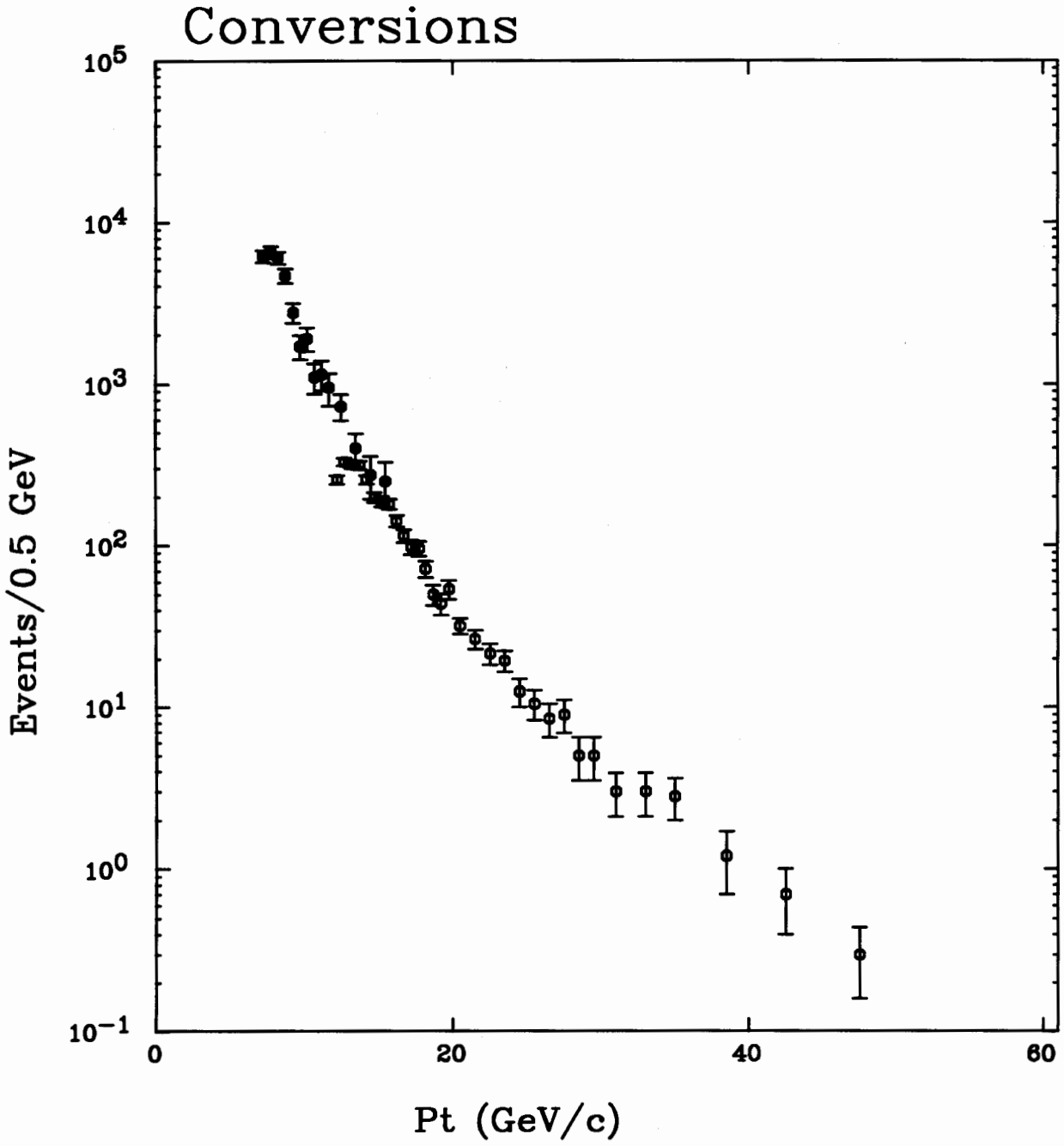

Figure 3.14: Observed p_T spectrum of identified photon conversion electrons.

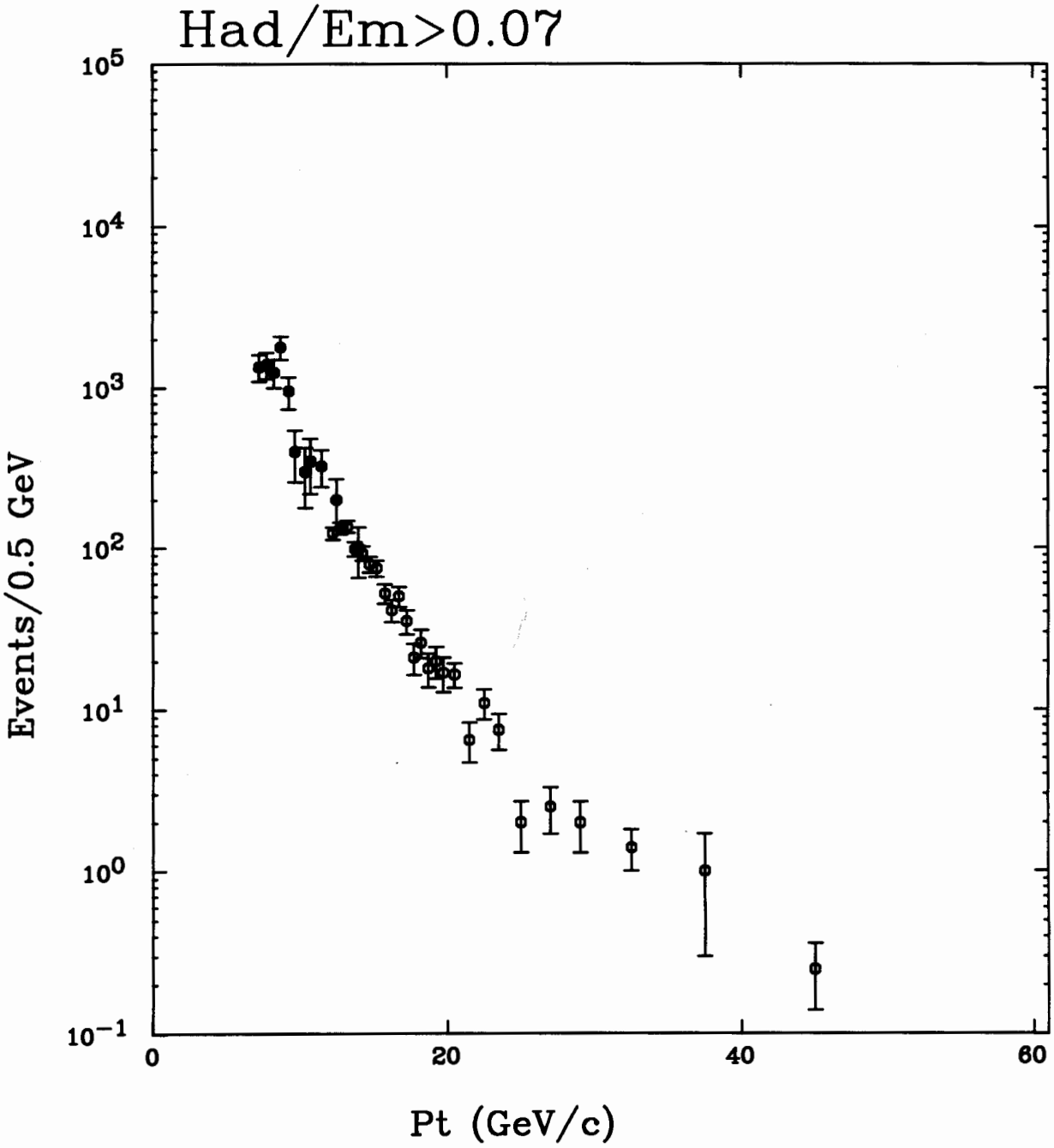

Figure 3.15: Observed p_T spectrum of the electromagnetic clusters with large hadronic energy fraction.

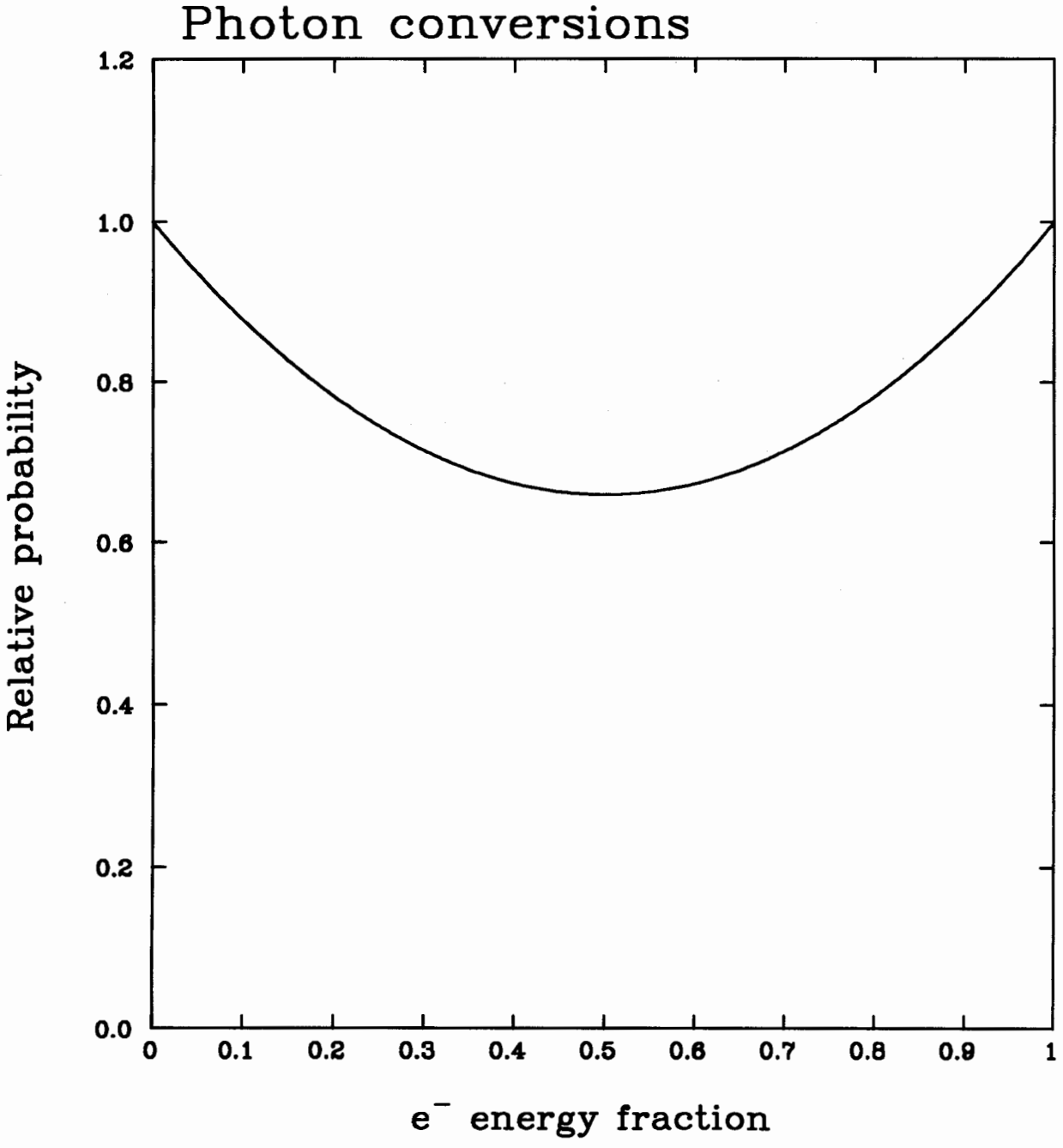

Figure 3.16: The energy sharing function between the electron and the positron in a conversion of an extremely relativistic photon.

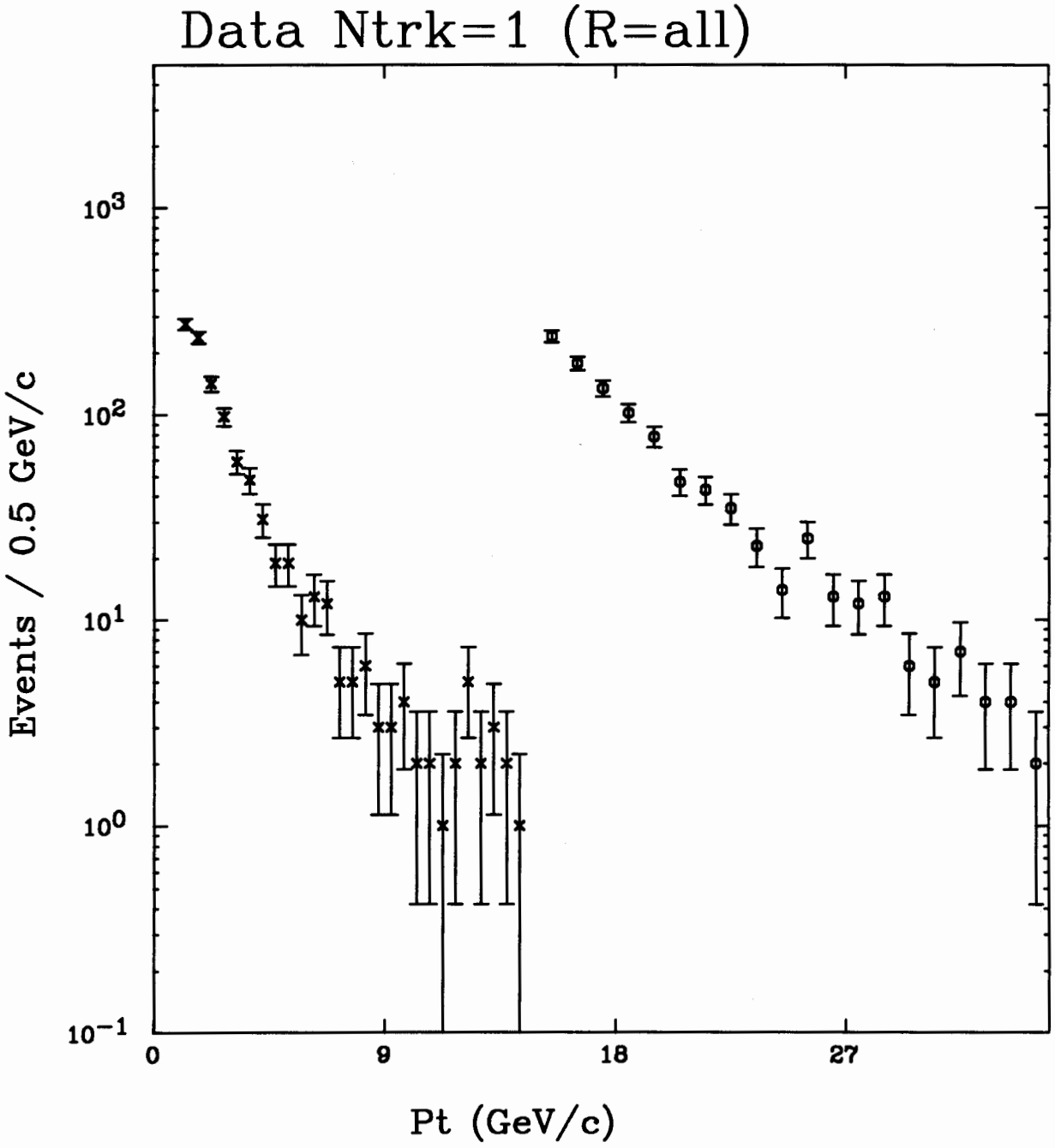

Figure 3.17: The spectra of the electron cluster E_T and the partner positron p_T for the real data photon conversion pairs. The cut at 1 GeV is made for the positron p_T.

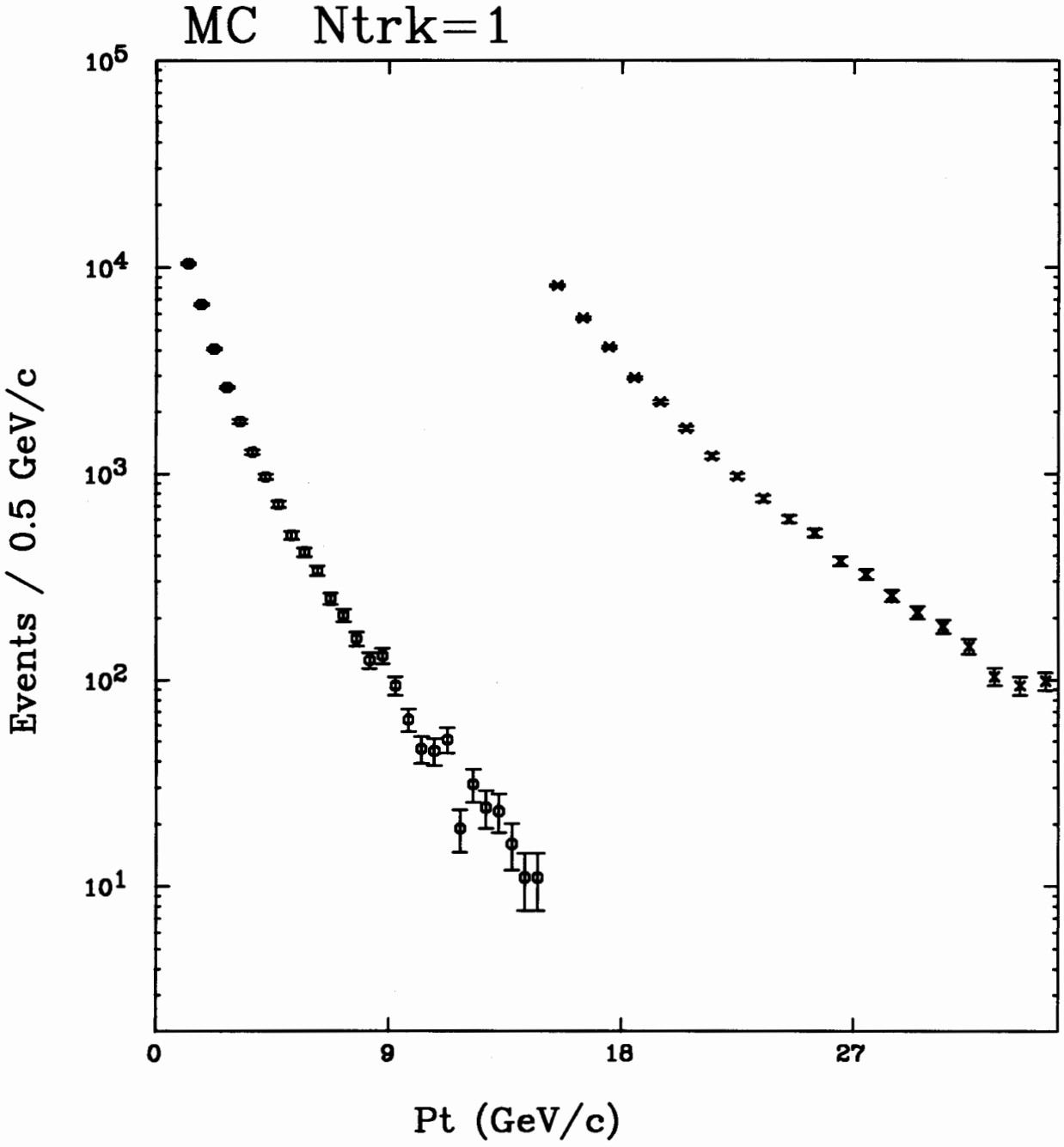

Figure 3.18: The spectra of the electron cluster E_T and the partner positron p_T for the Monte Carlo photon conversion pairs. The cut at 1 GeV is made for the positron p_T.

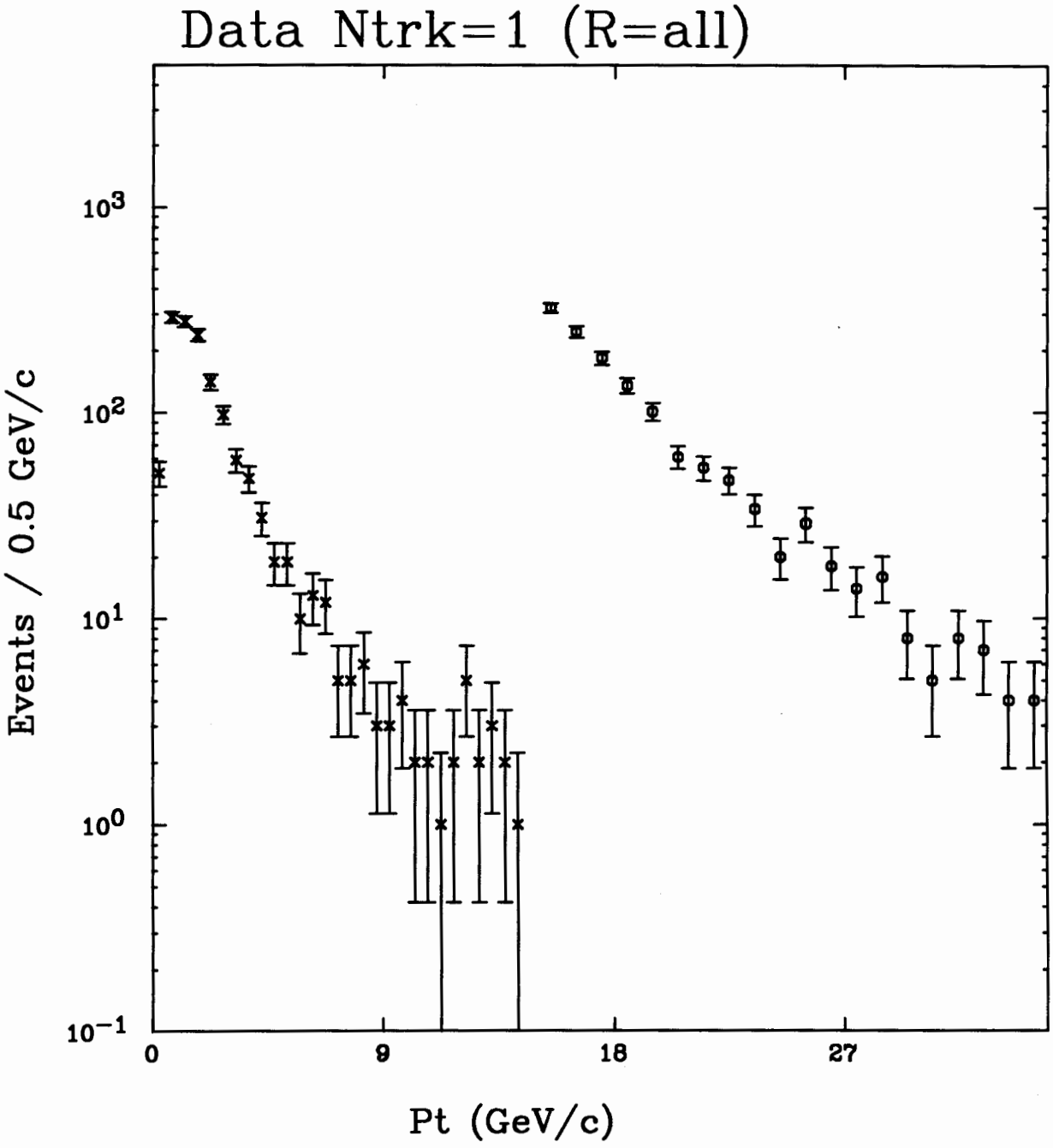

Figure 3.19: The full spectra of the electron cluster E_T and the partner positron p_T for the real data photon conversion pairs.

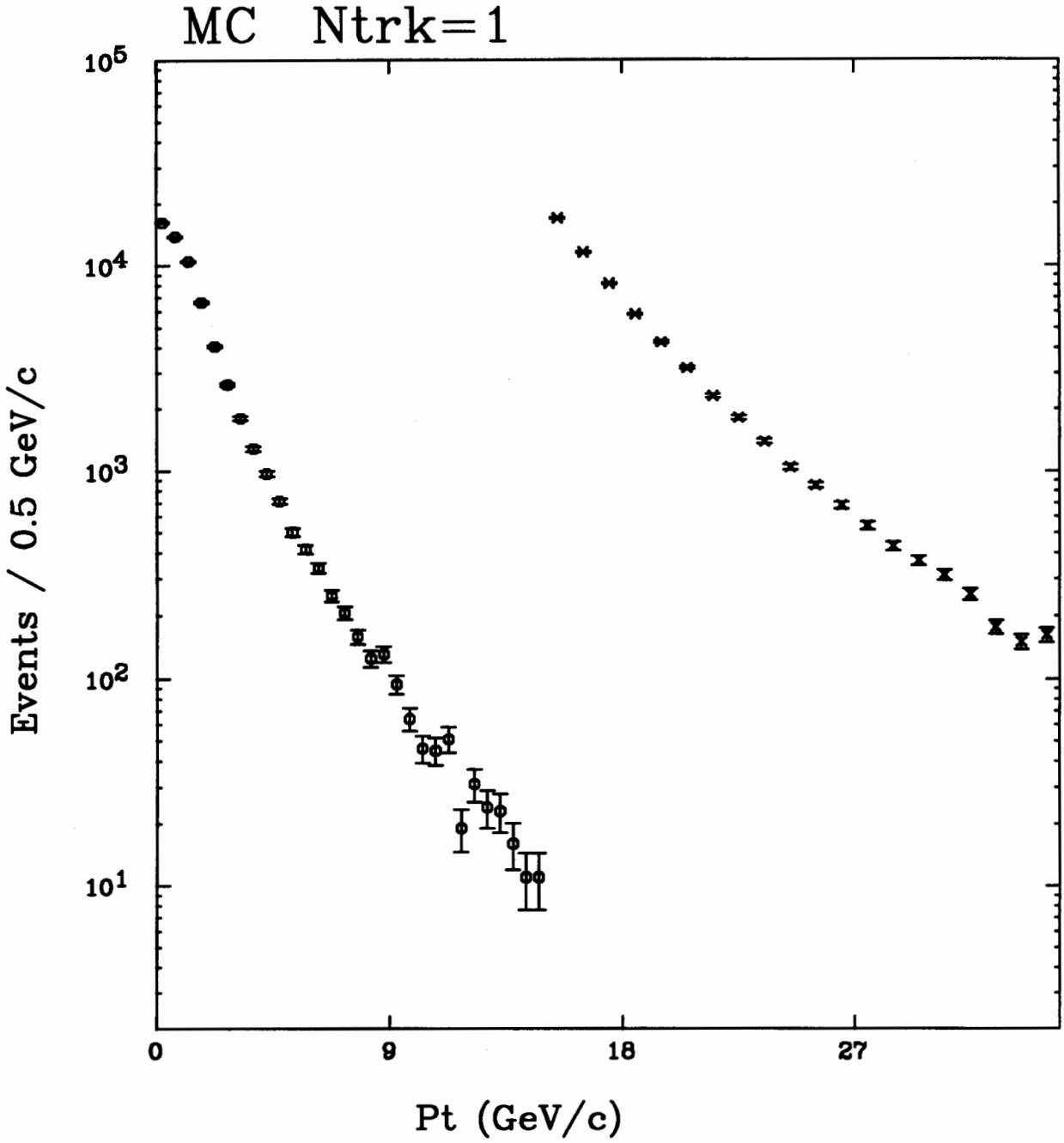

Figure 3.20: The full spectra of the electron cluster E_T and the partner positron p_T for the Monte Carlo photon conversion pairs.

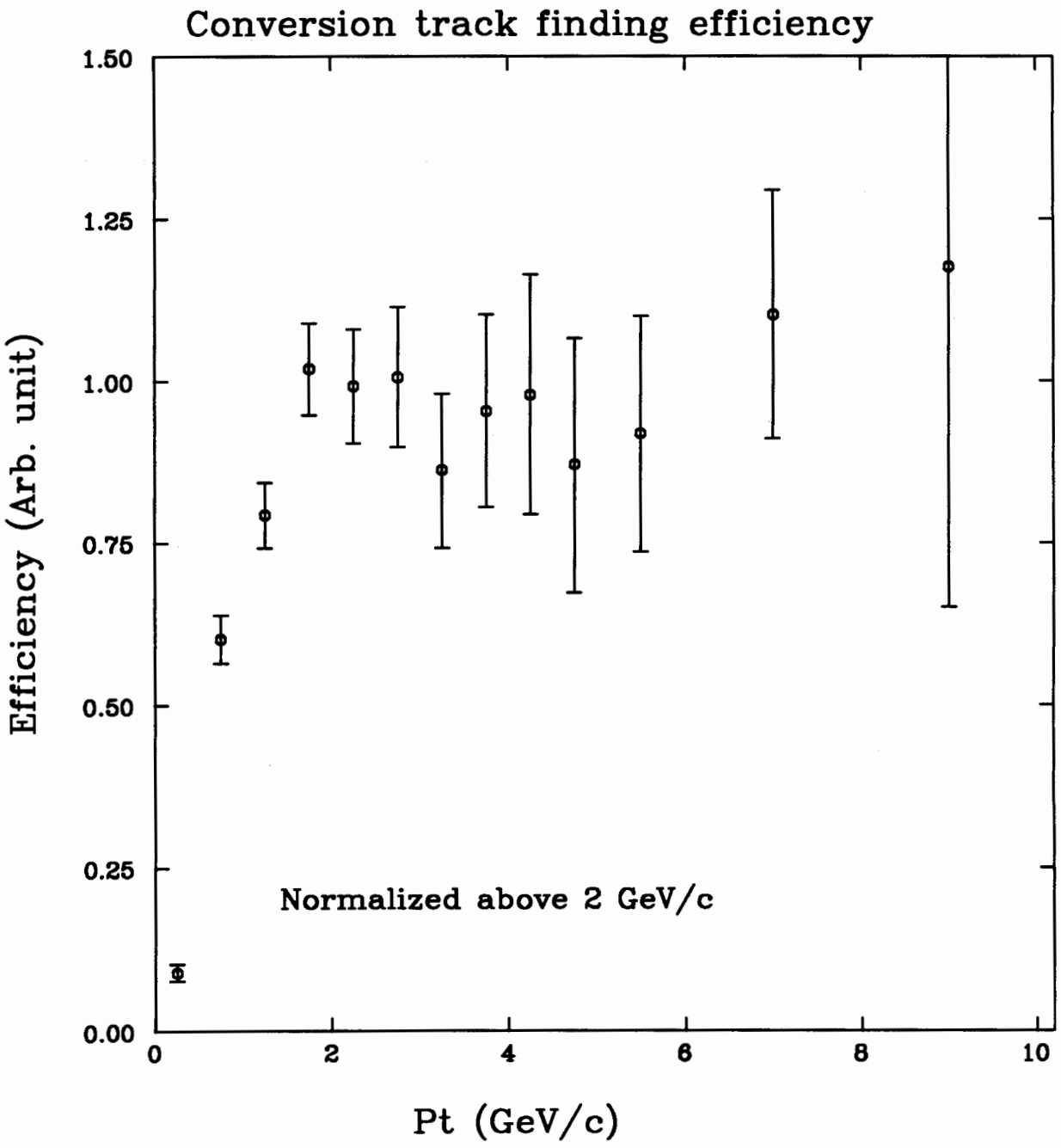

Figure 3.21: The track finding efficiency for the positrons.

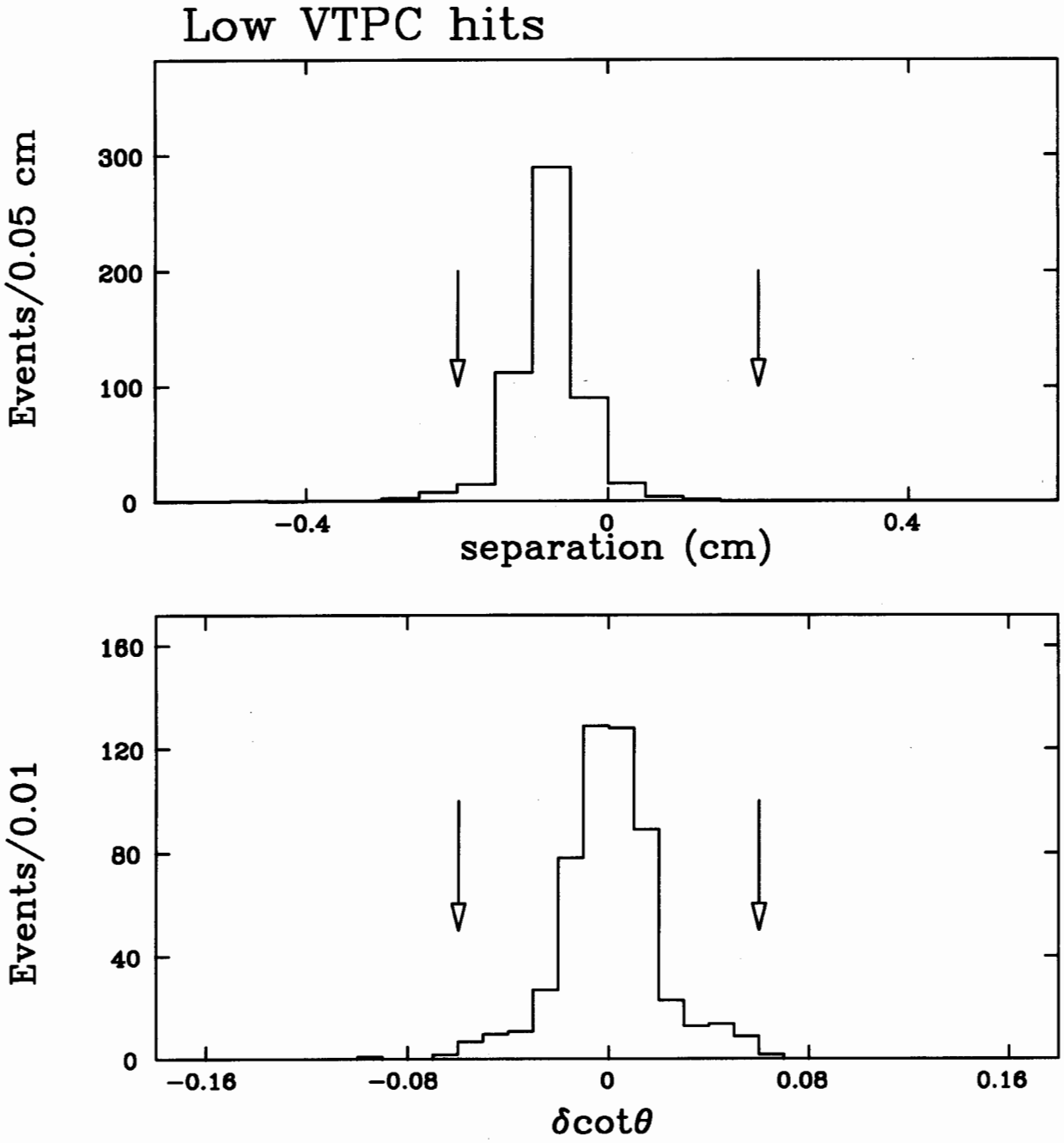

Figure 3.22: The distributions of the $\Delta \cot\theta$ and the separation S for the track pairs with low VTPC occupancy.

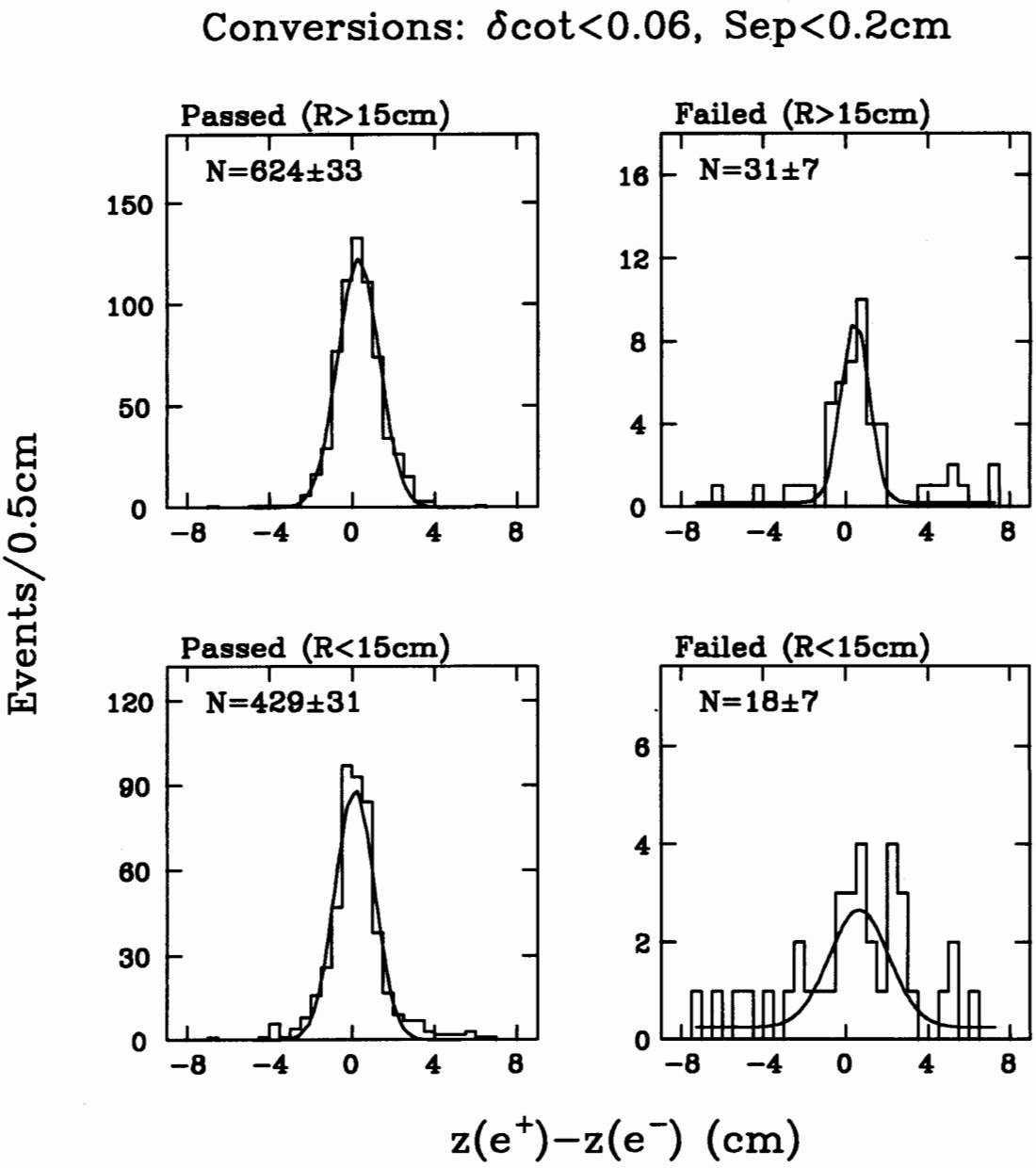

Figure 3.23: The difference of the electron and the positron z coordinates on the CES for the pairs passing and failing the cuts on $\Delta \cot \theta$ and the separation S.

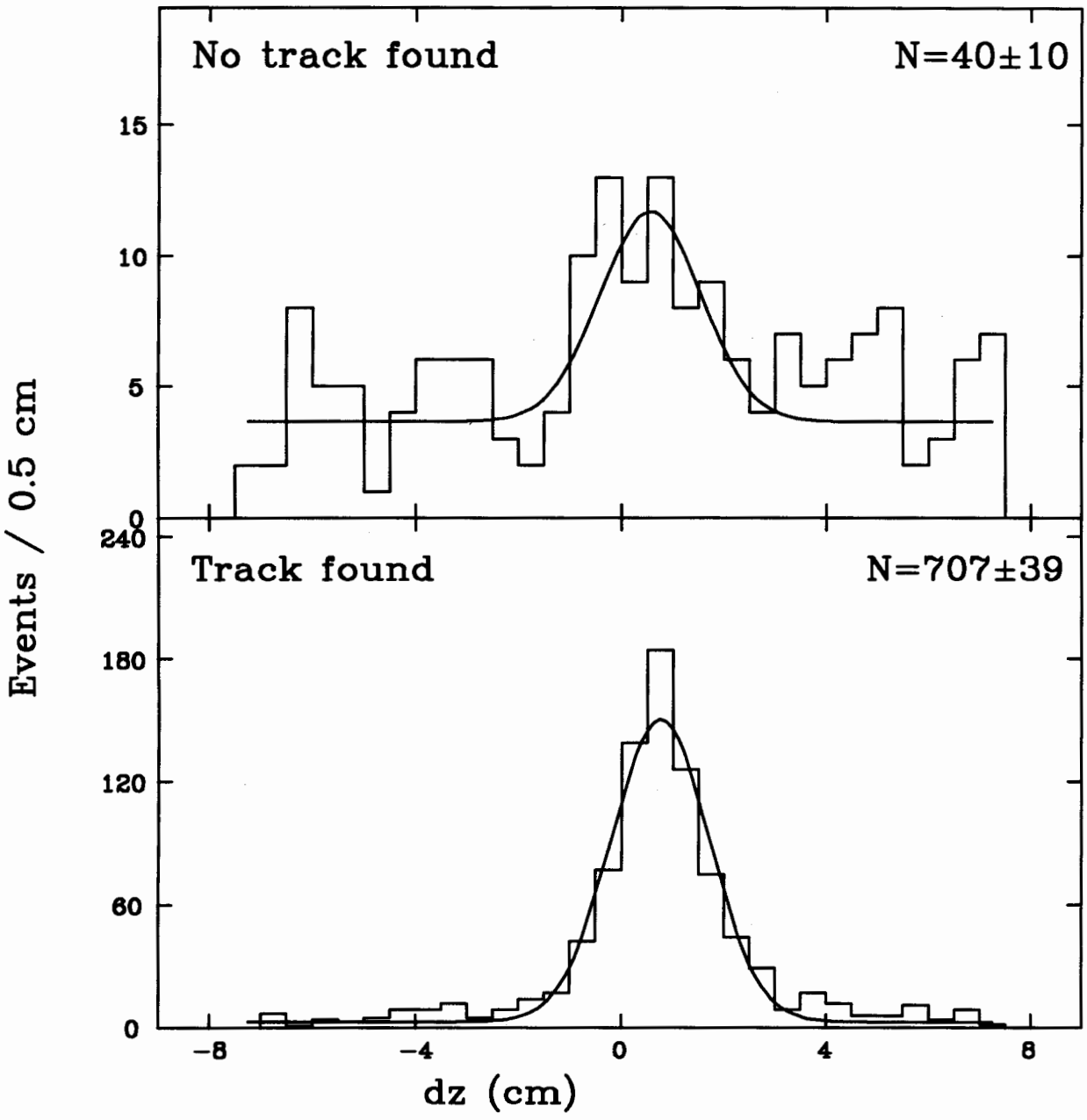

Figure 3.24: The difference of the CES shower positions z on adjacent wedges for events with and without a track found.

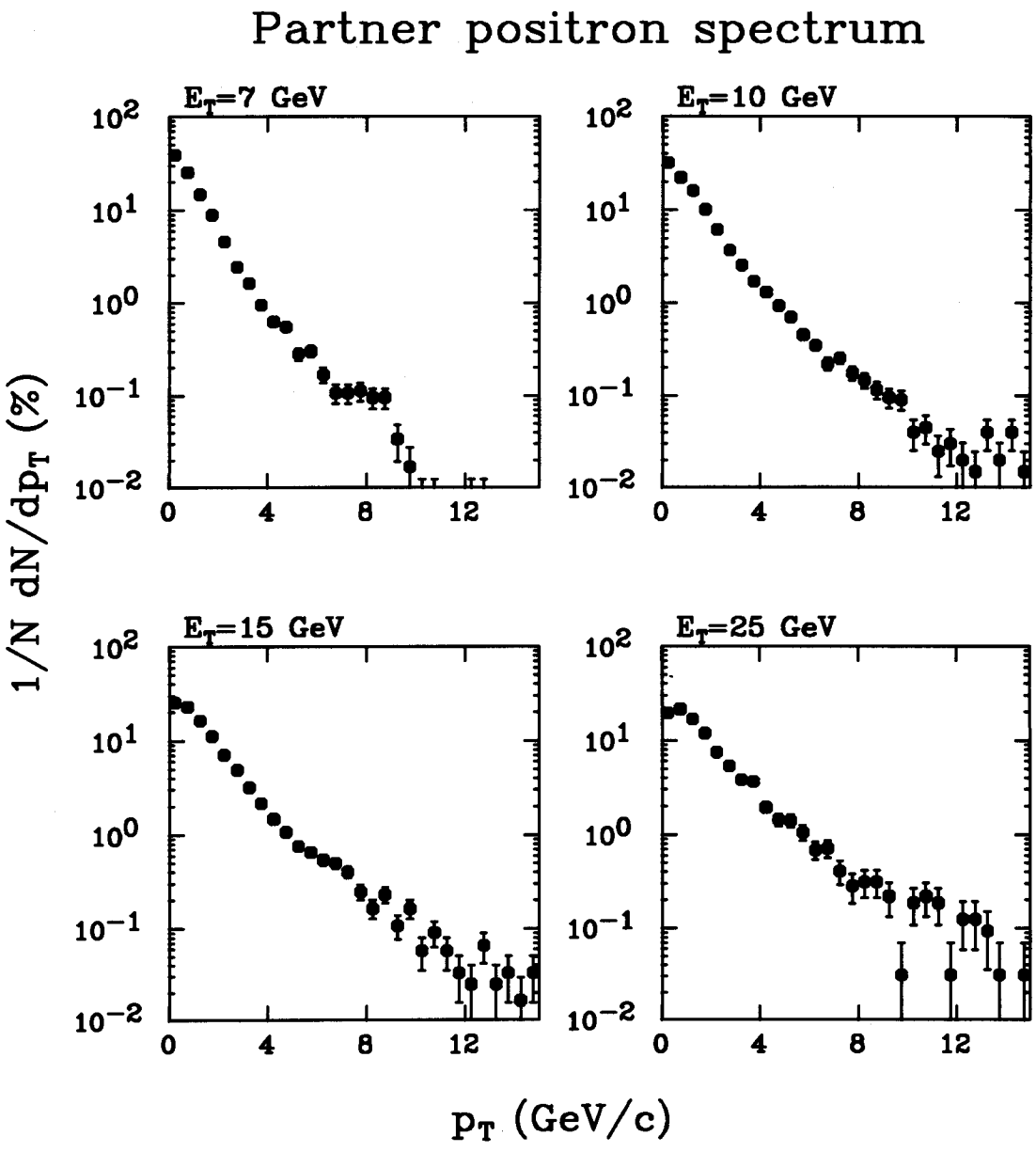

Figure 3.25: The Monte Carlo partner positron spectra.

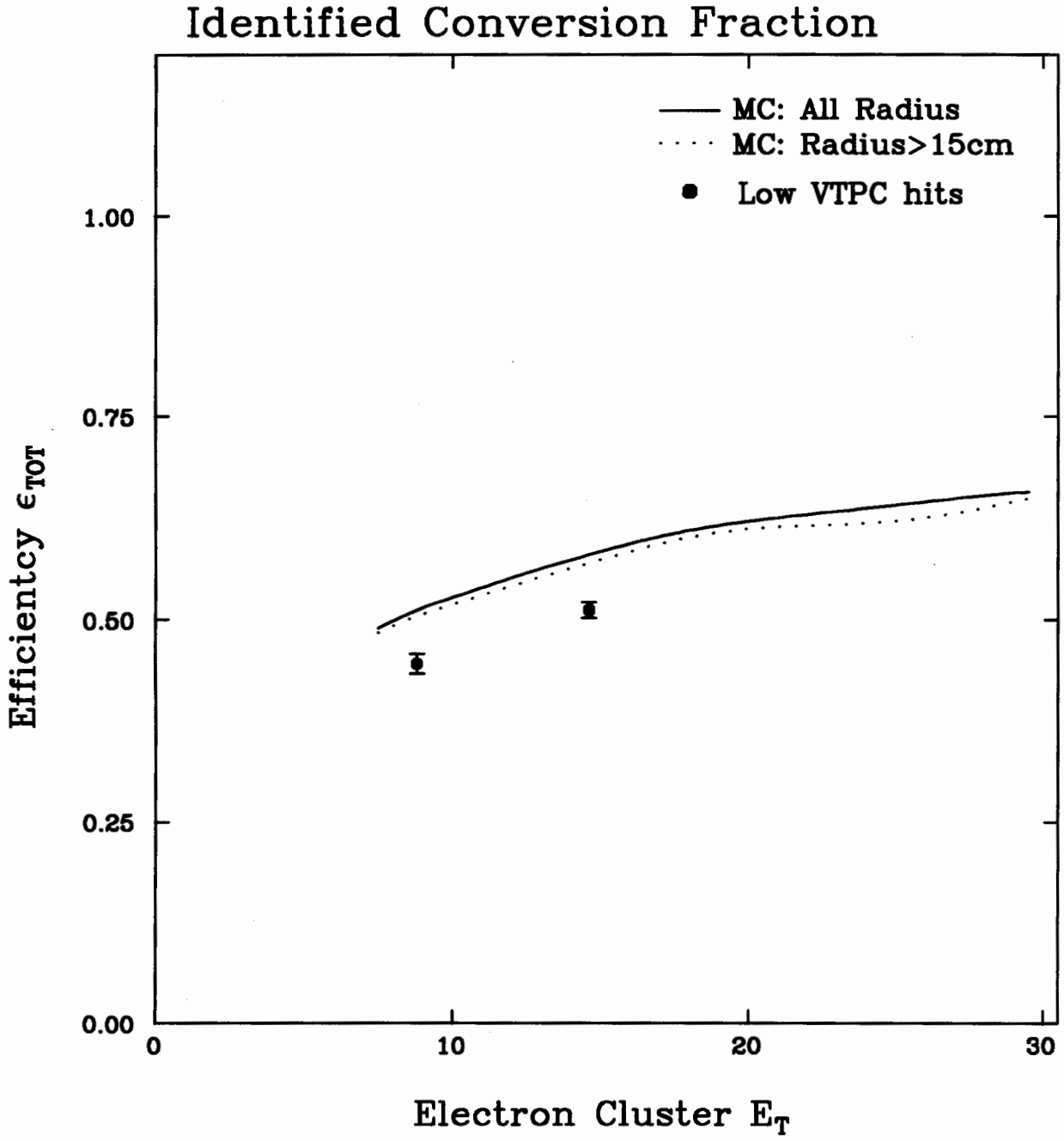

Figure 3.26: The overall efficiency of the photon conversion finding algorithm.

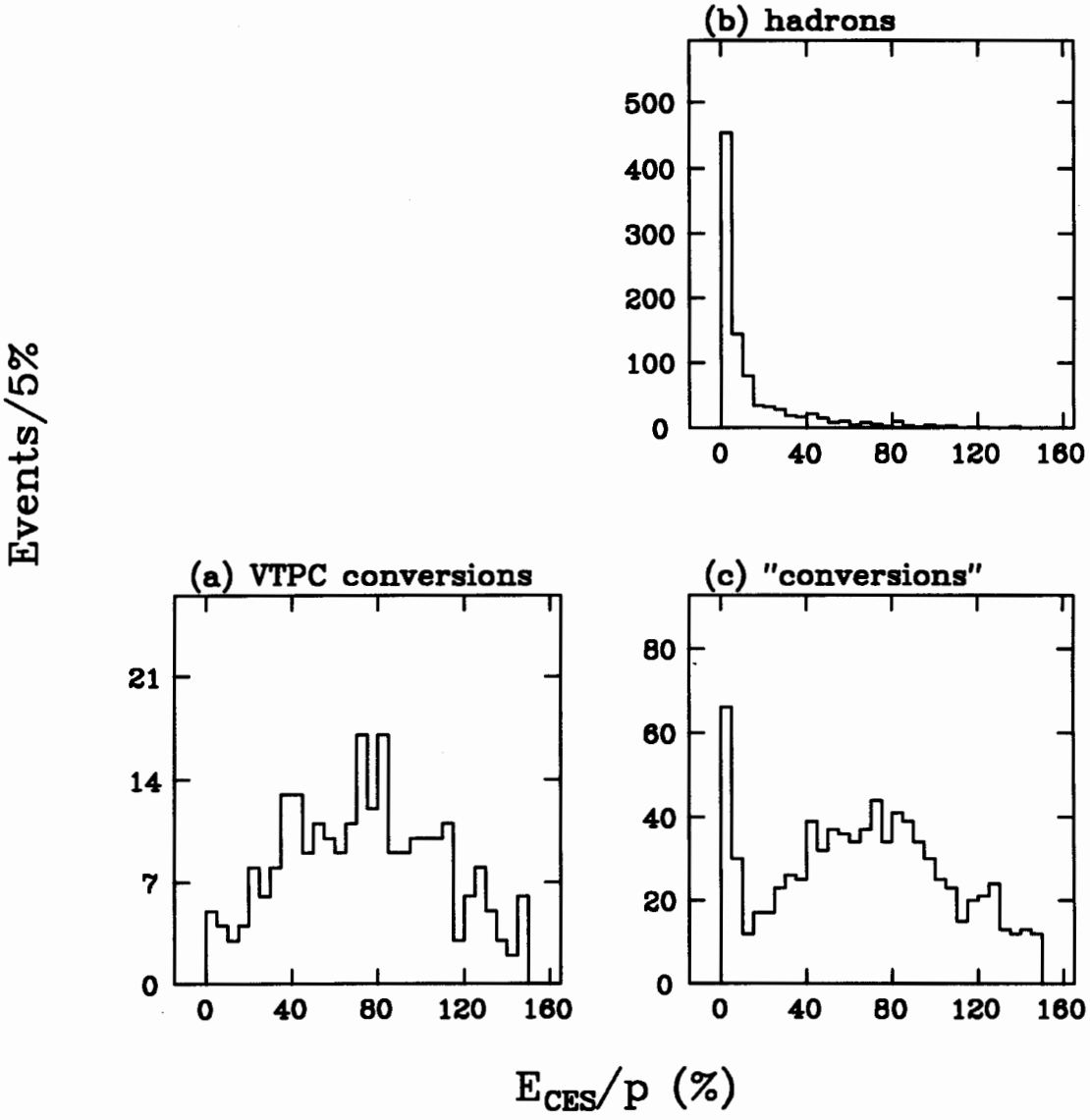

Figure 3.27: The normalized CES pulse height for (a) the positron tracks in the VTPC identified conversion pairs, (b) the random tracks and (c) the candidate positron tracks in the photon conversions found by the pair algorithm.

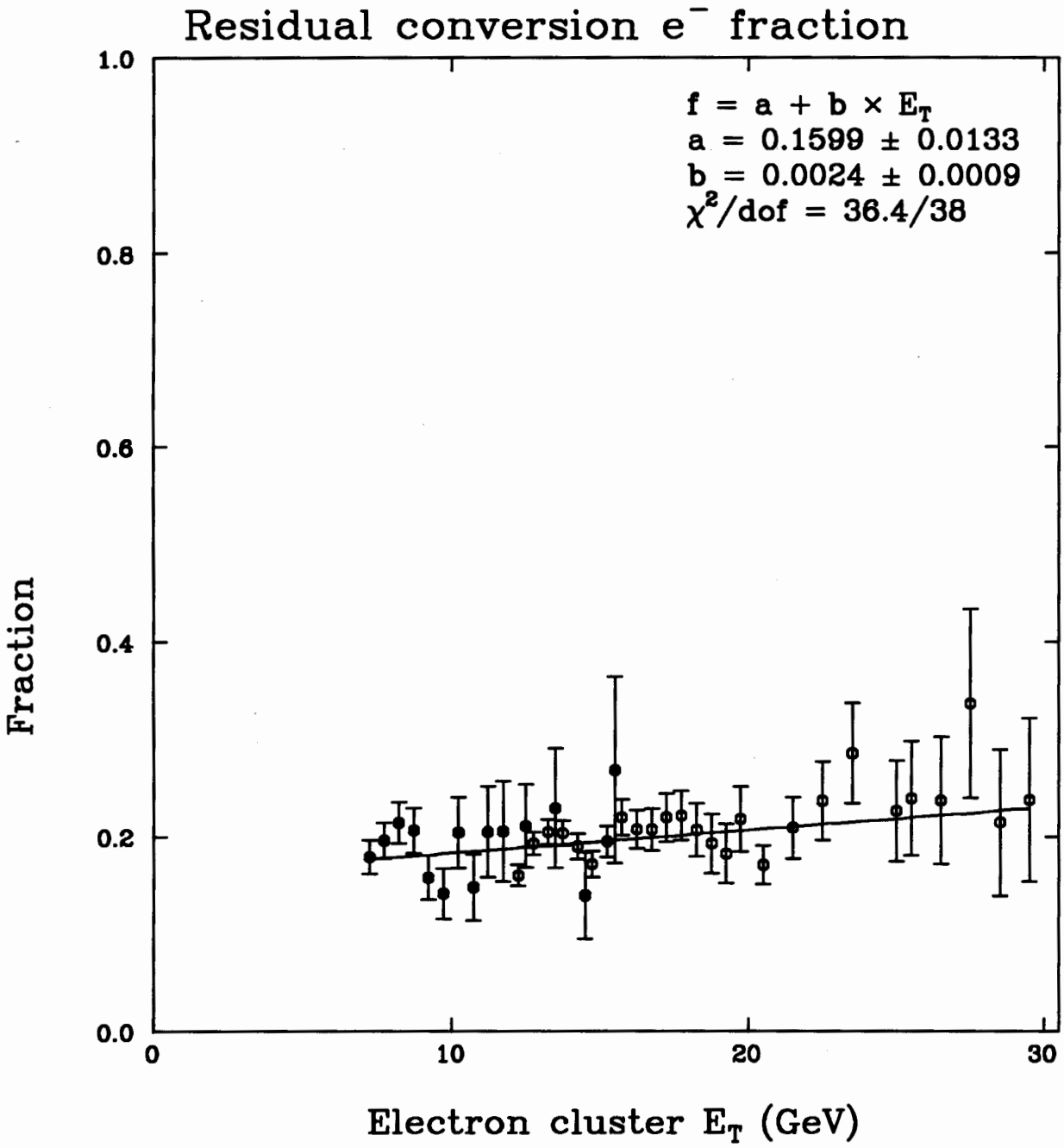

Figure 3.28: The fraction of the residual photon conversion background in the prompt electron sample.

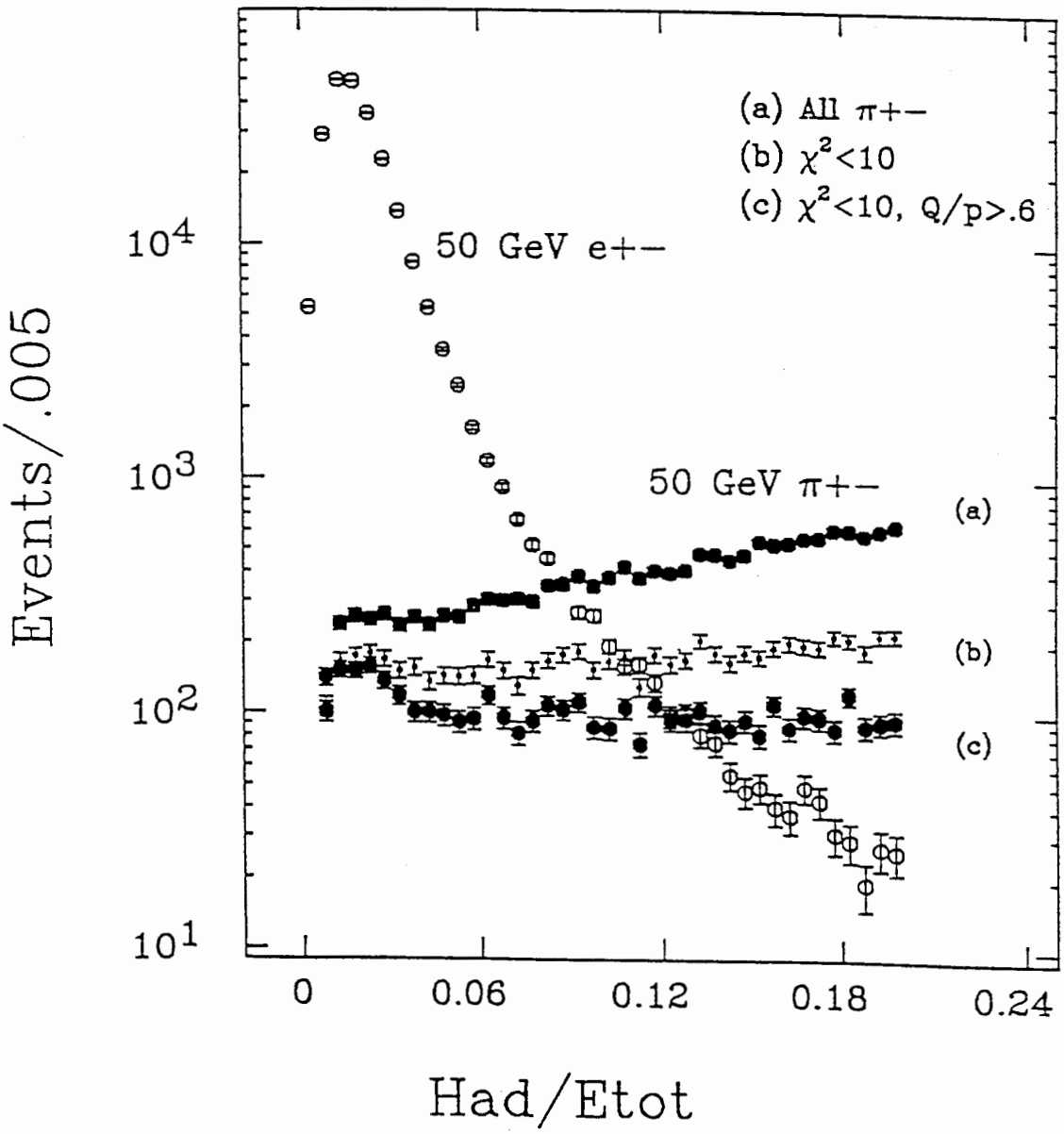

Figure 3.29: Hadronic energy fraction distributions for test beam pions and electrons. For the pions, three curves correspond to (a) no CES cut at all, (b) with CES χ^2 cut, and (c) with additional CES pulse height cut.

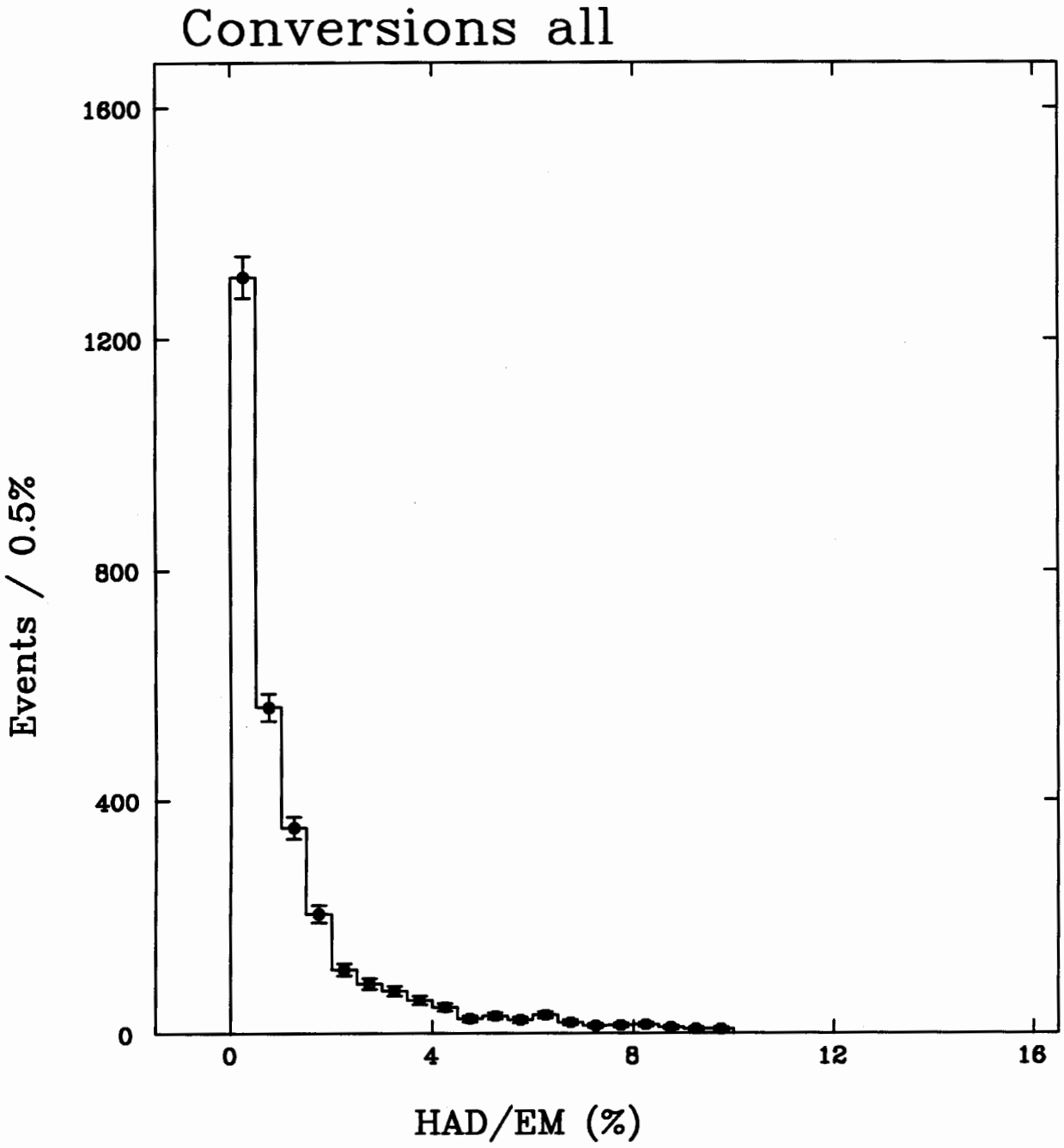

Figure 3.30: HAD/EM distribution for photon conversion electrons in real data.

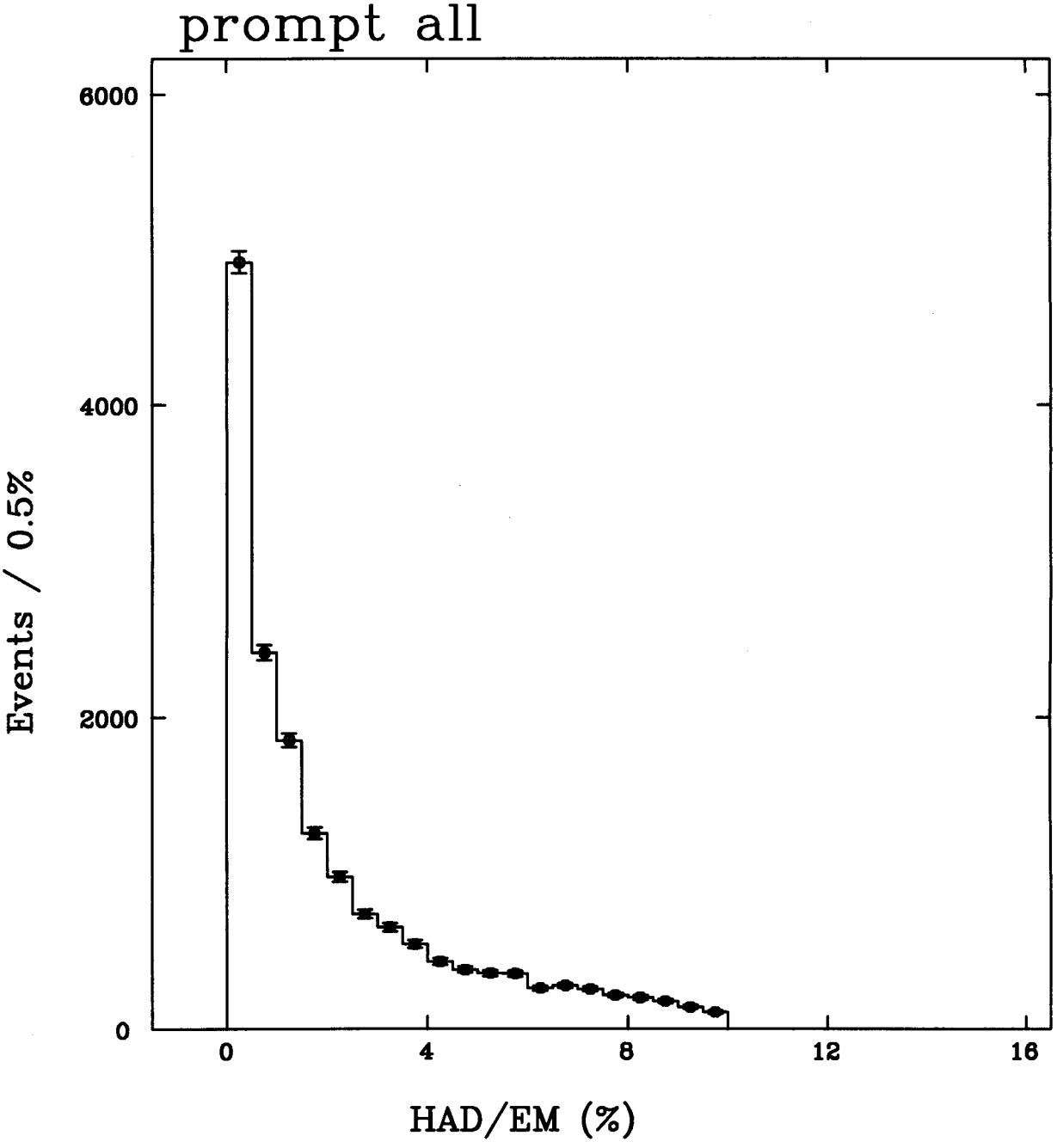

Figure 3.31: HAD/EM distribution for "prompt" electrons in real data.

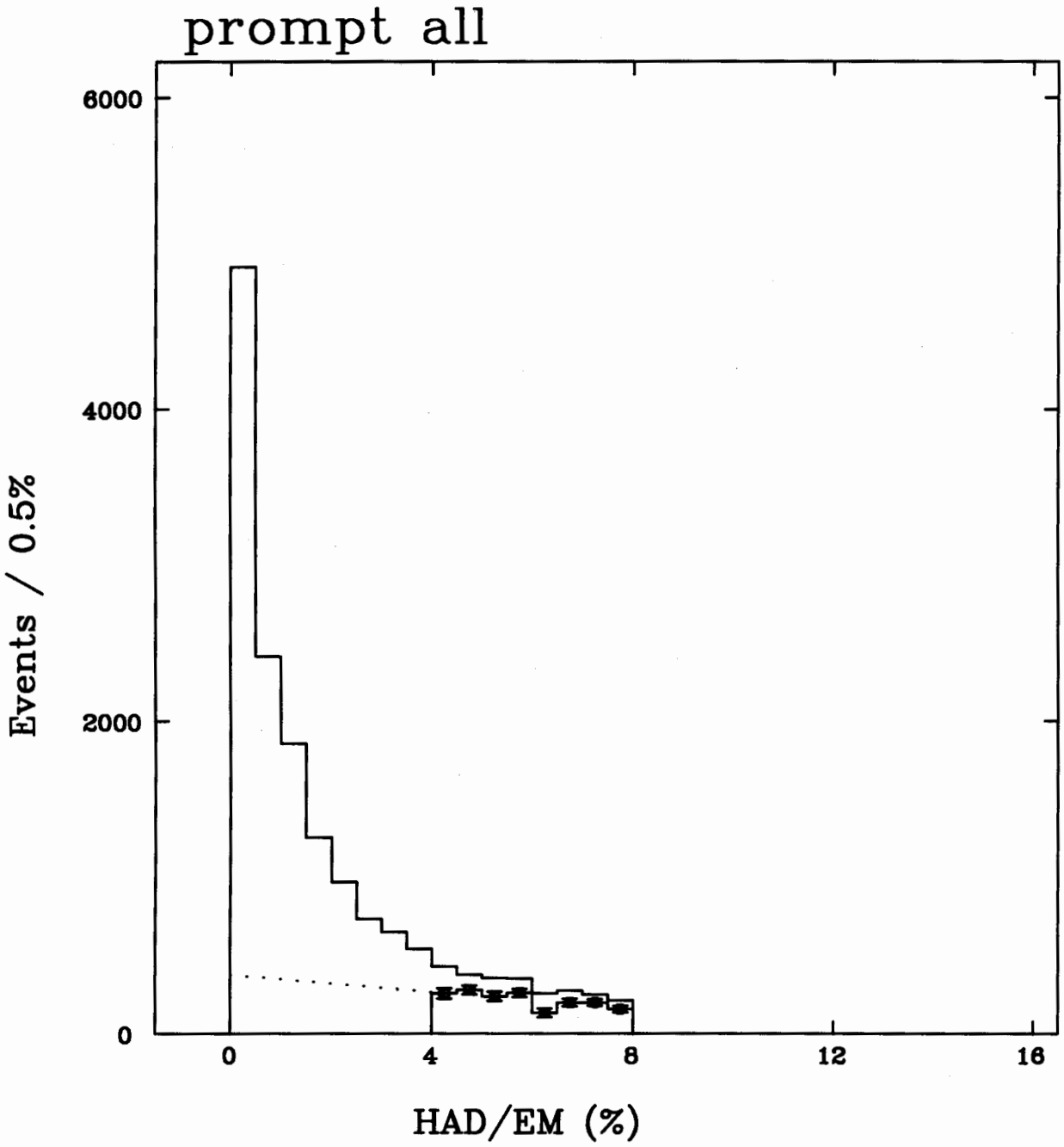

Figure 3.32: Estimated HAD/EM distribution for the "pions" in the prompt electrons.

Chapter 4

Extraction of Bottom Events

This Chapter is devoted to the extraction of the bottom events from the inclusive electron events. We first consider a physics background, charm decay electrons. Kinematics differences predict a relative enhancement of the bottom electrons in the inclusive electron events.

We then present the partial reconstruction of the semileptonic decays of B hadrons. We reconstruct charm and strange particles produced near the electrons.

4.1 Bottom and charm decay electrons

As noted earlier, semileptonic decays of heavy quarks are expected to be the dominant source of prompt electrons at high transverse momenta. The relevant heavy quarks are charm and bottom quarks. They both have similar branching fractions into semileptonic decays, of order 10%. Therefore charm electrons can be a physics background for the bottom electrons. We now discuss the relative rates of bottom and charm electrons at high transverse momenta.

The production of high p_{T} electrons in heavy quark events can be expressed schematically in the following steps:

- Production of a heavy quark, with a steeply falling p_{T} spectrum.

Source	$B_{u,d}$	B_s	B_{baryons}	$b \to c \to e$	$B \to \psi \to e$	$c \to e$
% Production	60	9	5	4	1	20
Efficiency	.43	.43	.35	.13	.55	.17
% Observed	72	12	5	2	1	9

Table 4.1: Fractions of the electrons with p_T above 12 GeV in ISAJET b and c jets.

- Hadronization (fragmentation) of the heavy quark into a heavy hadron.
- Decay of the heavy hadron into an electron and a system of lighter hadrons.

At the Tevatron bottom and charm quarks are produced in strong interactions, which are flavor independent. The quark mass is the only difference between them. In the lowest order processes in QCD the differential cross section falls with $(p_T^2 + m_Q^2)^{-2}$. Therefore two quarks are produced at the same rates when p_T is large enough compared to their masses. This is the very region we are interested in now. We plot in Figure 4.1 the differential production cross sections of the b and the c quarks at the Tevatron energy predicted by the ISAJET Monte Carlo program [41]. As expected two cross sections are almost identical at high transverse momentum.

It is known from e^+e^- experiments that heavy quark fragmentation is "hard", that is, a hadron containing the heavy quark carries a large fraction of the parent heavy quark's energy-momentum (Appendix A). The fragmentation becomes harder as the heavy quark mass increases. As described in Appendix A, bottom hadrons carry 83% of the parent quark's momentum on the average. This number is 67% for the charm quark. Given the same production cross sections at the quark level, which fall rapidly with p_T, the harder b quark fragmentation results in a harder p_T spectrum of B hadrons than charm hadrons at high p_T. This is shown in Figure 4.2.

The p_T spectra of decay electrons are accordingly harder in bottom than in charm decays. The larger mass of bottom hadrons, or the larger Q values in decays, also helps this.

On an experimental side, bottom electrons are more isolated because of the larger

B hadron masses, and are easier to detect. The electron selection efficiency is about three times higher for bottom electrons than for charm electrons (Section 5.3.4). This fact enhances bottom electrons, too, in the observed electron rates. The $p_{\rm T}$ spectra of electrons after the inclusion of the detection efficiencies are shown in Figure 5.12.

Table 4.1 summarizes a Monte Carlo study of electron rates. Here we have started from the almost same production rates at the quark level for bottom and charm. In the electron rates the electron selection efficiencies are taken into account. We see that charm electrons account for only 1/10 of the total electrons.

In summary, the relative rate of about 1 to 10 is predicted for charm and bottom electrons when we assume the same quark level rates at high $p_{\rm T}$, which is the prediction of the QCD. We use 10% as the fraction of charm electrons in our prompt electron sample after the photon conversion and fake hadron backgrounds are subtracted. Although this is a plausible number, we allow a factor of two variation in the production cross section ratio. That is, we use

$$f_{\rm charm} = 0.10^{+0.10}_{-0.05}. \tag{4.1}$$

4.2 Partial reconstruction of semileptonic B decays

In this Section we study the production of charmed and strange particles in association with the electrons, or the partial reconstruction of semileptonic B hadron decays. It serves as a rather direct evidence for bottom quark production and its semileptonic decays.

Semileptonic decays of B hadrons are expressed at the parton level as

$$b \to \ell^- \bar{\nu} c, \tag{4.2}$$

where the small b-to-u transition is neglected. At the hadron level the charm quark c is replaced by a charm particle, D^0, D^+, D_s^+ and so on. We do not expect charm particles to be created from vacuum in hadronization processes because of their large masses.

Therefore a lepton and a charmed particle is the unique signature of the semileptonic B decays. Since we have tagged the flavor (or charge) of the parent b quark through the electron charge, the expected charm flavor is accordingly determined.

4.2.1 Charmed particles

We look for charmed particles produced near the electron. Although we can think of reconstructing various charmed particles in various decay modes, the neutral charmed meson decay into charged particles,

$$\begin{aligned} \bar{B}_{u,d} &\rightarrow e^- \bar{\nu} D^0 X, \\ D^0 &\rightarrow K^- \pi^+, \end{aligned} \tag{4.3}$$

would be the only mode[1] we can reconstruct now with reasonable statistics and a signal-to-noise ratio.

Since the D^0 decays to $K^-\pi^+$, but not to $K^+\pi^-$, the charge of the kaon is identical to that of the electron ("right sign" combination) in the semileptonic B decays.

Since the CDF lacks particle identification, we use all oppositely charged CTC track pairs and assign kaon and pion masses. In order to reduce combinatorial background, we use tracks within a cone of 0.6 in the η-ϕ space around the electron. We also apply the following kinematical cuts on the tracks:

$$\begin{aligned} p_{\mathrm{T}}(K) &> 1.5 \text{ GeV}/c, \\ p_{\mathrm{T}}(\pi) &> 0.5 \text{ GeV}/c. \end{aligned} \tag{4.4}$$

Figure 4.3 shows the invariant mass distributions for the right sign $K^-\pi^+$ pairs in the electron events. The D^0 signal is apparent.

The signal is absent in the "wrong sign" combinations with the prompt electrons (Figure 4.4), and with the photon conversion electrons (Figure 4.5). These facts suggest

[1] In this Section a reference to a particular charge state also indicates the charge conjugate mode.

that the D^0 and the electron are the decay products of a single $\bar{B}$ meson.

The inclusive D^0 rate in the semileptonic decays of non-strange B mesons has been measured by the CLEO collaboration at $\Upsilon(4S)$. Therefore it is possible to predict a rather firm number of expected D^0 events we should observe in our electron sample. Conversely, we can measure the production cross section of b quarks using the number of reconstructed D^0's. We will do this in the next Chapter. We just note here that our observed D^0 rate is consistent with the prediction based on our estimate of non-prompt and fake backgrounds in our electron sample and the assumed charm fraction.

We now describe another charmed particle, D^{*+}. We try its reconstruction through the decay chain

$$D^{*+} \rightarrow D^0\pi^+, \;\; D^0 \rightarrow K^-\pi^+. \tag{4.5}$$

The D^{*+} mass is 2010 MeV, which barely allows the first decay. We plot in Figure 4.6 the mass difference

$$\Delta m \equiv m(K^-\pi^+\pi^+) - m(K^-\pi^+) \tag{4.6}$$

for the $K^-\pi^+$ pairs within the D^0 mass window (1865 ± 30 MeV). We observe a clean peak. When we require the wrong charge on the second pion, the peak is absent (dotted histogram).

4.2.2 Strange particles

Strange particles are produced in B decays via sequential decays of the charm particle:

$$b \rightarrow \ell^-\bar{\nu}c, \; c \rightarrow s. \tag{4.7}$$

In this process flavors are also uniquely determined. We should observe a negatively charged lepton and a particle containing a strange quark, not an anti-strange quark. We cannot use single charged kaons for the study, because CDF cannot separate kaons from pions. Thus we try to reconstruct resonances of strange particles.

K^* and ϕ production

A vector strange meson, $\bar{K}^{*0}(= s\bar{d})$, is a candidate for such a reconstruction. It has a mass of 896 MeV and a broad width of about 50 MeV. It decays into $K^-\pi^+$ about 2/3 of the time. The charge of the kaon tags the flavor of the parent K^*, in the same way as in $D^0 \to K^-\pi^+$ decay. The "right sign" combination is a negative electron and a $\bar{K}^{*0}$,

$$\bar{B} \to e^-\bar{\nu}DX, \quad D \to \bar{K}^{*0}X', \quad \bar{K}^{*0} \to K^-\pi^+, \tag{4.8}$$

where D is a particle containing a charm (not anti-charm) quark. Semileptonic charm decays

$$c \to e^+\nu s \tag{4.9}$$

are a source of the "wrong sign" combination, a positron and a $\bar{K}^{*0} \to K^-\pi^+$.

Since strange particles are lighter, we would expect that they are also produced in the hadronization process of partons. A Monte Carlo study [42] shows that requiring high transverse momentum is effective in suppressing these "fragmentation" K^*'s and in enhancing K^*'s coming from the B decays. We require that the p_T of K^* is above 2 GeV/c. We show in Figure 4.7 the invariant mass distributions of the right and wrong sign $K^-\pi^+$ pairs. The wrong sign pairs are scaled by a factor of 0.75 for the display purpose. A peak is present near 0.89 GeV in right sign pairs, and is absent in wrong sign pairs. Curves show a fit to a Breit-Wigner resonance function and a smooth background representing the phase space. The number of right sign K^{*0}'s is 844 ± 150 for the combined 7 and 12 GeV electron sample. It is rather difficult to predict an accurate K^{*0} rate, because there exist no measurements of the K^* rate in semileptonic B decays, or of the inclusive branching fractions into K^{*0} of various charm particles (D^0, D^+, D_s^+ and so on). We estimate from Monte Carlo events that about 780 right sign K^{*0}'s are observed per 20,000 bottom electrons, which is an estimated number of prompt electrons in the data sample.

The absence of a peak in wrong sign pairs supports the conclusion in Section 4.1

that our electron sample consists mainly of bottom decay electrons rather than charm decays.

We next consider the production of ϕ, which is a vector $s\bar{s}$ state. The mass (1020 MeV) is just above the $K\bar{K}$ pair threshold. We cannot use the flavor correlation in the case of ϕ. But we expect that high $p_{\rm T}$ ϕ's come mainly from the B decay, because ϕ is as heavy as K^* and quite a similar kinematics is expected. We try to reconstruct ϕ decays into a charged kaon pair,

$$\phi \rightarrow K^+K^-, \tag{4.10}$$

in a similar way as for K^* decays. Figure 4.8 shows the invariant mass spectrum of kaon pairs. A peak is observable near 1.02 GeV. We check that the peak is absent in the control sample, consisting of photon conversion electrons.

It is interesting to investigate the origin of the ϕ's. In the decays of the strange charmed meson, D_s^+ $(= c\bar{s})$, ϕ is expected to be rich, since a pair of strange quarks is provided automatically. On the other hand, in the case of non-strange charmed mesons, D^0 and D^+, the rate is expected to be low, because the production of ϕ requires a creation of an $s\bar{s}$ pair from vacuum. A Monte Carlo study [42] shows that about 90% of ϕ's in semileptonic B decays come from the strange B meson, B_s, which produces a D_s^+ 100% of the time in the spectator decay picture. This would be a useful tool in identifying semileptonic B_s decays, once we get higher statistics in future runs.

K_S^0 and Λ production

We now extend our study of the strange particle production to K_S^0 and Λ. They are identified through decays

$$K_S^0 \rightarrow \pi^+\pi^-, \tag{4.11}$$

$$\Lambda \rightarrow p\pi^-, \tag{4.12}$$

at a displaced secondary vertex. A more detailed discussion on the reconstruction of these neutral vees may be found in [43]. We plot invariant mass distributions in Fig-

ures 4.9 and 4.10. K^0_S and Λ peaks are apparent, and the distributions are fairly clean with a relatively low combinatorial background.

The production rates and the flavor correlation (for Λ's only) are also studied in [43]. K^0_S's and Λ's are observed about 5% and 1% of the time, respectively. These rates are, however, quite similar for the prompt electron sample and for control samples of photon conversion electrons and hadrons faking electrons. Also the charge correlation in Λ's is weak. Probably these particles are produced in fragmentation processes in comparable rates as in B decays, because of their lighter masses.

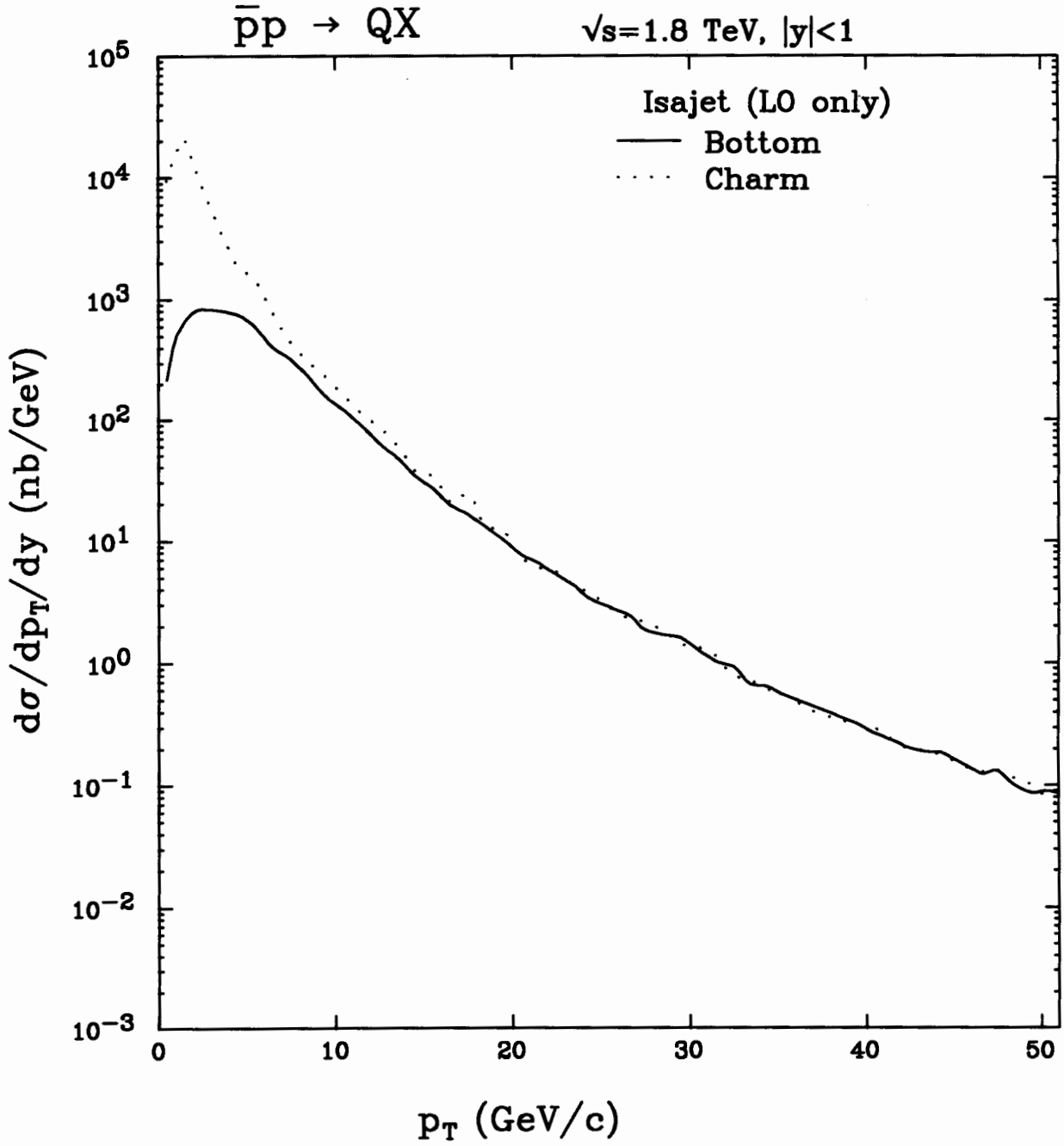

Figure 4.1: The bottom and charm quark production cross sections from the lowest order ISAJET prediction.

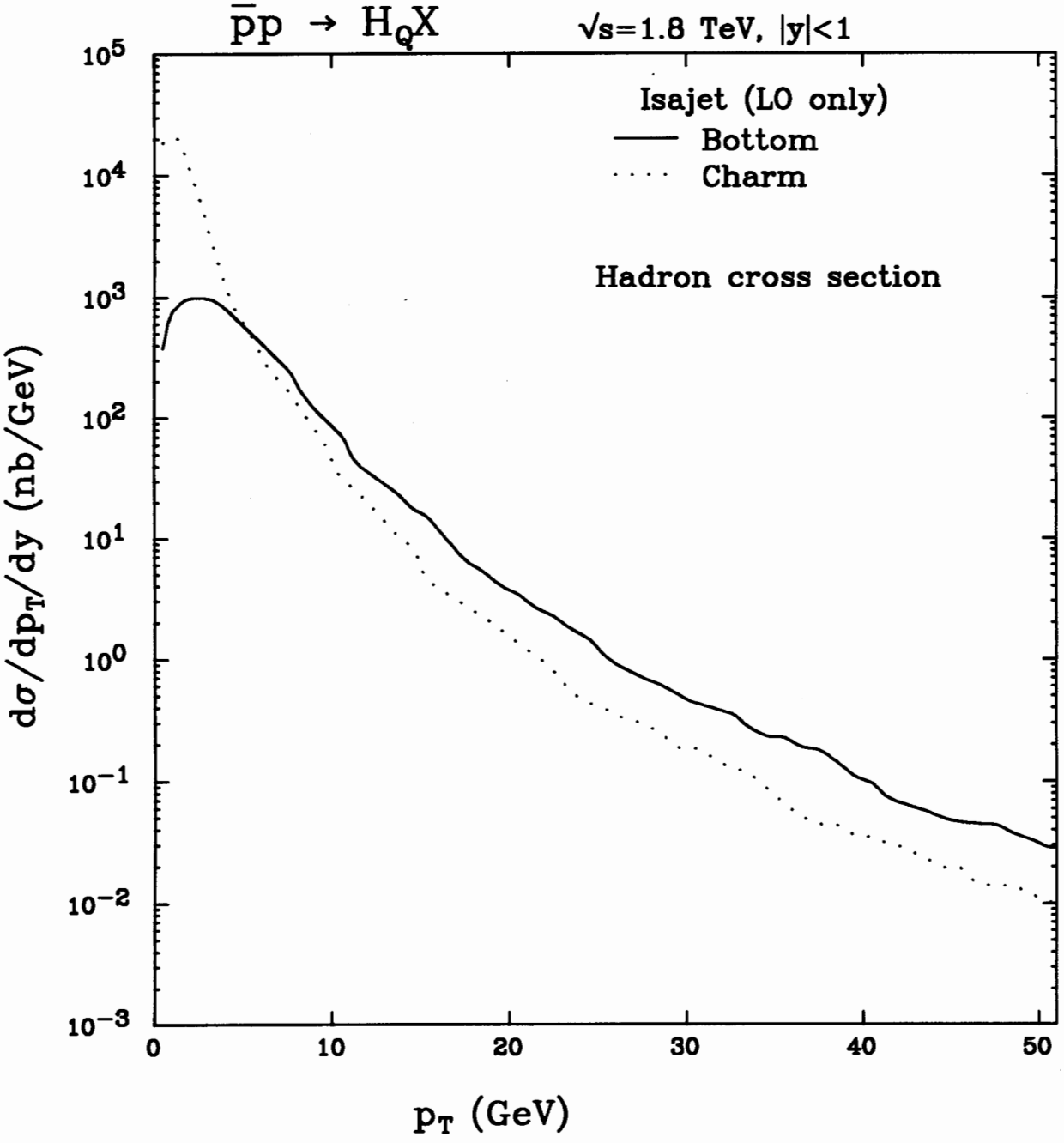

Figure 4.2: The bottom and charm hadron production cross sections from the lowest order ISAJET prediction.

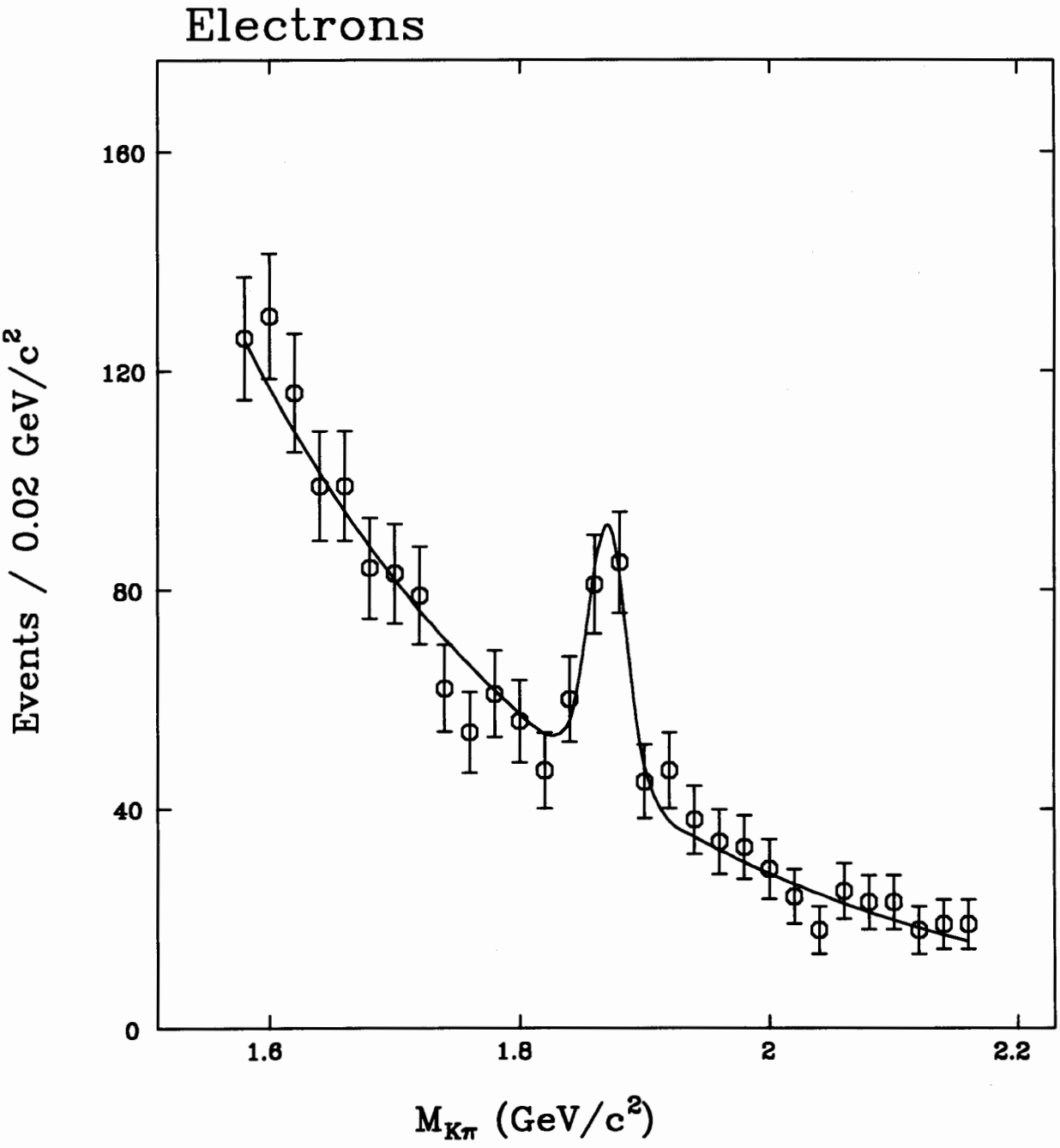

Figure 4.3: Right sign $K^-\pi^+$ invariant mass distribution in the electron events.

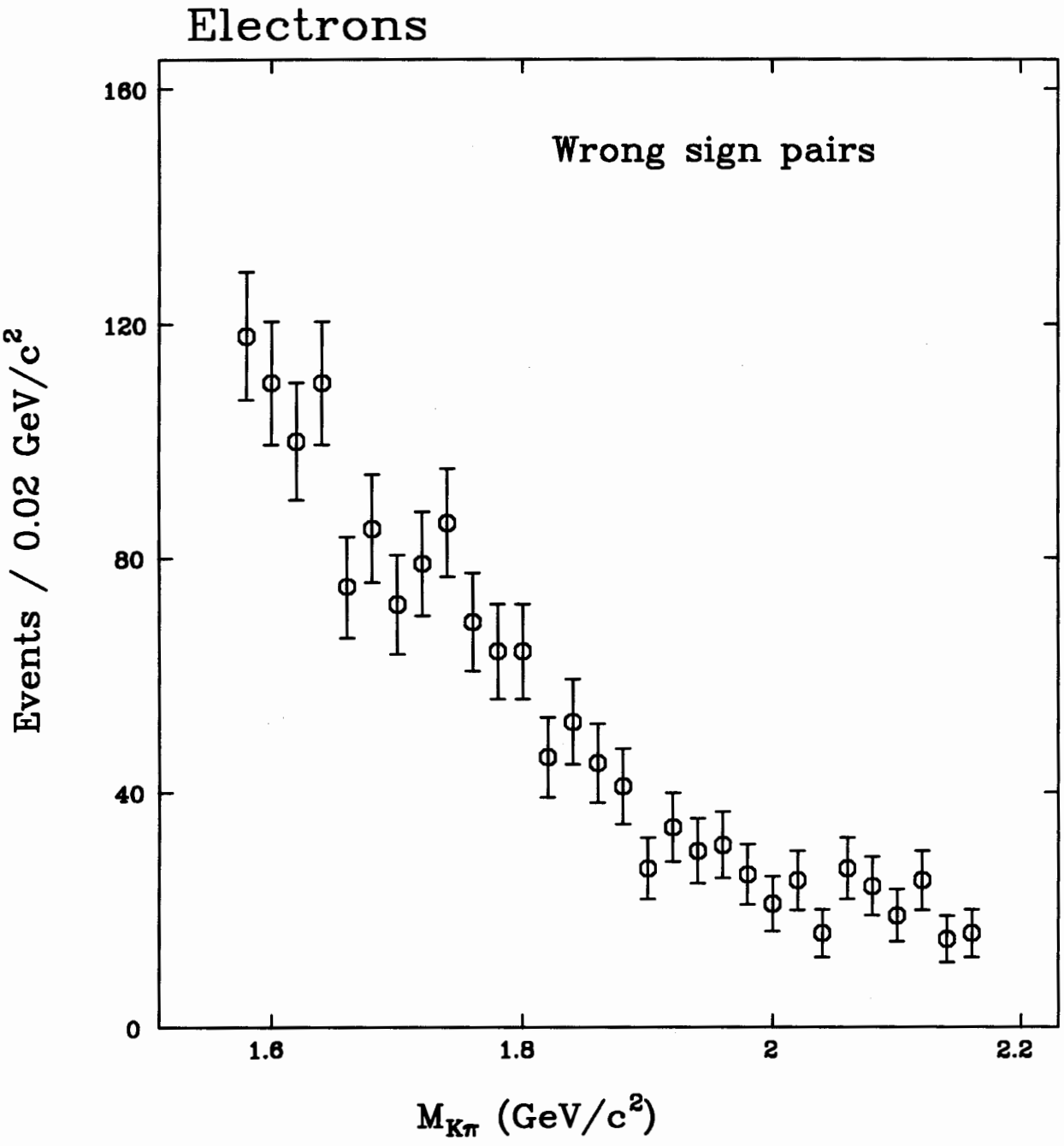

Figure 4.4: Wrong sign $K\pi$ invariant mass distribution in the electron events.

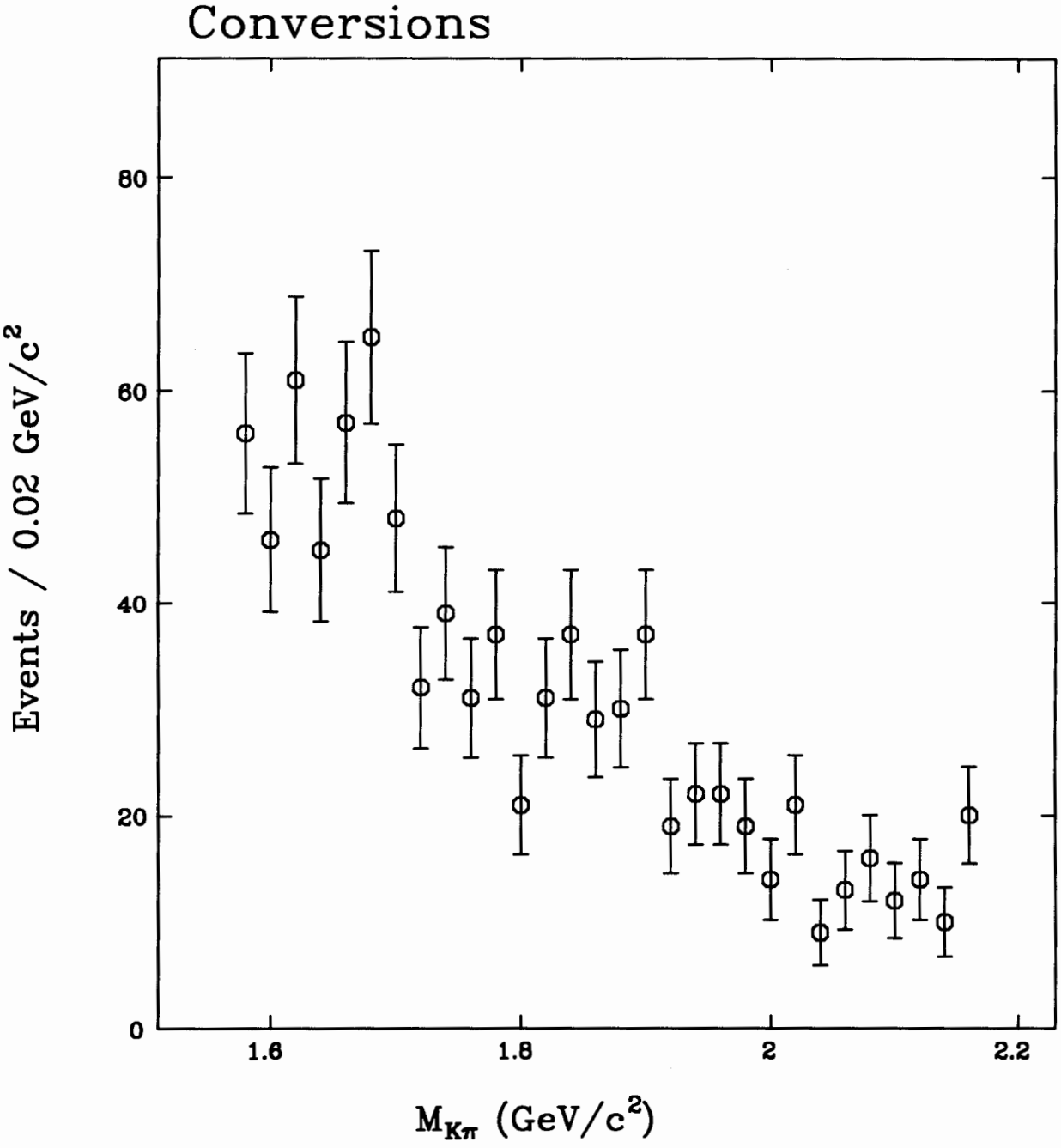

Figure 4.5: $K^-\pi^+$ invariant mass distribution in the photon conversion events.

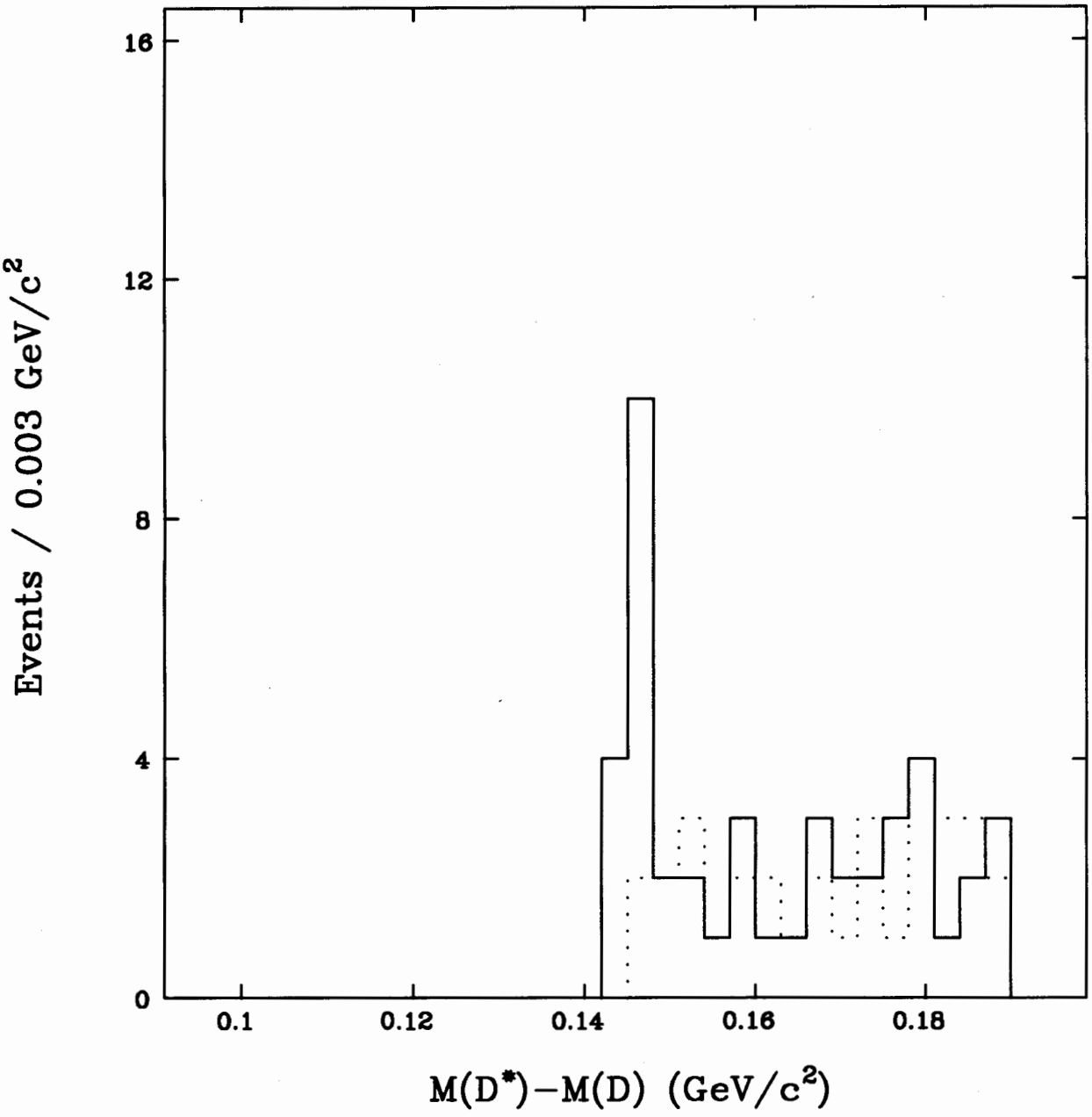

Figure 4.6: $K\pi\pi$ and $K\pi$ mass difference distributions.

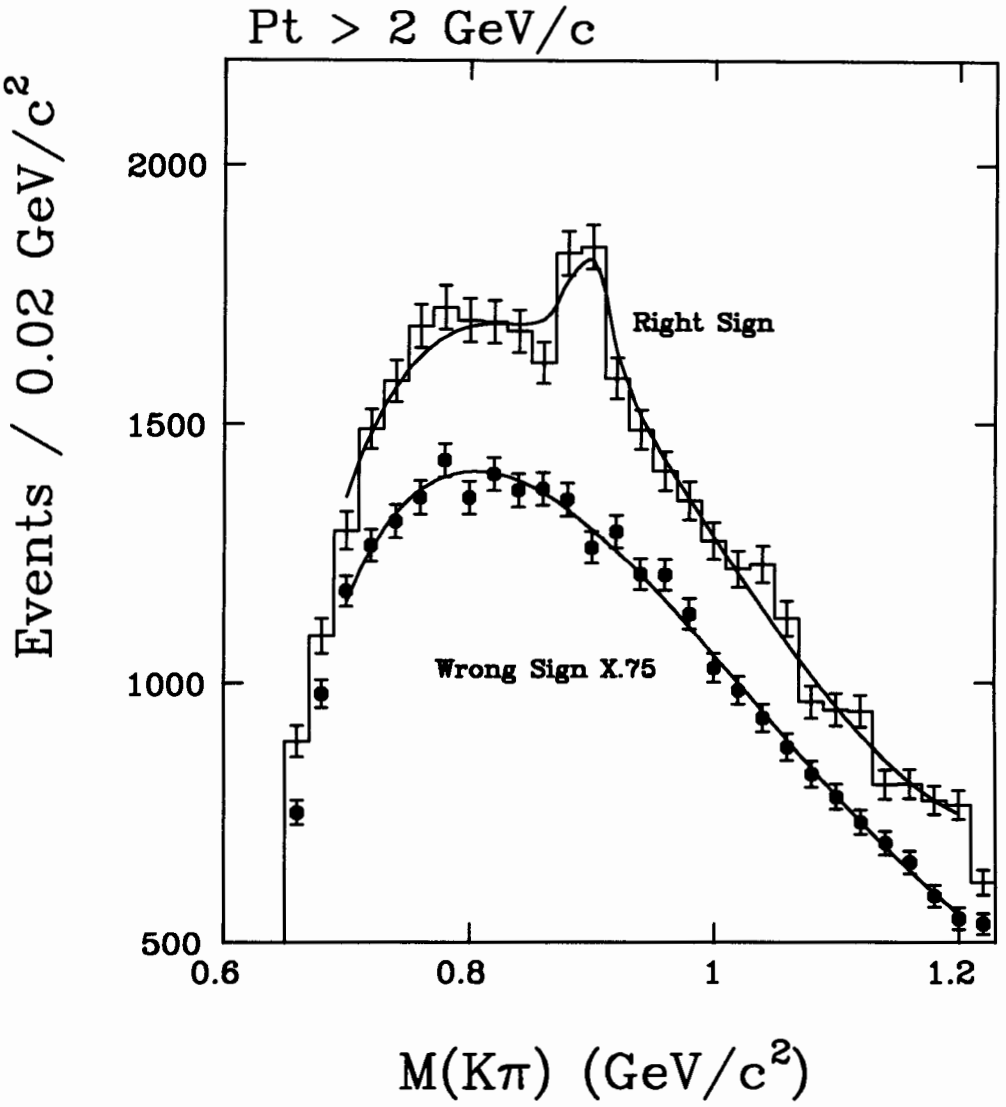

Figure 4.7: Right and wrong sign $K^-\pi^+$ invariant mass spectra near $K*$ region.

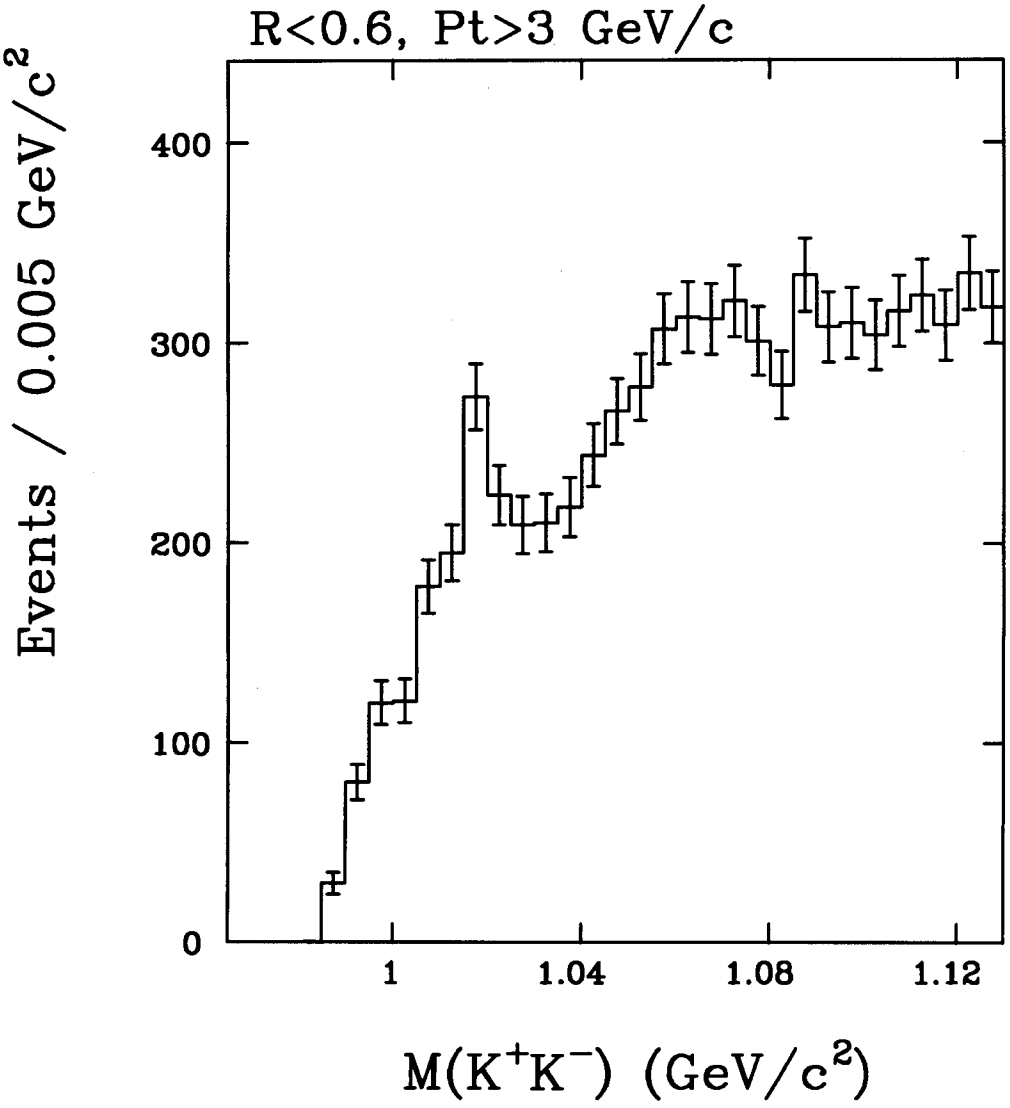

Figure 4.8: K^+K^- invariant mass distribution near ϕ region.

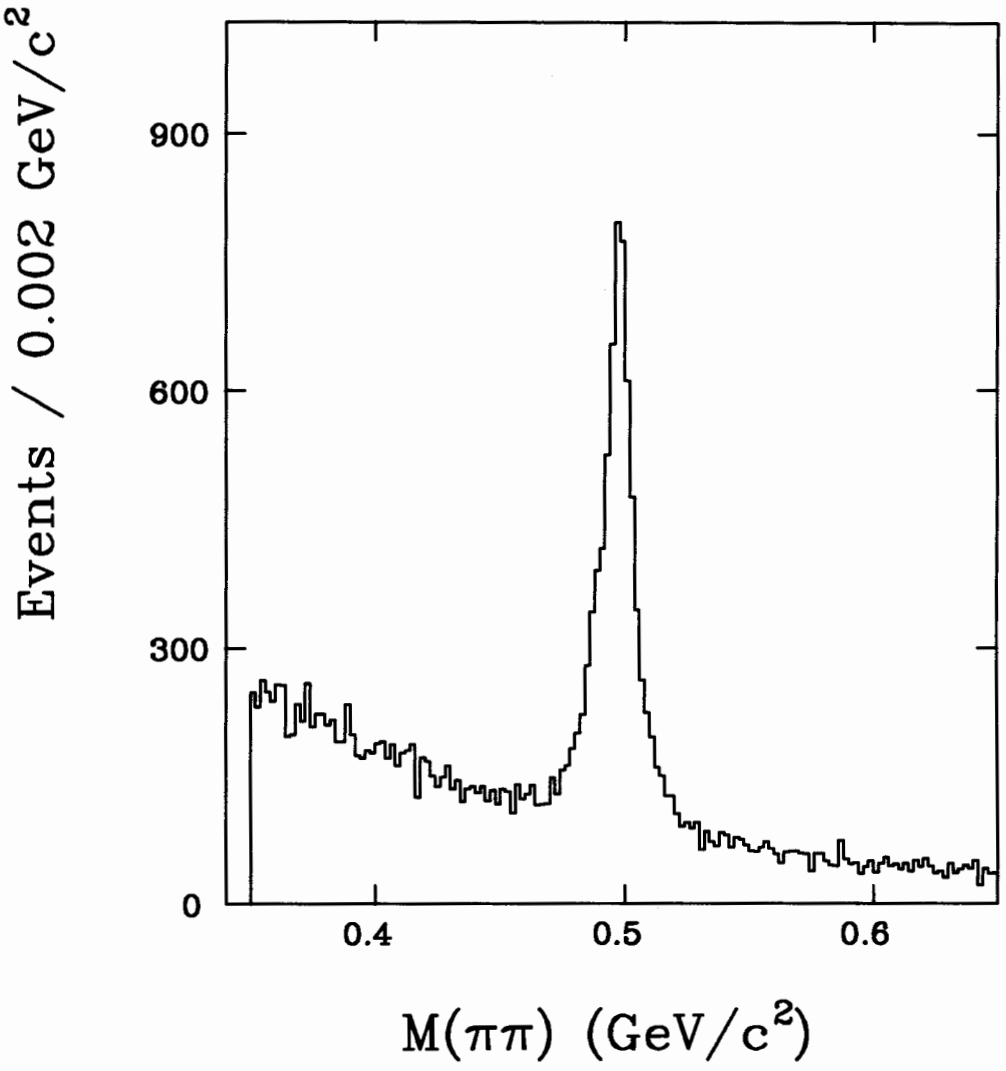

Figure 4.9: $\pi^+\pi^-$ invariant mass distribution near K^0 region.

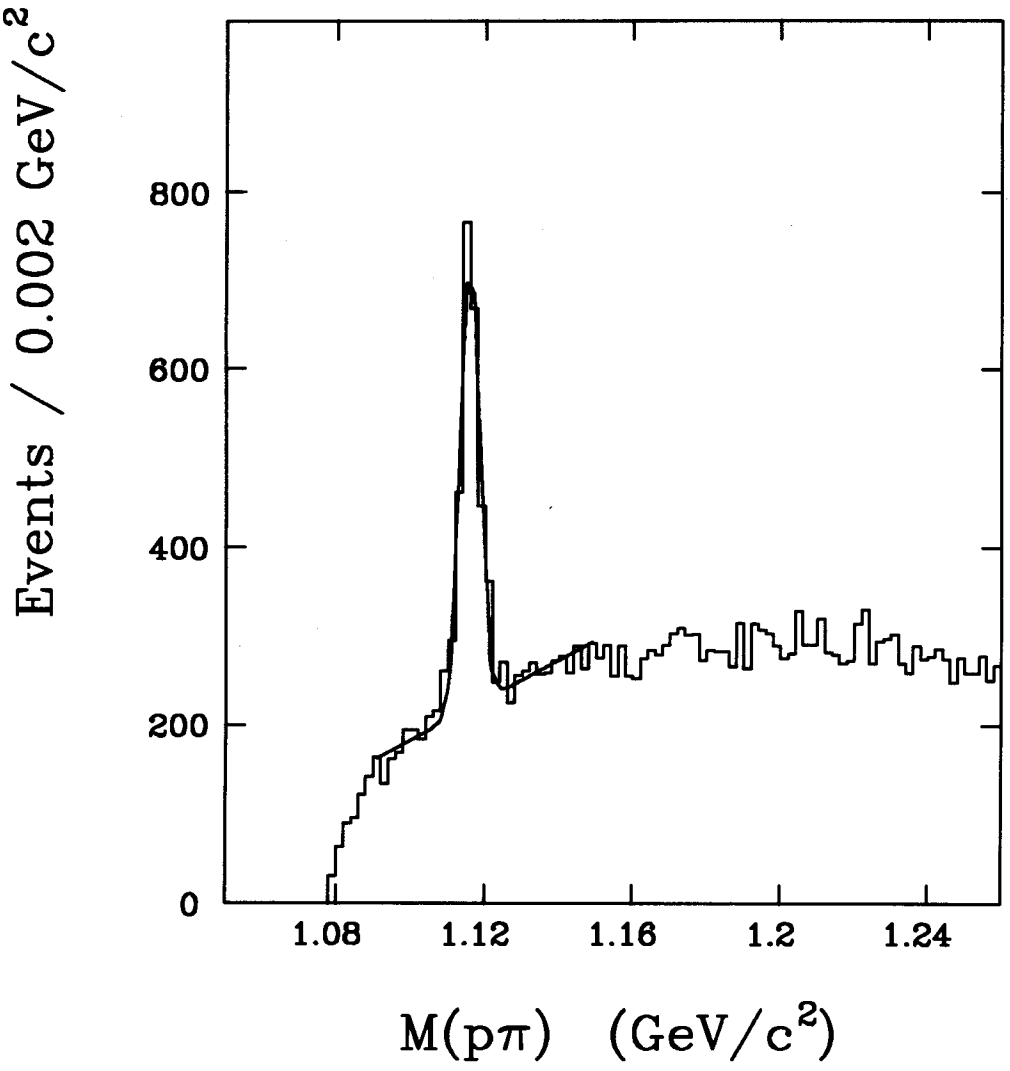

Figure 4.10: $p\pi^-$ invariant mass distribution near Λ region.

Chapter 5

Measuring the b Quark Production Cross Section

Now we turn to the measurement of the bottom quark production cross section using the observed rate of the inclusive electrons, which we have discussed in Chapters 3 and 4. The process requires the knowledge of the kinematical relationship between the quark and its decay electron, and of the electron selection efficiency. We determine them using the Monte Carlo method. We describe below the Monte Carlo models employed and the estimate of the electron selection efficiency, and derive the bottom quark production cross section from the inclusive electron rates. We also describe the measurement of the b quark production cross section using the rate of the correlated electron-D^0 production, which complements the above method.

5.1 Relating the electron and the b quark rates

A Monte Carlo calculation predicts a certain electron production rate, given a b quark rate. Since we measure the electron rates, we can obtain the b quark rates once we know the relation between them. Several factors go into this relation, including

- b quark production $p_{\rm T}$ spectrum,

- b quark fragmentation into B hadron,
- Semileptonic decay branching ratio of the B hadron,
- Decay kinematics/dynamics of the B hadron into the electron.

In addition to these, we need to know the electron selection efficiency, which is $p_{\rm T}$ dependent to some extent.

There can be various ways of extracting the b quark cross section from the decay electron cross sections, and we follow the one by UA1 [17]. We measure electron cross sections and relate them to the b quark cross section integrated over a certain kinematic range using a Monte Carlo calculation:

$$\sigma_b(\text{data}) = \sigma_e(\text{data}) \frac{\sigma_b(\text{MC})}{\sigma_e(\text{MC})}. \tag{5.1}$$

We choose three $p_{\rm T}$ intervals for the electrons, 10-15, 15-20 and 20-25 GeV, corresponding to the b quark $p_{\rm T}$ thresholds of 15, 23 and 32 GeV, respectively.

5.2 Model of b quark production and decay

We use Monte Carlo events to simulate bottom and charm jets. It is important to correctly model them because they are used to relate the electron rates to the b quark rates, and also to estimate the electron selection efficiencies.

Fairly good understandings on the B meson decays are available from the CLEO and the ARGUS experiments, as well as on charm hadron properties from a number of experiments. Thus it is reasonable to expect that the decays of these heavy hadrons are well reproduced by Monte Carlo generators. The fragmentation properties of the b and c quarks are also measured by e^+e^- experiments at PEP, PETRA and LEP. The momentum range of the current interest is about 15 to 30 GeV for b quarks, or 10 GeV/c and above for their decay electrons, and it is covered with these experiments.

We use the ISAJET [41] Monte Carlo program to describe the hard collision processes of the heavy quark production, and its fragmentation into hadrons. We use the CLEO Monte Carlo (QQ) [44] to describe the weak decays of pseudoscalar non-strange B mesons. One of the important quantities in the B meson decays is an electron spectrum. Electron and muon spectra have been measured at $\Upsilon(4S)$ state with contribution from continuum subtracted. A measurement [45] from CLEO is shown in Figure 5.1, together with the spectrum given by the QQ Monte Carlo generator. In the real data contribution from the sequential charm decay is not separable, which occupies low energy region. Another important quantity is the spectrum of the charmed particle. In the latest CLEO Monte Carlo, the semileptonic decays of heavy hadrons are described with the nonrelativistic quark model by Isgur, Scora, Grinstein and Wise (ISGW) [46]. The charmed particle momentum spectra in this model are shown in Figure 5.2.

The ISAJET employs the Peterson model for the heavy quark fragmentation. In order to reproduce the e^+e^- experimental results on the b quark fragmentation, we apply a slight modification to ISAJET routines. A more detailed discussion on the Peterson model and fragmentation issues will be given in Chapter 6.3.

The underlying event, particle activities originating from other than the hard collision subprocess, is not well reproduced by Monte Carlo generators in general. We thus use the real data to empirically model it. This is discussed later in this Chapter.

5.3 Electron selection efficiencies

In measuring the b quark production cross section using semileptonic decay electrons, the observed electron rates are subject to the correction for the electron selection efficiency. The electron identification methods impose an implicit isolation requirement on an electron, by cutting on quantities like longitudinal shower leakage (HAD/EM), lateral shower shape tests (LSHR and CES χ^2) and so on. Therefore the efficiencies of the cuts vary depending on the source of the electron. For example, W/Z decay electrons

are well isolated. On the other hand, the electrons from bottom and charm decays are located in jets; there exist other particles close to the electron. The mass of the parent particle (or the Q value of the parent particle decay) and the magnitude of the Lorentz boost, which creates most of the electron momentum in the kinematic range of interest, are what determines the isolation degree of the electrons.

A typical set of the electron identification cuts is as follows (Section 3.2):

- LSHR < 0.2.
- CES-track position matching, $|\Delta x| < 1.4$ cm and $|\Delta z \sin\theta| < 2.0$ cm.
- CES $\chi^2 < 10$ on the average of wire and strip view.
- HAD/EM < 0.04.
- Number of charged tracks pointing to the electron cluster is 1.
- $0.75 < E/p < 1.40$

These cuts minimize the contamination of additional particles within the electron cluster towers, and makes the electron energy measurement more accurate. Cutting on the number of charged tracks associated with the cluster, of which additional contribution comes mostly from charged hadrons, makes the estimate of the electron finding efficiency easier and more reliable.

5.3.1 Simulating electromagnetic showers

Given the correctly generated Monte Carlo events of a b or c jet, the next step is to simulate the detector responses to these particles. Since most of the electron cuts are placed on the quantities measured with the calorimeter, including the strip chambers, it is crucial to simulate correctly the particle responses on the calorimeter.

CEM and CES responses

Phototube responses to electromagnetic particles are relatively easy to reproduce, as long as we know the shower shape and treat properly the fluctuations due to sampling and photoelectron statistics. We use a parameterization of shower shapes based on test beam measurements in order to calculate energies on adjacent towers, and model the fluctuation with the nominal CEM resolution of $14\%/\sqrt{E \sin\theta}$.

As showers on the strip chambers are more complicated, we use real electron showers obtained from the test beam. This is the same method used for the CDF prompt photon production analyses [47]. A virtue of using real showers is that the fluctuations are given naturally. Then the distributions of CES χ^2, for example, are reproduced almost by definition. We use 10-GeV test beam electrons to simulate showers of Monte Carlo electrons. There are additional photons, although they are very low energy, which can change the shower shapes, thus the χ^2 value and the reconstructed shower position. Therefore the pulse heights by those low energy photons relative to the main electron shower are important. The CES response is nonlinear because the CES samples a shower at different age in its longitudinal development for a different incident photon/electron energy. We use a parameterization (Section 3.1.1) based on test beam measurements above 10 GeV. In this region, the ratio $E_{\rm CES}/E_{\rm CEM}$ decreases slowly with the increasing energy. We assume the response is linear below 10 GeV.

We reconstruct the CES showers and calculate LSHR using the standard electron code. The efficiency for the CES-track matching cut is calculated by comparing the reconstructed CES shower and the extrapolated track positions.

A check of the CES shower simulation is performed using the W decay electrons in the following subsection.

Bremsstrahlung effect

A photon can be emitted from an electron while passing through material preceding the tracking chambers (external radiation), or in the process of radiative decays (internal

radiation). Presence of a photon near the electron can change the shower shape on the strip chambers and thus can affect the efficiency of the cuts such as CES χ^2 on the r-ϕ (wire) view, the track-shower position matching and the E/p.

We use a simple equivalent radiator approximation to describe the radiation. A photon is generated according to the spectrum [48]

$$\frac{dN}{dy} = \frac{dT}{y}\left[\frac{4}{3}(1-y)+y^2\right], \tag{5.2}$$

where y is the electron energy fraction carried off by a photon, dT is the thickness of the equivalent radiator. Since the number of photons diverges as y approaches zero, we place a cutoff at 0.01. A photon is emitted collinear to the electron.

The thickness of the equivalent radiator for the W decay is estimated to be 0.072 X_0 by examining the E/p tail [49]. Roughly a third of it ($0.0252 \pm 0.0012\,X_0$) is accounted for by the internal radiation [50], leaving $0.046 \pm 0.008\,X_0$ due to detector material. In the semileptonic decays of the b quark, the effect of the internal radiation is equivalent to the external Bremsstrahlung in a radiator of thickness 0.015 X_0 [51].

Checking with W electrons

The validity of our detector simulation can be checked with unbiased W decay electrons selected by means of the missing $E_{\rm T}$ information. The missing $E_{\rm T}$ W's are selected with the following cuts:

- Electron $E_{\rm T} > 25$ GeV
- Missing $E_{\rm T} > 25$ GeV
- Event vertex $|z| < 60$ cm
- CTC track z position matches to the event vertex within 6 cm.

An additional E/p cut at 2.0 was applied by the missing $E_{\rm T}$ event selection.

Figure 5.3 shows the E/p distribution and Figure 5.4 shows the CES χ^2 distributions, where the Monte Carlo includes the radiation effect. We see a resonable agreement between the data and the Monte Carlo.

5.3.2 Underlying event

Although we expect that each quark jet is well described by the Monte Carlo, it is not necessarily the case with the "underlying event". In fact we usually observe poor agreement between real data and Monte Carlo predictions in various processes.

The best way would be to use real data events we observe and overlay one of them to the Monte Carlo single heavy quark jet.

Figure 5.5 shows distributions of the jets observed in our electron events. A jet is defined by an energy cluster of a fixed cone size of 0.7 in η-ϕ space with $E_{\rm T}$ greater than 7 GeV. The jet including the electron in it ("toward jet"), and the highest $E_{\rm T}$ jet ("recoil jet") other than the toward jet are removed. "Recoil jets" show a basic two jet structure of events, locating back-to-back in transverse plane (Figure 5.6). Other jets are distributed fairly flat with respect to the electron in ϕ and η, except for the region close to the electron, where less jets are observed because any activities have been merged into the toward jet.

This way we can include in the "underlying event" everything other than a heavy quark jet which produced the electron. It includes "minimum bias" part of the events, initial state radiations, and any additional jet which may be, for example, a $\bar{b}$ jet which happens to come close to the b jet producing the electron.

We pick up at random an event with an electron from the real data, and a wedge which is 6 modules (90°) away in ϕ from the one with the observed electron, and is flipped in east and west. The pulse heights of the CEM and CHA phototubes and the strip chambers are added to the previously simulated responses to the single Monte Carlo b jet particles. Then calorimeter showers are reconstructed. Given the above definition of the good electrons, a random charged track from the underlying event activity can

kill the electron when it points to the electron cluster. We check this by looking at the wedge which is picked up from the real data. If there is any track pointing to that wedge, the simulated Monte Carlo electron is killed. The addition of the underlying event changes the electron selection efficiency by about 8% (relative).

5.3.3 Simulating hadron showers

If there are only electromagnetic showers on the electron cluster cell, the HAD/EM cut efficiency should be essentially the same as for the isolated electrons. This is not strictly the case with bottom and charm electrons, because there are additional particles around the electron. Neutral hadrons within the electron cell, which cannot be gotten rid of with the number of track requirement, and the lateral leakage of the hadron showers across the cell boundary can change the original HAD/EM distribution.

In order to study this effect, we need to simulate hadron showers. We have to reproduce the energy sharing between electromagnetic and hadronic components, and the fluctuation in the total amount of energy deposited, with a proper correlation between them. In order to achieve this, we employ the same approach as in the CES simulation. We make a file which is a collection of the real data charged tracks. Each record contains the momentum, and electromagnetic and hadronic energies. We just need to read a record to simulate a hadron shower. Energy dependence of various distributions is taken care of by choosing a track with similar momentum. Lateral sharing of the shower is calculated according to the impact point of a Monte Carlo track using the average shower size. A study of hadron showers necessary for the simulation is described in Appendix B.

HAD/EM cut efficiency

Figure 5.7 shows the HAD/EM distribution before the hadron simulation, or for isolated single electrons. It is based on test beam measurements. Figure 5.8 shows the corresponding distribution for the bottom electrons with the hadron simulation, where

the electrons have passed all the identification cuts except the HAD/EM cut. Cutting at 0.04 retains about 85% of the events. This may be compared with the distribution for the photon conversion electrons in real data, shown in Figure 5.9. Figure 5.10 shows the same distribution for the charm electrons. Bottom and charm electrons have rather different distributions; the latter has a larger tail and thus have lower efficiency. This is natural because of the lower mass of the charmed particles, producing hadrons closer to the electron.

Level-2 trigger efficiency

A good electron cluster passing the offline cuts may have been lost at the level-2 trigger selection, which imposes a loose cut on the hadronic energy (HAD/EM < 0.125) of the electromagnetic cluster which is defined in a different way than at offline. A trigger tower consists of two physical towers of the central calorimeter. The level-2 clustering algorithm finds an electromagnetic cluster starting from a tower with transverse energy deposit of 4 GeV or more and adding neighboring (shoulder) towers with E_{T} above 3.6 GeV. Hence a level-2 cluster can be larger in size than an offline cluster. When one of shoulder towers have a large hadronic energy deposit, the cluster can fail the HAD/EM cut even if the offline cluster (three towers at most) has small hadronic energy.

By using the hadron simulation, we can study the effect of the level-2 cut. The Monte Carlo predicts that 12% of the bottom electrons have at least one shoulder tower hit, and the efficiency is 98% for the good offline clusters, roughly independent of the electron p_{T}.

5.3.4 Results

Including all the effects described above, we obtain the electron selection efficiencies for bottom and charm electrons as shown in Figure 5.11. The efficiency is defined as the fraction of the electrons which satisfied the cuts described on page 104, with respect to all the electrons which fall into the fiducial volume of central calorimeter.

At 12 GeV the efficiency is around 50% for bottom electrons and decreases as the p_T increases. This is because we need more boost on the parent quark or B hadron in order to get higher p_T electron, and then the particles are more collimated in the lab frame and come closer to the electron. The efficiency for charm electrons are about a third of that for bottom electrons.

In Figure 5.12 we compare the observed electron spectrum to that predicted by ISAJET b jets and the estimated efficiency. In data we observe the inefficiency of the the level-2 hardware trigger below 15 GeV, so we normalize at the bin 15-15.5 GeV. The agreement is good.

5.3.5 Other corrections

Over-efficiency of the photon conversion removal algorithm

It is known that the photon conversion removal algorithm is over-efficient; it sometimes kills a real electron by picking up a random charged track in the event and recognizing it as a conversion partner positron.

This effect depends on how the particles distribute around the electron and then on the source of the electron. Hence we study this effect using the Monte Carlo and include in the electron selection efficiency.

We use the algorithm and cuts described in Section 3.4. We look at particles arising from the same b quark jet as the electron, and also the "underlying event" tracks mentioned earlier. We find that the loss of the b quark electrons passing the identification cuts is $3.3 \pm 0.2\%$ (Figure 5.13), and that it comes most entirely from the jet particles rather than underlying event tracks. This number is consistent with an independent estimate (Eq. (3.26)).

W and Z removal

We have removed the W and Z electrons using the following cuts (Section 3.3):

- Corrected missing $E_{\rm T}$ $< 8\sqrt{E_{\rm T}}$, where $E_{\rm T}$ is the electron transverse energy measured in GeV.

- Mass $(e,\text{jet}) < 80$ if the jet has EM fraction above 0.85.

The efficiency of these cuts for b electrons is studied using the photon conversion events. What really determines the missing $E_{\rm T}$ in the b electron events is the resolution in the jet energy measurement, rather than the true missing energy due to neutrinos in semileptonic decays.

We first show that the two set of events, "prompt" electrons and photon conversions, are quite similar in jet activities. The electron cluster $E_{\rm T}$ is limited to below 20 GeV in order to avoid any confusion by the W/Z electrons.

Figure 5.14 shows the $E_{\rm T}$ distribution of the jet including the electron in it ("toward jets") for the prompt and photon conversion electron sample. The jets are defined by the CDF standard jet algorithm with a cone size of 0.7. The transverse energies are uncorrected. Also shown is the $E_{\rm T}$ flow within a cone of 0.7 around the electron. We also plot the distributions for other jets in the event. We observe that the "prompt" electron sample and the photon conversion sample are virtually identical in those jet activities.

Figure 5.15 shows the fraction of the photon conversion electrons surviving the W/Z removal cuts. We lose $3.4 \pm 0.3\%$ of the photon conversions independent of $p_{\rm T}$. We use this number as the loss of b quark decay electrons.

5.4 Cross section from the inclusive electron rate

Nason, Dawson and Ellis (NDE) present the b quark cross section integrated over a rapidity range of $|y| < 1$ and a $p_{\rm T}$ range from a certain threshold $p_{\rm T}^{\rm min}$ to infinity [14]. We obtain the same quantity using the electron rates as

$$\sigma_b = \frac{(N_{e^-} + N_{e^+})}{2 \int \mathcal{L}dt \; (\sigma_e/\sigma_b)_{\rm MC} \; Br(B \rightarrow \ell)}, \tag{5.3}$$

$p_{\rm T}^{e}$	$p_{\rm T}^{\rm min}(b)$	Number of $e^+ + e^-$	$(\sigma_e/\sigma_b)_{\rm MC}$	σ_b (nb)
10 - 15	15	40650/23780	0.0273	1220
15 - 20	23	4083/2389	0.0153	220
20 - 25	32	772/452	0.0109	56

Table 5.1: b quark cross section from the inclusive electron rates.

where N_{e^-} (N_{e^+}) is the number of bottom decay electrons (positrons) observed in data, and is given by

$$N_{e^\pm} = N_{e^\pm}^{\rm raw}\,(1 - f_{\rm conv} - f_{\rm hadron})\,(1 - f_{\rm charm}), \tag{5.4}$$

where $N_{e^\pm}^{\rm raw}$ is the raw number of electron candidates, and f's are the background fractions discussed earlier (Eqs. (3.30), (3.31), (4.1)). The numbers before and after the background subtraction are given in the third column of Table 5.1. $\int \mathcal{L}dt$ is the integrated luminosity of the data (4.1 pb^{-1}). $(\sigma_e/\sigma_b)_{\rm MC}$ is the ratio of the electron and the b quark rates obtained using the Monte Carlo, defined by

$$(\sigma_e/\sigma_b)_{\rm MC} = \frac{N_{e^-}}{N_b}, \tag{5.5}$$

where N_{e^-} is the number of electrons (not including positrons) passing the same geometrical, kinematical and identification cuts as in data, and N_b is the number of all b quarks produced in the kinematic ranges ($p_{\rm T}$ and rapidity) and decaying into electron channel. In calculating the quantity using the Monte Carlo events, we use the bottom quark $p_{\rm T}$ spectrum shape as predicted by NDE, rather than the ISAJET spectrum, although they are quite similar. The quantity does not include the semileptonic decay branching ratio of the B hadrons, $Br(B \to \ell)$. We use 10.3% as $Br(B \to \ell)$ [52]. The overall factor of two is necessary to get the b quark cross section (not including $\bar{b}$).

The choice of the b quark's minimum $p_{\rm T}$ value is made so that 90% of the electrons in a given $p_{\rm T}$ interval (10-15, 15-20 or 20-25 GeV) come from the b quark of $p_{\rm T}^{\rm min}$ and above. Figure 5.16 shows the Monte Carlo $p_{\rm T}$ distributions of the parent b quarks for the

electrons of the three $p_{\rm T}$ intervals. We find $p_{\rm T}^{\rm min}$ as 15, 23 and 32 GeV/c. respectively. It is worth noting that the choice is mathematically arbitrary, as long as the assumed shape of the b quark $p_{\rm T}$ spectrum is correct.

We obtain

$$\begin{aligned}
\sigma(\bar{p}p \rightarrow bX;\ p_{\rm T} > 15\ {\rm GeV}/c,\ |y| < 1) &= 1220\ {\rm nb}, \\
\sigma(\bar{p}p \rightarrow bX;\ p_{\rm T} > 23\ {\rm GeV}/c,\ |y| < 1) &= 220\ {\rm nb}, \\
\sigma(\bar{p}p \rightarrow bX;\ p_{\rm T} > 32\ {\rm GeV}/c,\ |y| < 1) &= 56\ {\rm nb}, \qquad (5.6)
\end{aligned}$$

for the three kinematic regions. They are summarized in Table 5.1. We discuss the systematic uncertainties in the above numbers in the next Chapter.

5.5 Cross section from the electron-D^0 rate

In this Section we derive the bottom quark production cross section from the rate of D^0 production in association with the electron. The reconstruction of D^0 is discussed in Section 4.2.1.

5.5.1 $D^0 \rightarrow K^-\pi^+$ efficiency estimate

In order to turn the D^0 rate into the b quark cross section, we need to correct for the D^0 reconstruction efficiency. It consists of the kinematical acceptance, the track finding efficiency of the kaon and the pion tracks, and the probability that a kaon exits the CTC before its decay.

$$\epsilon_{K\pi} = \epsilon_{\rm kin} \cdot \epsilon_{\rm track} \cdot \epsilon_{\rm decay}. \qquad (5.7)$$

We need to start with the events with an electron which has passed the various quality cuts, as in the real data. We use the Monte Carlo B meson events for this purpose. The Monte Carlo models and the estimate of the electron selection efficiency for the inclusive mode are described earlier in this Chapter. We use the same method

for the present purpose, the "exclusive" mode ($D^0 \to K^-\pi^+$).

The exclusive mode is a subsample of the inclusive mode, and we can use the Monte Carlo events we already have. In order to achieve high statistics for the exclusive mode with a small branching fraction, we force the D^0 to decay into $K\pi$ channel. Instead of re-generating the events, we modify the inclusive events. We look for a D^0 in the semileptonic B decays, and replace its daughter particles with the charged kaon and pion. This is easily done because the D^0 is a spinless particle and thus involves no angular correlations and polarization.

The $D^0 \to K^-\pi^+$ events thus obtained are then simulated for the calorimeter responses and subject to the electron cuts, in the same way as in the inclusive mode. We consider only those $D^0 \to K^-\pi^+$ decay events where the associated electron has passed the identification cuts.

Figure 5.17 shows the distributions of the transverse momenta of kaons, pions and the parent D^0 in these events. The average values are 3.2, 3.0 and 5.8 GeV/c, respectively. Figure 5.18 shows the distributions of the distance in the η-ϕ space between the electron and the kaon or the pion track.

Out of 3033 $D^0 \to K^-\pi^+$ decays 1848 have passed the transverse momentum cuts (Eq. (4.4)). The cone cut at 0.6 reduces the number of events to 1343. Thus the combined kinematical cut efficiency is

$$\epsilon_{\rm kin} = \frac{1343}{3033} = 0.443 \pm 0.009. \tag{5.8}$$

The next question is what fraction of these kaon and pion pairs are reconstructed as D^0's with the correct mass.

We are dealing with events with a relatively low charged multiplicity. The track density is low, therefore we expect a high track finding efficiency.

We use the CDFSIM [53] detector simulation program to estimate the efficiency of the pattern recognition and the momentum reconstruction. The $D^0 \to K^-\pi^+$ events after the transverse momentum cuts are used as input to the CDFSIM. The standard set

of detector effects are included in the simulation, except that the kaon decay is disabled. The simulated tracks are then reconstructed using the same program as for the real data events. Figure 5.19 shows the invariant mass formed with the reconstructed track parameters. The curve is a fit to a single Gaussian. The rms width is 16.2 MeV.

The D^0 reconstruction efficiency is defined as the fraction of pairs with the reconstructed mass falling within the $\pm 3\sigma$ mass window. We find

$$\epsilon_{\text{track}} = 0.948 \pm 0.008. \tag{5.9}$$

In the above plot the track parameters are fit without constraining to the beam position. Figure 5.20 shows the invariant mass distribution when the constraint to the beam position $(x, y) = (0, 0)$ is used in the fit of track parameters. Here B and D mesons are treated as having zero lifetimes. That is, kaons and pions are produced at (0,0). The width now shrinks to 12.0 MeV.

Of course B and D mesons have finite lifetimes, and thus the beam constraint fit does not necessarily improve the mass resolution. The lifetime effect on the beam constraint fit is studied as follows. The D^0 decay vertex, $\vec{V} = (x, y, z)$, is generated using the momenta and the nominal lifetimes of B and D^0. The tracks are fit with the constraint to the position $(-x, -y)$. Figure 5.21 shows the invariant mass distribution. The width is now 16.4 MeV, which is not better than the unconstrained fit.

A kaon can decay in the CTC volume and may fail to be reconstructed as a track. The probability that a kaon exits the CTC without decay is 0.939 ± 0.003, where we have averaged over the kaon momentum spectrum (Figure 5.17) above 1.5 GeV/c. We use this number as the efficiency:

$$\epsilon_{\text{decay}} = 0.939 \pm 0.003. \tag{5.10}$$

Combining the efficiencies above, we find

$$\epsilon_{K\pi} = 0.367 \pm 0.008. \tag{5.11}$$

5.5.2 Cross section measurement

The number of the reconstructed $D^0 \to K^-\pi^+$ decays in the electron events, N_{eD^0}, can be expressed using the number of produced semileptonic B decay electrons as

$$N_{eD^0} = N_{e^-}^{\rm prod} \cdot B_{eD^0} \cdot \epsilon_{\rm exc} \cdot \epsilon_{K\pi}. \tag{5.12}$$

Here $\epsilon_{\rm exc}$ is the electron selection efficiency for the exclusive mode, and $\epsilon_{K\pi}$ is the total reconstruction efficiency of the $D^0 \to K^-\pi^+$ decay described in the previous section. B_{eD^0} is the product of the branching fractions

$$B_{eD^0} \equiv R_{\ell D^0} \cdot Br(D^0 \to K^-\pi^+). \tag{5.13}$$

The first term is the number of D^0 particles per semileptonic B decay, defined as

$$R_{\ell D^0} \equiv \frac{Br(\bar{B} \to D^0 X' \ell^- \bar{\nu})}{Br(\bar{B} \to X \ell^- \bar{\nu})}. \tag{5.14}$$

This quantity has been measured by the CLEO collaboration at the $\Upsilon(4S)$. Therefore knowing the electron selection and $D^0 \to K^-\pi^+$ reconstruction efficiencies enables us to extract the produced number of the semileptonic decay electrons. We can derive the b quark production cross section from it in the same way as we did for the inclusive mode. The numbers of produced and observed inclusive electrons are related by

$$N_{e^-}^{\rm obs} = N_{e^-}^{\rm prod} \cdot \epsilon_{\rm inc}, \tag{5.15}$$

where $\epsilon_{\rm inc}$ is the electron selection efficiency for the inclusive mode. Substituting this into Eq. (5.12) leads to

$$N_{eD^0} = N_{e^-}^{\rm obs} \cdot \frac{\epsilon_{\rm exc}}{\epsilon_{\rm inc}} \cdot B_{eD^0} \cdot \epsilon_{K\pi}. \tag{5.16}$$

The number of inclusive electrons is expressed using the b quark production cross section as

$$N_{e^-}^{\rm obs} = \sigma_b \cdot (\frac{N_{e^-}^{\rm obs}}{\sigma_b})_{\rm MC}, \tag{5.17}$$

where we have used the last quantity to relate the electron rate to the b quark rate in the inclusive analysis. Solving for σ_b and using Eq. (5.16) we get

$$\sigma_b = \frac{N_{eD^0}}{(\frac{N_{e^-}^{\rm obs}}{\sigma_b})_{\rm MC} \cdot B_{eD^0} \cdot \epsilon_{K\pi}} \cdot \frac{\epsilon_{\rm inc}}{\epsilon_{\rm exc}}. \tag{5.18}$$

The electron selection efficiencies can in principle be different between the inclusive mode and the exclusive mode. This is because the isolation degree of the electron, which determines the electron selection efficiency, may be different for the different decay modes of the charmed particles produced in semileptonic B decays. We plot the efficiencies for the exclusive mode in Figure 5.22 and for the inclusive mode in Figure 5.11. We also plot the ratio of the two, $\epsilon_{\rm exc}/\epsilon_{\rm inc}$ in Figure 5.23. We see a constant behaviour as a function of $p_{\rm T}$. The ratio integrated over the $p_{\rm T}$ spectrum between 11 and 30 GeV/c is 1.029 ± 0.012. We use this value for the ratio:

$$\frac{\epsilon_{\rm exc}}{\epsilon_{\rm inc}} = 1.029 \pm 0.012. \tag{5.19}$$

The CLEO collaboration [52] measures the number of D^0's per semileptonic B meson decay, $R_{\ell D^0}$, to be

$$R_{\ell D^0} = 0.67 \pm 0.09 \pm 0.10, \tag{5.20}$$

using the $D^0 \rightarrow K^-\pi^+$ decay mode. The first error is the combined statistical and systematic error inherent to the CLEO analysis, and the second is the systematic error

purely due to the uncertainty in the $D^0 \to K^-\pi^+$ branching fraction. Since we use the same $D^0 \to K^-\pi^+$ decay channel for the D^0 reconstruction, we only need to know the product branching fraction B_{eD^0} (Eq. (5.13)). In this quantity the second error due to the $D^0 \to K^-\pi^+$ branching fraction drops off:

$$\begin{aligned} B_{eD^0} &= (0.67 \pm 0.09) \times 0.042 \\ &= 0.0281 \pm 0.0038, \end{aligned} \tag{5.21}$$

where 0.042 is the $D^0 \to K^-\pi^+$ branching fraction used by CLEO to extract the number 0.67.

The quantity is an average over the mixture of B_u and B_d mesons produced in $\Upsilon(4S)$ decays. The mixture is unknown, but is considered to be close to unity, since the masses are similar.

We have used the electrons of the p_T between 11 and 30 GeV/c from the 12 GeV trigger. Since the trigger hardware is not fully efficient below about 15 GeV, we have to correct for it. We use the 7 GeV trigger electron events for this purpose. We find the efficiency for the electrons of p_T between 11 and 30 GeV/c, weighted by the p_T spectrum, as

$$\epsilon_{L2} = 0.538 \pm 0.015. \tag{5.22}$$

Using this efficiency, we modify Eq. (5.15) to

$$N_{e^-}^{obs} = N_{e^-}^{prod} \cdot \epsilon_{inc} \cdot \epsilon_{L2}, \tag{5.23}$$

and accordingly the cross section formula.

We show in Figure 5.24 the p_T spectrum of parent b quarks which produced the electrons with p_T between 11 and 30 GeV/c. As in the inclusive analysis we choose p_T^{min} so that 90% of electrons come from b quarks of p_T^{min} and above. The Monte Carlo

calculation gives 19 GeV/c as $p_{\rm T}^{\rm min}$. For this $p_{\rm T}^{\rm min}$ value, we find

$$(N_{e^-}^{\rm obs}/\sigma_b)_{\rm MC} = 0.0386. \tag{5.24}$$

In calculating this ratio we use a perfect level-2 trigger turn-on in the Monte Carlo events, because we explicitly correct for the level-2 efficiency in Eq. (5.23). However, the turn-on effect is taken into account in obtaining the $p_{\rm T}^{\rm min}$ value above.

The observed number of D^0's is 68 ± 15. On the other hand, we can predict the number of expected D^0's in our electron sample by substituting into Eq. (5.16) the observed number of electrons with our estimate of the backgrounds, the electron and $D^0 \to K^-\pi^+$ efficiencies, and the combined branching fraction from CLEO. The D^0's are produced only in the semileptonic decays of non-strange B mesons, not in B_s or other B hadron decays. We that 78% of the observed bottom electrons come from non-strange B mesons. We obtain $77 \pm 10 \pm 19$ events as the number of expected D^0's. The first error is due to the CLEO measurement of the combined branching fraction, and the second reflects the uncertainty in the estimate of backgrounds in the electron sample. The two numbers, observed and predicted, are consistent.

Putting the numerical values into Eq. (5.18), we find

$$\sigma(\bar{p}p \to bX;\ p_{\rm T} > 19\,{\rm GeV}/c,\ |y| < 1) = 440 \pm 100 \pm 60\ {\rm nb}, \tag{5.25}$$

where the first uncertainty is statistical and the second is the systematic uncertainty due to the uncertainty in the combined branching fraction B_{eD^0}.

There exist other sources of systematic uncertainties, which are common to both this and the inclusive methods. We will discuss them in the next Chapter.

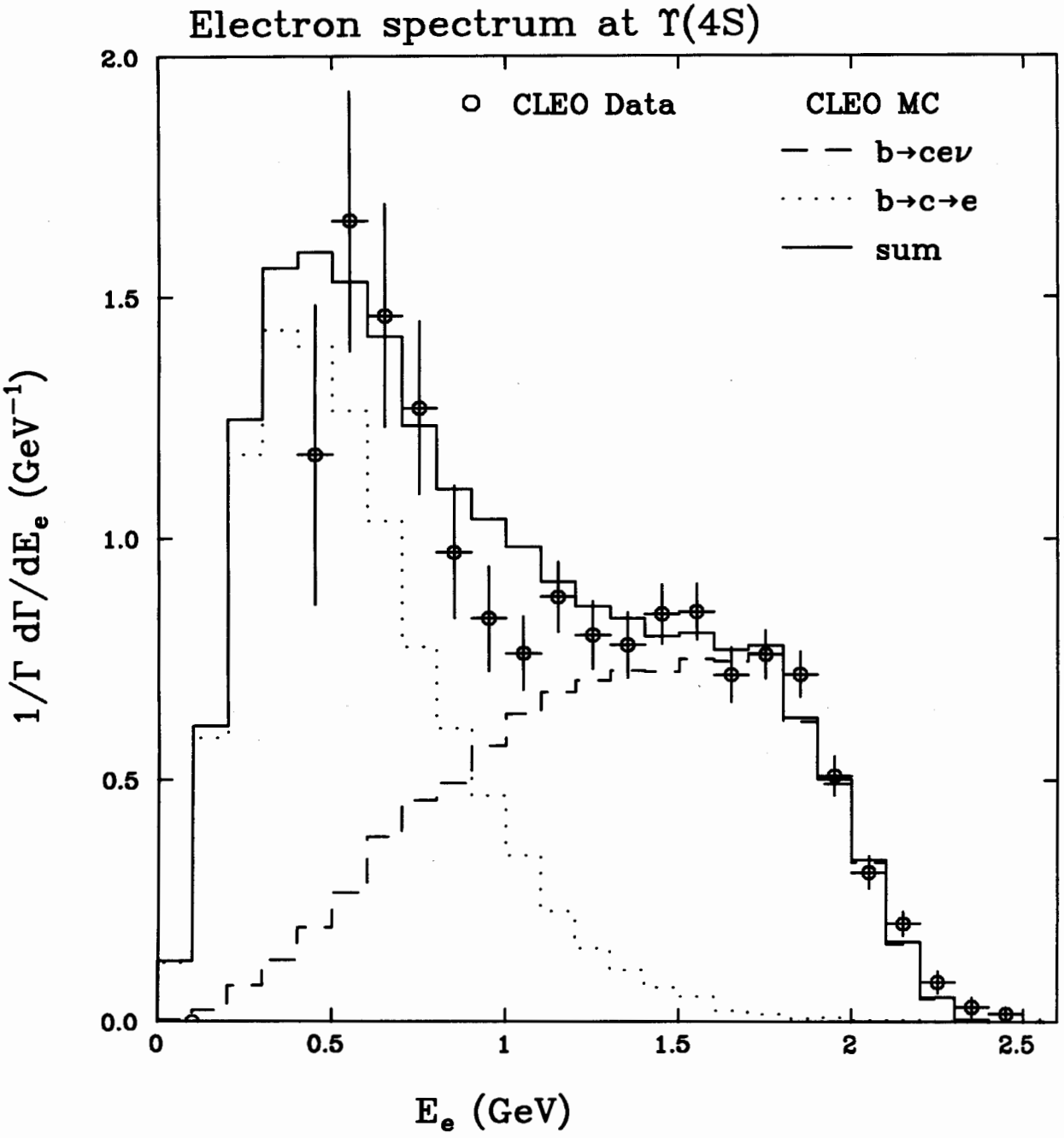

Figure 5.1: Electron spectrum observed in B decay at $\Upsilon(4S)$ at CLEO, compared with the CLEO Monte Carlo spectrum.

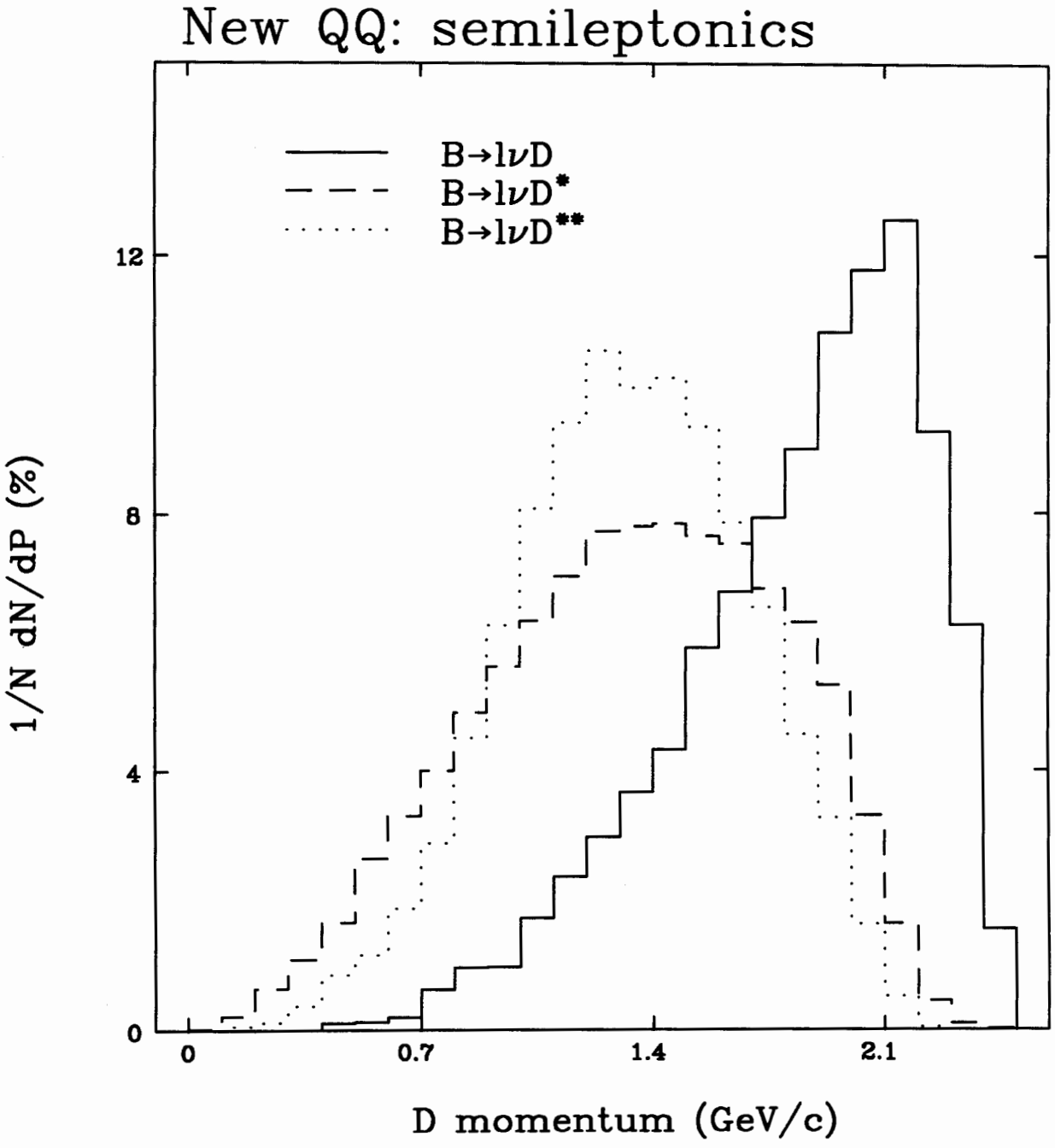

Figure 5.2: Pseudoscalar D meson momentum spectra in semileptonic B decays.

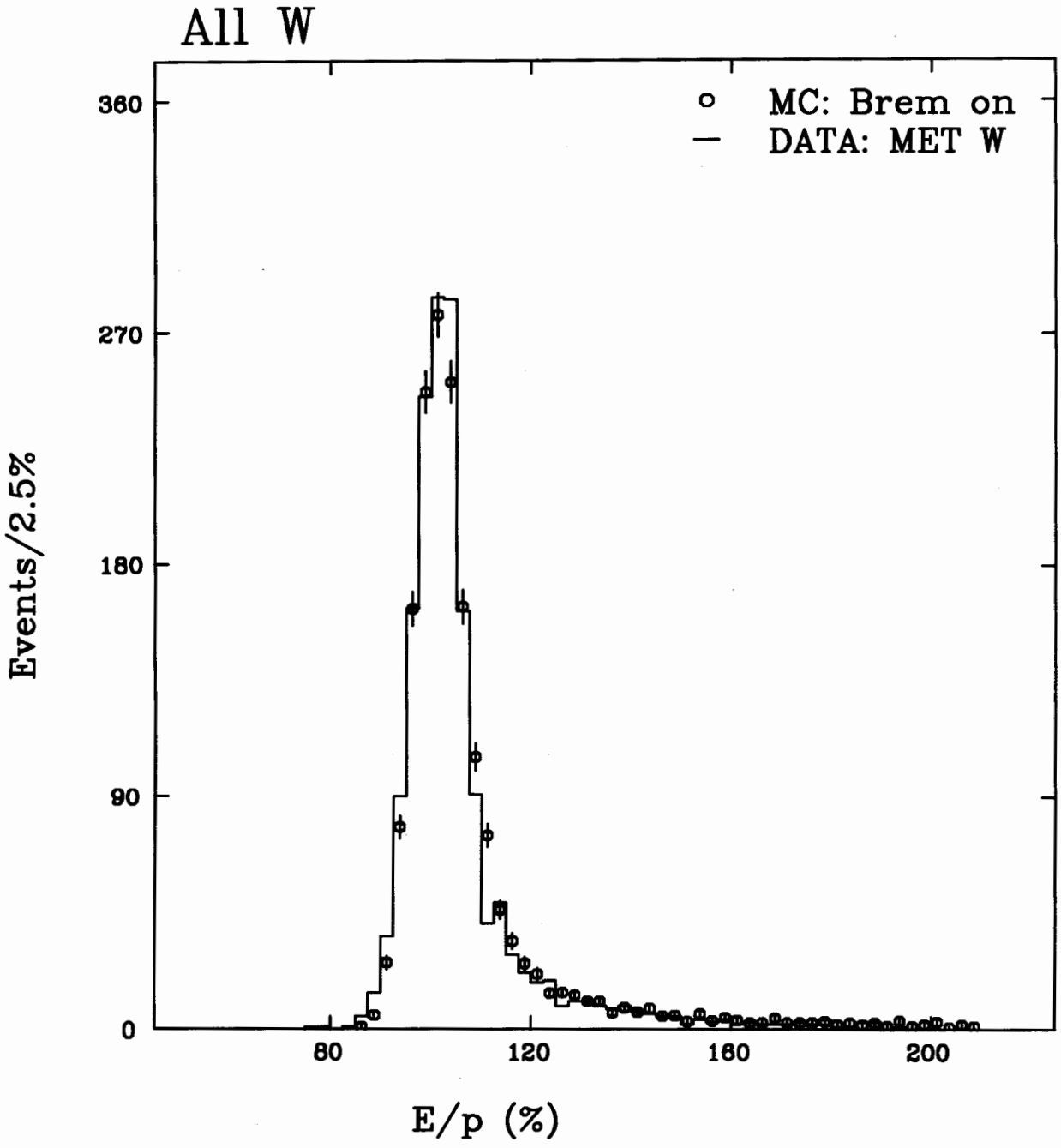

Figure 5.3: E/p distribution for the W electrons.

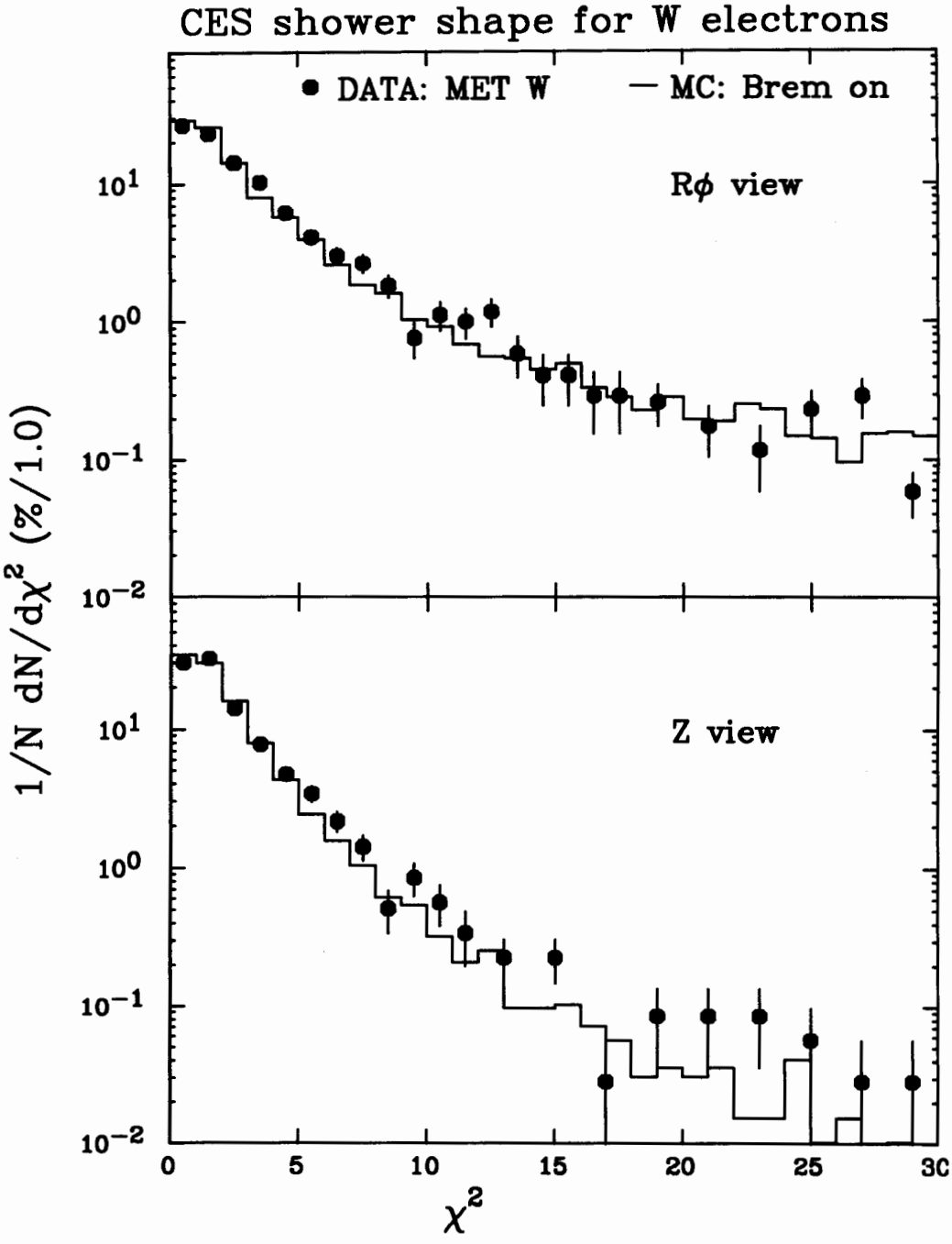

Figure 5.4: CES χ^2 distributions for W electrons.

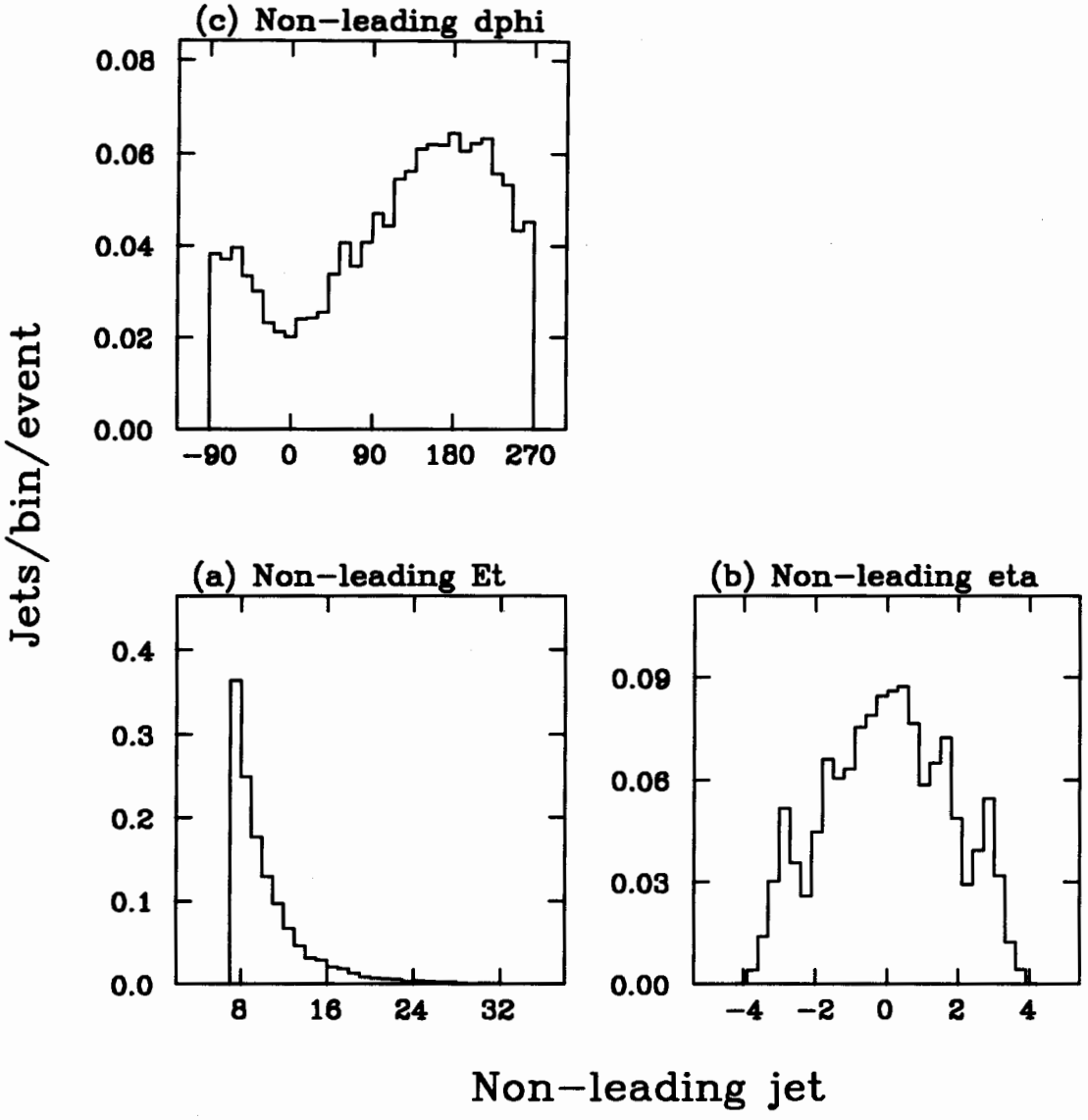

Figure 5.5: Distributions of jets other than "toward jets" and "recoil jets" observed in the real data.

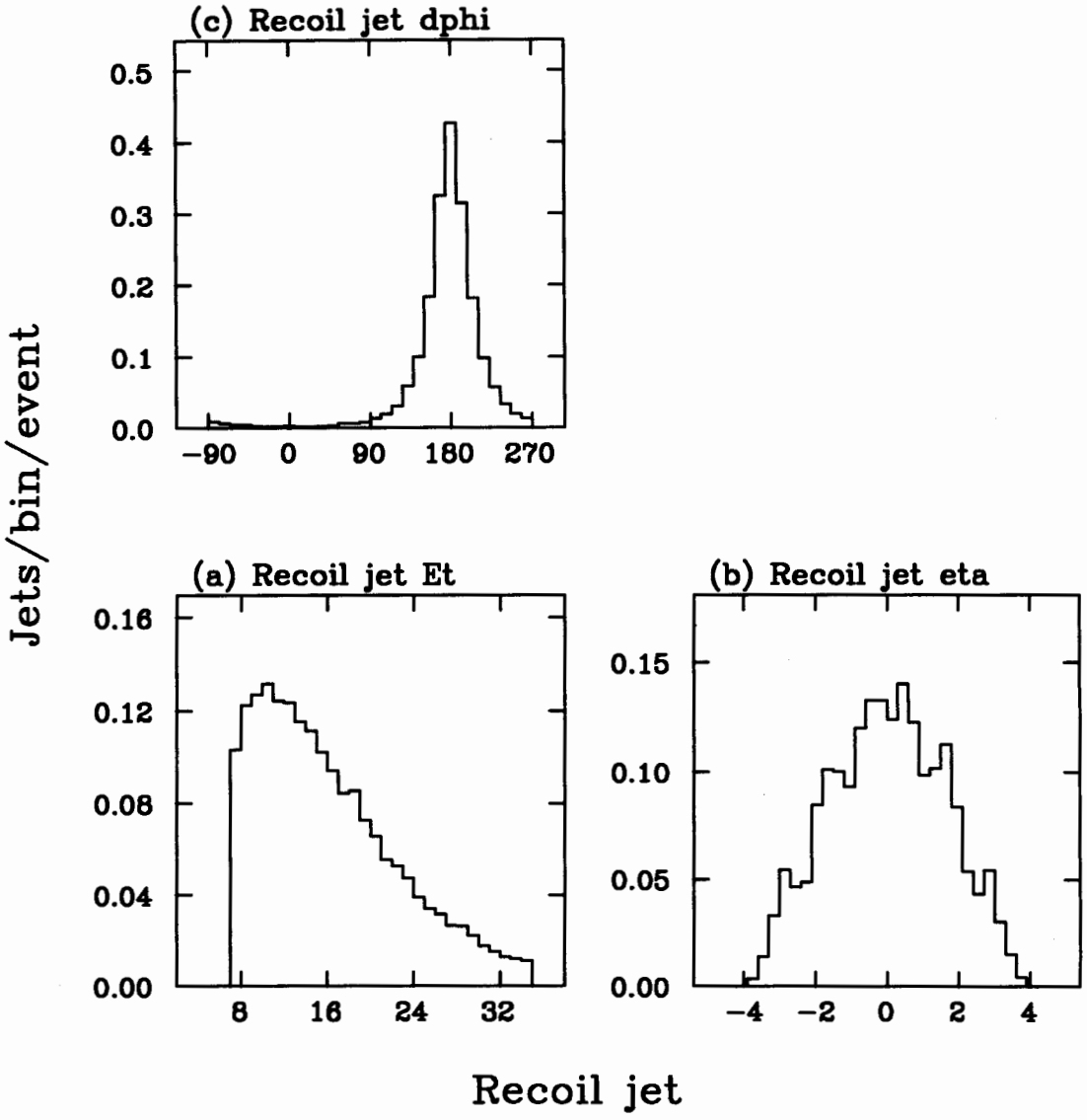

Figure 5.6: Distributions of the "recoil jets".

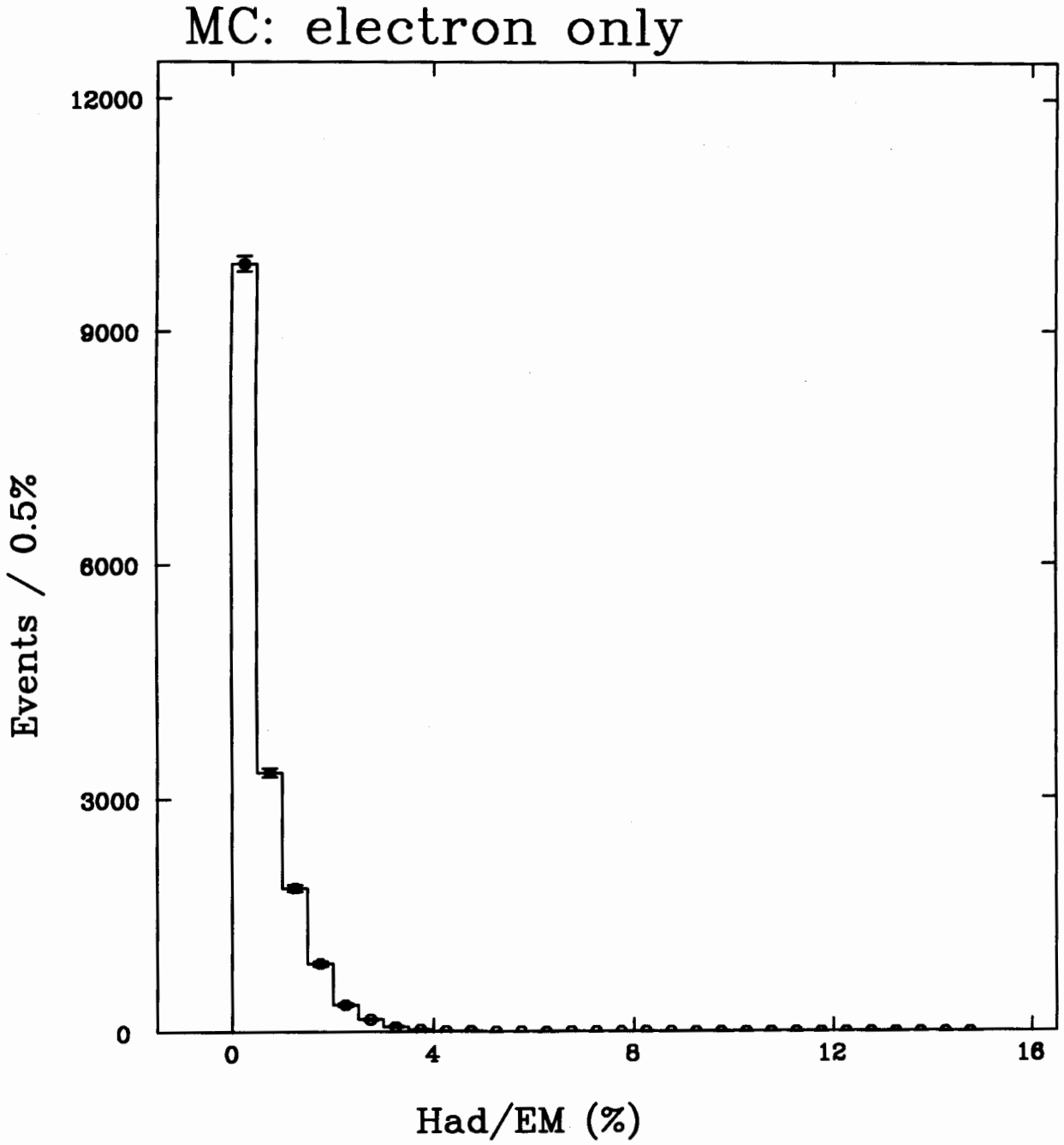

Figure 5.7: HAD/EM distribution used in the electron simulation.

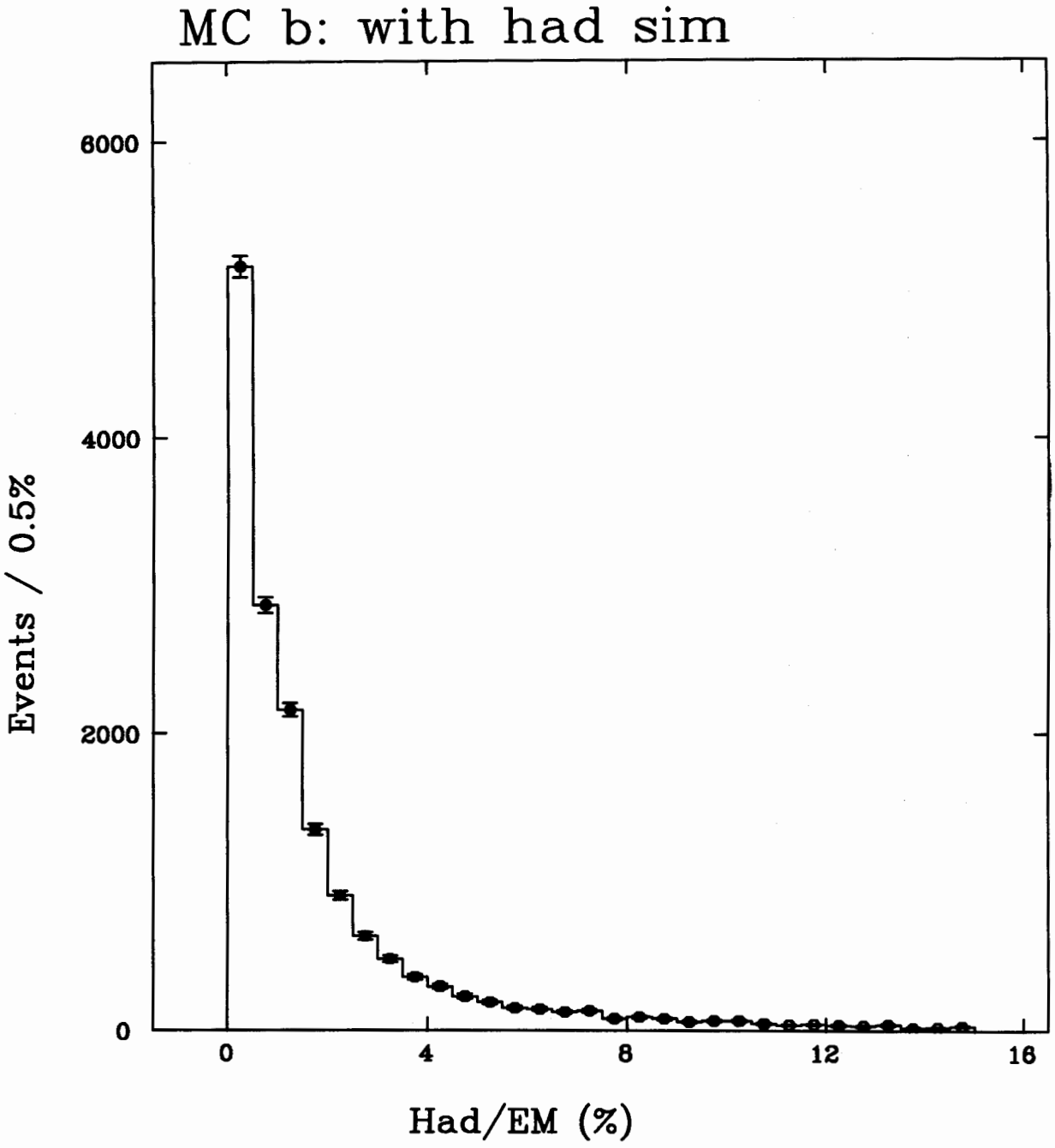

Figure 5.8: Monte Carlo HAD/EM distribution for bottom electrons.

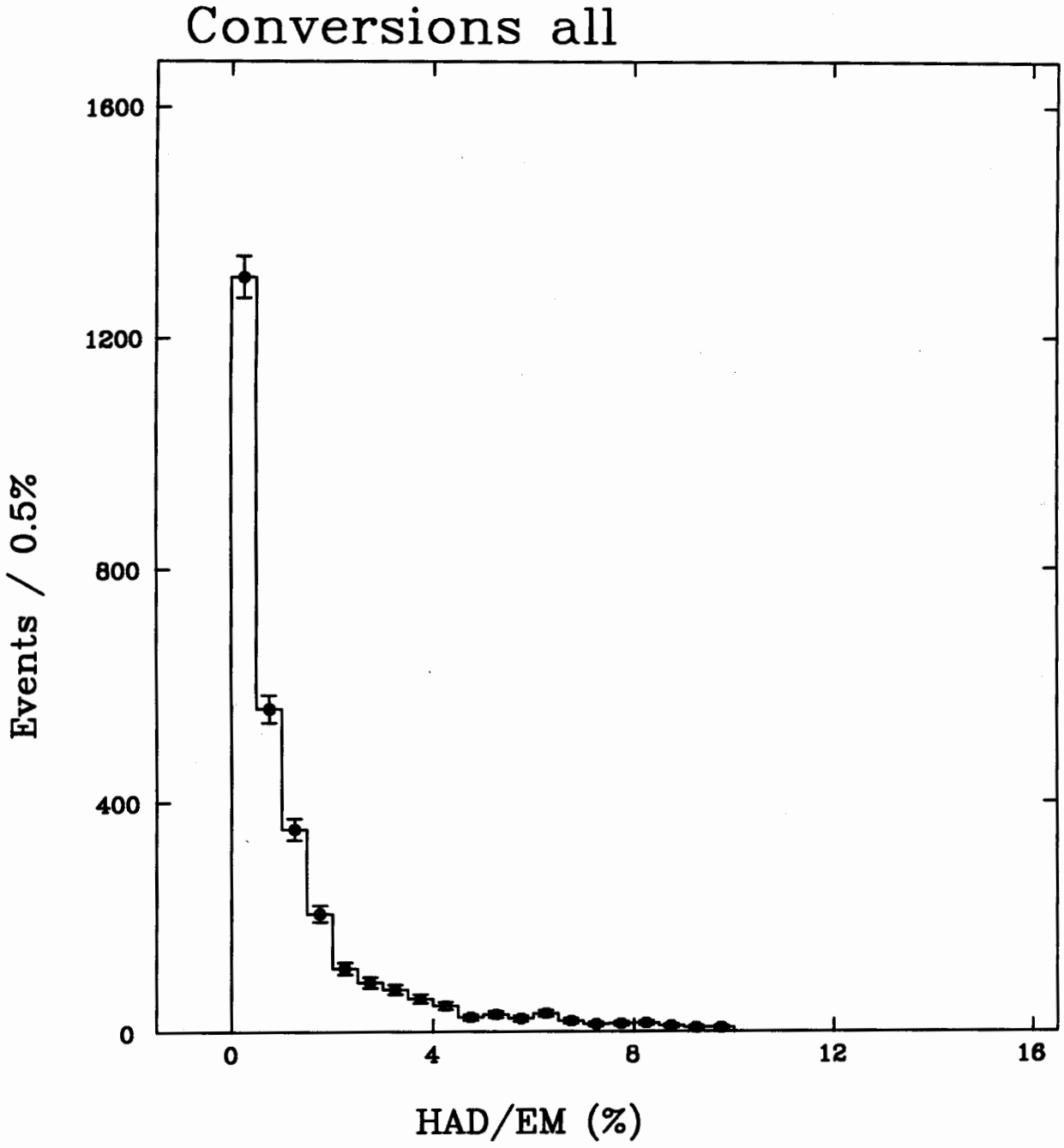

Figure 5.9: HAD/EM distribution for photon conversion electrons in real data.

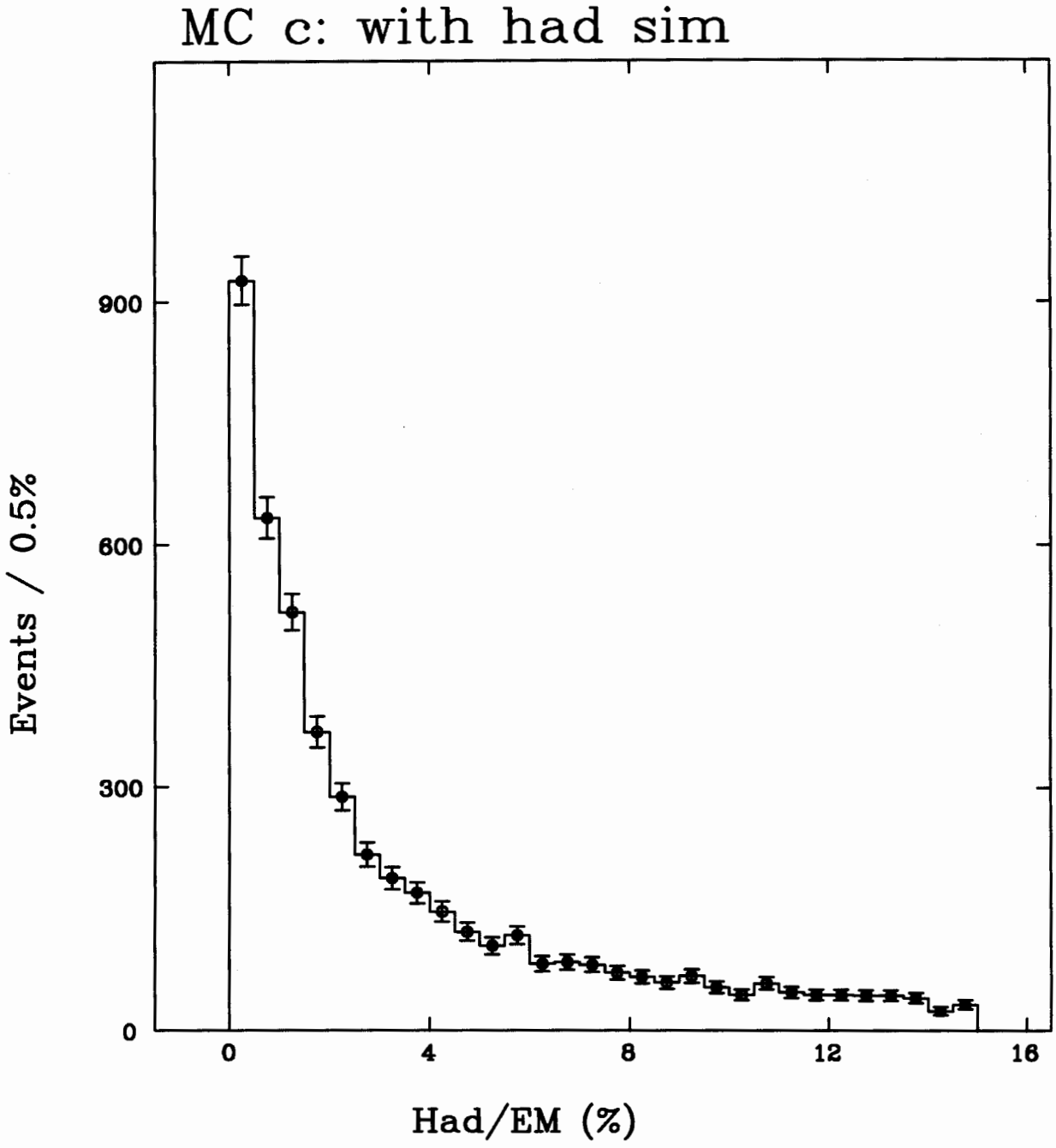

Figure 5.10: Monte Carlo HAD/EM distribution for charm electrons.

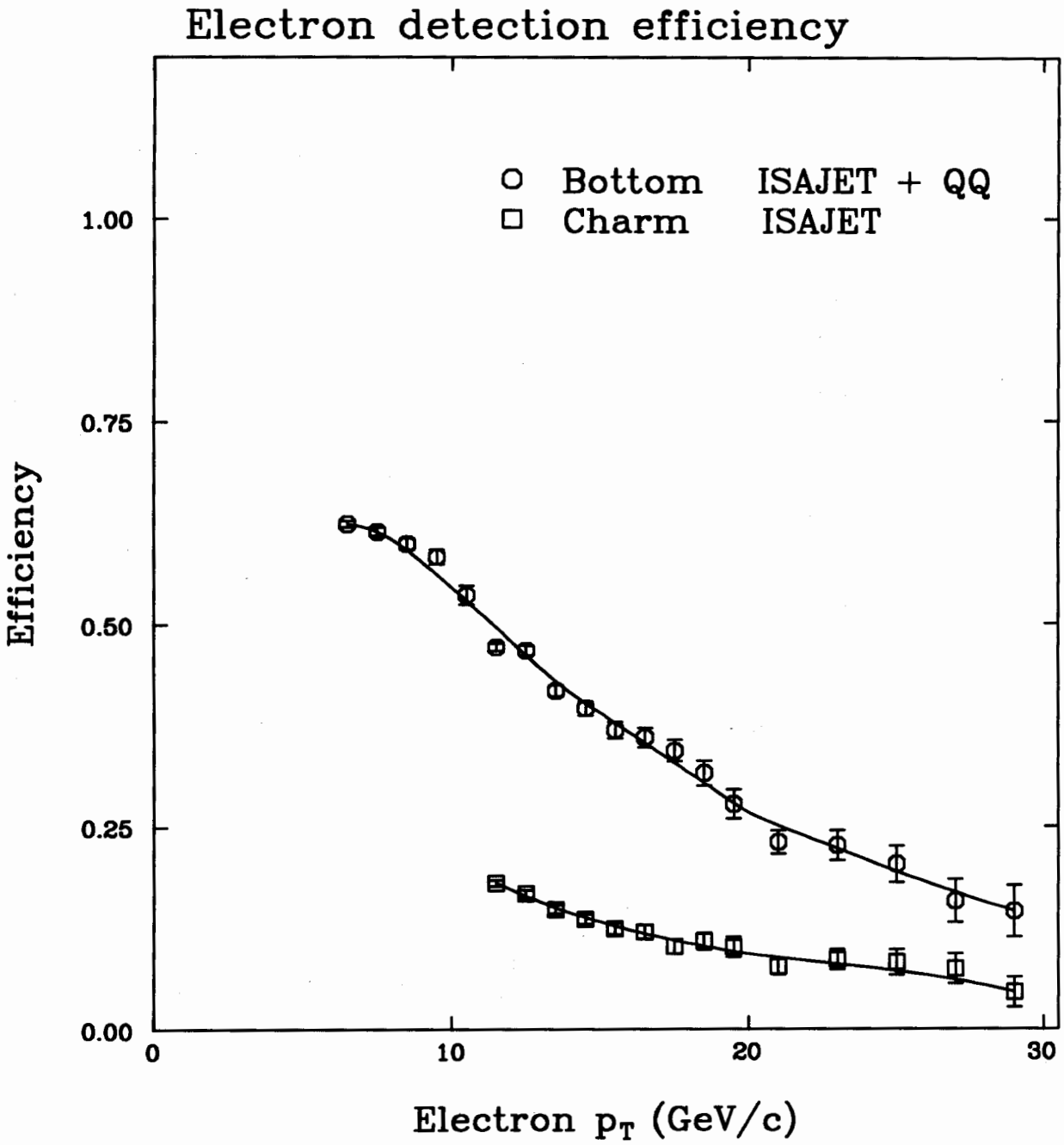

Figure 5.11: Electron selection efficiencies for bottom and charm decay electrons.

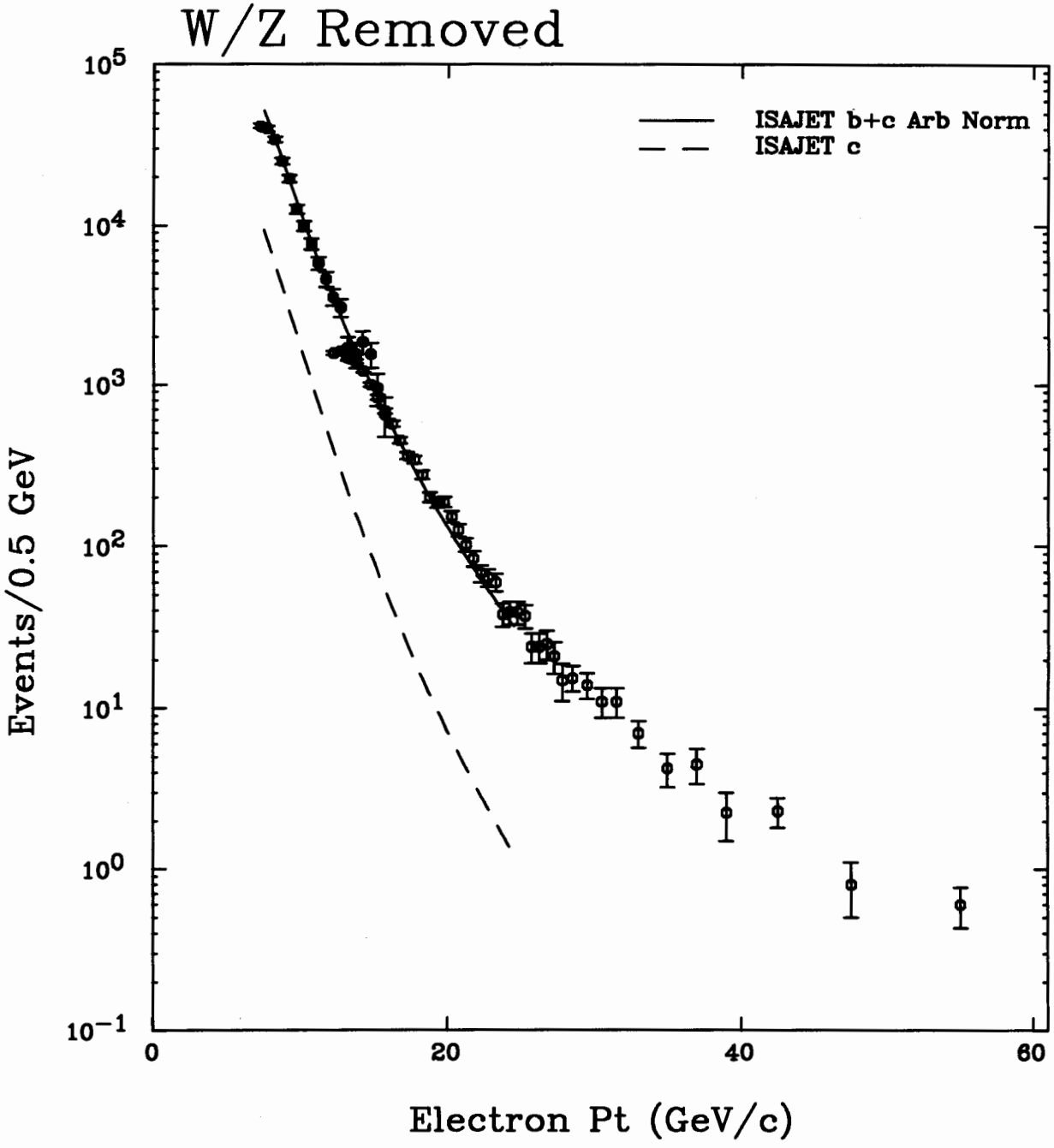

Figure 5.12: The electron p_T spectra observed in the real data and the prediction from the Monte Carlo. The normalization is arbitrary.

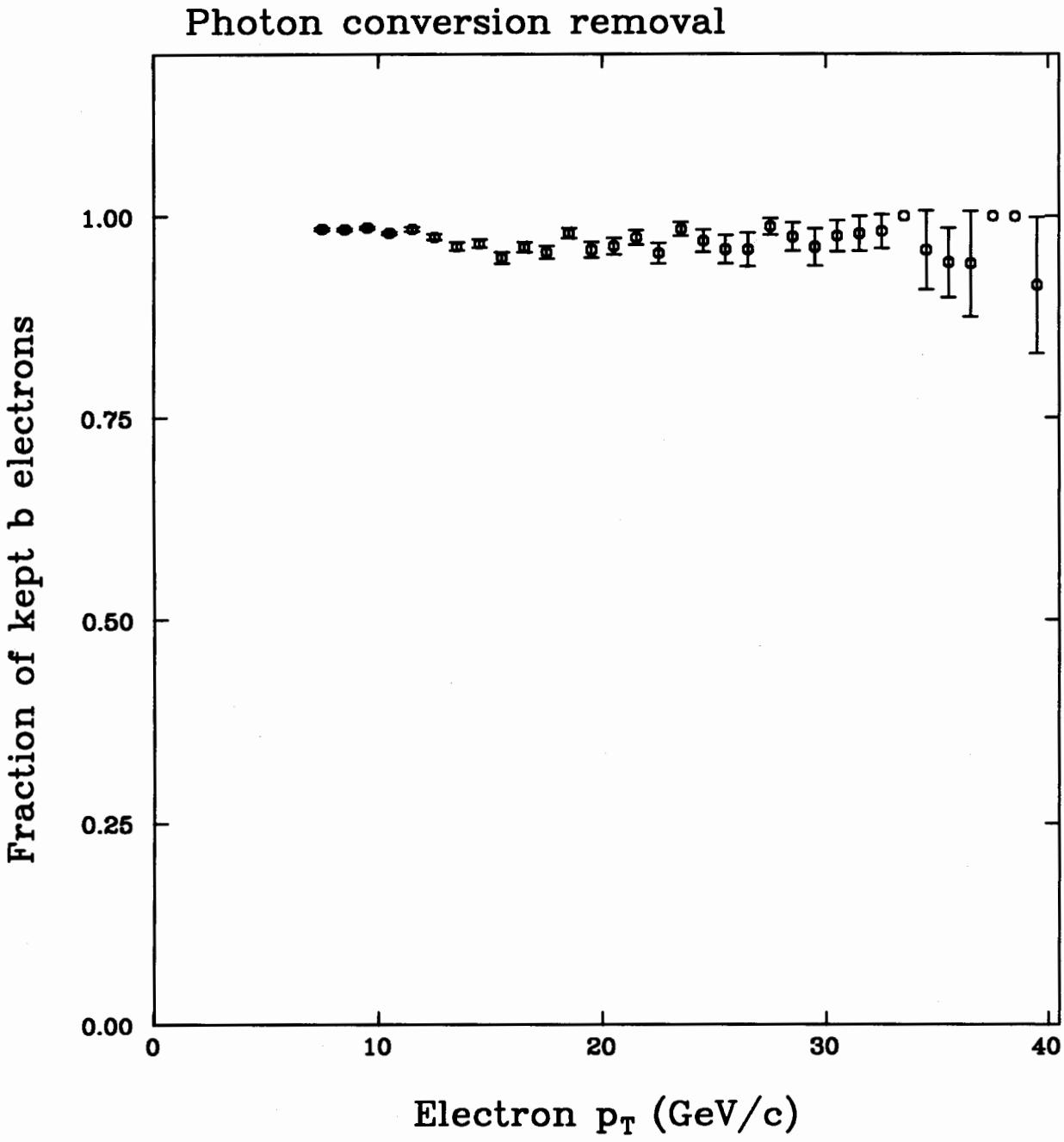

Figure 5.13: Fraction of bottom electrons surviving the the photon conversion removal cuts.

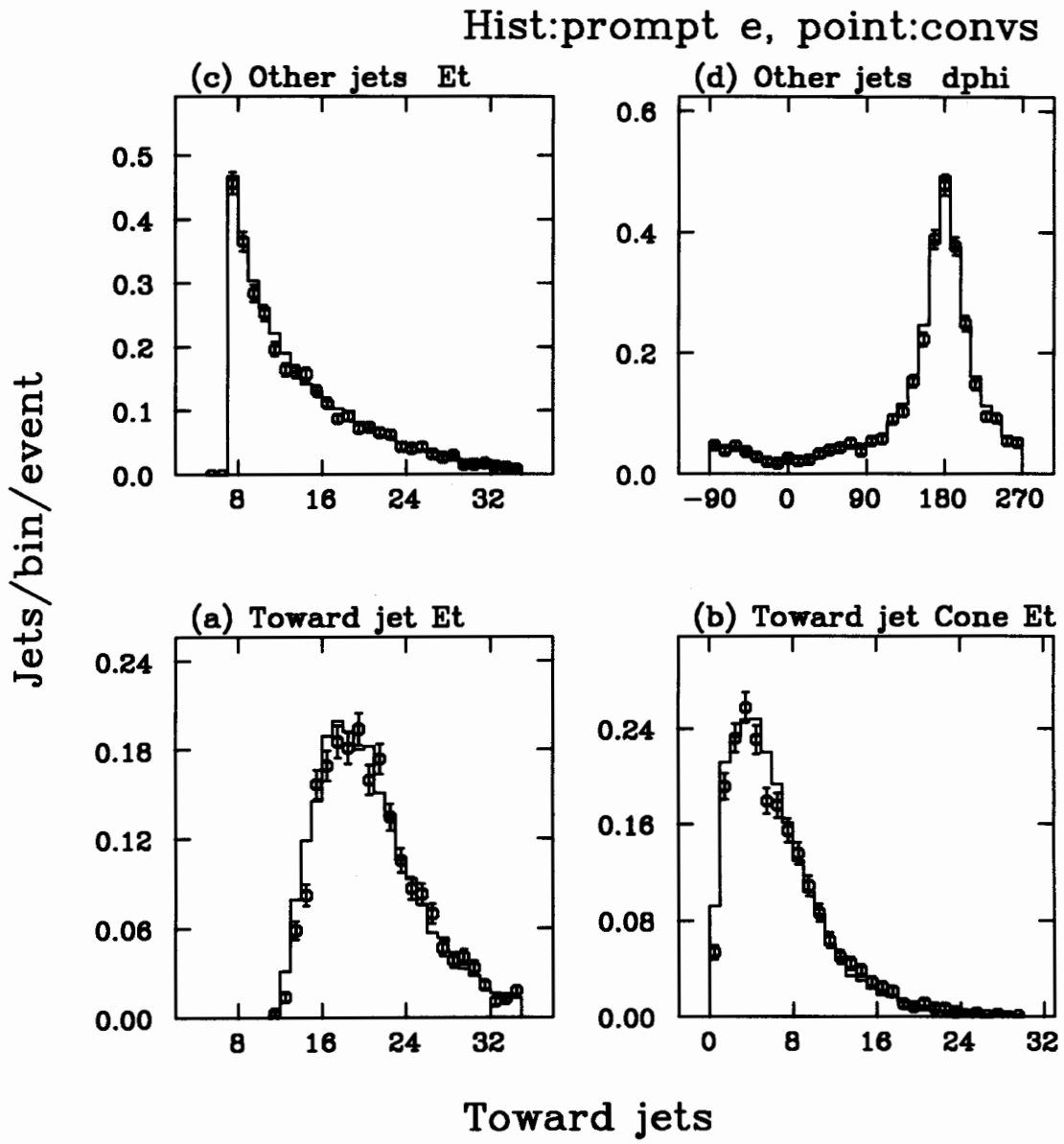

Figure 5.14: Jet activities in the "prompt" electron (histogram) and the photon conversion (points) events.

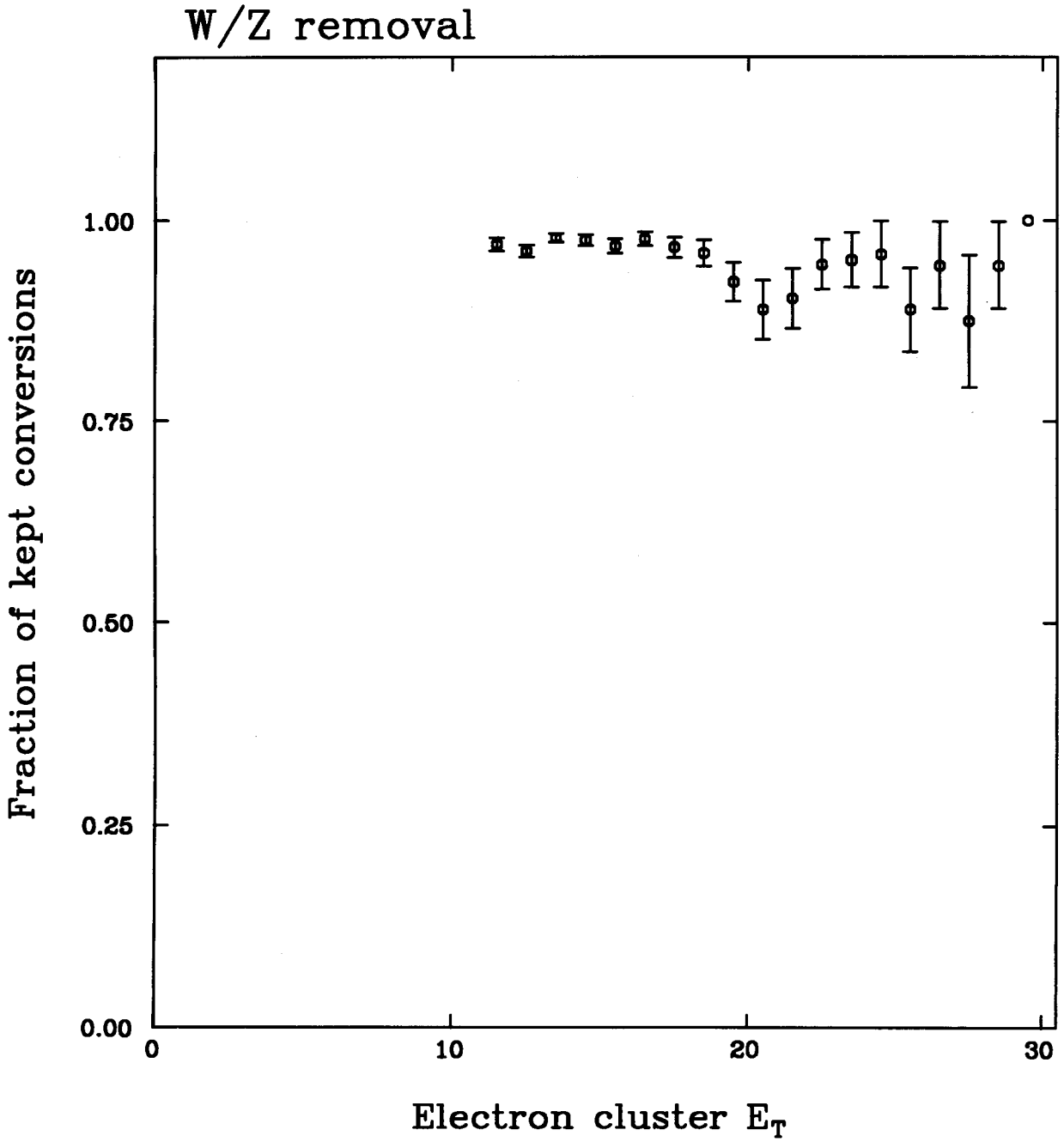

Figure 5.15: Fraction of the photon conversion electrons retained by the W and Z removal cuts.

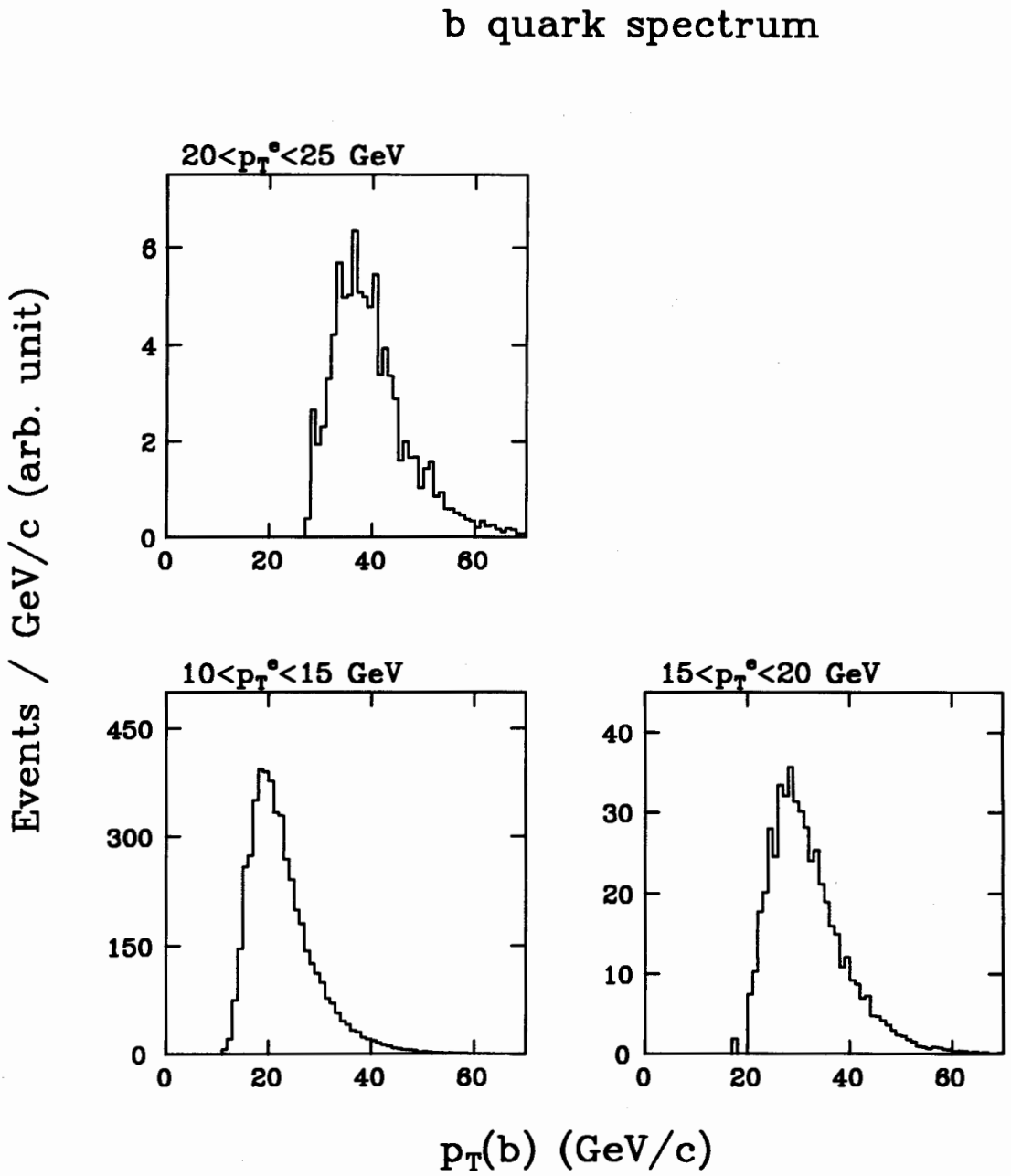

Figure 5.16: Monte Carlo p_{T} spectra of parent b quarks for the electrons with three p_{T} intervals.

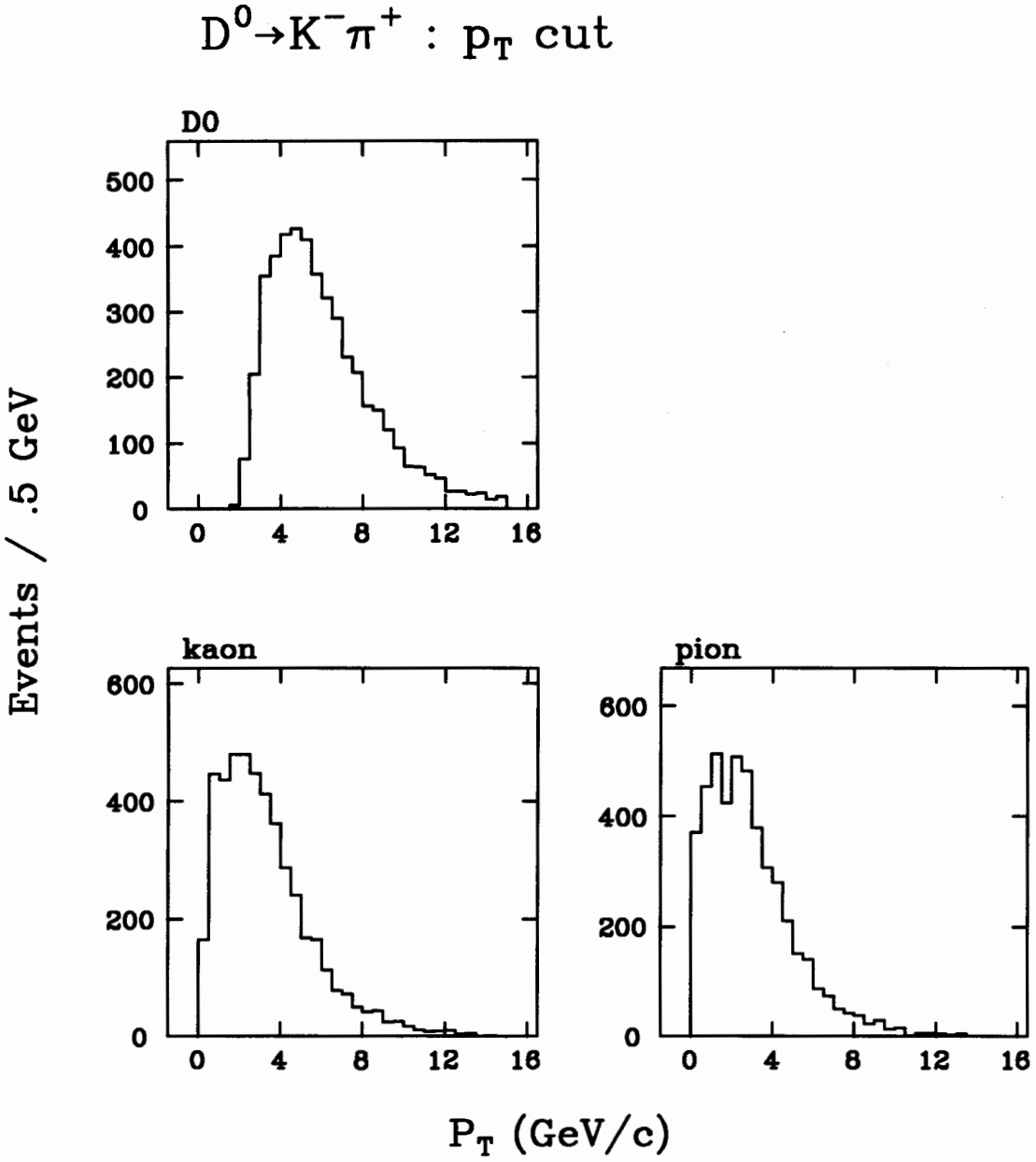

Figure 5.17: Transverse momentum spectra of kaons, pions and D^0's in the semileptonic decay $\bar{B} \to e^- \bar{\nu} D^0 X, D^0 \to K^- \pi^+$ (Monte Carlo).

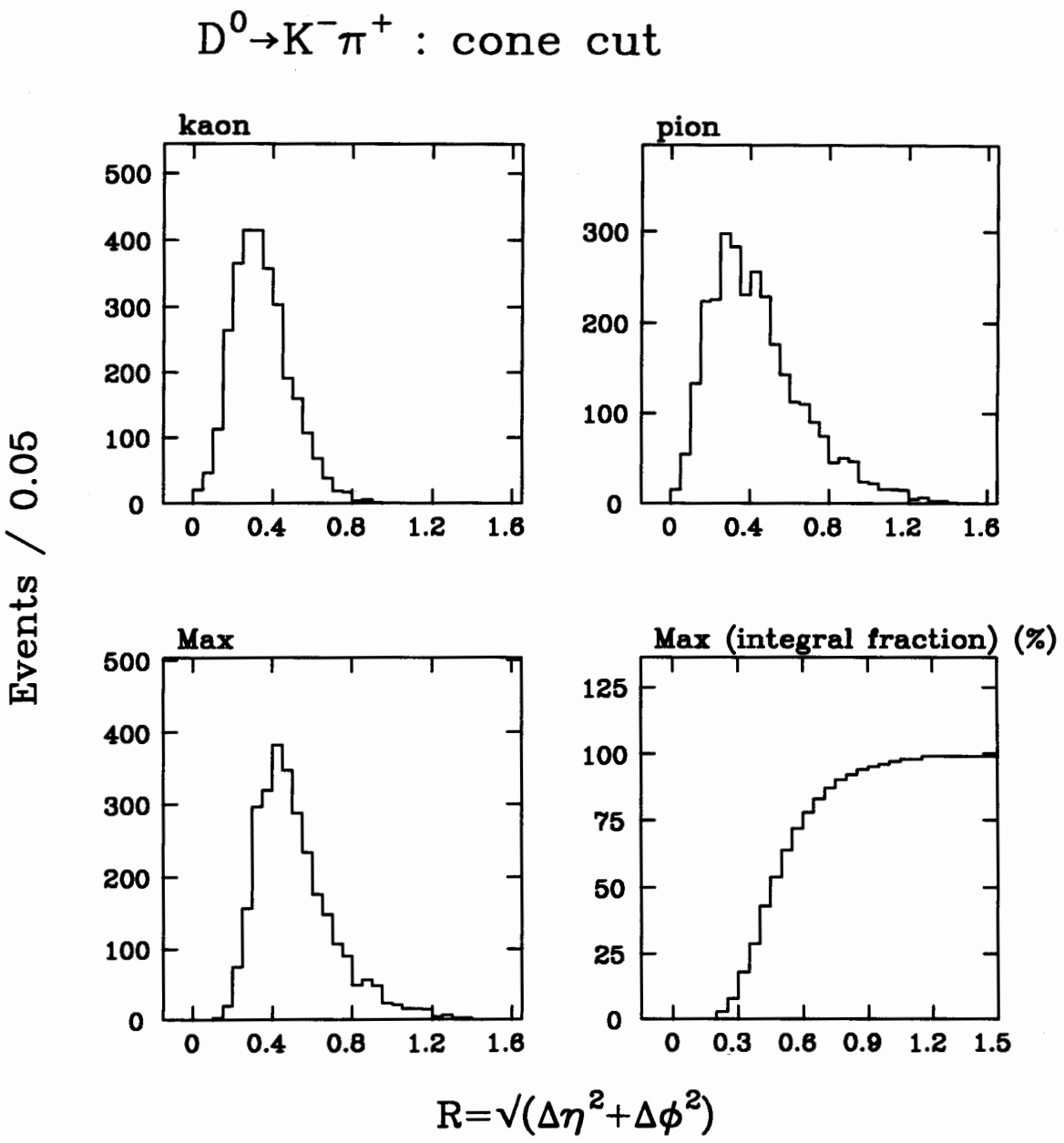

Figure 5.18: Distributions of distances of the D^0 decay kaons and pions in η-ϕ space with respect to the electron (Monte Carlo).

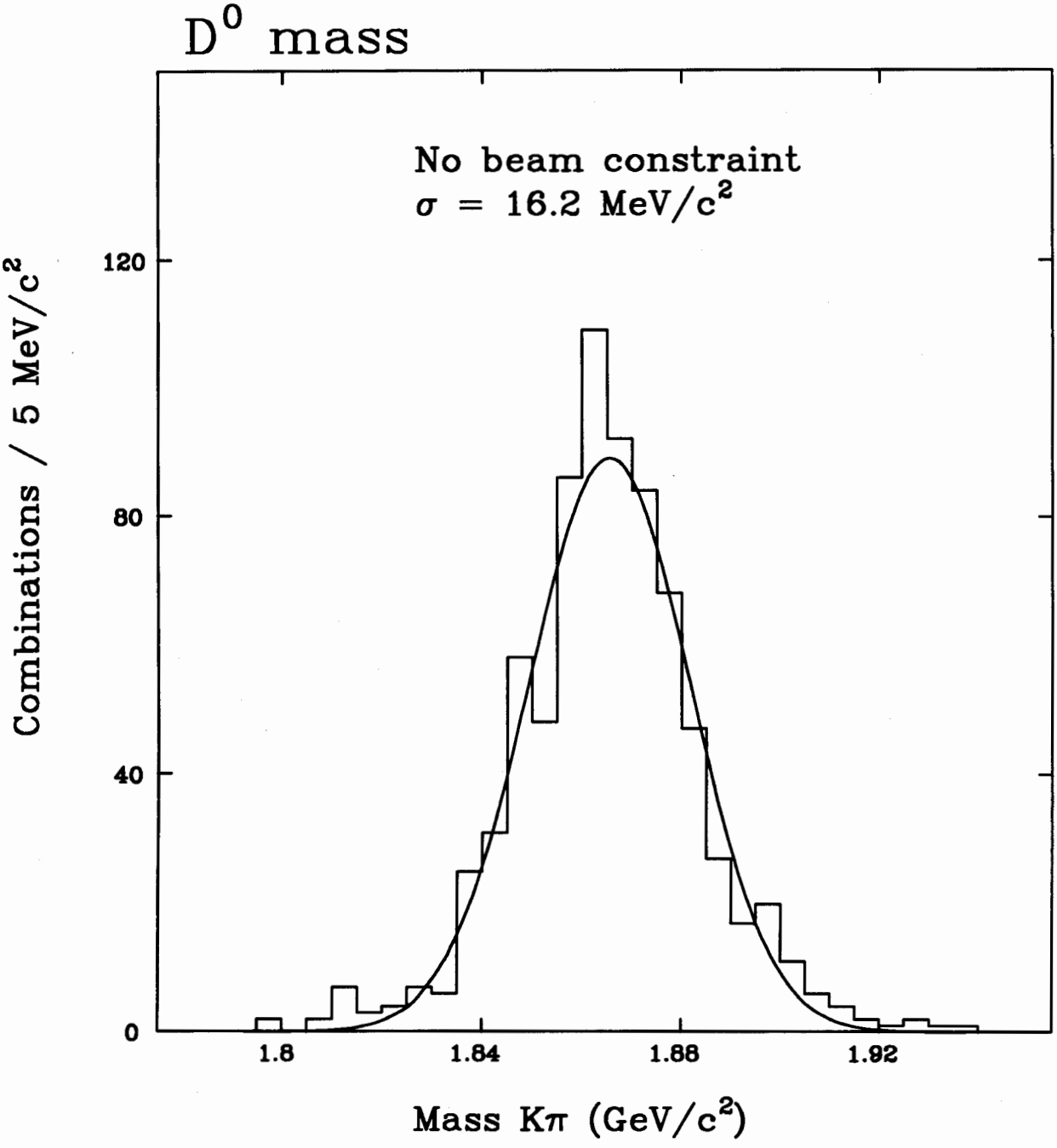

Figure 5.19: The $K^-\pi^+$ invariant mass distribution from the Monte Carlo events.

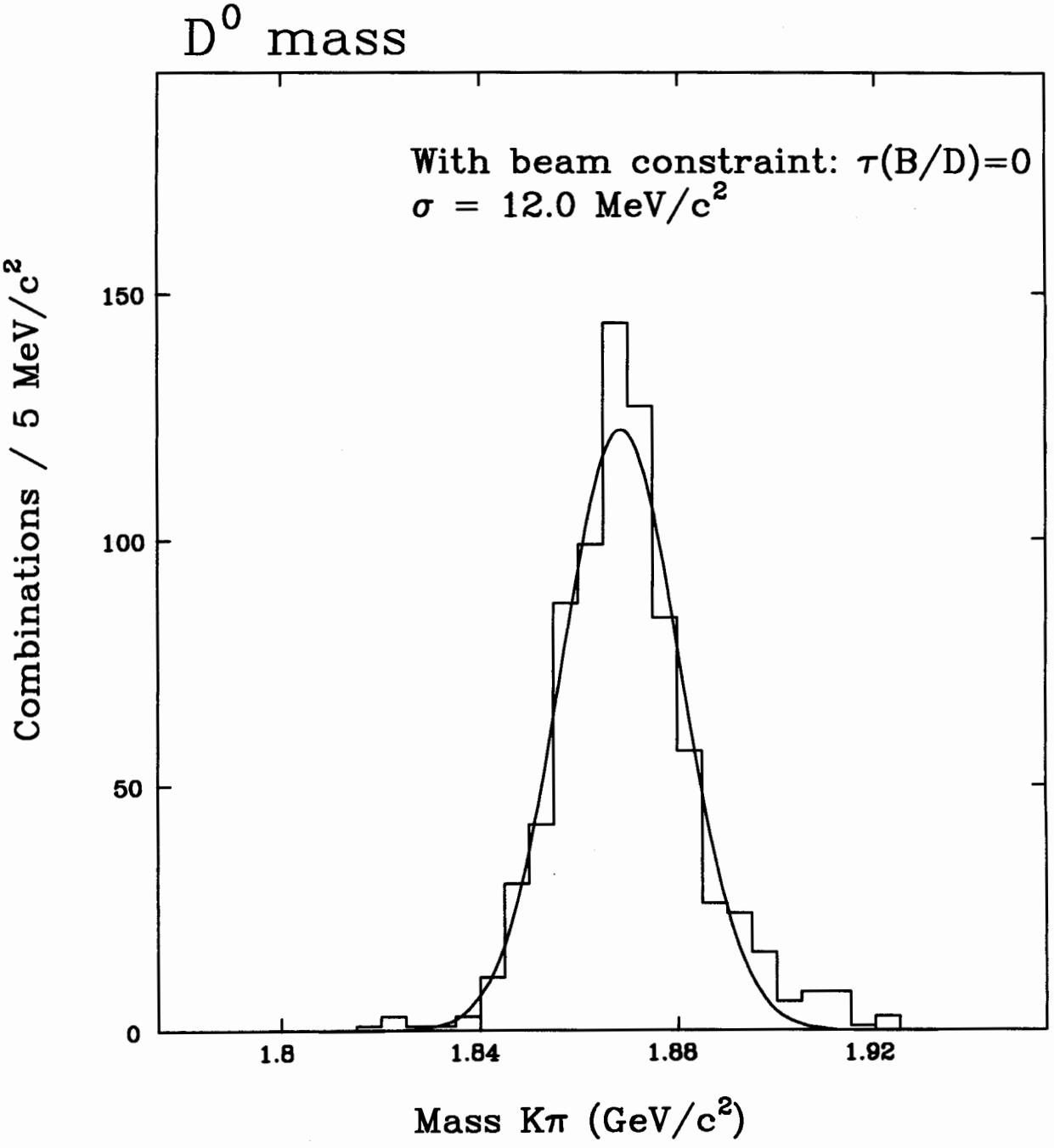

Figure 5.20: The $K^-\pi^+$ invariant mass distribution from the Monte Carlo e^- events with beam constraint.

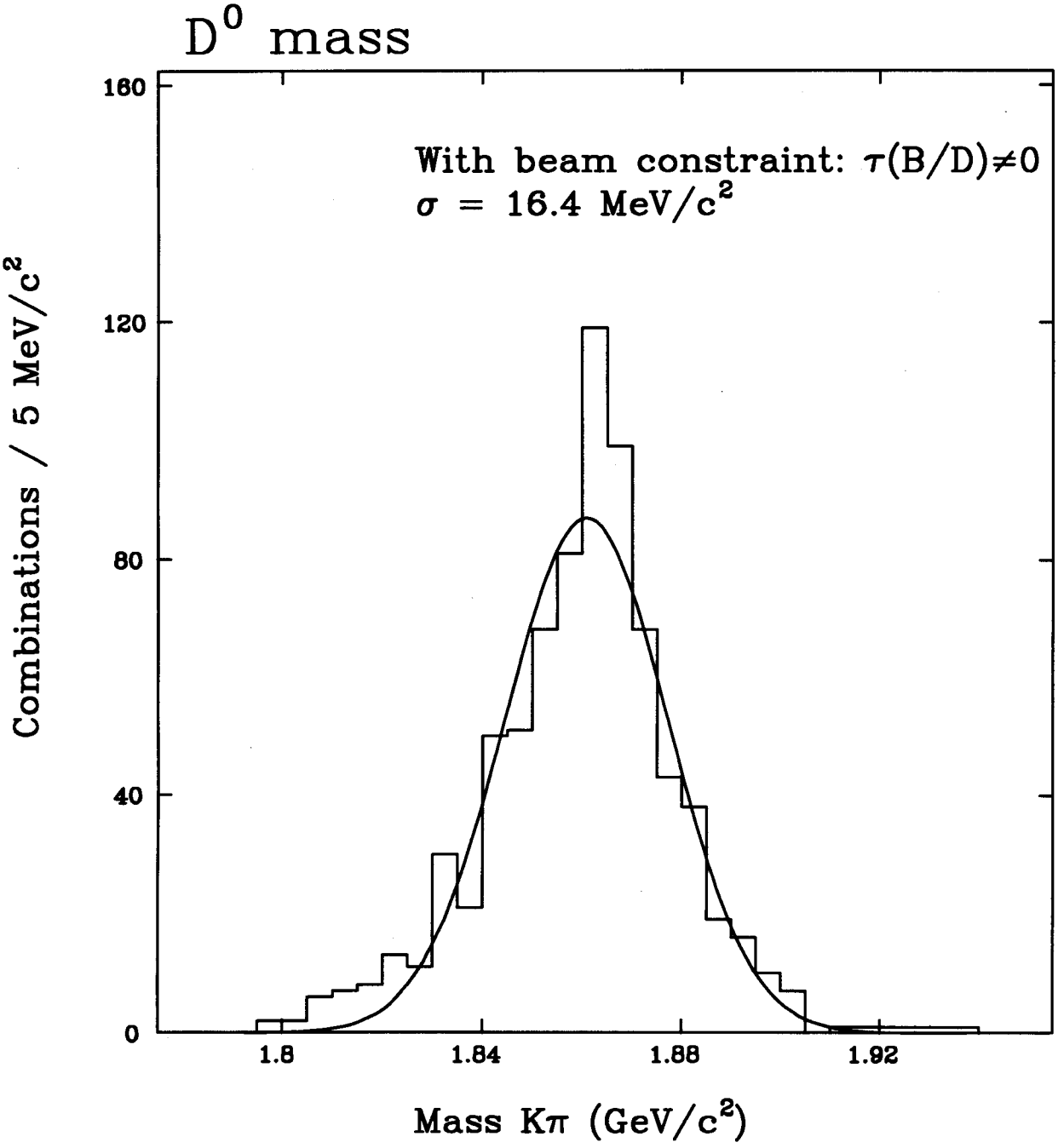

Figure 5.21: The $K^-\pi^+$ invariant mass distribution from the Monte Carlo e^- events with beam constraint and with the finite B and D lifetimes being taken into account.

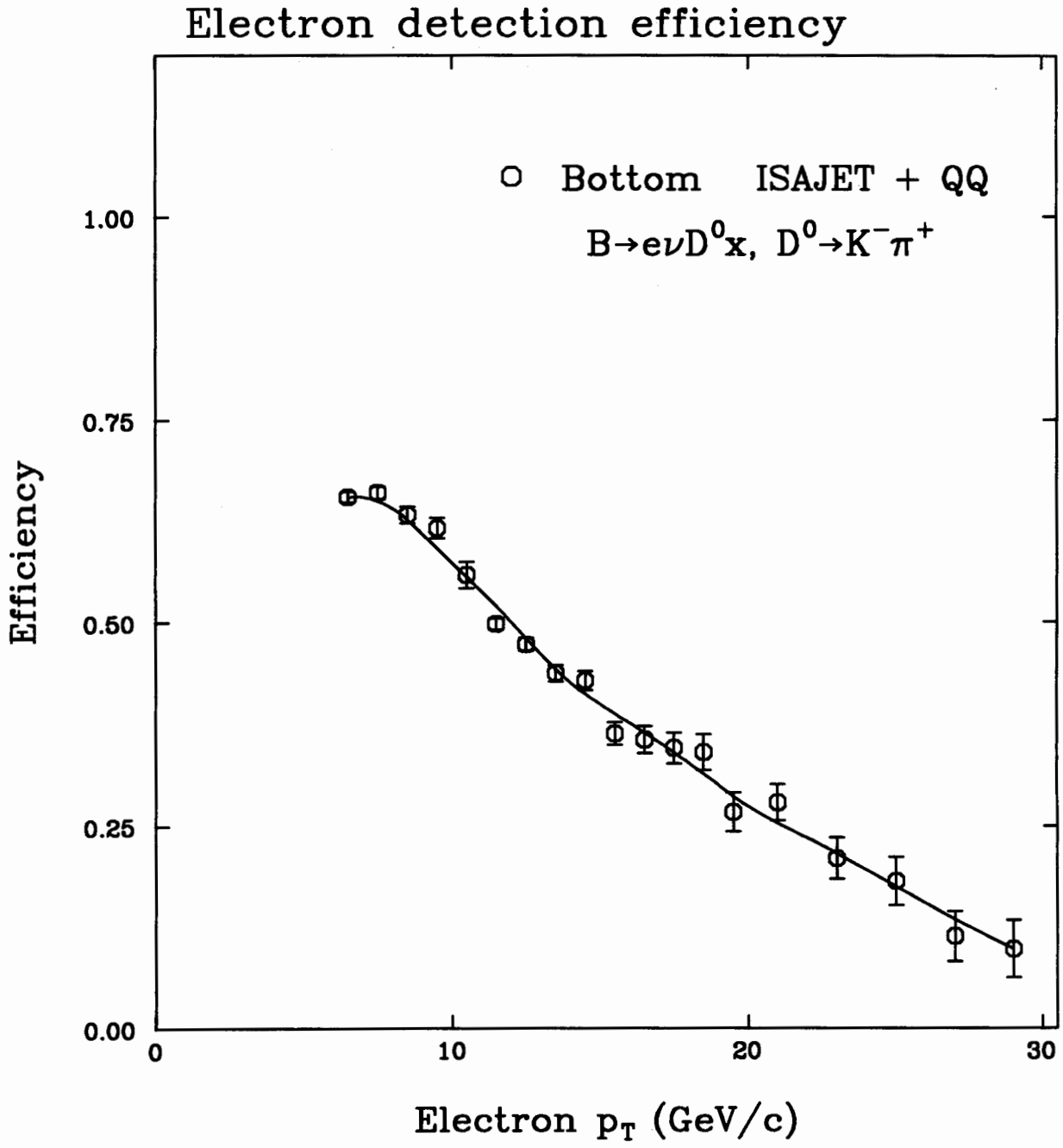

Figure 5.22: Electron selection efficiency for the exclusive mode.

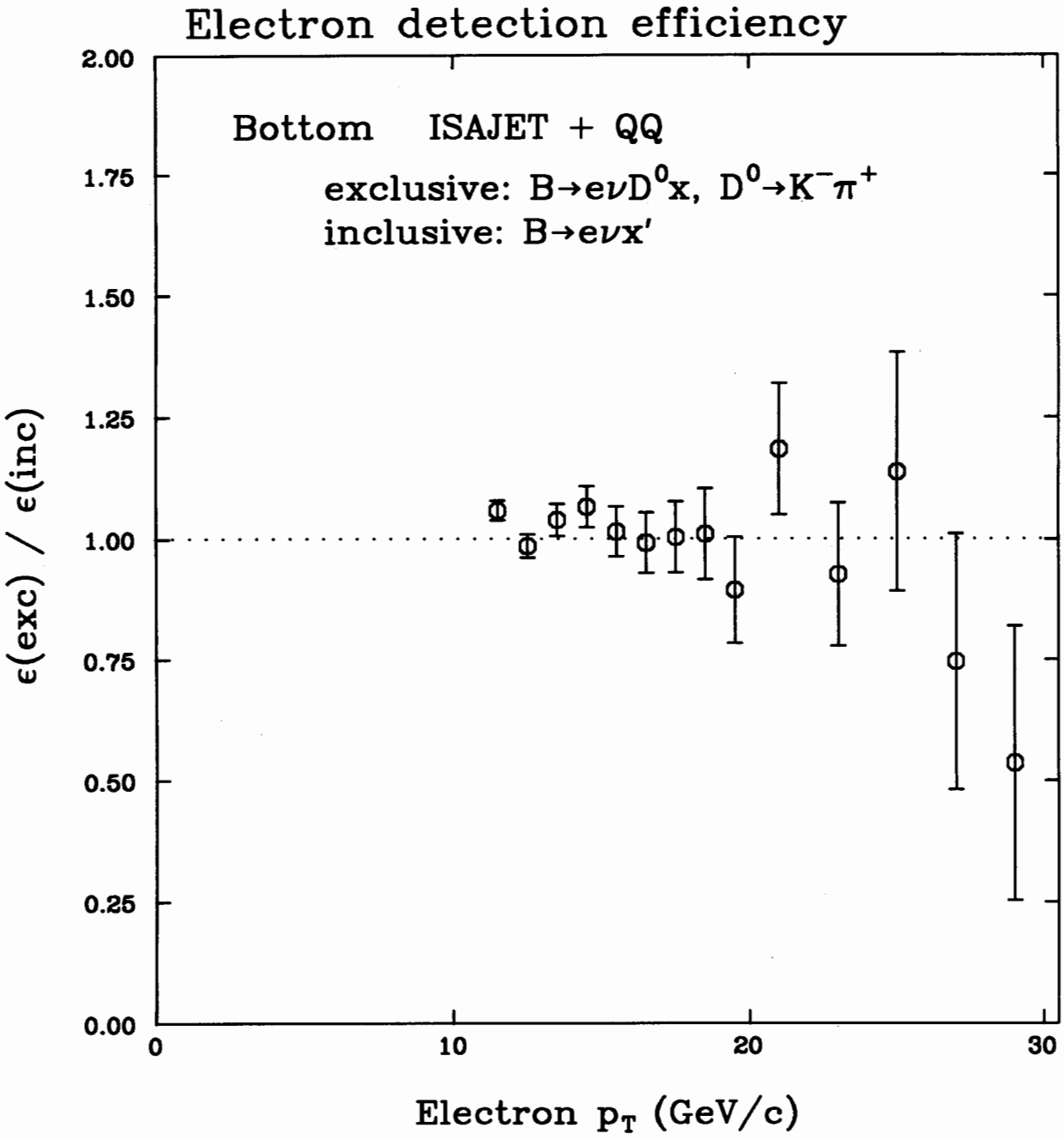

Figure 5.23: The ratio of the electron selection efficiencies for the exclusive and the inclusive modes.

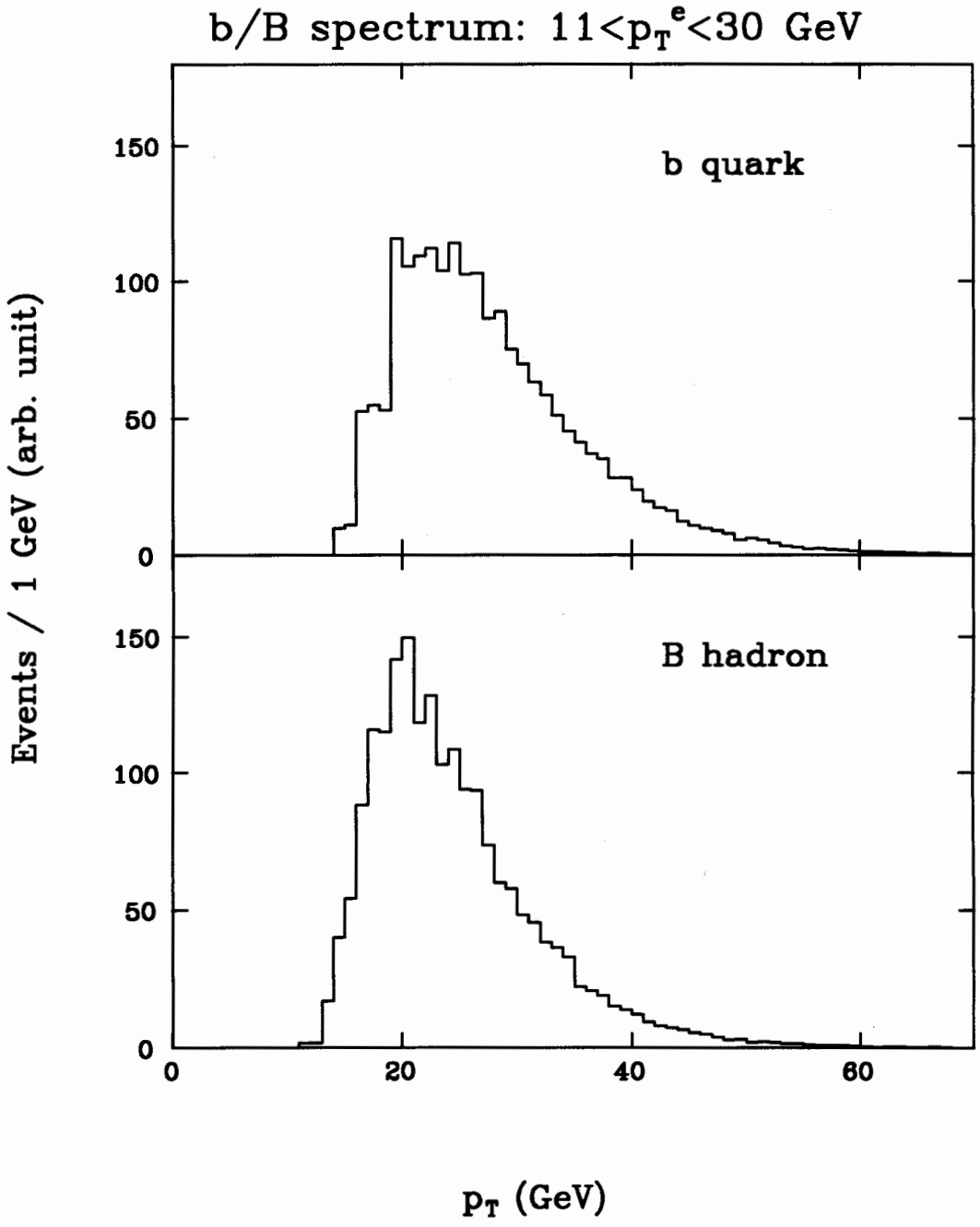

Figure 5.24: Monte Carlo p_{T} spectra of parent b quarks and B hadrons for the electrons with p_{T} of 11 through 30 GeV/c.

Chapter 6

Systematic Uncertainties

In this Chapter we investigate various sources of systematic uncertainties in the bottom quark cross section measurement.

6.1 Backgrounds

The uncertainties discussed in this section is relevant for the inclusive method only.

6.1.1 Photon conversion electrons

We have discussed photon conversion electrons in Section 3.4. We found the fraction of residual photon conversion electrons in the prompt electron sample as

$$f_{\rm conv} = 20 \pm 5\,\% \tag{6.1}$$

independent of the electron $p_{\rm T}$. The uncertainty in this quantity arises from the uncertainty in the estimation of the efficiency for finding photon conversion pairs.

6.1.2 Misidentified charged hadrons

We have discussed hadron background in Section 3.5. We found the fraction of misidentified hadrons in the electron sample as

$$f_{\rm hadron} = 15 \pm 15\,\%. \tag{6.2}$$

We take 15% as the uncertainty in the b quark cross section due to the hadron background.

6.1.3 Charm electrons

We have assumed the lowest QCD prediction of the ratio of the bottom and charm quark production cross sections. Although the absolute values of the production cross sections may be uncertain in the theoretical calculations, the uncertainties are expected to cancel each other in the ratio. The relative electron rates of bottom and charm quarks are about 10 to 1, given the production ratio of about unity. This is because of the different kinematics in the quark fragmentation and decays. We allow a factor of two variation in the production ratio, which gives a resultant charm electron fraction of 20% and 5% in the final electron sample. We use $\pm$10% as the uncertainty in the bottom quark cross section.

6.2 Monte Carlo models and electron selection efficiencies

In this section we discuss the uncertainties related to the estimate of the electron selection efficiency. We have used the CLEO Monte Carlo to describe the semileptonic decays of B mesons. The most important quantity here is the electron momentum spectrum in the B meson rest frame. The Monte Carlo reproduces the CLEO measurement well. Another important quantity is the spectrum of charm mesons in the decay, because it

determines the isolation degree of the electrons. We try another model, where the decays are treated by a pure spectator picture, that is, the quark level decay $b \rightarrow e\nu c$, rather than the hadron level decays. When we repeat the procedure to calculate the quantity $(\sigma_e/\sigma_b)_{\rm MC}$, the results differ by about 10%. We take this as the uncertainty.

The activities underlying the hard collision subprocesses (underlying event) is modelled using the real data electron events, instead of using Monte Carlo events. We have found in Section 5.3.2 that the electron selection efficiencies change by 8% with and without the inclusion of the underlying event, and use it as the uncertainty.

We have used the test beam data to simulate electromagnetic showers, and the behavior of W electrons was reproduced well. Thus we believe the uncertainty is small. As for the hadron simulation, we also used real data as much as possible. We have found in Section 5.3.3 that 15% of the Monte Carlo bottom electrons are killed by the HAD/EM cut due to the presence of nearby charged hadrons through their shower leakage across tower boundaries. We assign 10% uncertainty in the final answer due to this effect.

6.3 Fragmentation issues

When we measure b quark production cross section using the semileptonic decay electrons, the momentum of the parent B hadron or the b quark is not directly accessible. We can convert the electron rate to the quark rate, once the kinematical relations between the two is obtained using the Monte Carlo events. The fragmentation of the b quark into the B hadron is obviously important since it determines the b quark's energy-momentum fraction transferred to the B hadron.

In this section we discuss the issues related to the fragmentation of the bottom quark in measuring its production cross section. We first summarize the Peterson model and the e^+e^- experimental results of the heavy quark fragmentation. Next we discuss the adequate values of the parameter to be used as an input to a particular Monte Carlo, ISAJET. Finally we investigate the effect on the electron rates due to the uncertainty

in the fragmentation.

6.3.1 The Peterson model

Since it is impossible to describe the hadronization (fragmentation) of partons starting from the first principles, we have to rely on some models. The fragmentation of heavy quarks is known to be "hard"; the hadron containing the heavy quark carries a large fraction of the energy-momentum of the parent quark. This is quite contrary to the light quarks and the gluon, which produce many soft particles. This has been understood with simple kinematical arguments [54]. Later Peterson *et al.* [55] derived an analytic form of the fragmentation function $D(z)$ for heavy quarks as

$$D(z) = \frac{N}{z\,[\,1 - (1/z) - \epsilon/(1-z)\,]^2}, \tag{6.3}$$

where z is the fraction of the parent quark energy-momentum carried by the hadron, and N is a normalization constant. The function includes only one parameter ϵ, which is approximately

$$\epsilon \simeq \frac{m_q^2}{m_Q^2}, \tag{6.4}$$

where $m_q(m_Q)$ is the mass of the light (heavy) quark. In practice it is to be determined experimentally for each quark species. The parameter controls the "hardness" of the fragmentation; the smaller the ϵ value, the harder the fragmentation. The quark mass dependence of the ϵ parameter predicts a harder fragmentation for a heavier quark. The energy-momentum fraction z is defined as

$$z = \frac{(E + p_{||})_{\rm hadron}}{(E+p)_{\rm quark}}, \tag{6.5}$$

where $(E + p_{||})_{\rm hadron}$ is the sum of the energy and the momentum component parallel to the quark direction, and $(E+p)_{\rm quark}$ is the sum of the energy and the momentum of the quark after the gluon and photon radiation in the final state.

Although it is very simple and includes no dynamical arguments, the Peterson function is widely accepted as a standard form of the heavy quark fragmentation function.

6.3.2 Results from e^+e^- experiments

The fragmentation of heavy quarks has been measured in various e^+e^- experiments at PEP, PETRA and LEP. Since it is hard to completely reconstruct the hadronic decays of B hadrons, the measurement of the b quark fragmentation is done through its decay leptons, whose kinematic distribution reflects that of the parent hadron, and thus the fragmentation of the parent quark. Here z value is not obtained on an event-by-event basis, and a typical way of determining the b quark fragmentation is to fit the observed lepton spectrum with the Monte Carlo distributions where ϵ is varied as a free parameter.

Here complications arise. First, different experiments quote fragmentation values using different definitions of the energy-momentum fraction. Some use the energy-momentum fraction with respect to the beam energy, instead of the energy-momentum of the quark just before the fragmentation. This definition is usually referred to as x, and has been popular because it is more easily accessible experimentally, once a heavy hadron, for example D^{*+} meson, is fully reconstructed. x is not identical to z because of the existence of the initial and final state photon and the final state gluon radiation. By definition x is smaller than z.

The second complication is a purely technical one associated with the Monte Carlo event generation. In Monte Carlo events the $< z >$ value reconstructed using the final hadron and the parton energies and momenta is not in general identical to what we expect from the Peterson function with a given ϵ. Generally the reconstructed z value is larger than the Peterson function's value. As we see later, this is also the case with the ISAJET Monte Carlo. In the Monte Carlo generators which employ the independent fragmentation model, such as ISAJET, there exists a problem of the energy-momentum non-conservation. This happens because massive jets of physical hadrons are created from the massless parton. In order to remedy this, the final state hadron momenta

are re-scaled so that they balance the parton momentum, after all hadronizations are complete. Due to this procedure, the original kinematical relations between the parton and the hadrons, z for example, are only approximately retained.

Taking these effects into account, Chrin [56] presents a compilation of the PEP and PETRA results as

$$\begin{aligned} < z >_b &= 0.83 \pm 0.01 \pm 0.02, \\ < z >_c &= 0.67 \pm 0.02 \pm 0.02, \end{aligned} \tag{6.6}$$

where z is the momentum fraction defined by Eq. (6.5). These values correspond to the ϵ parameter values of

$$\begin{aligned} \epsilon_b &= 0.006^{+0.001+0.002}_{-0.001-0.002}, \\ \epsilon_c &= 0.06^{+0.02+0.02}_{-0.01-0.01}. \end{aligned} \tag{6.7}$$

The first error is statistical and the second error is systematic. More recently, a measurement by ALEPH [57] at LEP gives

$$\epsilon_b = 0.006^{+0.004}_{-0.003}, \tag{6.8}$$

where the quoted error includes both the statistical and systematic effects. These are shown in Figure 6.1. These experiments cover the kinematical region of our interest, between about 15 and 40 GeV/c in transverse momentum. The results show that $< z >$ is independent of the quark energy, and is 0.83.

6.3.3 Choice of ϵ parameter value for ISAJET

Now the question is what ϵ value we should use as an input to ISAJET. As noted earlier, the Monte Carlo generators do not in general reproduce the $< z >$ value of the Peterson function. Figure 6.2 shows the $< z >$ as a function of the ϵ parameter for the ISAJET b jets with the average transverse momentum ($p_{\rm T}$) of 26 GeV/c. We observe that the ISAJET $< z >$ value is larger than the Peterson function value. The same tendency is observed in other Monte Carlo generators [56].

Moreover, the relation turns out to be dependent on the quark momentum, as shown in Figure 6.3. We note that this effect is of no physics origins; it is an artifact caused while ISAJET is trying to restore the energy-momentum conservation between the parton and the physical hadrons.

Now we want the Monte Carlo events with $< z >$ value of 0.83, independent of the quark momentum. We modify ISAJET fragmentation routines so that they give a constant $< z >$ behavior as a function of the jet momentum, and provide with the ϵ parameter value so as to give the desired $< z >$ value. In practice, this is achieved by changing the input ϵ parameter on a jet-by-jet basis knowing the jet momentum. Figure 6.4 shows the input ϵ value necessary for ISAJET to give the $< z >$ value of 0.83 ± 0.03, as a function of the b quark $p_{\rm T}$. It seems that the ISAJET $< z >$ approaches asymptotically to the Peterson function's $< z >$ value as the quark $p_{\rm T}$ goes to infinity. The effect of the quark/hadron mass differences certainly vanishes in the infinite momentum frame.

6.3.4 Effect on the electron rates

Here we investigate the effect on the electron rates. We use 0.83 as a nominal value for $< z >$ and 0.03 as its uncertainty.

Analytic calculation

First we present results of an analytic calculation, which does not involve the difficulties mentioned earlier. For a given b quark $p_{\rm T}$, we generate the B hadron momentum according to the Peterson function. The electron momentum is generated in the B meson rest frame as measured by CLEO, and then Lorentz-boosted to the laboratory frame of the B hadron. We convolute them with the parent b quark $p_{\rm T}$ spectrum calculated by Nason, Dawson and Ellis (NDE) [14].

The electron $p_{\rm T}$ spectrum thus obtained is shown in Figure 6.5 together with the NDE b quark spectrum. Only b quarks with $p_{\rm T}$ of 10 GeV and above are used. Two

p_{T}^{e}	$p_{\mathrm{T}}^{\mathrm{min}}(b)$	Relative electron rates		
		$< z >= 0.80$	$< z >= 0.83$	$< z >= 0.86$
10 - 15	15	0.877 ± 0.015	1.0	1.131 ± 0.017
15 - 20	23	0.841 ± 0.024	1.0	1.152 ± 0.028
20 - 25	32	0.823 ± 0.039	1.0	1.155 ± 0.043

Table 6.1: Electron rates for three b quark fragmentation values.

solid lines correspond to the bounds on $< z >$, 0.80 and 0.86. The shape of the electron spectrum remains almost the same against the change in the fragmentation value, while the absolute rate changes by about $\pm 12\%$ in the p_{T} range of our interest, between 10 and 25 GeV/c.

Figure 6.6 and 6.7 shows the electron spectrum when the parent b quark spectrum is changed by a factor of 2 in every 10 GeV/c p_{T} interval. We observe that the electron spectrum is rather sensitive to the parent b quark spectrum.

Full Monte Carlo calculation

In order to include the possible effects on the electron selection efficiencies, we generate b jets with the ISAJET Monte Carlo with the modification applied, simulate the detector responses, and calculate the electron rates after the identification cuts are applied. Here we calculate the ratio of the electron rate to the b quark rate defined by

$$(\sigma_e/\sigma_b)_{\mathrm{MC}} = \frac{N_{e^-}}{N_b}, \tag{6.9}$$

where N_{e^-} is the number of electrons (not including positrons) passing the same geometrical, kinematical and identification cuts as in data, and N_b is the number of all b quarks produced in the kinematic range (p_{T} and rapidity) and decaying into electron channel.

Source	Uncertainty
Photon conversion $e^{\pm}$ subtraction	5%
Hadron background subtraction	15%
Charm electron subtraction	10%
Models of B decays	10%
Underlying event contribution	8%
Hadron simulation	10%
b quark fragmentation	15%
B hadron semileptonic decay branching ratio	10%
Luminosity	7%
Total	32%

Table 6.2: Systematic uncertainties in the b quark cross section measurement.

We use three kinematic ranges:

$$\begin{aligned} 10 < p_{\mathrm{T}}^{e} < 15\,\mathrm{GeV}/c, \;\; p_{\mathrm{T}}^{b} > 15\,\mathrm{GeV}/c. \\ 15 < p_{\mathrm{T}}^{e} < 20\,\mathrm{GeV}/c, \;\; p_{\mathrm{T}}^{b} > 23\,\mathrm{GeV}/c. \\ 20 < p_{\mathrm{T}}^{e} < 25\,\mathrm{GeV}/c, \;\; p_{\mathrm{T}}^{b} > 32\,\mathrm{GeV}/c. \end{aligned} \tag{6.10}$$

In calculating the quantity, we generate the b quarks with a flat p_{T} spectrum rather than that by ISAJET, and later convolute them with the p_{T} spectrum by NDE.

The relative electron rates for the three fragmentation values are given in Table 6.1 and in Figure 6.8. A modest change in the electron rates is observed. We take 15% as the uncertainty in the b quark cross section due to this fragmentation effect.

6.4 Semileptonic decay branching ratios of B hadrons

The semileptonic decay branching ratio of the non-strange B mesons has been measured at both CLEO and ARGUS. The latest CLEO value [52] is

$$Br(\bar{B}_{u,d} \to \ell^{-}\bar{\nu}X) = 10.3 \pm 0.1 \pm 0.2\%. \tag{6.11}$$

PEP and PETRA experiments measure the similar branching ratio averaged over all B hadrons produced at their energies. It suggests either that all B hadrons have similar semileptonic branching ratios, or that the hadron mixture at PEP and PETRA energies is not so different from that at the $\Upsilon(4S)$, or both. We use 10% for the systematic error.

6.5 Luminosity

As discussed in Section 2.4, the uncertainty in our luminosity measurement is 7%.

We summarize the systematic uncertainties in Table 6.2. The first three items are the uncertainties due to background subtraction, and are relevant only for the cross section using the inclusive electron rates. The other items in the Table are common to both the inclusive and the exclusive ($D^0 \to K^-\pi^+$) methods.

We add all items in quadrature to obtain 32% as the total systematic uncertainty.

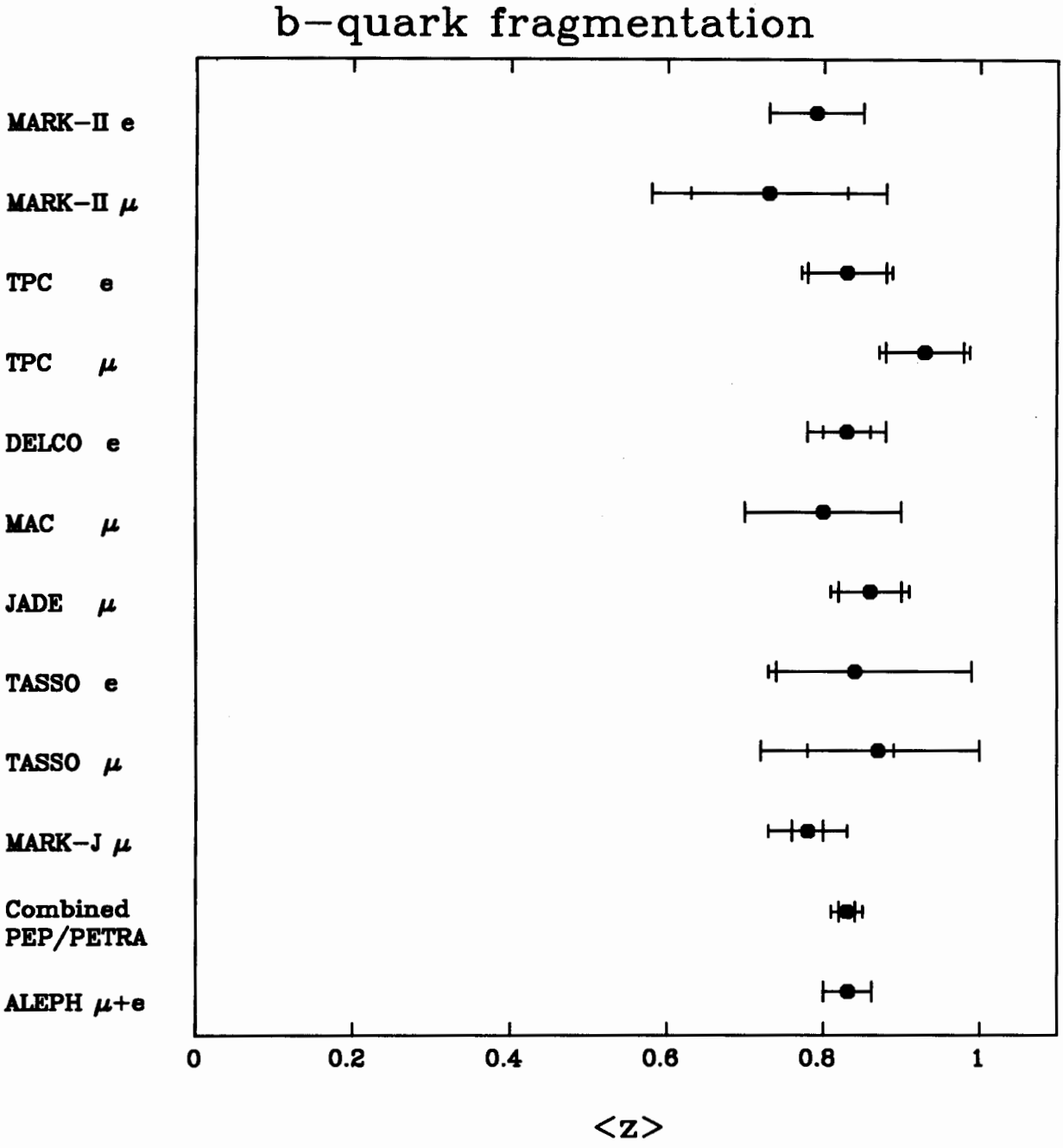

Figure 6.1: The b quark fragmentation measurements from the various e^+e^- experiments at PEP, PETRA and LEP.

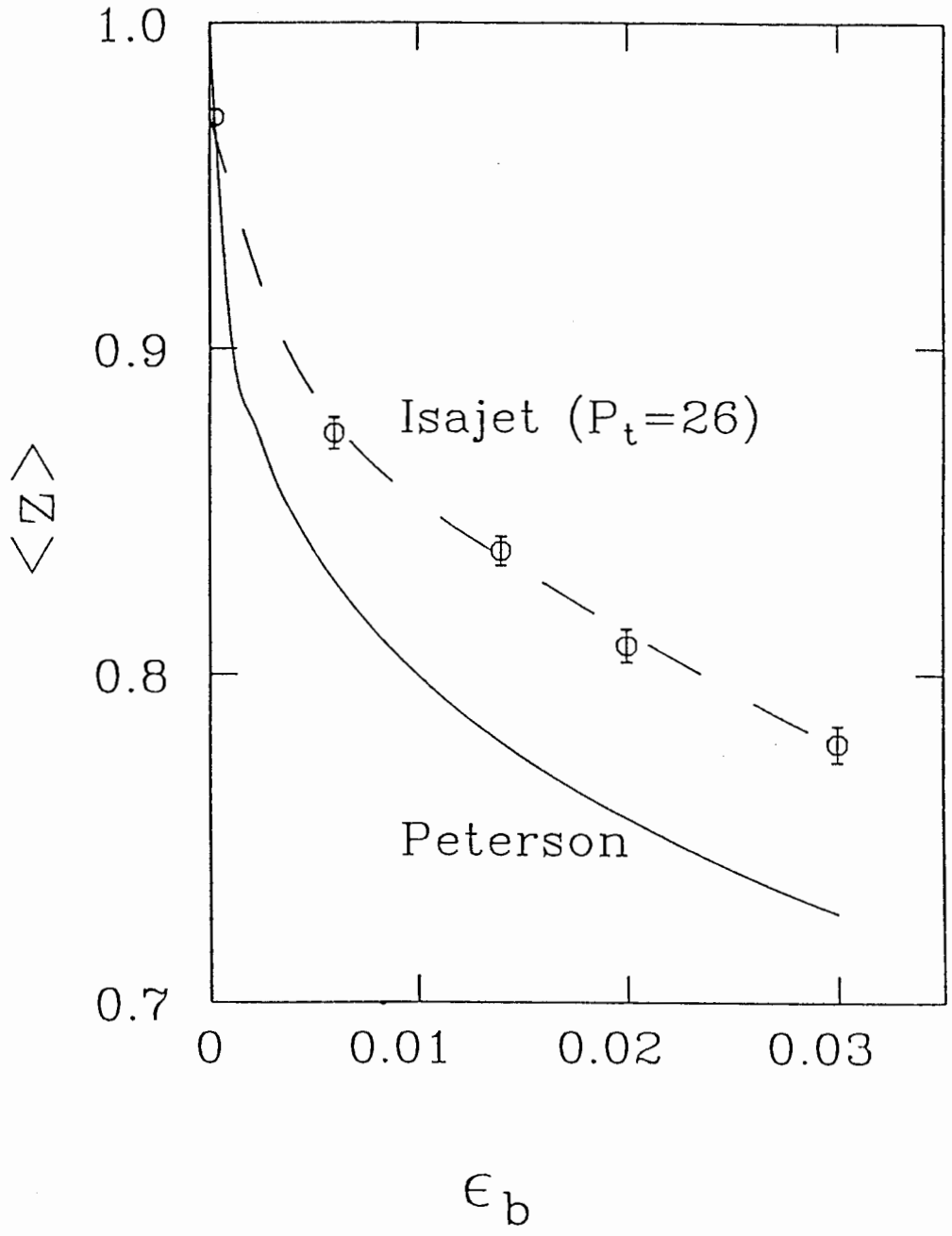

Figure 6.2: The average z value for ISAJET b jets as a function of the input ϵ. Also shown is the relation expected from the Peterson function.

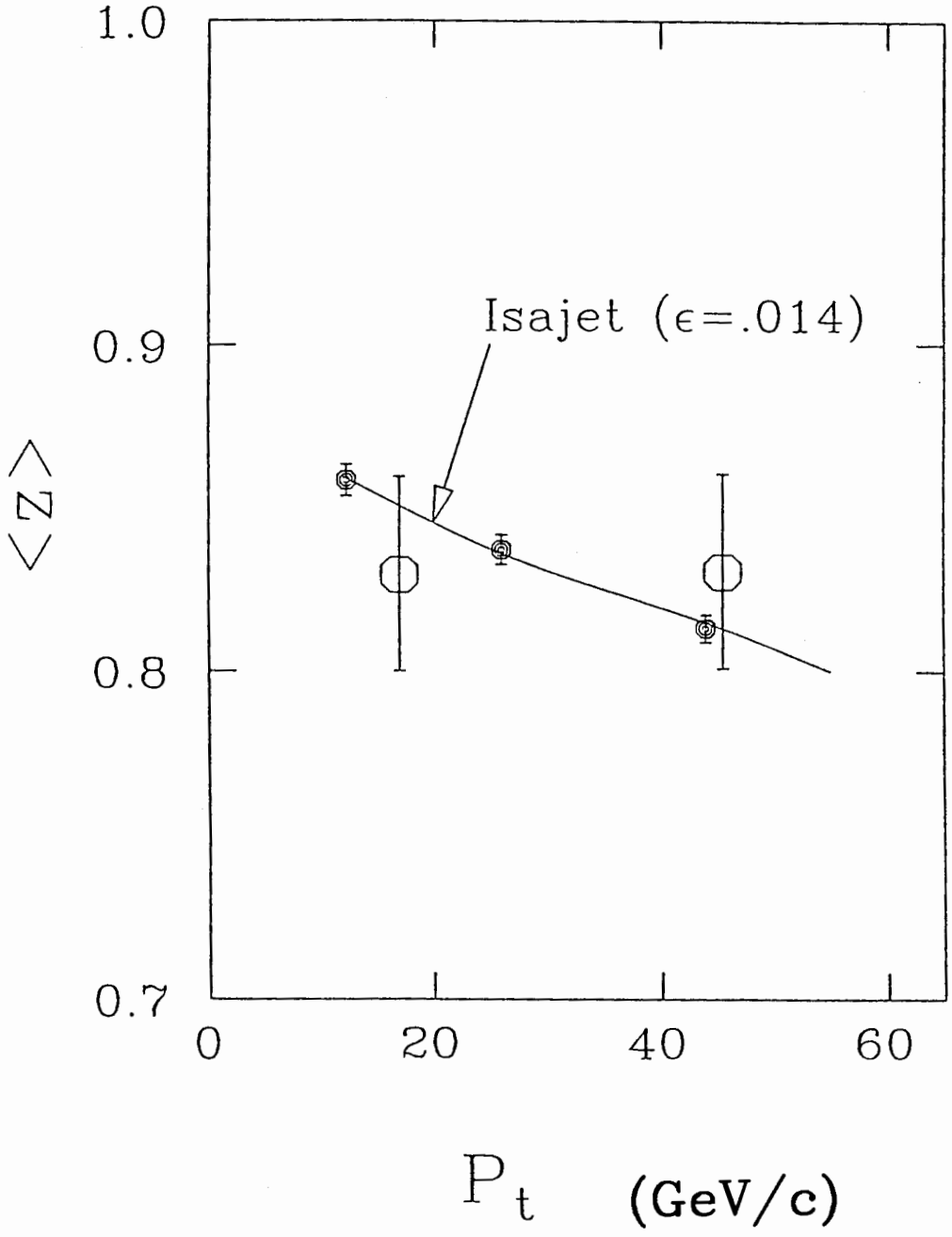

Figure 6.3: The reconstructed $< z >$ values for ISAJET b-jets for a fixed input ϵ parameter value of 0.014, as a function of the b quark p_T. Open circles are the e^+e^- experimental measurements.

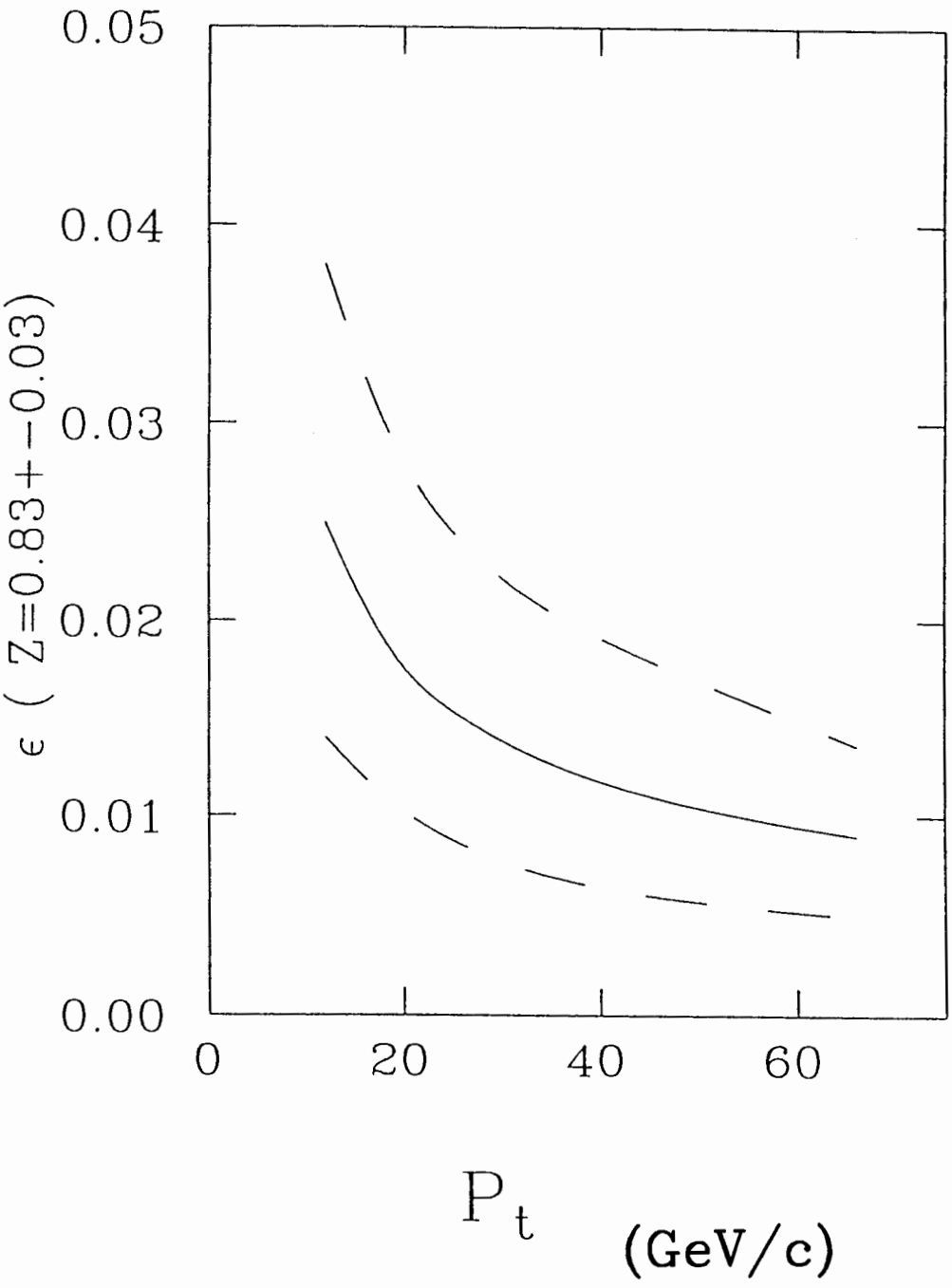

Figure 6.4: The input ϵ value for ISAJET b-jets to reproduce the $< z >$ value of 0.83 ± 0.03 as a function of b quark p_T.

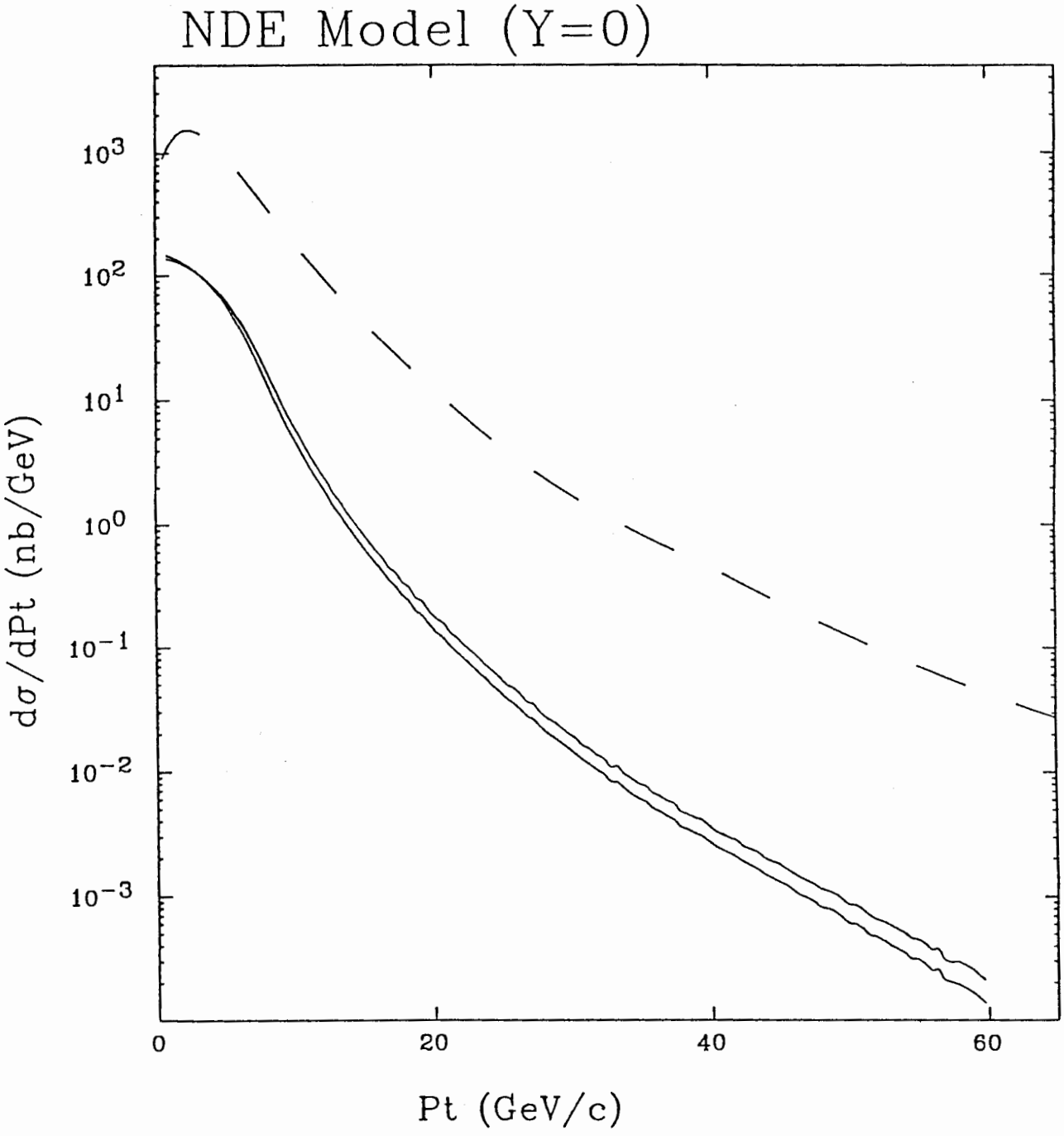

Figure 6.5: The analytic calculation of the electron p_T spectrum (solid curves) for the $< z >$ values of 0.80 and 0.86, along with the assumed parent b quark spectrum (dashed curve).

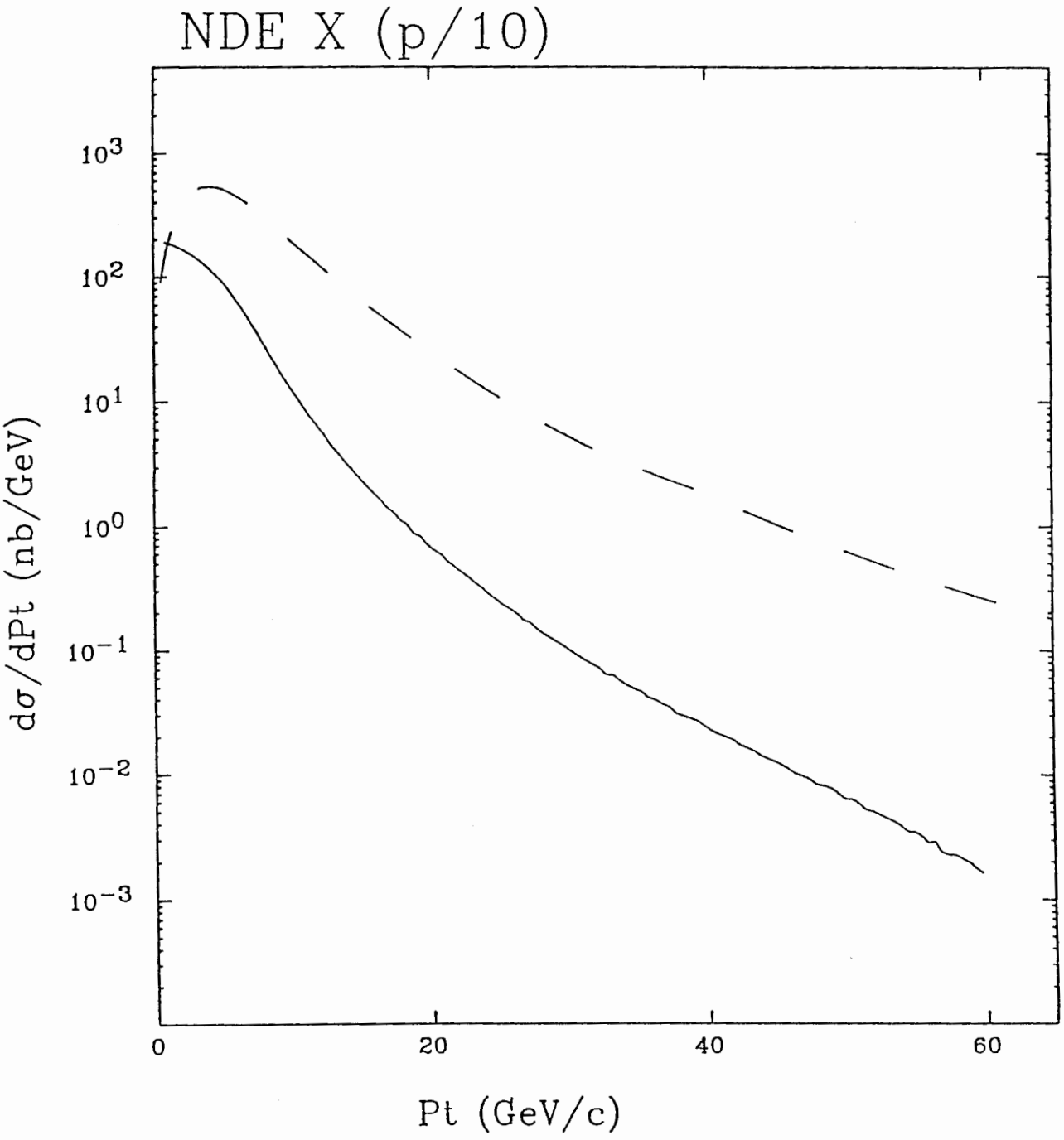

Figure 6.6: The electron p_T spectrum for a harder b quark p_T spectrum than the NDE model.

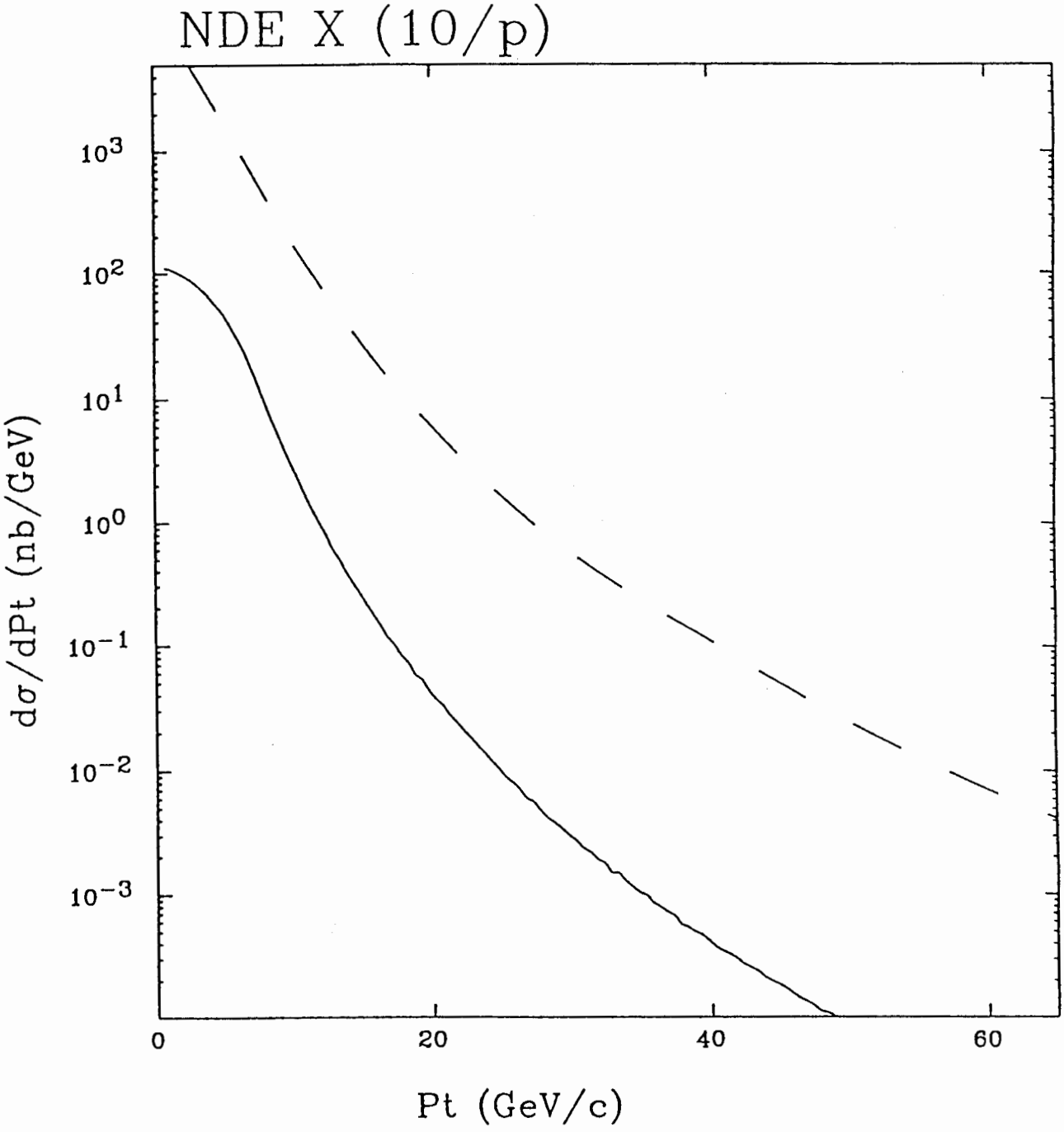

Figure 6.7: The electron p_T spectrum for a softer b quark p_T spectrum than the NDE model.

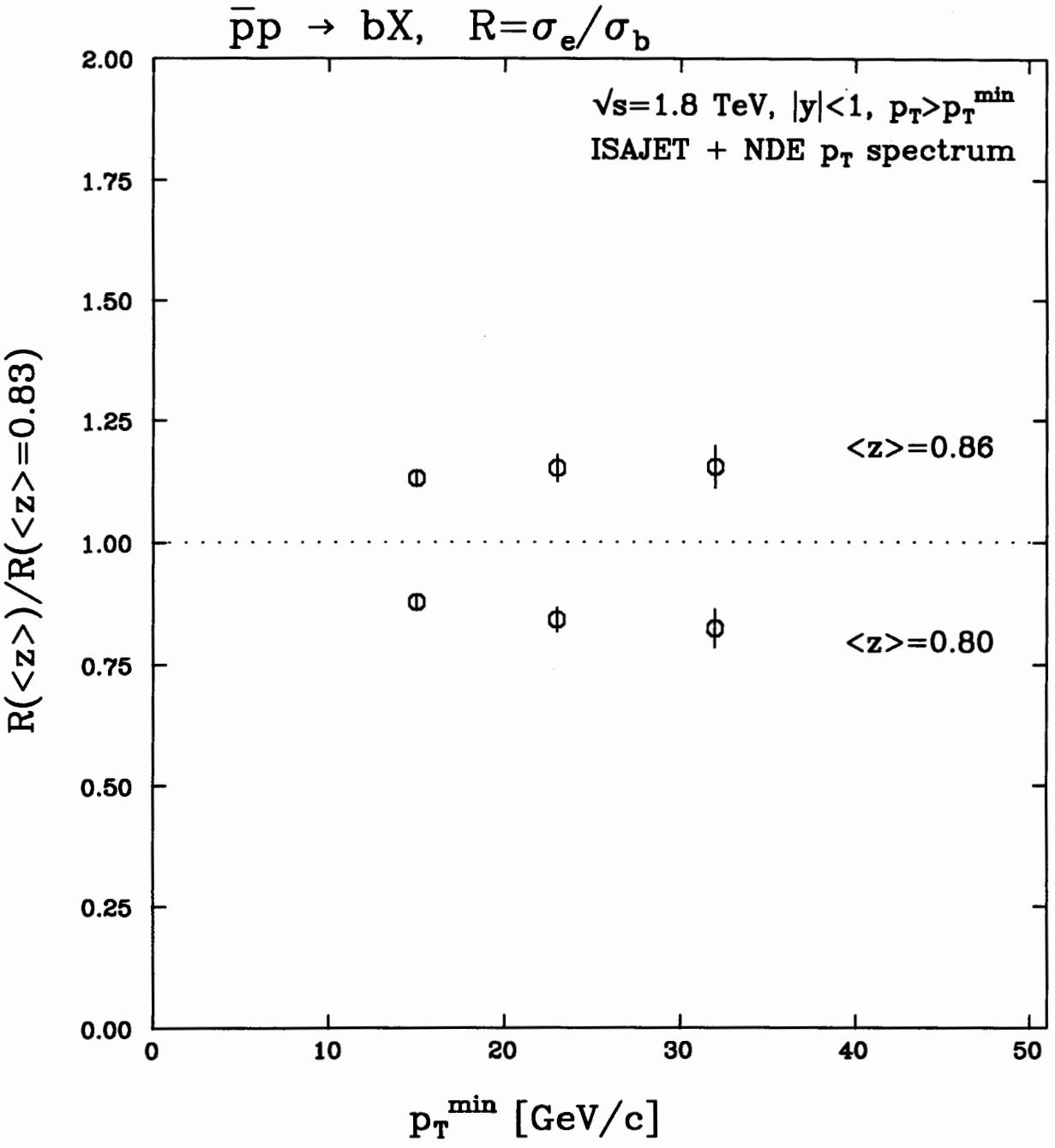

Figure 6.8: The ratio of the electron rate to the b quark rate for three fragmentation values, normalized to the nominal fragmentation of $< z >= 0.83$.

Chapter 7

Results and Conclusion

Using the results in Chapter 5 and the systematic uncertainties discussed in the previous Chapter, we obtain the final b quark production cross sections as

$$\begin{aligned}
\sigma(\bar{p}p \to bX;\ p_{\rm T} > 15\,{\rm GeV}/c,\ |y| < 1) &= 1220 \pm 390\ {\rm nb}, \\
\sigma(\bar{p}p \to bX;\ p_{\rm T} > 23\,{\rm GeV}/c,\ |y| < 1) &= 220 \pm 70\ {\rm nb}, \\
\sigma(\bar{p}p \to bX;\ p_{\rm T} > 32\,{\rm GeV}/c,\ |y| < 1) &= 56 \pm 18\ {\rm nb}, \qquad (7.1)
\end{aligned}$$

from the inclusive electron rates.

The method using the electron-D^0 rate is free from the uncertainty in the background subtraction. We find

$$\sigma(\bar{p}p \to bX;\ p_{\rm T} > 19\,{\rm GeV}/c,\ |y| < 1) = 440 \pm 100 \pm 130\ {\rm nb}, \qquad (7.2)$$

where the first uncertainty is statistical and the second uncertainty is systematic, including the 13% uncertainty in the combined branching fraction B_{eD^0} (Eqs. (5.13) and (5.21)), and others which are common to both the inclusive and the exclusive methods. This method using the charmed particle D^0 is sensitive to only non-strange B mesons, B_u and B_d, while the b quark fragments into other B hadrons also. We assume the fraction of non-strange B mesons relative to all B hadrons produced to be 78%, and use

it without systematic uncertainty.

We plot the results of the two methods in Figure 7.1. We show the systematic uncertainty which is common to the two methods separately.

The curves in the plot are the theoretical calculation by Nason, Dawson and Ellis (NDE) [14] in the next-to-leading order of QCD. The dotted curves corresponds to an estimate of the uncertainty in the theoretical prediction, which reflects the uncertainties in the choice of renormalization (evolution) scale μ and the bottom quark mass.

The studies of bottom quark production properties have also been performed using events containing J/ψ's by other collaborators in CDF. By using the number of fully reconstructed $B^{\pm}$ events, the production cross section of the bottom quark is obtained [58] as

$$\sigma\,(\bar{p}p \rightarrow bX;\ p_{\mathrm{T}} > 10.5\,\mathrm{GeV}/c,\ |y| < 1) = 6.40 \pm 2.36 \pm 1.98\ \mu\mathrm{b}, \qquad (7.3)$$

where the first uncertainty is statistical, and the second is systematic. The number is consistent with the extrapolation of the electron results, as shown in Figure 7.2. In this plot the error bars denote the combined statistical and systematic uncertainties. Our results show somewhat higher values than the theoretical predictions.

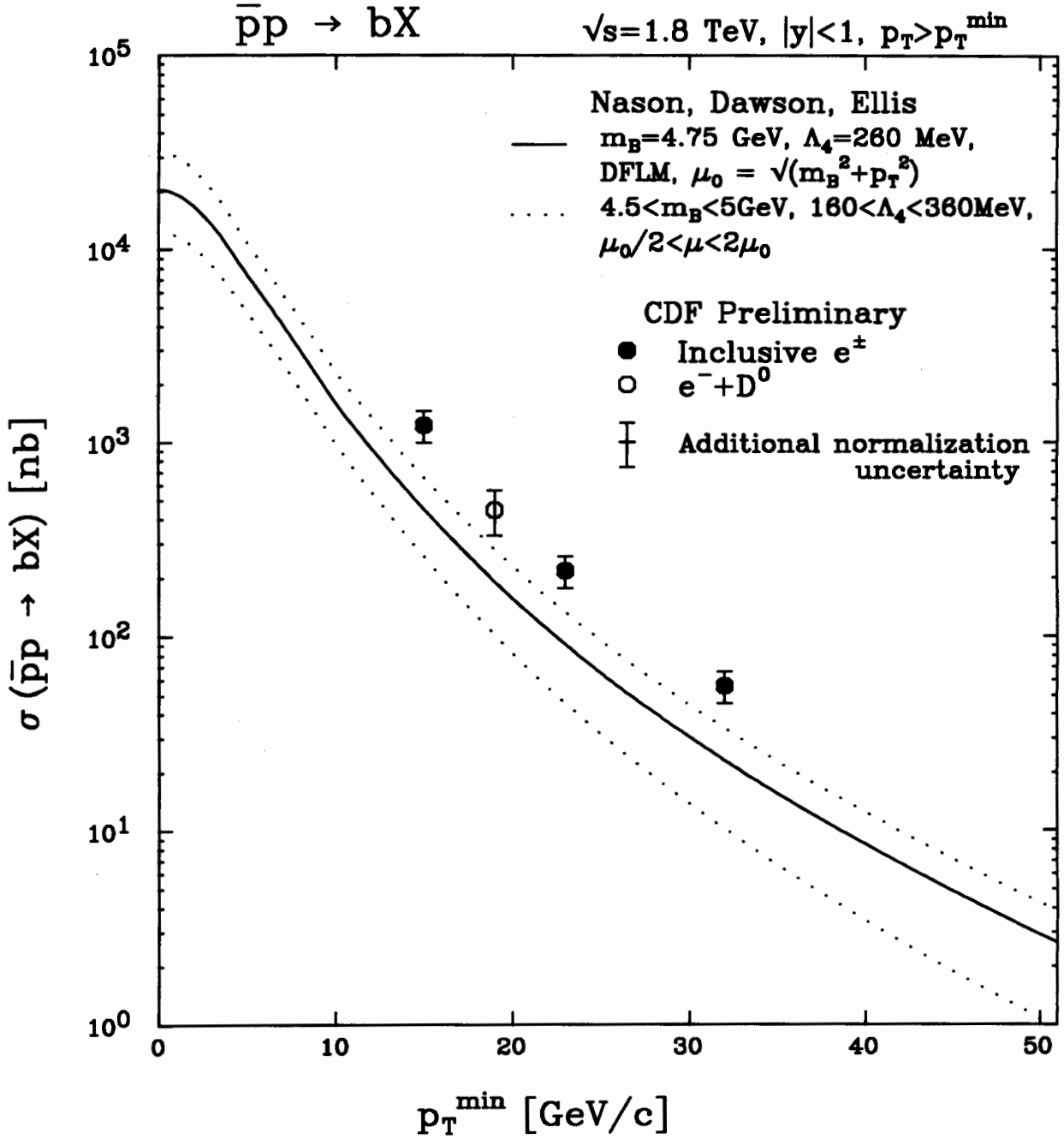

Figure 7.1: The b quark production cross sections measured using the inclusive electron rates and the e^--D^0 rate. Also shown is the theoretical calculation by Nason, Dawson and Ellis.

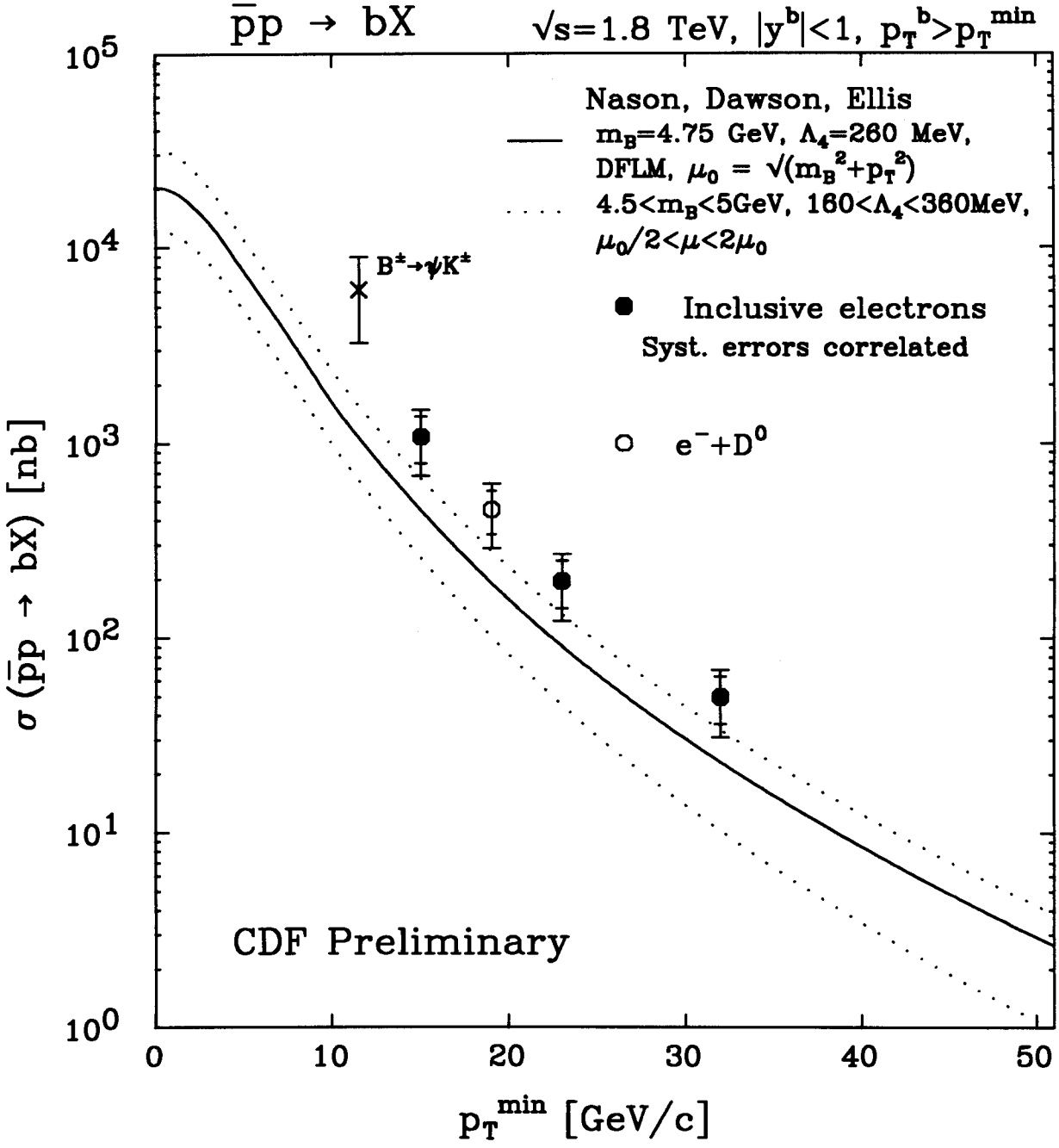

Figure 7.2: The b quark production cross sections from the J/ψ events and the inclusive electron events.

Appendix A

Properties of Heavy Quarks

This Appendix summarizes the current understandings of the fragmentation and decay properties of heavy quarks.

A.1 Fragmentation of Heavy Quarks

Let us discuss the hadronization process of the quarks produced with high momenta. An outgoing quark forms a color field along with its movement and produces a quark antiquark pair or diquark. Together with a parent quark, they form hadrons. This process is called "fragmentation", and it is very hard to describe it from the first principles. Since perturbative approach can not be applied to such "soft" or long distance processes, where an effective coupling constant becomes large, we need phenomenological models for it.

An initiative work was done by Field and Feynman [59]. For simplicity we consider the case where only mesons are produced in the hadronization process. They describe the hadronization of the quark as a recursive process: The initial quark q_0 picks up a quark antiquark pair $q_1\bar{q}_1$ from the sea, produces a meson $q_0\bar{q}_1$, which carries a certain fraction z of the energy-momentum of the parent quark, and leaves the fraction $1-z$ for the remaining quark q_1. Then the quark q_1 undergoes exactly the same process. This is

repeated until the quark loses its energy-momentum, in practice, until the momentum is reduced down to a cutoff of order pion mass.

A.1.1 Fragmentation function

In order to describe fragmentation and hadronization processes of the quarks, the variable z is commonly used, which is defined as a fraction of parent quark's energy-momentum carried by a resultant hadron. There exist several definitions of z, and the following definition is commonly used because it is invariant under Lorentz boost along the quark direction:

$$z \equiv \frac{(E + p_{||})_{hadron}}{(E + p)_{quark}}, \tag{A.1}$$

where $p_{||}$ is a hadron momentum component parallel to the quark direction. The z can take a value between 0 and 1 by definition. The fragmentation function $D_q^h(z)$ is defined as a probability that we see a hadron of type h carrying the energy-momentum fraction z of the initial quark of type q. With this definition, the average total multiplicity of the hadrons is obtained by integrating over z and summing over the hadron species h,

$$< N >= \sum_h \int_0^1 D_q^h(z)\, dz. \tag{A.2}$$

The momentum conservation gives the relation

$$1 = \sum_h \int_0^1 D_q^h(z)\, z\, dz. \tag{A.3}$$

The fragmentation of the light and heavy quarks has been studied in various e^+e^- annihilation experiments. Originally it was assumed that the fragmentation of heavy quarks was similar to that of light quarks, which hadronizes mainly to pions and kaons with a steeply falling spectrum with increasing z. However, it turned out to be quite contrary, that is, the heavy hadron carries most of the quark energy-momentum. This is due to a kinematic effect by a massive quark, first postulated by Bjorken and Suzuki

[54]. The key feature here is that a heavy quark Q loses only a small fraction of its energy in forming a hadron containing the heavy quark, because of its large inertia or mass. This results in a "hard" distribution of the leading hadron energy, or a large mean value of z.

A.1.2 The Peterson model of heavy quark fragmentation

Peterson *et al.* introduced [55] an analytical form of the fragmentation function for the heavy quarks. The amplitude for a fast moving heavy quark Q to fragment into a hadron $H = Q\bar{q}$ and a light quark q (Figure A.1) is determined by the value of the energy transfer ΔE in the break-up process,

$$\begin{aligned} \Delta E &= E_H + E_q - E_Q, \\ \text{Amplitude}\,(Q \to H + q) &\propto \Delta E^{-1}. \end{aligned} \tag{A.4}$$

Expanding the energies using an approximation $m_H \sim m_Q$, we get

$$\begin{aligned} \Delta E &= \sqrt{m_H^2 + z^2p^2} + \sqrt{m_q^2 + (1-z)^2p^2} - \sqrt{m_Q^2 + p^2} \\ &\simeq zp + m_Q^2/2zp + (1-z)p + m_q^2/2(1-z)p - p - m_Q^2/2p \\ &\propto 1 - (1/z) - \epsilon_Q/(1-z). \end{aligned} \tag{A.5}$$

Introducing a factor $1/z$ for the longitudinal phase space, the following form is derived for the heavy quark fragmentation:

$$D_Q(z) = \frac{N}{z\,[\,1 - (1/z) - \epsilon_Q/(1-z)\,]^2}. \tag{A.6}$$

The parameter ϵ_Q is approximately m_q^2/m_Q^2, the ratio of the effective quark masses. The light quark mass m_q is expected to be of order of the nonperturbative strong interaction scale $\sim$ (1/2 to 1)m_ρ which gives $\epsilon_Q \sim$ (1/8 to 1/2)$/m_Q^2$. The function peaks at $z \simeq 1 - 2\epsilon_Q$ with a width $\sim \epsilon_Q$. This is illustrated in Figure A.2.

Although the Peterson model is very simple and includes only the kinematical con-

sideration, it describes the experimental data very well. The fragmentation of the heavy quarks is measured in e^+e^- experiments mainly in two ways. One is to use the inclusive leptons [60] which arise from the semileptonic decay of heavy quarks. The lepton momentum is dependent on the parent hadron momentum, and thus it enables us to extract information on the fragmentation. The other way is to use the charged multiplicity [61]. The contribution to the total multiplicity comes from the primary hadrons containing a heavy quark, and the remainder of the fragmentation. If the contribution from the primary hadrons is known, we can get information of the rest of the fragmentation. There is another way which is applicable to the charm quark fragmentation measurement. Heavy hadrons can be reconstructed in some decay modes, for example, D^{*+} meson in $D^{*+} \rightarrow D^0\pi^+$ followed by $D^0 \rightarrow K^-\pi^+$. In this method the momentum of a heavy hadron is directly obtained. But it is difficult to apply to bottom hadrons since the decay modes of bottom hadrons are much more complicated.

A compilation [56] of the various e^+e^- experiment results give $< z >_c = 0.67 \pm 0.02 \pm 0.02$ and $< z >_b = 0.83 \pm 0.01 \pm 0.02$, which correspond to the parameter ϵ_Q values

$$\begin{aligned} \epsilon_c &= 0.06^{-0.01-0.01}_{+0.02+0.02} \\ \epsilon_b &= 0.006^{-0.001-0.002}_{+0.001+0.002}. \end{aligned} \tag{A.7}$$

The ratio ϵ_c/ϵ_b gives a value of 10^{+4+5}_{-2-4}, in agreement with an expectation of about 10.

A.2 Bottom Quark Decays

Decay properties of bottom quark are extensively studied [62] by e^+e^- machines, as well as those of charm quark [63]. The hidden form of the bottom quark like three lowest states of the Υ resonances does not give any information on the bottom quark decay. We need the bare form of the bottom quark, particles with the net bottom quantum number. The $\Upsilon(4S)$ resonance gives such a chance, since it resides higher than the $B\bar{B}$ pair production threshold. The $\Upsilon(4S)$ resonance is considered to decay into a B meson

pair exclusively.

Let us consider B mesons, which consist of a bottom quark b and a light antiquark $\bar{q}$. A bottom quark b cannot decay into a lighter quark via the strong or the electromagnetic interaction, since they strictly conserve the flavor quantum number. Hence it can decay only via the weak interaction.

A weak decay of a heavy quark Q is proceeded by an emission of a virtual charged intermediate vector boson W^+ or W^-,

$$Q \rightarrow Q'W, \tag{A.8}$$

where Q' is a lighter flavor quark, followed by a decay of the W boson into either a lepton pair or a quark pair.

A.2.1 Kobayashi-Maskawa matrix

In the Standard Model of the electroweak theory [64], the transition amplitudes between quarks are proportional to the Kobayashi-Maskawa (KM) matrix [65] elements, which must be determined by the experiments. There are three known "generations" or "families" of quarks and leptons, each of which consists of a left handed weak isospin doublet and a right handed isospin singlet. (The sixth t quark is yet to be discovered, but nobody doubts its existence.) The matrix, V, which is an extension of the Cabbibo matrix [66], links weak eigenstates (d', s', b') and mass eigenstates (d, s, b) of quarks,

$$\begin{pmatrix} d' \\ s' \\ b' \end{pmatrix} = \begin{pmatrix} V_{ud} & V_{us} & V_{ub} \\ V_{cd} & V_{cs} & V_{cb} \\ V_{td} & V_{ts} & V_{tb} \end{pmatrix} \begin{pmatrix} d \\ s \\ b \end{pmatrix}. \tag{A.9}$$

The current experimental knowledge and the constraints from the unitarity of the matrix provide the limits [67] on the magnitudes of these complex elements on 90%

confidence level as

$$|V_{ij}| = \begin{pmatrix} 0.9747 \text{ to } 0.9759 & 0.218 \text{ to } 0.224 & 0.001 \text{ to } 0.007 \\ 0.218 \text{ to } 0.224 & 0.9734 \text{ to } 0.9752 & 0.030 \text{ to } 0.058 \\ 0.003 \text{ to } 0.019 & 0.029 \text{ to } 0.058 & 0.9983 \text{ to } 0.9996 \end{pmatrix}. \quad \text{(A.10)}$$

The off-diagonal elements are small, which means that transitions between different generations are relatively suppressed. Hence s and b quarks have longer lifetimes than c and possibly t, respectively.

A.2.2 Spectator model

A so-called "spectator model" is frequently used to describe a decay of a hadron with a heavy quark. Here a light quark q consisting a meson M together with a heavy quark Q is assumed not to contribute to the decay process at all, or behave as a passive "spectator", as illustrated in Figure A.3. In other words, the decay of heavy hadrons is regarded as the decay of the heavy quark. This model is considered to be a good approximation because the energy released by the decay is large enough compared to the confinement energy scale, which is of order of the ρ meson mass. This model provides amplitudes for various decay modes, and predicts that all hadrons containing the same heavy quark have the same lifetimes. This is not the case with D mesons, where non-spectator effects are considered to be large. Hadronic decays are in general subject to large correction by QCD effects, and are enhanced relative to the semileptonic decays. In semileptonic decays this model is expected to give more reliable predictions because there is no QCD effect between the final state leptons and quarks. In fact all the D mesons have the very similar semileptonic decay widths [68], although the total widths or the lifetimes are different.

To be specific, let us consider a bottom quark decay. First, there are two possibilities for b quark decay, that is, $b \to cW^-$ and $b \to uW^-$. Of these, the $b \to c$ transition dominates over the $b \to u$ transition with the KM-matrix elements given in Eq. (A.10).

At the other W vertex, the $W^- \to d\bar{u}, s\bar{c}$ transitions dominate over the $W^- \to s\bar{u}, d\bar{c}$ transitions for the same reason. Hence there are nine possibilities of b decay,

$$b \to c(e^-\bar{\nu}_e,\ \mu^-\bar{\nu}_\mu,\ \tau^-\bar{\nu}_\tau,\ d\bar{u},\ s\bar{c}), \tag{A.11}$$

with a color factor of three for quarks. The $\tau^-\bar{\nu}_\tau$ and $s\bar{c}$ channels are suppressed by the phase space factor of order 1/5 to 1/10. If we adopt 1/5 for these modes, the total decay width is expressed in analogy to muon decay as

$$\Gamma(b \to \text{all}) \simeq \frac{5.8\, G_F^2\, m_b^5}{192\,\pi^3}\, |V_{bc}|^2\, F(m_c^2/m_b^2), \tag{A.12}$$

where F is a phase space factor given by

$$\begin{aligned} F(x) &= 1 - 8x + 8x^3 - x^4 - 12x^2 \ln x, \\ F(m_c^2/m_b^2) &\simeq 0.5. \end{aligned} \tag{A.13}$$

The electronic or muonic decay branching ratio of b is predicted to be

$$Br(b \to e) \simeq 1/5.8 \simeq 0.17. \tag{A.14}$$

QCD corrections to the simple spectator model can be taken into account. These are expressed in Figure A.4. As seen in the figure, the corrections are important mainly in the hadronic decay modes and enhance them relative to the semileptonic modes by 10 to 15% [62].

A.2.3 Semileptonic b decays

Semileptonic decays of the bottom hadrons are expected to be well described by the spectator model, because no strong interactions can happen between the final state quarks and leptons.

Measurements on semileptonic decay branching ratios from the various groups are

now available for both at the $\Upsilon(4S)$ resonance [69] and at the continuum at PEP/PETRA [70]. The combined results give $11.6 \pm 0.6\%$ at $\Upsilon(4S)$ and $12.4 \pm 0.8\%$ at continuum. These values are smaller than the prediction of the spectator model, which indicates that nonleptonic channels are enhanced. At $\Upsilon(4S)$ only non-strange B mesons are produced. At higher energy continuum a mixture of various B-flavored hadrons is produced. The nearly equal semileptonic branching ratios at two energies suggest that all B hadrons have the similar semileptonic branching ratios, or that the mixture of hadrons at the continuum is not so different than that at $\Upsilon(4S)$, or both.

It is known that the b quark decays into c quark almost entirely. The charm contents in the semileptonic decays have been measured both inclusively and exclusively for non-strange B mesons [52]. Semileptonic $b \to c$ transitions are dominated by exclusive modes,

$$\bar{B} \to \ell^- \nu D, \tag{A.15}$$

$$\bar{B} \to \ell^- \nu D^*, \tag{A.16}$$

where D and D^* are pseudoscalar and vector charmed mesons. These two lowest lying charm states account for $64 \pm 10\%$ of the total semileptonic decays.

A.2.4 Nonspectator effects

A process where a light quark participates in the decay of a heavy hadron is called a nonspectator process. Examples of such processes are shown in Figure A.5, where a B meson produces a quark antiquark pair by annihilation into or by an exchange of a W boson. The annihilation process is restricted to the charged B meson, and the exchange process is restricted to the neutral one. In these diagrams initial states are spin-0, so light particle final states are suppressed by helicity conservation, in the same way as in the $\pi^\pm$ decay.

Another example of the nonspectator process is the $B^0\bar{B}^0$ mixing. This process can

occur by the box diagrams shown in Figure A.6. An evidence for the $B^0\bar{B}^0$ mixing is first reported by the UA1 collaboration [71] and the ARGUS collaboration [72].

Figure A.1: Schematic diagram of a heavy quark (Q) fragmentation into a a heavy meson (h_Q).

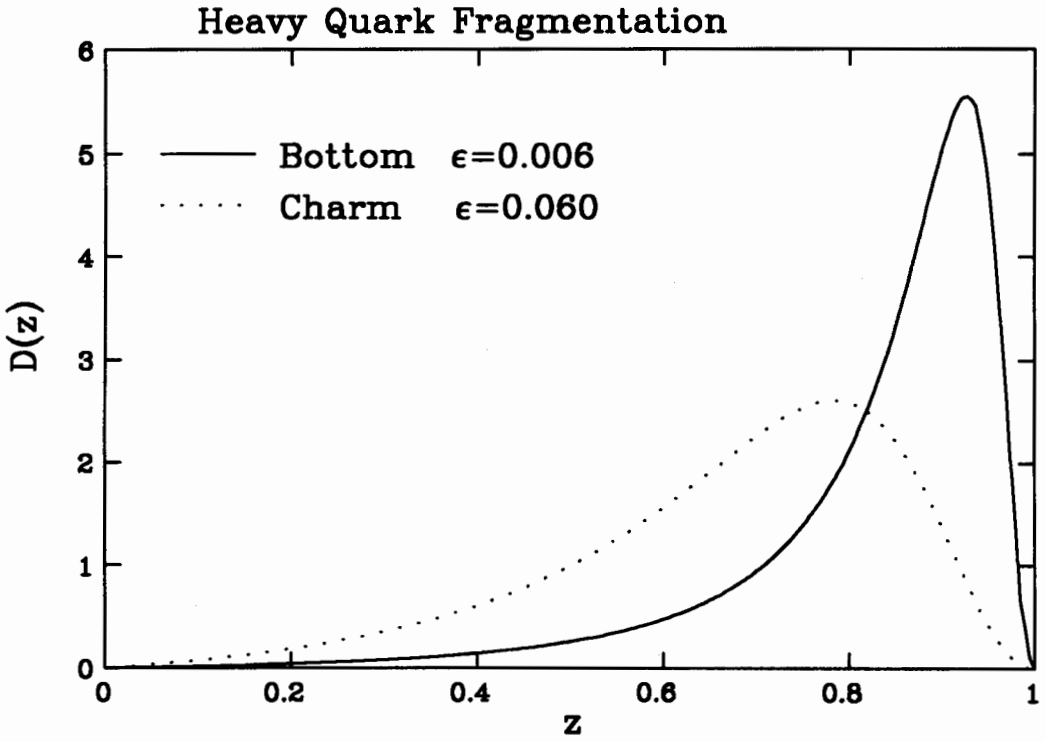

Figure A.2: The Peterson fragmentation function for heavy quarks.

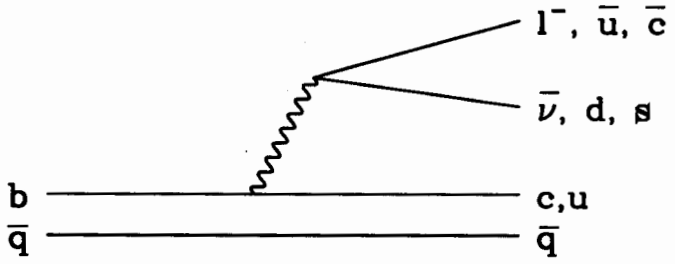

Figure A.3: Feynman diagram of the spectator decay of a heavy meson.

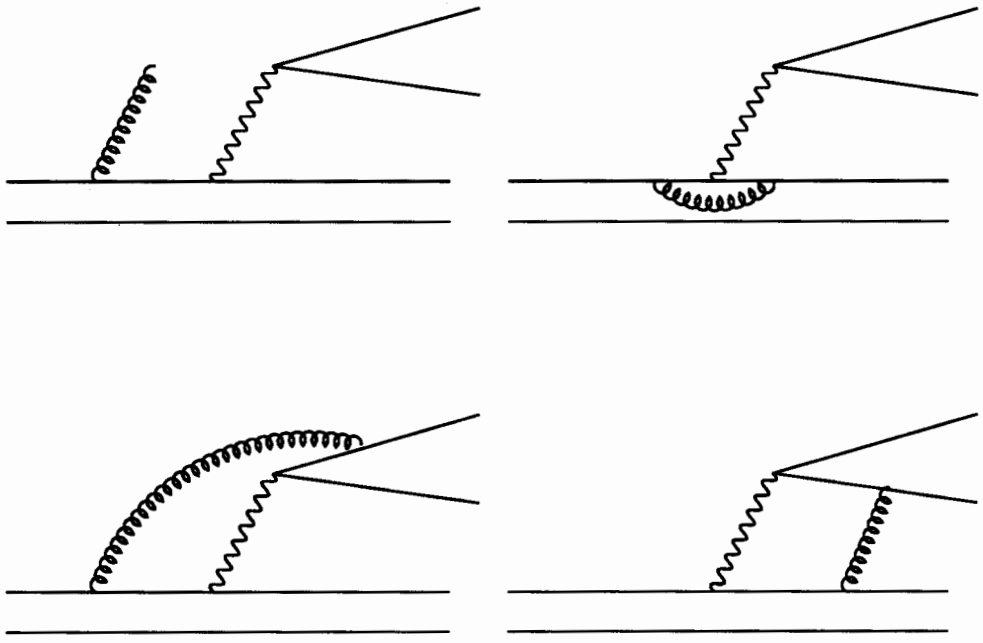

Figure A.4: QCD corrections to the simple spectator decays.

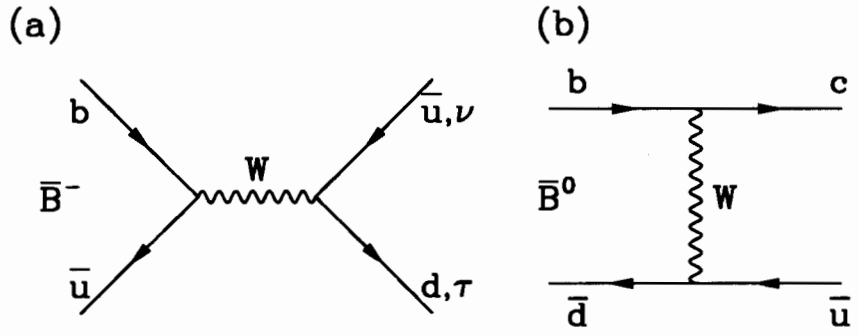

Figure A.5: Examples of non-spectator decay diagrams. (a) annihilation into W and (b) W exchange.

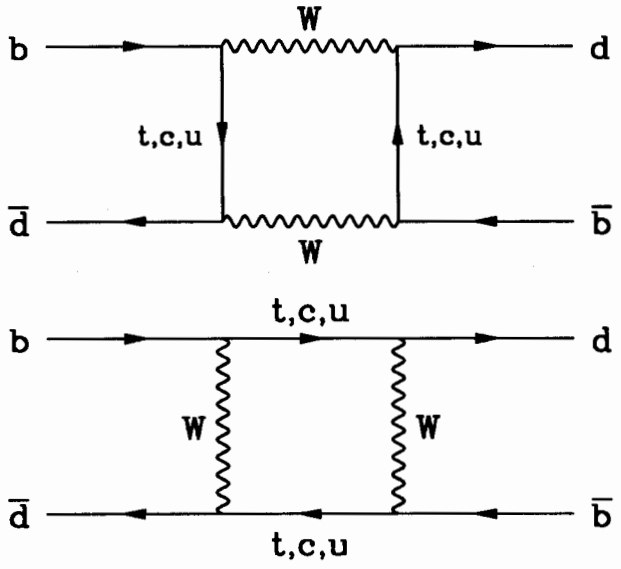

Figure A.6: Box diagrams responsible for the $B^0\bar{B}^0$ mixing.

Appendix B

Study of Hadron Showers

In this Appendix we describe a study of the longitudinal and lateral developments of low energy hadron showers in the central hadron calorimeter. It is aimed for the better understandings of the central electrons, their reconstruction efficiency and the backgrounds.

An example is the energy deposit on the hadron calorimeter. The hadronic leakage energy is used as a primary handle for the estimate of the charged hadron background faking prompt electrons. Therefore it is crucial to understand the behavior of hadrons well, especially at lower energies, where test beam data lack high statistics and quality.

It is also important to understand the lateral development of hadron showers. It is known that the hadron shower is larger than the electromagnetic shower. As we will see later the size is of order 10 cm, thus a hadron can deposit its energy on more than one calorimeter towers even with a relatively coarse segmentation of the CDF calorimetry. It means that a hadron near the electron can veto it through a cut on the hadronic energy fraction even if not in the same cell.

We investigate these features of hadron showers using real data at B0. Any data sample serves for this purpose, as long as it includes a track which is isolated, for example, within 3 by 3 calorimeter towers. We use events in tapes CC2615 and CC2616, which are triggered on a stiff track and therefore cover a wide range of the transverse

momentum (p_T) spectrum with reasonably high statistics.

A good track is selected as follows. We start with a three-dimensionally reconstructed CTC track which points to the central calorimeter (towers 0-8). The minimum p_T of 1 GeV/c is required for the track. We use 3 by 3 calorimeter cells around the seed tower. In order to minimize contamination of other particles on the calorimeter cells we require there be no additional tracks pointing to the 9 towers.

The calorimeter energy associated with the track is defined by 9 tower sum for the hadronic component and three tower sum in a single wedge for the electromagnetic component. The center tower is defined by the extrapolated track position on the CES plane, with the wedge alignment correction [37] applied.

B.1 Longitudinal shower development

The longitudinal development of hadron showers, the sharing of the energy between the electromagnetic and hadronic components, is one of the separation variables of hadrons from electrons. It is important to understand the behavior of hadrons, especially at lower energy.

First we check the total energy distribution. Figures B.1 and B.2 show the distributions of the sum of the electromagnetic and hadronic calorimeter energies divided by the track momentum (E_{TOT}/p), for different track momentum ranges. They are behaving reasonably; The distributions are rather wide, the peak shifts downward as the momentum decreases (non-linearity). One thing we do not understand well is spikes at zero calorimeter energy, which become more noticeable for the lowest momentum tracks. Probably some of them are caused by fake tracks, others may be a true effect. For example, a hadron with very low momentum may lose its energy in the coil before reaching the calorimeter.

Next we look at the energy sharing between the electromagnetic and hadronic components. Figures B.3 and B.4 show the distributions of the ratio of hadronic to total energy

($E_{\rm HAD}/E_{\rm TOT}$) for the same tracks as in the previous plots. For higher momentum tracks peaks near 100% hadronic energy, or minimum ionizing on the electromagnetic calorimeter, are clear. The other "flat" part of the distribution corresponds to those hadrons which started showering earlier in the calorimeter. As we go down in momentum, the fraction of these early showers increases. At the lower end of the momentum spectrum we observe zero hadronic energy at a fair fraction of the time. This may be partly due to lower photoelectron statistics of the hadron calorimeter (about 10/GeV/tube) and an MX digitization cutoff at 10 ADC counts (about 60 MeV). Others may be due to photon conversion electrons.

Figures B.5 and B.6 show the blowups of the same distributions in the region which is relevant to electron analyses. We again note that the distributions of $E_{\rm HAD}/E_{\rm TOT}$ for the hadrons of the momentum of 10 GeV and above are flat or have only a slight slope and do not peak at 0. Here we have applied no "electron" cuts to these hadrons, like CES χ^2 cuts and an implicit CES pulse height requirement in track-shower matching. Those cuts can in principle change the shape of the $E_{\rm HAD}/E_{\rm TOT}$ distributions.

B.2 Lateral shower development

A CTC track points to a random point on the surface of the calorimeter. When a charged hadron comes close to a tower boundary it can deposit its energy on multiple towers. A collection of many tracks effectively scans across the boundary and enables us to measure the shower shapes.

Suppose we observe energy H_1 (H_2) on tower 1 (2), where towers 1 and 2 are any pair of towers sharing a boundary. We can always normalize so that H_i represents a fraction. And suppose that a track hits a point on tower 1 with the distance x to the boundary. We make x positive definite. The energy fraction H_2 is the shower fraction

	$r\phi$ view			z view		
$E_{\rm EM}/E_{\rm TOT}$	λ (cm)	I_0	χ^2/dof	λ (cm)	I_0	χ^2/dof
0.00 - 0.25	6.0 ± 0.2	0.025 ± 0.002	39.7/23	7.1 ± 0.4	0.037 ± 0.008	10.4/10
0.25 - 0.50	8.7 ± 0.4	0.041 ± 0.004	42.2/23	9.9 ± 1.1	0.032 ± 0.002	12.3/10
0.50 - 0.75	12.1 ± 0.7	0.050 ± 0.006	12.9/23	10.0 ± 1.3	0.098 ± 0.002	17.6/10
0.75 - 1.00	13.9 ± 1.0	0.096 ± 0.009	47.3/23	7.3 ± 1.3	0.188 ± 0.020	31.9/10

Table B.1: Lateral size of hadron showers as a function of the electromagnetic energy fraction.

integrated over the distance from the shower centroid between x and infinity

$$H_2 = I(x) \equiv \int_x^\infty \rho(x')\,dx', \tag{B.1}$$

where ρ is the shower density which is normalized to unity

$$\int_{-\infty}^{\infty} \rho(x')\,dx' = 1. \tag{B.2}$$

With this definition we have $I(0) = 0.5$.

As mentioned earlier we use 3 by 3 calorimeter towers, which gives three lateral samplings each direction, z or $r\phi$. The track points to the central tower in both directions by definition. Then we have three energy fractions for a given event, H_1, H_2 and H_3, integrated over the other direction, and only two of them are independent. We cover the distance of 48.5 cm (24 cm) along $r\phi$ (z) direction.

We consider only the hadronic component of the calorimeter. The integral shower shape thus obtained is plotted in Figures B.7 and B.8 for four different ranges of the electromagnetic energy fraction ($f_{\rm EM} \equiv E_{\rm EM}/E_{\rm TOT}$). Solid lines show a fit to a single exponential function

$$I(x) = I_0 + (0.5 - I_0)\, e^{-x/\lambda} \tag{B.3}$$

with an attenuation length λ. An offset I_0 is introduced in order to account for a uniform underlying energy, which is presumably due to neutral hadrons. The fitting results of

momentum	$r\phi$ view		
(GeV/c)	λ (cm)	I_0	χ^2/dof
1 - 2	10.7 ± 0.3	0.124 ± 0.003	34.6/23
2 - 3	10.0 ± 0.6	0.094 ± 0.006	17.5/23
3 - 5	9.8 ± 0.6	0.075 ± 0.005	39.6/23
5 -	8.2 ± 0.2	0.034 ± 0.002	46.3/23

Table B.2: Lateral size of hadron showers as a function of the track momentum.

the shower size are given in Table B.1.

The hadron showers are larger than the electromagnetic showers, which are only a couple of cm wide (Chapter 3.1.1). Figure B.10(a) shows that the size depends modestly on the electromagnetic energy fraction $f_{\rm EM}$. This could be explained qualitatively in the following way. A smaller (larger) electromagnetic fraction means that the hadron component samples the earlier (later) stage of the longitudinal shower development. The observed tendency is that the lateral shower size becomes larger as the shower develops longitudinally. A fit of the observed data to a straight line gives

$$\lambda = (4.85 \pm 0.22) + (10.67 \pm 0.85)\ f_{\rm EM} \quad \text{(cm)}. \tag{B.4}$$

Here we have used the $r\phi$ view, although the other view is equally valid.

Next we check the energy dependence of the shower size. Figure B.9 shows the shower shapes for tracks with different momentum ranges. These are averaged over the electromagnetic energy fraction. Lines are again a fit to an exponential, whose results are given in Table B.2. We observe a slight dependence of the shower size on the track momentum, as shown in Figure B.10(b), which may arise indirectly from the energy dependence of the average electromagnetic energy fraction.

B.3 Monte Carlo implementation

Now we turn to the application of the study for a practical use, that is, to simulate hadron showers with a reasonable accuracy for the Monte Carlo events. We first create a data file containing the hadron shower information. Each record corresponds to a charged track observed in the real data, and consists of the electromagnetic and hadronic energy deposits and the track momentum. When we simulate a hadron shower, we read in a record from the file and put it onto the Monte Carlo event. This way various distributions, including correlations among them, are reproduced almost by definition. The energy dependence is taken care of by choosing a track of a similar momentum.

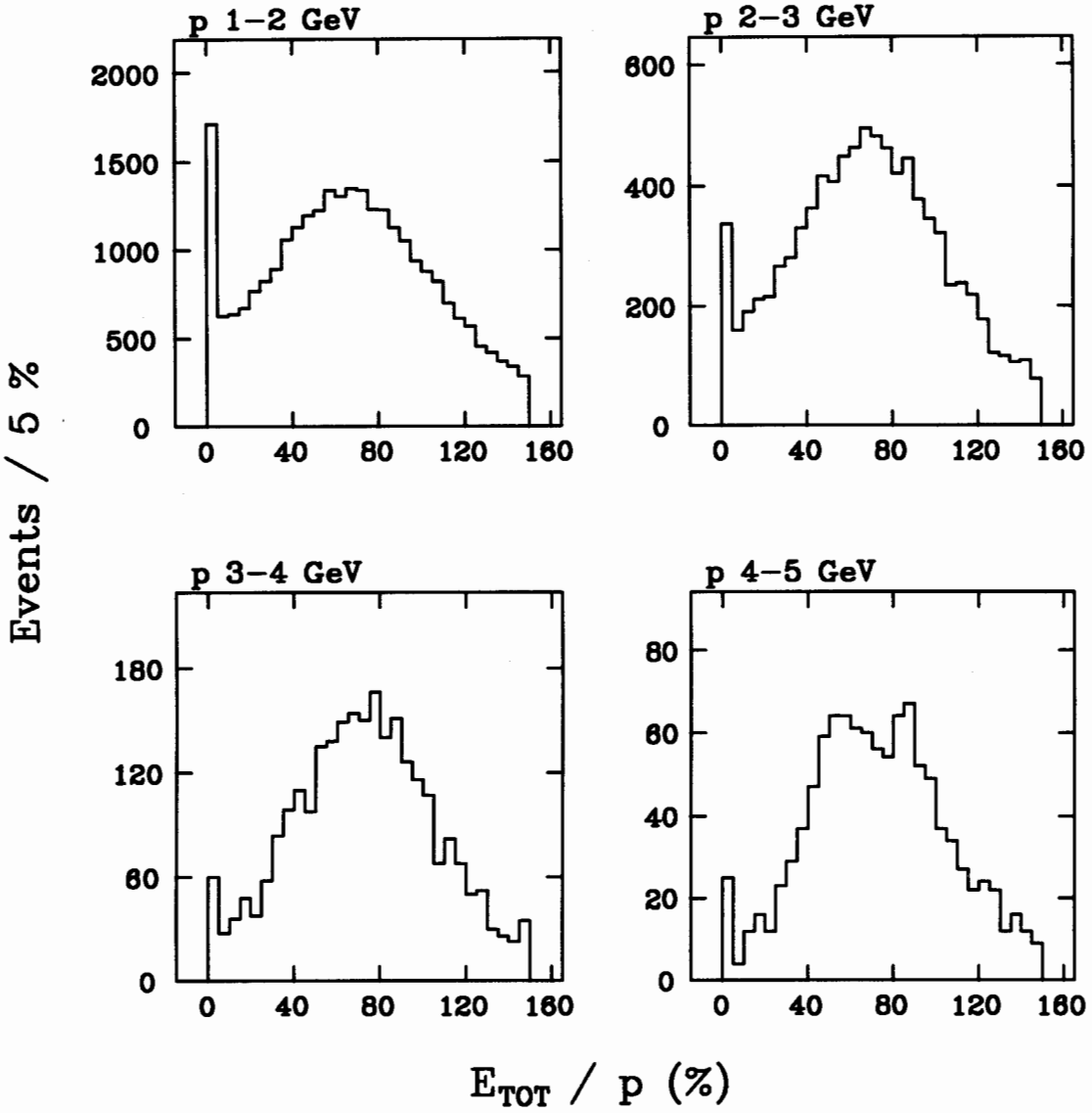

Figure B.1: The ratio of the calorimeter energy to the track momentum for lower momentum tracks.

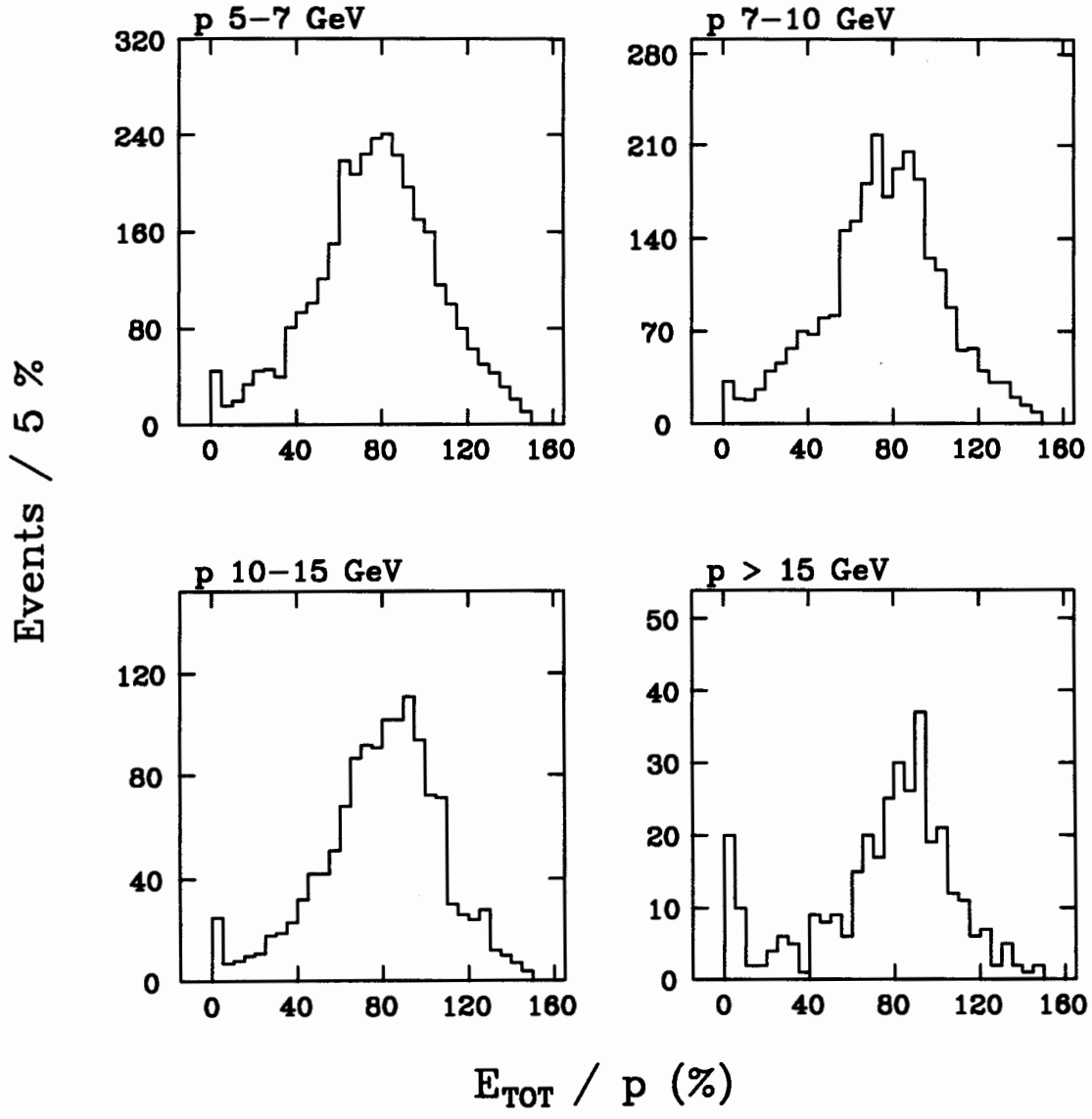

Figure B.2: The ratio of the calorimeter energy to the track momentum for higher momentum tracks.

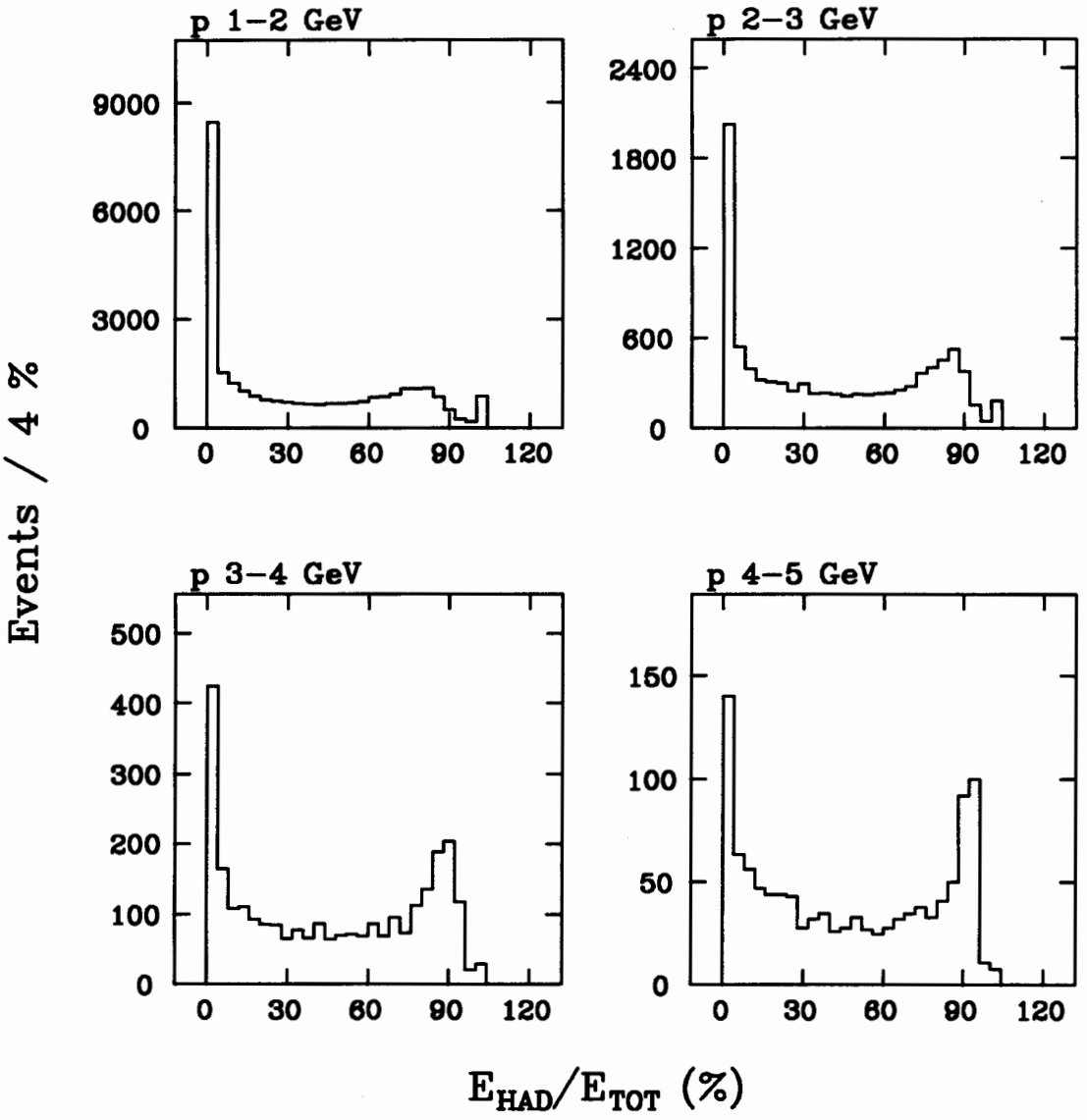

Figure B.3: The fraction of hadronic energy for lower momentum tracks.

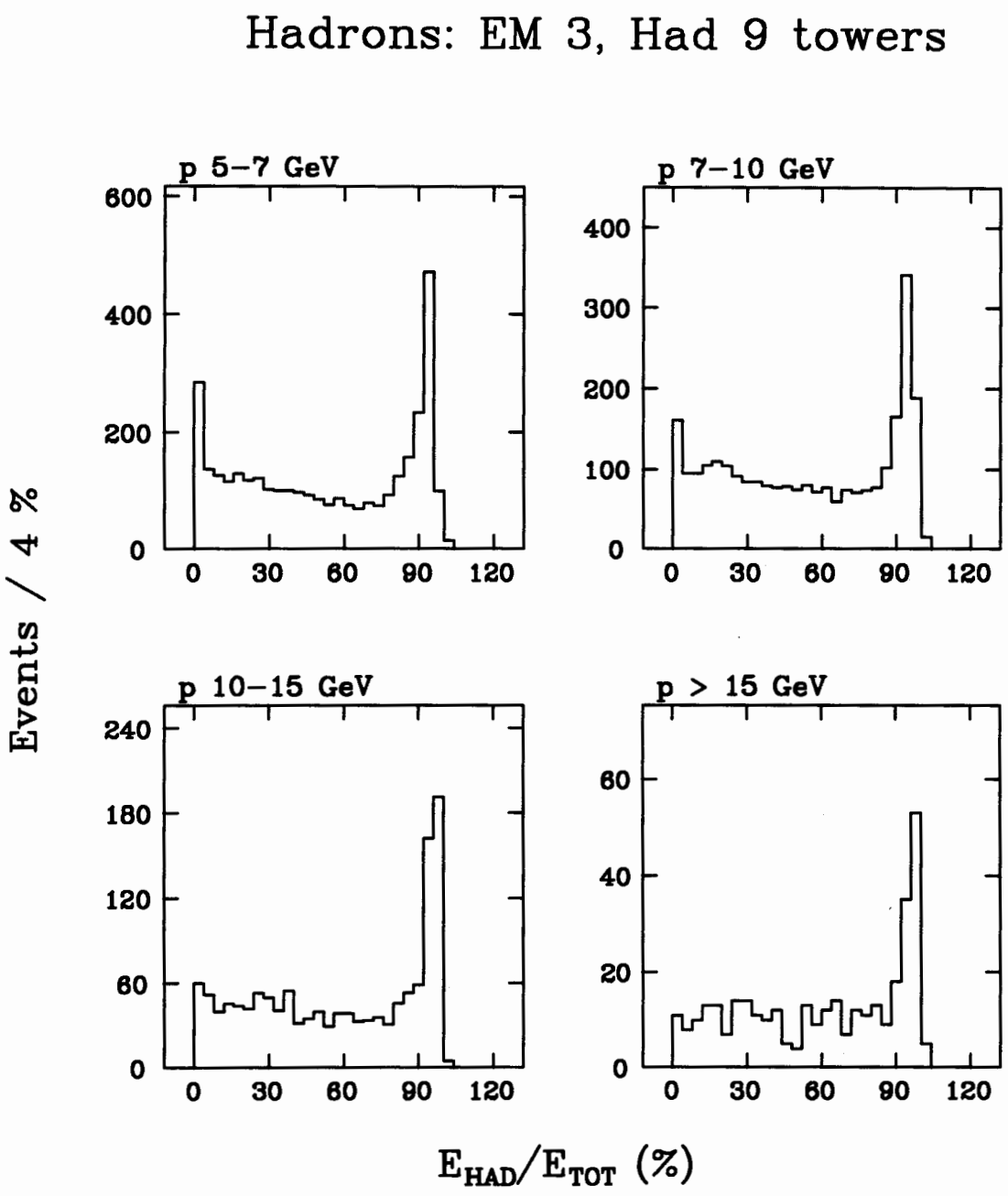

Figure B.4: The fraction of hadronic energy for higher momentum tracks.

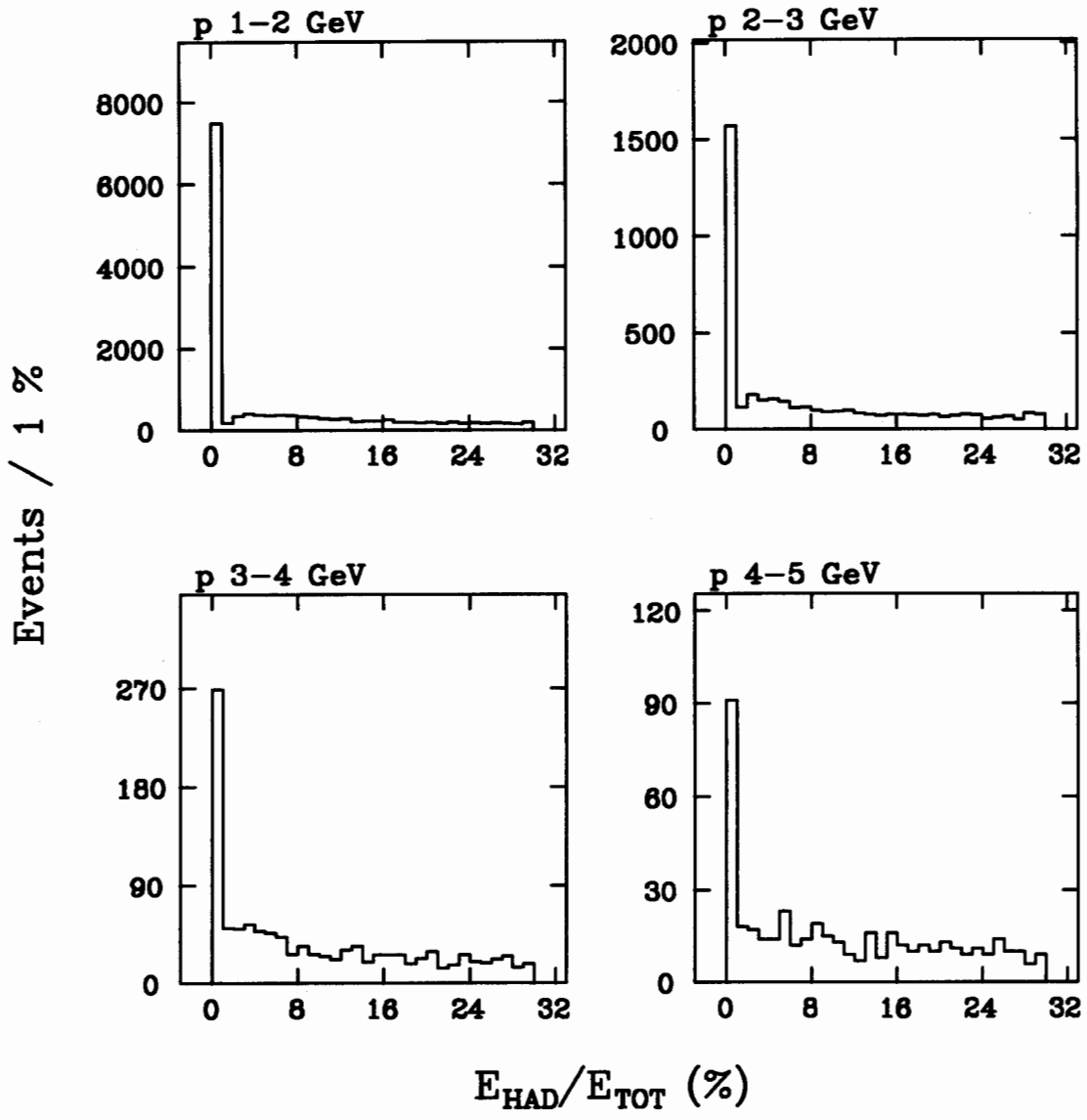

Figure B.5: The blowups of the hadronic energy fraction distributions for lower momentum tracks.

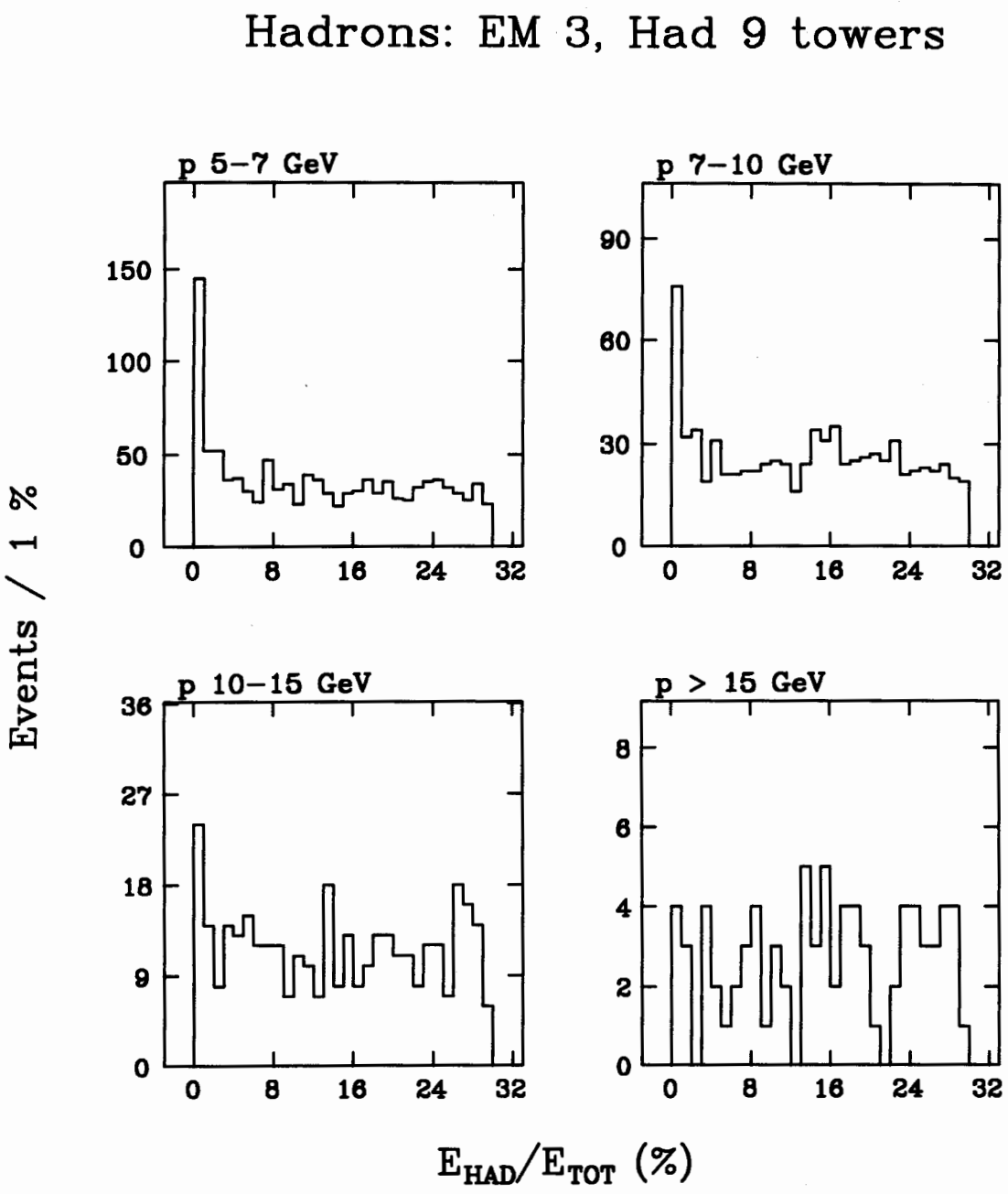

Figure B.6: The blowups of the hadronic energy fraction distributions for higher momentum tracks.

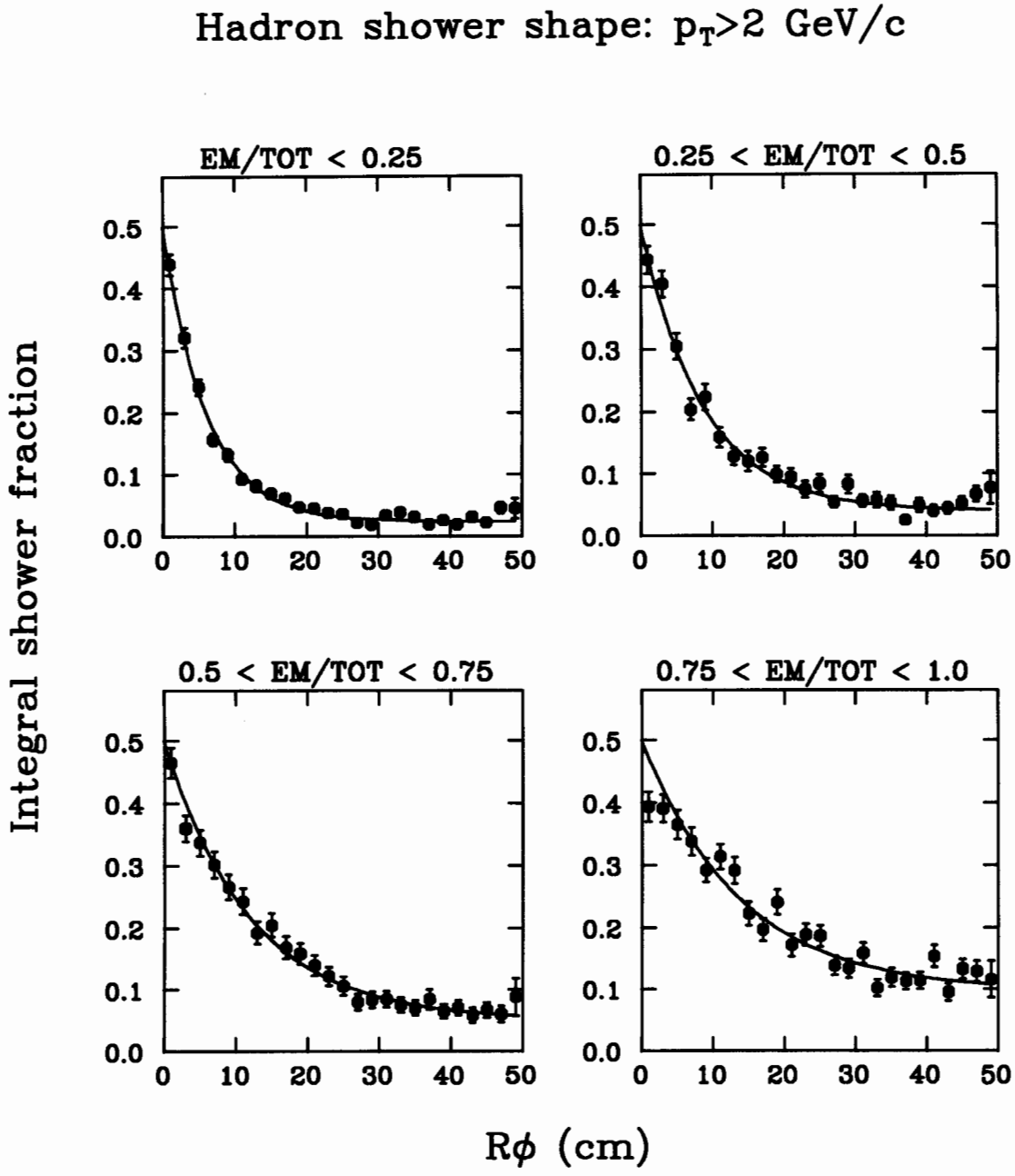

Figure B.7: Integral shower shapes on CHA in $r\phi$ view for different electromagnetic energy fractions.

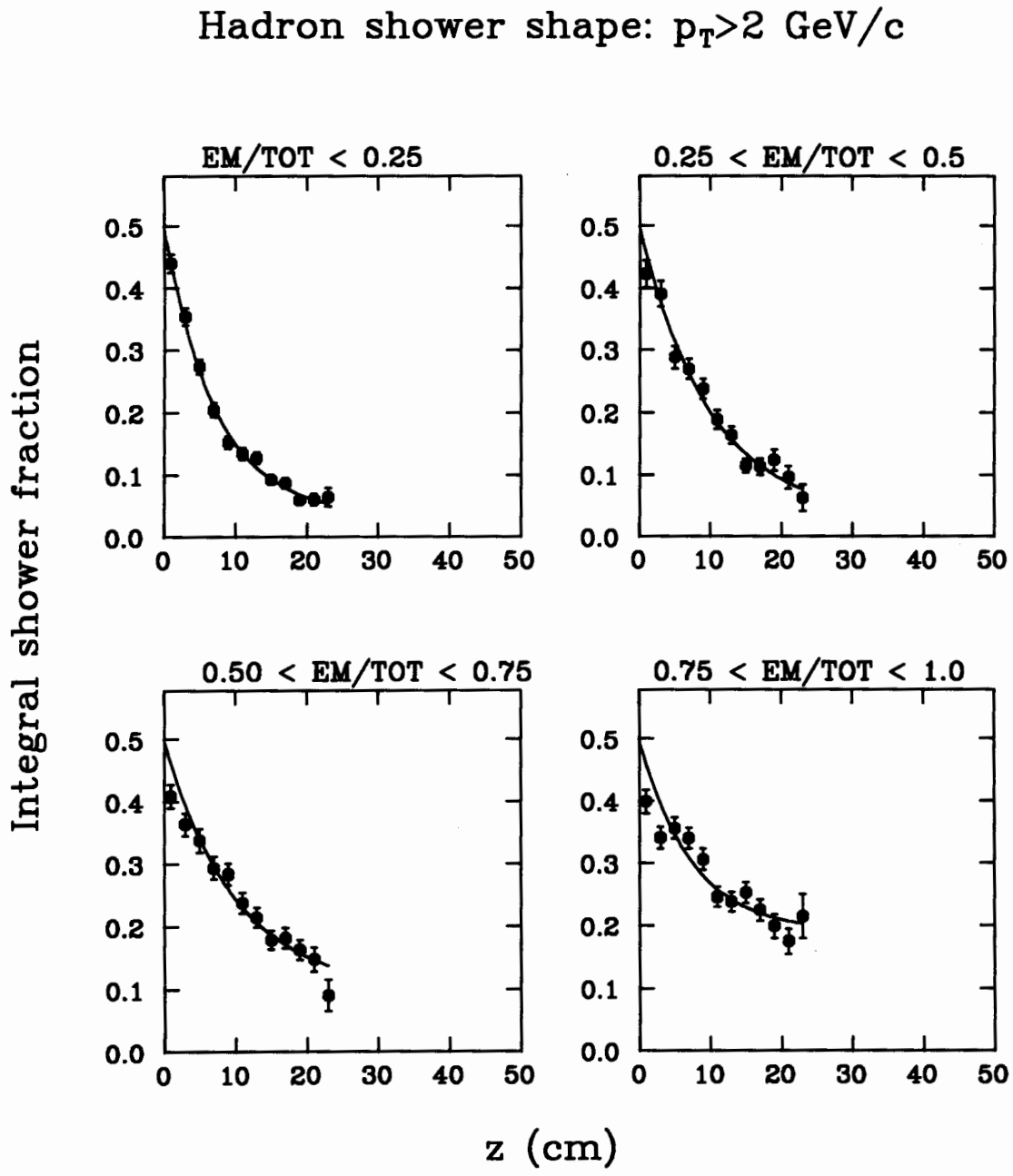

Figure B.8: Integral shower shapes on CHA in z view for different electromagnetic energy fractions.

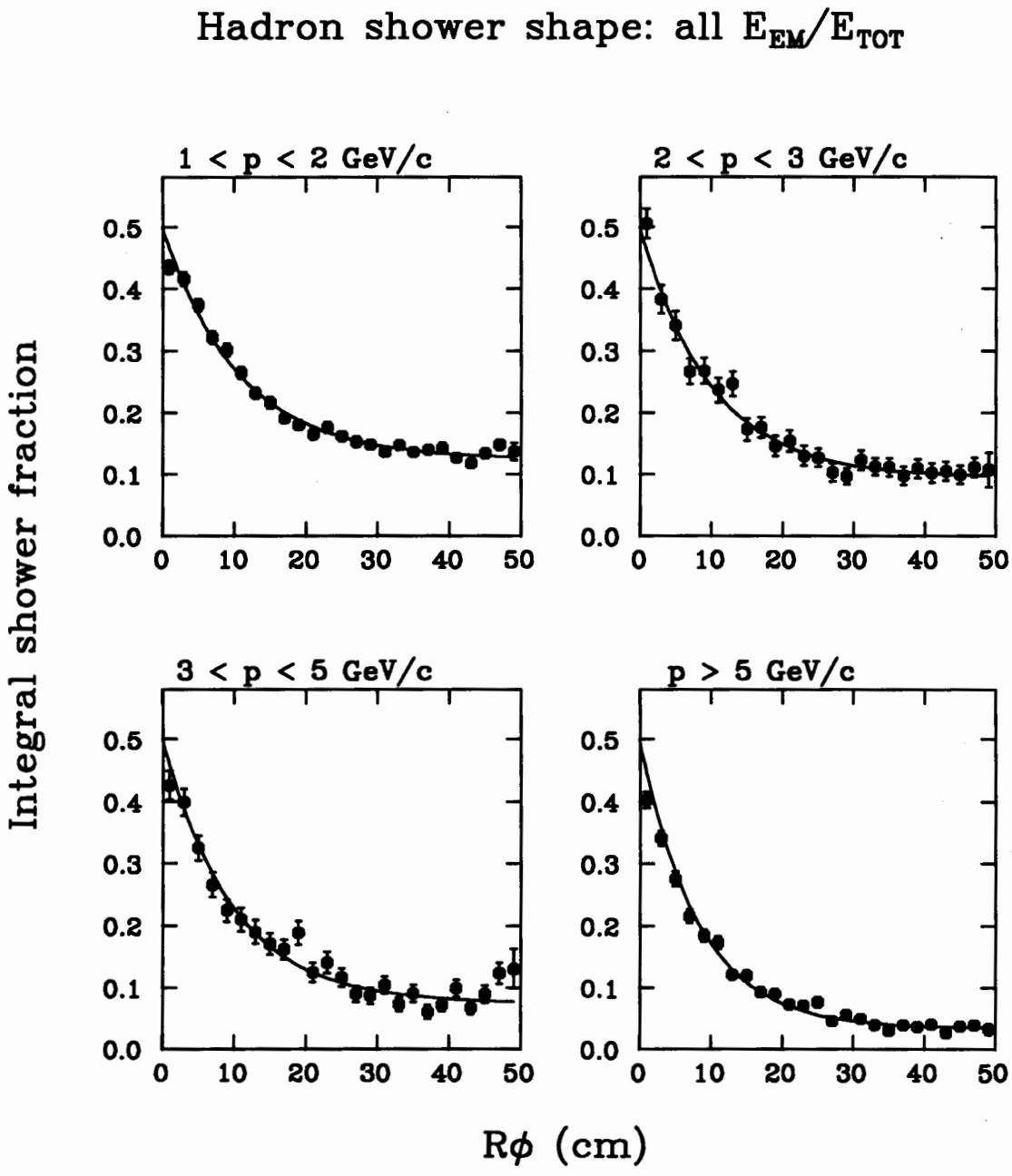

Figure B.9: Integral shower shapes on CHA in $r\phi$ view for different track momenta.

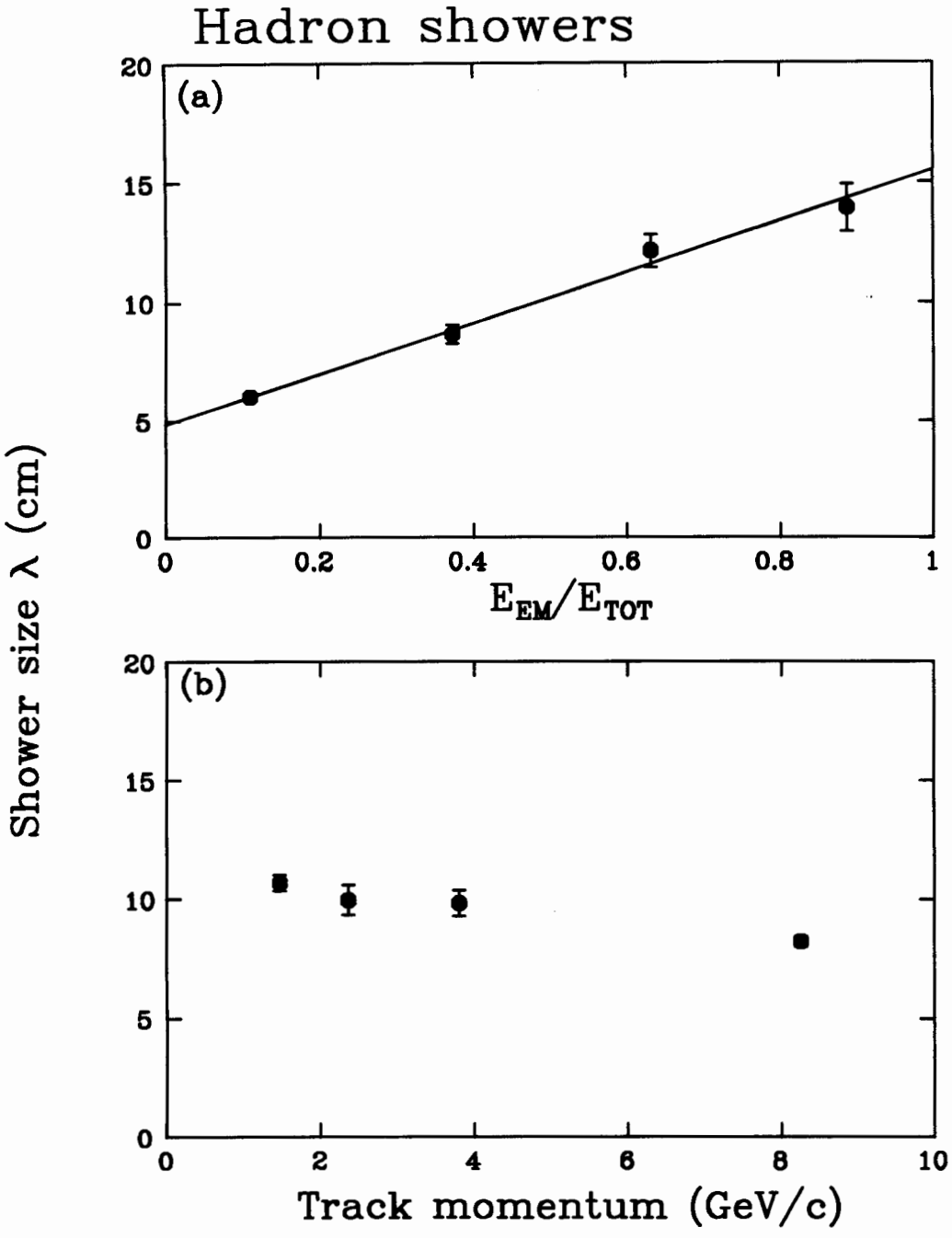

Figure B.10: Hadron shower size λ (in $r\phi$ view) as a function of (a) the electromagnetic energy fraction and (b) the track momentum.

Appendix C

CES Shower Shape and its Gain Dependence

In this Appendix, we describe a study of electromagnetic showers on the CES using test beam electrons. Data were taken during the 1987-88 fixed target run at the MT6 beam line [75].

A detailed knowledge of electromagnetic showers is important not only for the electron analyses, but also for the prompt photon production studies, for example, where a tighter cut on the CES χ^2 is applied. Here we consider shower shapes when we change the operational gain of the CES chambers.

Shapes of electron showers at various chamber gains are measured using 50 GeV/c test beam electrons, at four anode high voltage settings, 1360 V, 1420 V, 1470 V and 1525 V. [1]

We use the integral shower shape I, which we defined in Section 3.1.1. We measure the shower using seven wires, where the center channel has the maximum pulse height, which accounts for typically 70% of the shower. The strip view is equally valid, except for the presence of an asymmetry [76] in the shower shape on two sides with respect to the center. The origin of the asymmetry is the difference in the amount of materials

[1] In the 1988-89 run, CES was operated at 1450 V.

an electron traverses through until it reaches the CES depth, because of the slanted electron incidence with respect to the CES plane.

In order to get the shower center, we use the extrapolated beam position at the CES depth, obtained using the beam chamber hits on an event-by-event basis.

We show the obtained shapes in Figures C.1 through C.4. Curves are a two component exponential function. They are not the fit to data, but all are the same single curve representing the parameterization we usually use for the CDF analyses, determined based on 1985 test beam measurements.

We observe that data points lie below the curve for lower high voltage settings, then almost coincide, and finally become higher than the curve. In other words, the shower width becomes larger as the chamber gain increases.

To further investigate this effect, we show in Figure C.5 the CES pulse heights as a function of the applied high voltage. For 50 GeV/c test beam electron showers, we used seven channels around the highest pulse channel in an event. We plot three pulse heights, the pulse height of the center channel, the sum of the other six channels, and the sum of all seven channels. All points are normalized at 1360 V. A CES channel is typically 1.5 cm wide, and then the center channel sees a core of an electromagnetic shower or a high charge density. The outer channels observe a lower density. The gain slope is steeper for the lower shower density. The data points give

$$G \propto e^{V/78} \tag{C.1}$$

for the outer channels. On the contrary, we get

$$G \propto e^{V/87} \tag{C.2}$$

for the center channel. Shown by a solid line is the gain measurement using ^{55}Fe source peaks, with which we can by no means get high charge densities. It shows a good agreement with the behavior of the outer channels.

We think that a gas saturation is observed at the central channel, or at high charge densities. This can result in an energy dependent shape of the electron showers. When we consider the intrinsic shape of electromagnetic showers and its energy dependence, we would expect a narrower shower with increasing energy because of the energy dependence of the Bremsstrahlung emission angle. The gas saturation effect may compensate this and can result in a weaker energy dependence of the effective shower shape on the detector by choosing an optimal gain. Indeed we have obtained almost no energy dependence of the shower size as discussed in [76].

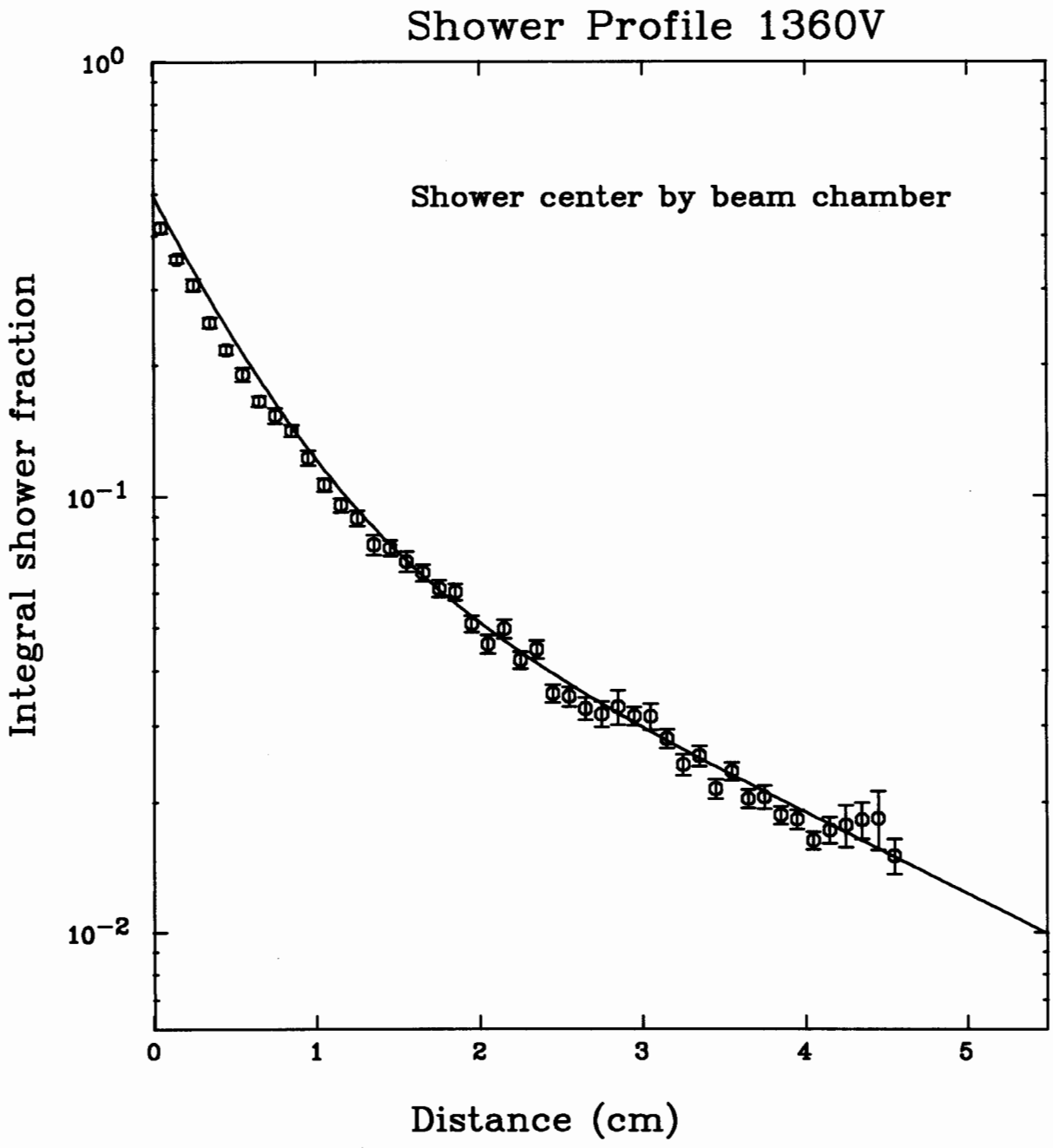

Figure C.1: CES shower shape I of 50 GeV test beam electrons at the anode voltage of 1360 V.

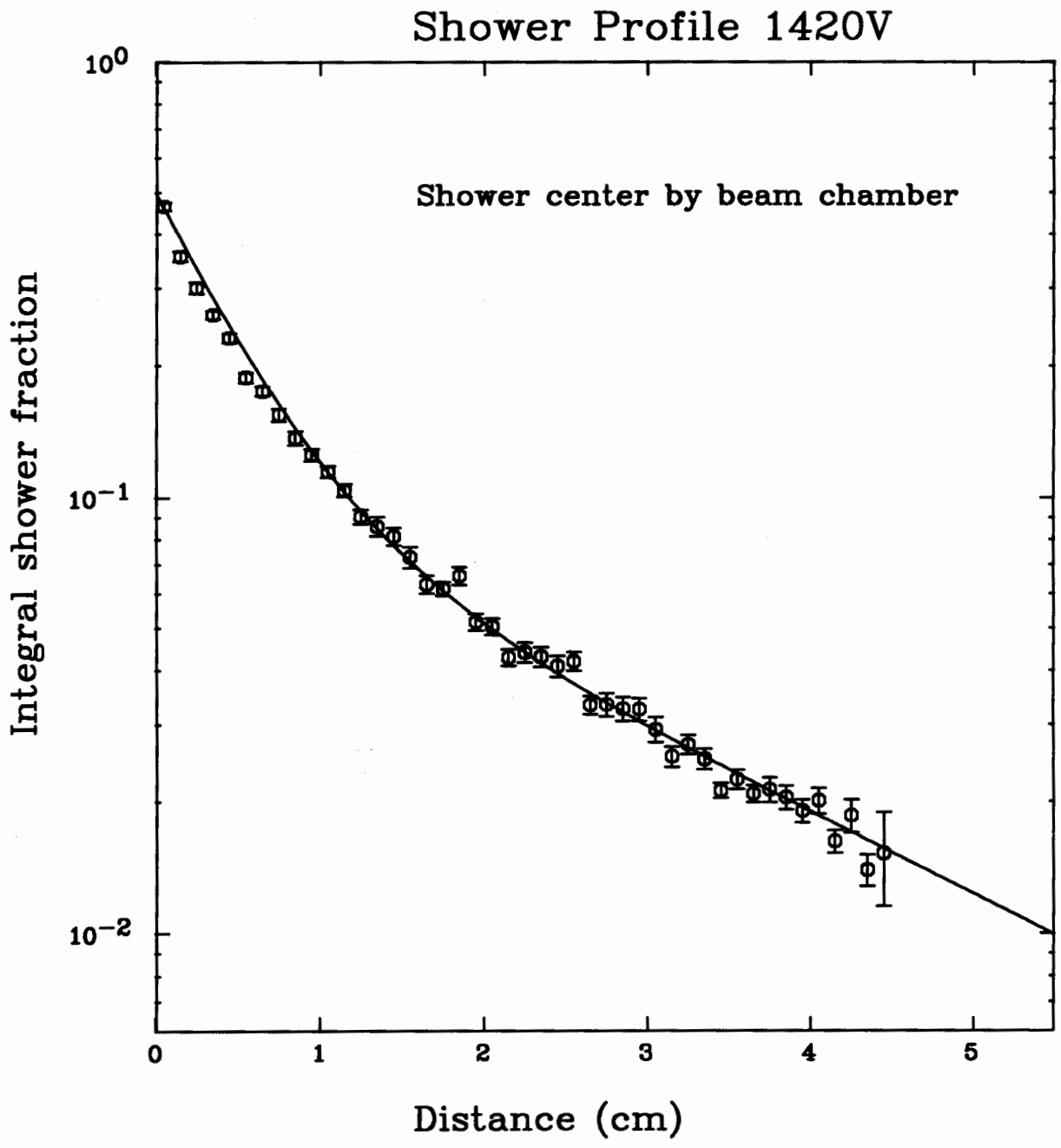

Figure C.2: CES shower shape I of 50 GeV test beam electrons at the anode voltage of 1420 V.

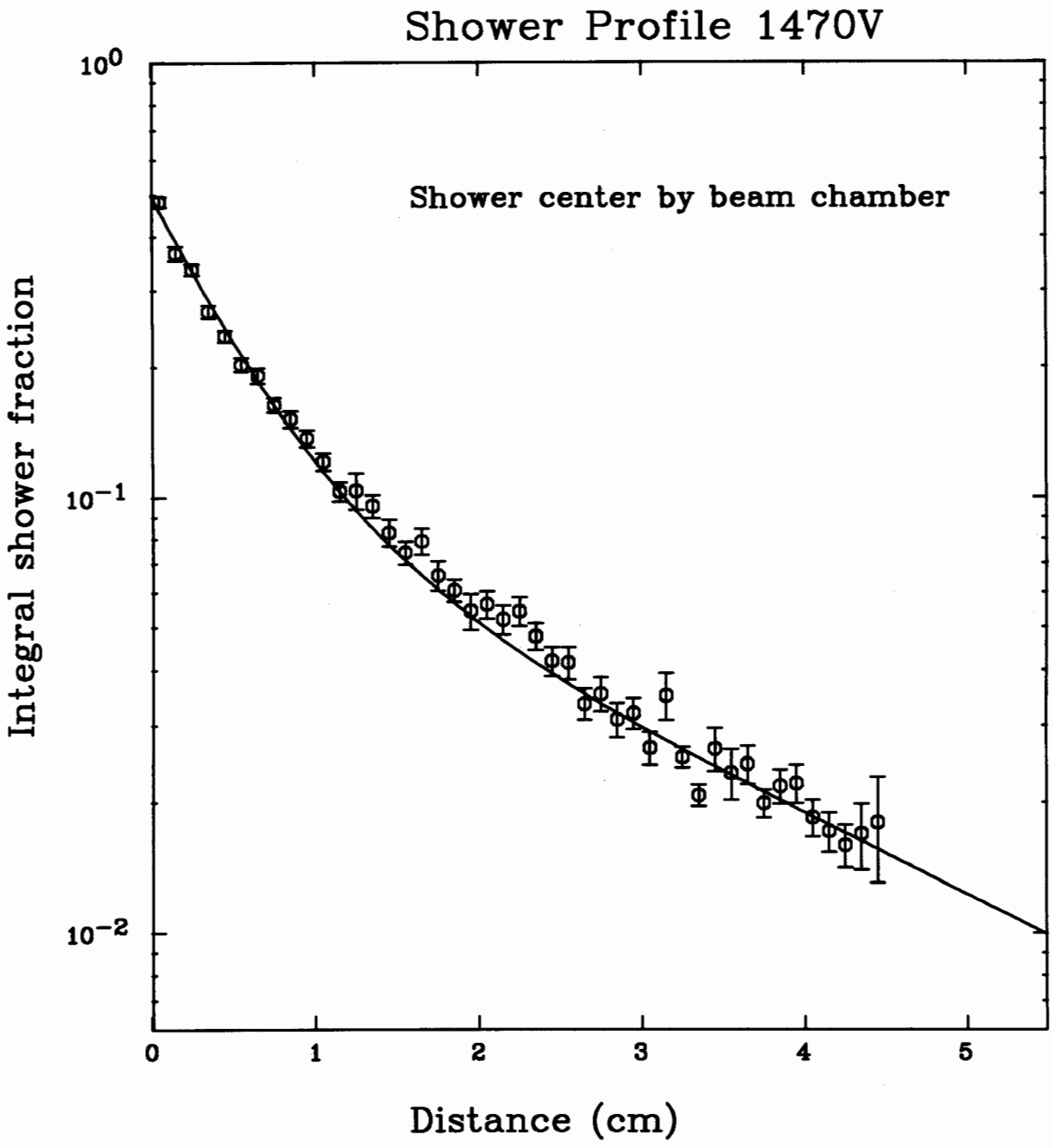

Figure C.3: CES shower shape I of 50 GeV test beam electrons at the anode voltage of 1470 V.

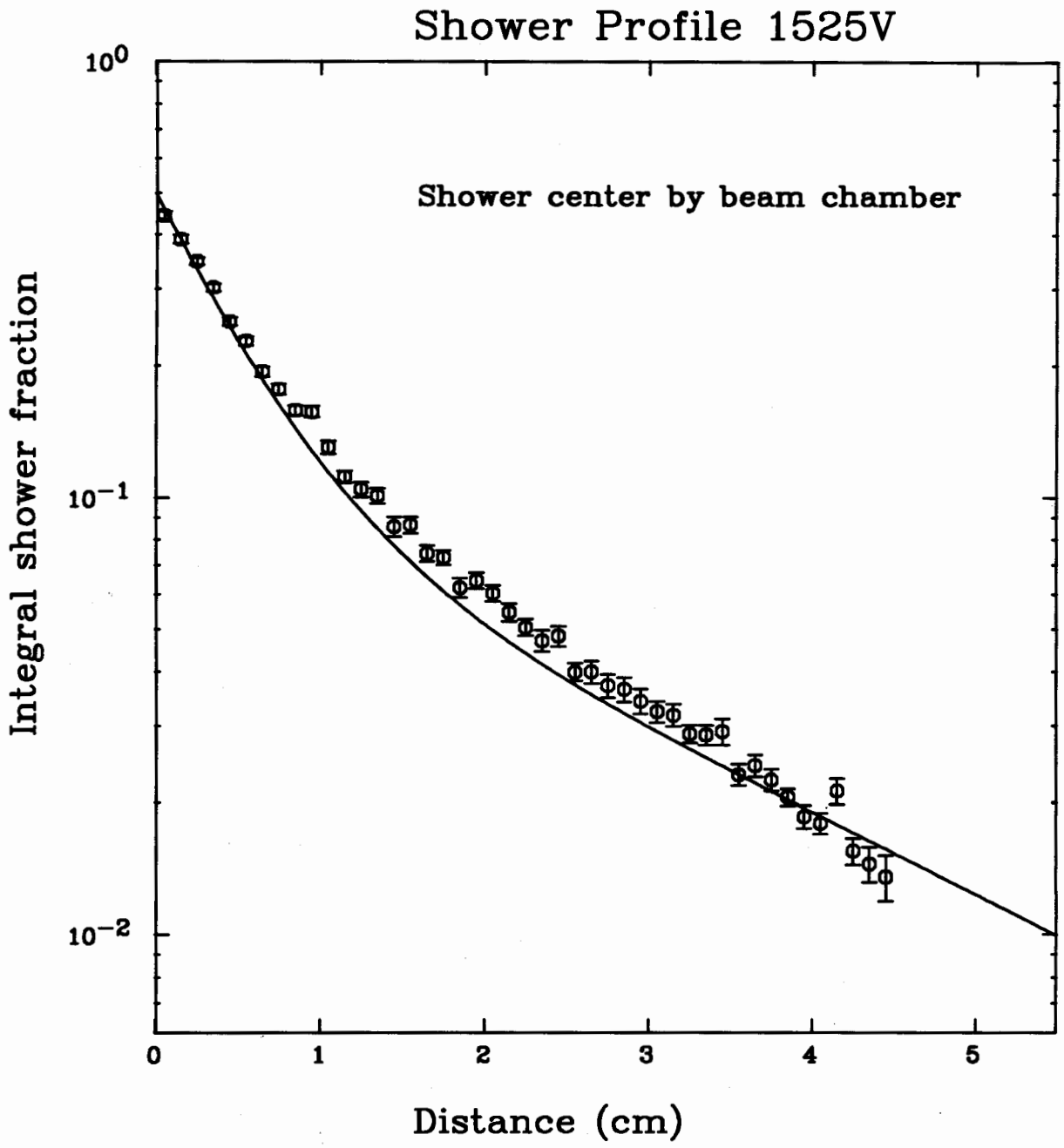

Figure C.4: CES shower shape I of 50 GeV test beam electrons at the anode voltage of 1525 V.

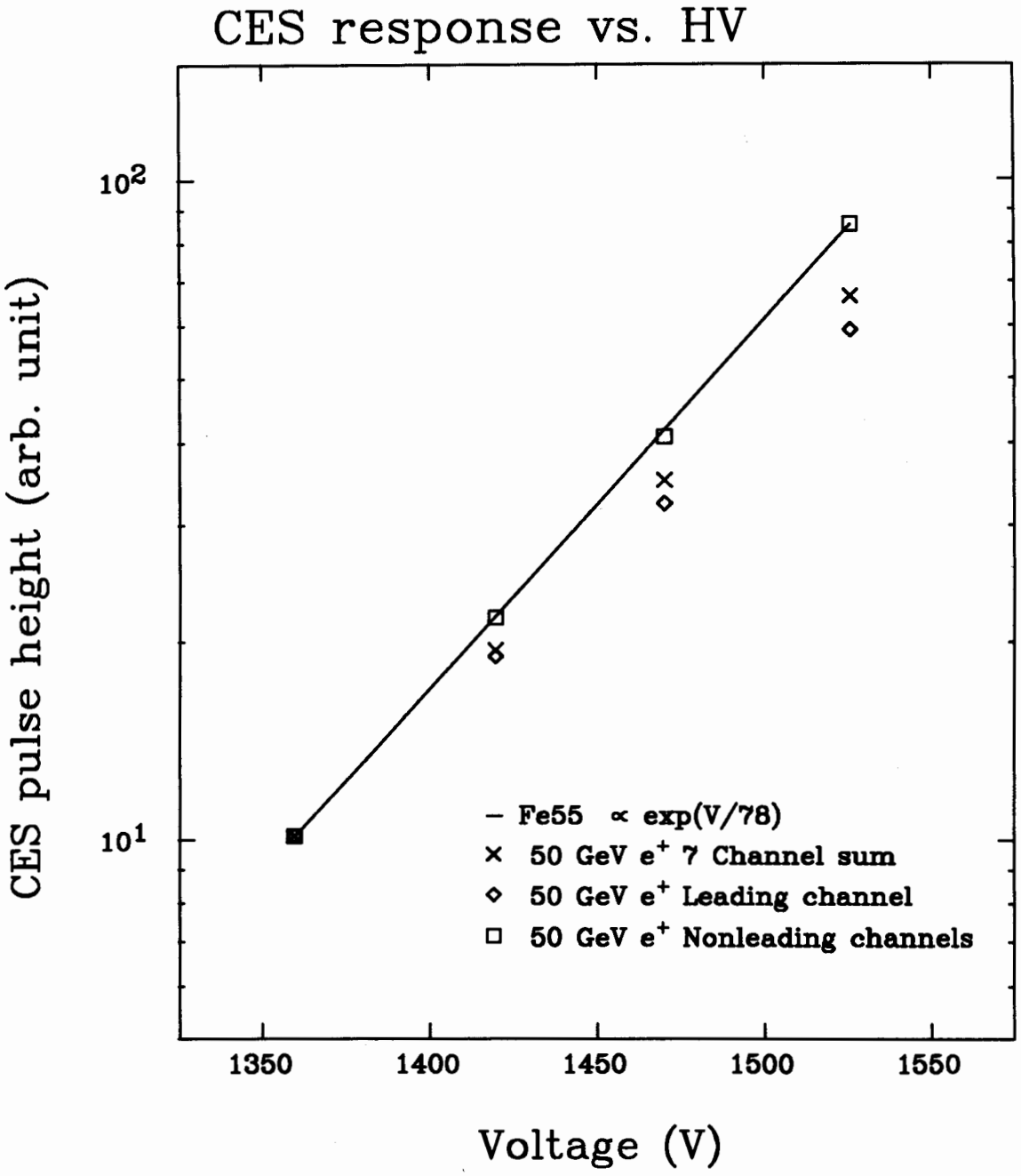

Figure C.5: CES chamber gain as a function of the applied anode voltage.

Bibliography

[1] J. J. Aubert *et al.*, Phys. Rev. Lett. 33 (1974) 1404.
J.-E. Augustin *et al.*, Phys. Rev. Lett. 33 (1974) 1406.

[2] G. Goldhaber *et al.*, Phys. Rev. Lett. 37 (1976) 255.
I. Peruzzi *et al.*, Phys. Rev. Lett. 37 (1976) 569.

[3] S. W. Herb *et al.*, Phys. Rev. Lett. 39 (1977) 252.

[4] C. Berger *et al.*, Phys. Lett. 76B (1978) 243.
C. W. Darden *et al.*, Phys. Lett. 76B (1978) 246.
J. K. Bienlein *et al.*, Phys. Lett. 76B (1978) 360.
C. W. Darden *et al.*, Phys. Lett. 78B (1978) 365.
D. Andrews *et al.*, Phys. Rev. Lett. 44 (1980) 1108.
T. Bohringer *et al.*, Phys. Rev. Lett. 44 (1980) 1111.

[5] D. Andrews *et al.*, Phys. Rev. Lett. 45 (1980) 219.
G. Finocchiaro *et al.*, Phys. Rev. Lett. 45 (1980) 222.

[6] W. Marciano and H. Pagels, Phys. Rep. 36 (1978) 137.

[7] R. P. Feynman, Phys. Rev. Lett. 23 (1969) 1415; *Photon Hadron Interactions*, W. A. Benjamin, Reading, Mass. (1972).

[8] Y. Yamaguchi, Il Nuovo Cimento 43A (1966) 193.
S. D. Drell and T.-M. Yan, Phys. Rev. Lett. 25 (1970) 316.

[9] For a recent review see, R. K. Ellis and W. J. Stirling, Fermilab-conf-90/164-T.

[10] B. L. Combridge, Nucl. Phys. B151 (1979) 429.
K. Hagiwara and T. Yoshino, Phys. Lett 80B (1979) 282.
L. M. Jones and H. Wyld, Phys. Rev. D17 (1978) 759.
H. Georgi *et al.*, Ann. Phys. (N.Y.) 114 (1978) 273.
J. Babcock, D. Sivers and S. Wolfram, Phys. Rev. D 18 (1978) 162.

[11] J. C. Collins, D. E. Soper and G. Sterman, Nucl. Phys. B263 (1986) 37.

[12] E. L. Berger, in *Hadrons, Quarks, and Gluons*, Proceedings of the XXII Recontre de Moriond, Les Arcs, France, edited by J. Tran Thanh Van (Editions Frontières, France, 1987) pp. 3-40.
E. L. Berger, Nucl. Phys. B (Proc. Suppl.) 1B (1988) 425.
E. L. Berger, Phys. Rev. D37 (1988) 1810.

[13] P. Nason, S. Dawson and R. K. Ellis, Nucl. Phys. B303 (1988) 607.
G. Altarelli, M. Diemoz, G. Martinelli and P. Nason, Nucl. Phys. B308 (1988) 724.
W. Beenakker, H. Kuijf, W. L. van Neeven and J. Smith, Phys. Rev. D40 (1989) 54.

[14] P. Nason, S. Dawson and R. K. Ellis, Nucl. Phys. B327 (1989) 49.

[15] A. H. Mueller and P. Nason, Phys. Lett. B157 (1985) 226.

[16] B. L. Combridge, Nucl. Phys. B151 (1979) 429.
R. Odorico, Nucl. Phys. B209 (1982) 77.

[17] C. Albajar *et al.*, CERN-PPE/90-155 Rev (1990), Submitted to Phys. Lett. B.
C. Albajar *et al.*, Phys. Lett. B186 (1987) 237.
C. Albajar *et al.*, Phys. Lett. B213 (1988) 405.
N. Ellis and A. Kernan, Phys. Rep. 195 (1990) 23.

[18] F. Abe *et al.*, Nucl. Instrm. Methods A271 (1988) 387.

[19] H. Minemura *et al.*, Nucl. Instrm. Methods A238 (1985) 18

[20] F. Snider *et al.*, Nucl. Instrm. Methods A268 (1988) 75.

[21] F. Bedeschi *et al.*, Nucl. Instrm. Methods A268 (1988) 50.

[22] L. Balka *et al.*, Nucl. Instrm. Methods A267 (1988) 272.

[23] T. Kamon *et al.*, Nucl. Instrm. Methods A213 (1983) 261.

[24] S. R. Hahn *et al.*, Nucl. Instrm. Methods A267 (1989) 351.

[25] K. Yasuoka *et al.*, Nucl. Instrm. Methods A267 (1989) 315.

[26] R. G. Wagner *et al.*, Nucl. Instrm. Methods A267 (1989) 330.

[27] S. Bertolucci *et al.*, Nucl. Instrm. Methods A267 (1988) 301.

[28] G. Drake *et al.*, Nucl. Instrm. Methods A269 (1988) 68.

[29] E. Barsotti *et al.*, Nucl. Instrm. Methods A269 (1988) 82.

[30] D. Amidei *et al.*, Nucl. Instrm. Methods A269 (1988) 51.

[31] G. W. Foster *et al.*, Nucl. Instrm. Methods A269 (1988) 93.

[32] G. Ascoli *et al.*, Nucl. Instrm. Methods A269 (1988) 63.

[33] H. Areti *et al.*, Proc. 23rd Conf. on High Energy Physics, Berkeley, California (July 1986).

[34] F. Abe *et al.*, Phys. Rev. D44 (1991) 29.

[35] R. E. Blair, J. Proudfoot and A. B. Wicklund, CDF 634 (1988).
J. Proudfoot, in *Calorimetry for the Superconductiong Supercollider*, proceedings, Alabama, 1989, edited by R. Donaldson and M. Gilchriese (World Scientific, Singapore, 1989).

[36] N. Solomey and A. B. Wicklund, CDF 247 (1984).

[37] J. Proudfoot, F. Ukegawa, A. B. Wicklund, CDF 933 (1989).

[38] M. Binkley and J. Hinkelman, CDF 841 (1988).

[39] J. Proudfoot, CDF 1011 (1989).

[40] B. Rossi, *High-Energy Particles*, Prentice-Hall.

[41] F. E. Paige and S. D. Protopopescu, BNL-38034 (1986).

[42] A. B. Wicklund and F. Ukegawa, CDF 1439 (1991).

[43] A. B. Wicklund and F. Ukegawa, CDF 1408 (1991).

[44] P. Avery, K. Read and G. Trahern, "QQ: A Monte Carlo Generator (Revised Standard Version)", CSN-212, March 1985.
The computer program is provided by Themis Bowcock.

[45] Mark Worris, private communication.

[46] N. Isgur, D. Scrota, B. Grinstein and M. Wise, Phys. Rev. D39 (1089) 799.

[47] See for example, R. M. Harris, Fermilab-Conf-90/118-E and the Proceedings of the Workshop on Hadron Structure Functions and Parton Distributions, Batavia, Illinois, April 1990.

[48] Y. S. Tsai, Rev. Mod. Phys. 46 (1974) 815; see Eq. 3.84.

[49] A. B. Wicklund, CDF 1233 (1990).

[50] Robert G. Wagner, CDF 1335 (1991).

[51] H. Albrecht *et al.*, Preprint DESY 90-088, July 1990.

[52] R. Fulton *et al.*, Phys. Rev. D43 (1991) 651.

[53] J. Freeman, Proceedings of the Workshop on Detector Simulation for the SSC, edited by L. E. Price, Argonne National Laboratory (1987), p. 190.

[54] M. Suzuki, Phys. Lett. 71B (1977) 139.
J. D. Bjorken, Phys. Rev. D17, (1978) 171.

[55] C. Peterson, D. Schlatter, I. Schmitt and P. M. Zerwas, Phys. Rev. D27 (1983) 105.

[56] J. Chrin, Z. Phys. C36 (1987) 165.
See also, S. Bethke, Z. Phys. C29 (1085) 175; W. Bartel *et al.*, Z. Phys. C33 (1987) 339.

[57] ALEPH Collaboration, D. Decamp *et al.*, Phys. Lett. B244 (1990) 551.

[58] R. Hughes *et al.*, CDF 1507 (1991); CDF 1382 (1991).

[59] R. D. Field and R. P. Feynman, Phys. Rev. D15 (1977) 2590.
R. D. Field and R. P. Feynman, Nucl. Phys. B136 (1978) 1.

[60] B. Adeba *et al.*, Phys. Rev. Lett. 51 (1983) 443.
M. Althoff *et al.*, Z. Phys. C22 (1984) 219.
M. Althoff *et al.*, Phys. Lett. 146B (1984) 443.
W. Bartel *et al.*, Z. Phys. C33 (1987) 339.
B. Fernandez *et al.*, Phys. Rev. Lett. 50 (1983) 2054.
T. Pal *et al.*, Phys. Rev. D33 (1986) 2708.
D. E. Koop *et al.*, Phys. Rev. Lett. 52 (1984) 970.
H. Aihara *et al.*, Phys. Rev. D31 (1985) 2719.
H. Aihara *et al.*, Z. Phys. C27 (1985) 39.
M. E. Nelson *et al.*, Phys. Rev. Lett. 50 (1983) 1542.

[61] M. Althoff *et al.*, Phys. Lett. 135B (1984) 243.
P. Kesten *et al.*, Phys. Lett. 161b (1985) 412.

M. Rowson *et al.*, Phys. Rev. Lett. 54 (1985) 2580.
H. Aihara *et al.*, Phys. Lett. 184B (1987) 299.
M. Sakuda *et al.*, Phys. Lett. 152B (1985) 399.

[62] E. H. Thorndike, Ann. Rev. Nucl. Part. Sci. 35 (1985) 195.
E. H. Thorndike and R. A. Poling, Phys. Rep. 157 (1988) 183.
H. Schröder, Rep. Prog. Phys. 52 (1989) 765.
B. Gittelman and S. Stone, in *High Energy Electron-Positron Physics*, ed. by A. Ali and P. Söding (World Scientific, Singapore, 1988).

[63] For a recent review see, R. J. Morrison and M. S. Witherell, Ann. Rev. Nucl. Part. Sci. 39 (1989) 183; D. G. Hitlin, preprint CALT-68-1420 (1987).

[64] S. Weinberg, Phys. Rev. Lett. 19 (1967) 1264.
A. Salam, in *Elementary Particle Physics: Relativistic Groups and Analyticity* (Nobel Symposium No.8), ed. by N. Svartholm (Almquist and Wiskell, Stockholm, 1968).

[65] M. Kobayashi and T. Maskawa, Progr. Theor. Phys. 49 (1973) 652.

[66] N. Cabbibo, Phys. Rev. Lett. 10 (1963) 581.

[67] Particle Data Group, Phys. Lett. B239 (1990) 1.

[68] R. M. Baltrusaitis *et al.*, Phys. Rev. Lett. 54 (1985) 1976.

[69] A. Chen *et al.*, Phys. Rev. Lett. 52 (1984) 1084.
C. Klopfenstein *et al.*, Phys. Lett. B130 (1983) 444.
G. Levman *et al.*, Phys. Lett. B141 (1984) 271.
S. Behrends *et al.*, Phys. Rev. Lett. 59 (1987).

[70] M. E. Nelson *et al.*, Phys. Rev. Lett. 50 (1983) 1542.
G. G. Hanson, Proc. Intern. Europhysics Conf. on High Energy Physics, Brighton,

Didcot; Rutherford Appleton Lab (1983) p. 147.

S. Stone, Proc. 1983 Intern. Symp, on Lepton Photon Interactions at High Energies, eds. D. G. Cassel and D. L. Kreinick (Cornell, 1983) p.203.

T. Pal *et al.*, Phys. Rev. D33 (1986) 2708.

H. Aihara *et al.*, Z. Phys. C27 (1985) 39.

H. Aihara *et al.*, Phys. Rev. D31 (1985) 2719.

B. Adeva *et al.*, Phys. Rev. Lett. 58 (1987) 339.

M. Althoff *et al.*, Z. Phys. C22 (1984) 219.

H.-J. Behrend *et al.*, Z. Phys. C19 (1983) 291.

W. Bartel *et al.*, Z. Phys. C33 (1987) 339.

[71] C. Albajar *et al.*, Phys. Lett. 186B (1987) 247.

[72] H. Albrecht *et al.*, Phys. Lett. 192B (1987) 245.

[73] H. Albrecht *et al.*, Phys. Lett. B209 (1988) 119.

[74] C. Bebek *et al.*, Phys. Rev. Lett. 62 (1989) 8.

D. Bortoletto *et al.*, Phys. Rev. Lett. 62 (1989) 2436.

[75] T. Kamon and F. Ukegawa, CDF 618 (1988).

[76] Robert M. Harris, CDF 1329 (1991).